

Feedback control and injection locking of the sawtooth oscillation in fusion plasmas

Citation for published version (APA):

Witvoet, G. (2011). *Feedback control and injection locking of the sawtooth oscillation in fusion plasmas*. [Phd Thesis 1 (Research TU/e / Graduation TU/e), Mechanical Engineering]. Technische Universiteit Eindhoven. <https://doi.org/10.6100/IR719868>

DOI:

[10.6100/IR719868](https://doi.org/10.6100/IR719868)

Document status and date:

Published: 01/01/2011

Document Version:

Publisher's PDF, also known as Version of Record (includes final page, issue and volume numbers)

Please check the document version of this publication:

- A submitted manuscript is the version of the article upon submission and before peer-review. There can be important differences between the submitted version and the official published version of record. People interested in the research are advised to contact the author for the final version of the publication, or visit the DOI to the publisher's website.
- The final author version and the galley proof are versions of the publication after peer review.
- The final published version features the final layout of the paper including the volume, issue and page numbers.

[Link to publication](#)

General rights

Copyright and moral rights for the publications made accessible in the public portal are retained by the authors and/or other copyright owners and it is a condition of accessing publications that users recognise and abide by the legal requirements associated with these rights.

- Users may download and print one copy of any publication from the public portal for the purpose of private study or research.
- You may not further distribute the material or use it for any profit-making activity or commercial gain
- You may freely distribute the URL identifying the publication in the public portal.

If the publication is distributed under the terms of Article 25fa of the Dutch Copyright Act, indicated by the "Taverne" license above, please follow below link for the End User Agreement:

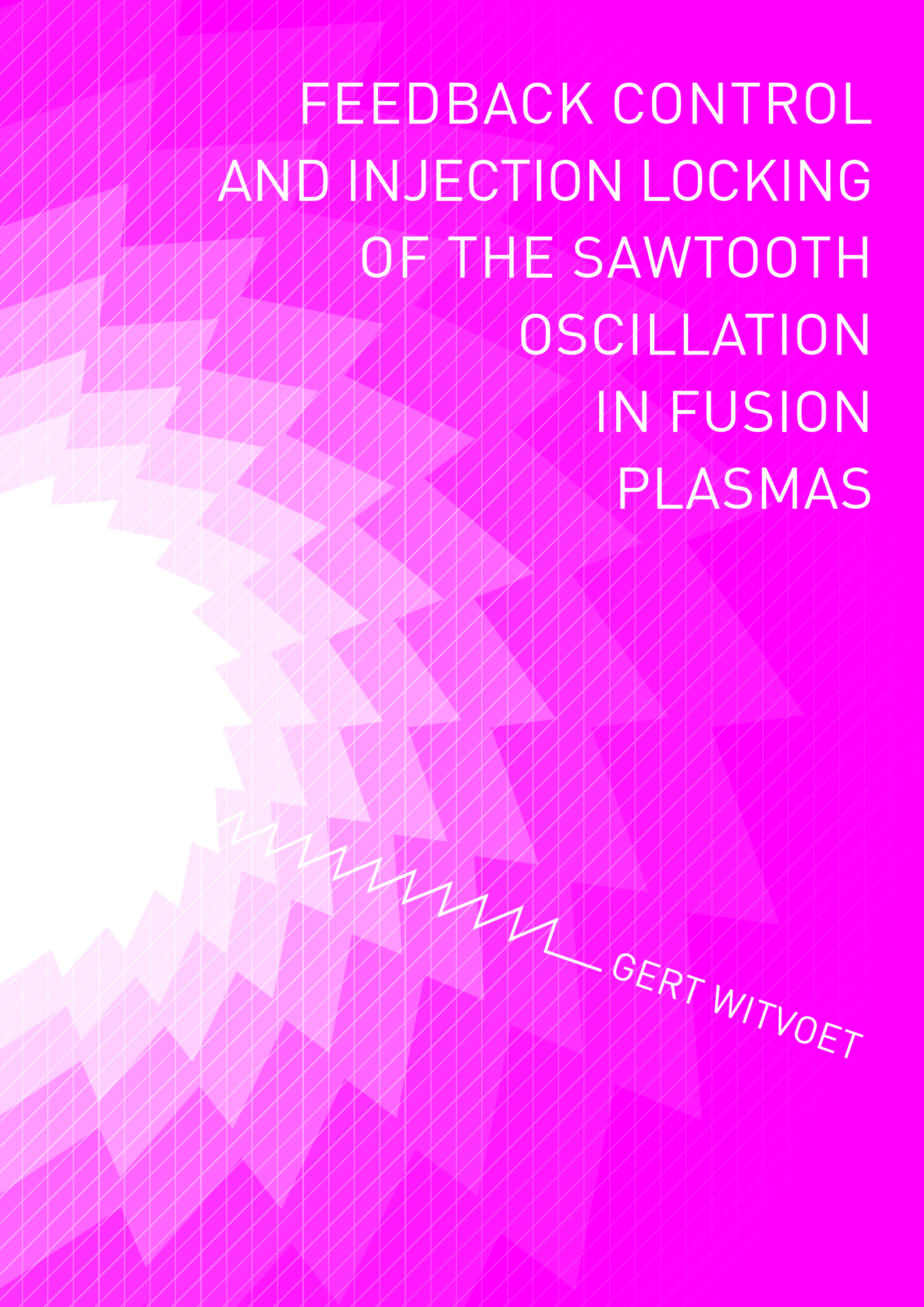
www.tue.nl/taverne

Take down policy

If you believe that this document breaches copyright please contact us at:

openaccess@tue.nl

providing details and we will investigate your claim.



FEEDBACK CONTROL
AND INJECTION LOCKING
OF THE SAWTOOTH
OSCILLATION
IN FUSION
PLASMAS



GERT WITVOET

**Feedback control and injection locking
of the sawtooth oscillation in fusion
plasmas**



The research presented in this thesis has been performed within the framework of the NWO-RFBR Centre of Excellence (grant 047.018.002) on Fusion Physics and Technology, as part of the research programme of the Foundation for Fundamental Research on Matter (FOM), which is part of the Netherlands Organisation for Scientific Research (NWO). This work, supported by ITER-NL and the European Communities under the contract of the Association EURATOM/FOM, was carried out within the framework of the European Fusion Programme. The views and opinions expressed in this thesis do not necessarily reflect those of the European Commission. The research was carried out partially at TNO Technical Sciences, in collaboration with the FOM-Institute for plasma physics Rijnhuizen.

disc

The research reported in this thesis is part of the research program of the Dutch Institute of Systems and Control (DISC). The author has successfully completed the educational program of the DISC graduate school.

Feedback control and injection locking of the sawtooth oscillation in fusion plasmas by Gert Witvoet – Eindhoven: Technische Universiteit Eindhoven, 2011 – Proefschrift.

A catalogue record is available from the Eindhoven University of Technology Library.
ISBN: 978-90-386-3030-4.

Typeset by the author in pdfL^AT_EX.

Reproduction: Ipskamp Drukkers B.V., Enschede, The Netherlands.

Cover design: Oranje Vormgevers, Eindhoven, The Netherlands.

Copyright © 2011 by G. Witvoet. All rights reserved.

Feedback control and injection locking of the sawtooth oscillation in fusion plasmas

PROEFSCHRIFT

ter verkrijging van de graad van doctor
aan de Technische Universiteit Eindhoven,
op gezag van de rector magnificus, prof.dr.ir. C.J. van Duijn,
voor een commissie aangewezen door het College voor Promoties
in het openbaar te verdedigen
op woensdag 21 december 2011 om 16.00 uur

door

Gerrit Witvoet

geboren te Leiden

Dit proefschrift is goedgekeurd door de promotoren:

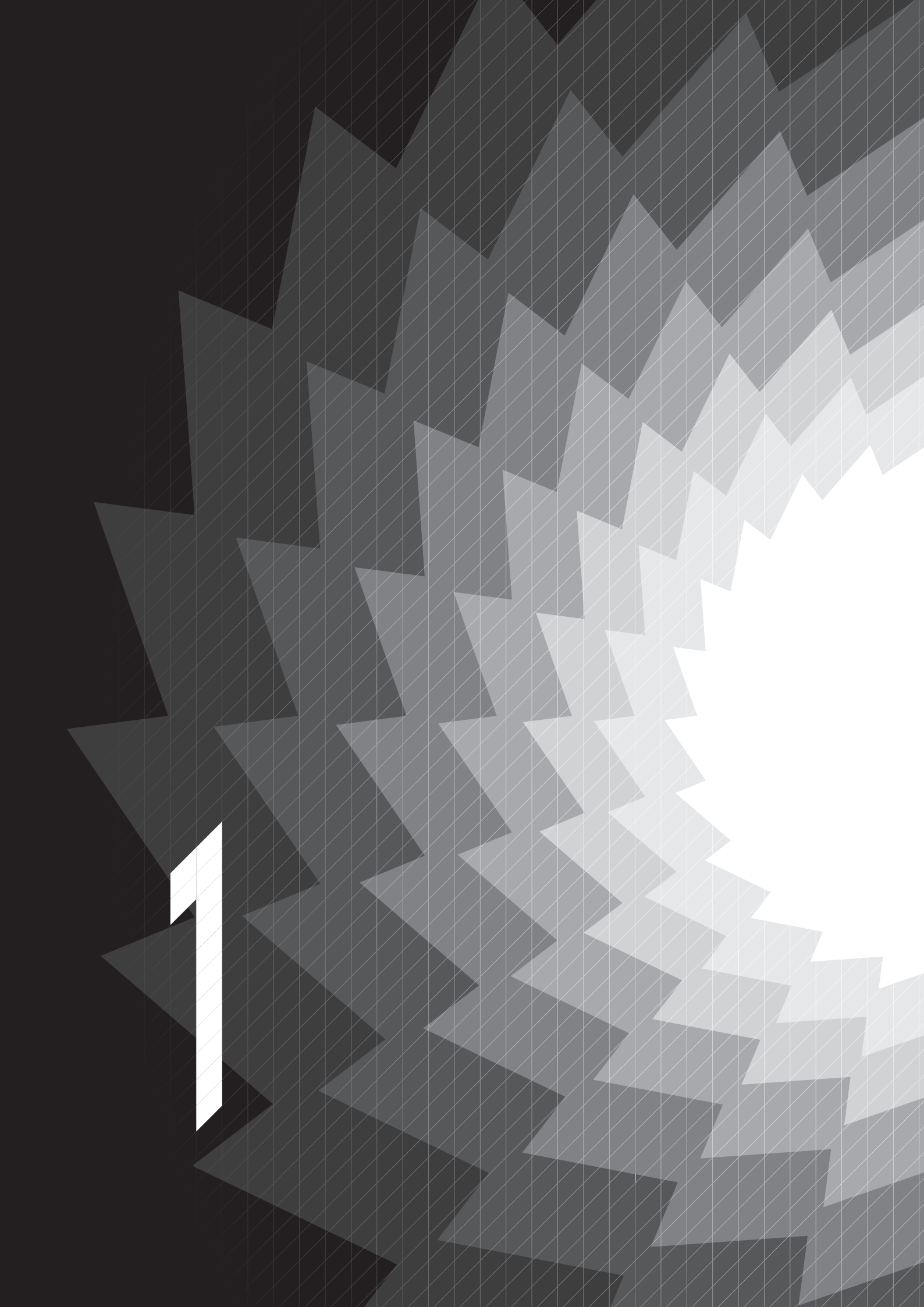
prof.dr.ir. M. Steinbuch
en
prof.dr. M.R. de Baar

Copromotor:
dr. E. Westerhof

Contents

1	Introduction	9
1.1	Nuclear fusion	10
1.2	The tokamak	10
1.3	The sawtooth instability	12
1.4	The sawtooth period control problem	14
1.5	Overview of this thesis	17
2	Systematic design of a sawtooth period feedback controller using a Kadomtsev–Porcelli sawtooth model	21
2.1	Introduction	22
2.2	The sawtooth model	24
2.3	Control-oriented system analysis	31
2.4	Controller design and simulation results	38
2.5	Influence of mirror launcher and period detection	44
2.6	Conclusions, future work and discussion	50
3	Sawtooth period control strategies and designs for improved performance	55
3.1	Introduction	56
3.2	The sawtooth model and its dynamic representation	57
3.3	Performance improving control strategies	62
3.4	Conclusions and discussion	77
4	Robust sawtooth period control based on adaptive online optimization	81
4.1	Introduction	82
4.2	Control problem formulation	84
4.3	Fundamentals of extremum seeking for sawtooth period control	86
4.4	Extremum seeking controller design	88
4.5	Simulation results	96

4.6	Extremum seeking and performance	104
4.7	Conclusions	106
5	Real-time determination of the sawtooth period using multi-scale wavelet analysis	111
5.1	Introduction	112
5.2	Methodology	113
5.3	Real-time implementation	122
5.4	Results	125
5.5	Conclusions	131
6	Numerical demonstration of injection locking of the sawtooth period by means of modulated EC current drive	135
6.1	Introduction	136
6.2	Methodology	138
6.3	Sawtooth locking results	142
6.4	Open-loop locking controller design	156
6.5	Conclusions and discussion	159
7	Demonstration of sawtooth period locking in TCV plasmas	165
7.1	Introduction	166
7.2	Experimental set-up	167
7.3	Predictive simulations	167
7.4	Experimental results	168
7.5	Conclusions	174
8	Conclusions, discussion and outlook	179
8.1	Conclusions	179
8.2	Discussion	181
8.3	Outlook	182
	Bibliography	195
	Summary	197
	Dankwoord	201
	Curriculum Vitae	205



CHAPTER 1

Introduction



Abstract

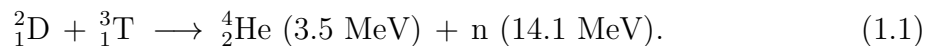
The sawtooth instability is an important repetitive phenomenon in the core of nuclear fusion tokamak plasmas. Its periodicity has an effect on both the triggering of neoclassical tearing modes (NTMs) and the regulation of fuels and ash in the plasma core. In this thesis a variety of strategies to control this sawtooth period is discussed, including various feedback controller designs and an open-loop injection locking technique.

In this chapter a short introduction on nuclear fusion and tokamaks is presented. This is followed by a more detailed discussion on the sawtooth instability, its importance and several actuation schemes to influence it. Finally, the accompanying sawtooth period control problem considered in this thesis is introduced.

1.1 Nuclear fusion

Nuclear fusion is the power source of our sun and other stars. It involves the coalescence, or fusion, of light atomic nuclei into a single heavier nucleus, which is generally accompanied by the release of an enormous amount of energy. The released energy is caused by the mass deficiency Δm of the process, i.e. the heavier nucleus (the product) weighs less than the sum of the lighter nuclei (the fuels), and is in accordance to Einstein's mass–energy equivalence $E = \Delta mc^2$.

In principle, a few milligrams of fusion fuels can produce the same amount of energy as a couple of barrels of oil. Moreover, fusion does not produce any greenhouse gasses and its fuels are abundantly available. For these reasons nuclear fusion is foreseen to be a viable energy source for the future to meet the globally increasing energy demand [1,2]. Although fusion reactions can occur between many different light nuclei, the primary candidate for use in a future reactor is the fusion between deuterium (D) and tritium (T), two hydrogen isotopes, producing helium (He) and a neutron (n):



Bringing the fuels together also requires a considerable amount of energy, as these nuclei are both positively charged and thus repel each other. In a fusion reactor this energy should be supplied by the fusion reaction itself, thereby maintaining the fusion process; this is referred to as *ignition*. The requirement for ignition has been formalized in the Lawson criterion [3]

$$n \cdot T \cdot \tau_E \geq \text{critical value}, \quad (1.2)$$

where n is the plasma density, T its temperature and τ_E is the energy confinement time. Expressed in simple words, (1.2) states that in order to achieve ignition there should be many nuclei close together (high n), moving with very high speeds (high T) for a sufficiently long amount of time (high τ_E). In practice this implies that the fuels need to be heated to extreme temperatures in the order of 10 keV (which is more than 100×10^6 K). At these temperatures all atoms are ionized, creating a gaseous state of separated nuclei and electrons called a *plasma*.

1.2 The tokamak

Confinement of such a hot ionized plasma can be achieved by means of a magnetic field. One of the most promising magnetic configurations is the *tokamak* [4], depicted in figure 1.1, consisting of a toroidal vessel in which the plasma resides, surrounded by external coils. The required helical magnetic field consists of: (1) the toroidal magnetic field B_ϕ produced by the coils surrounding the vessel; and (2) the poloidal field B_θ produced by the current inside the plasma. This current is induced by the transformer coils in the centre of the torus, where the plasma itself acts as the secondary winding of the transformer. Due to the non-zero plasma resistivity this current also heats the

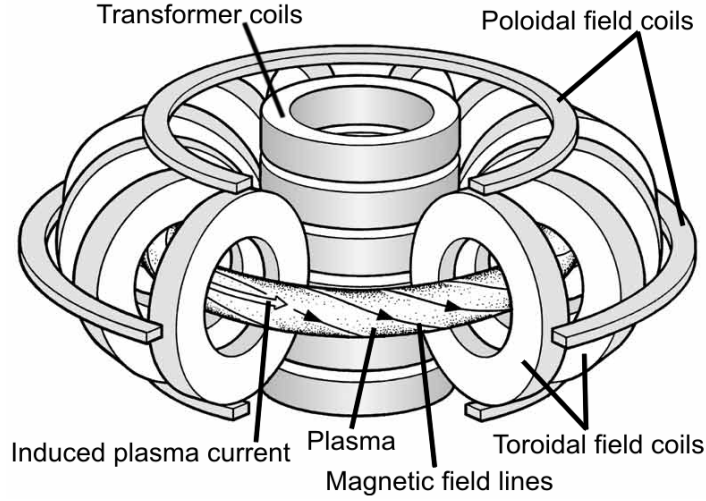


Figure 1.1: Representation of a tokamak, showing the plasma and the external coils.

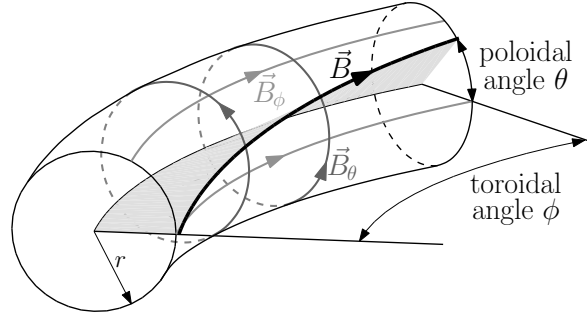


Figure 1.2: Illustration of the toroidal and poloidal field \vec{B}_ϕ and \vec{B}_θ , and the geometric variables r , ϕ and θ .

plasma, which is referred to as ohmic heating. The additional poloidal field coils in figure 1.1 are meant to alter the plasma position and shape.

The magnetic field \vec{B} inside a tokamak is such that there are surfaces of constant magnetic flux, which form nested toroidal tubes; a magnetic field line remains on the same flux surface as it goes around the tokamak. Consequently, transport of energy and particles is extremely fast along a flux surface, so quantities like temperature and pressure are uniform on such a surface. Hence, such quantities only vary in a direction perpendicular to the flux surfaces, which for circular cross-section tokamaks coincides with the radial coordinate r . The same holds for the safety factor q (the magnetic ‘pitch’) and the magnetic shear s . Under the assumption of circular large aspect-ratio tokamaks, which is used throughout this thesis, these q and s are defined as

$$q(r) = \frac{rB_\phi}{R_0B_\theta} \quad \text{and} \quad s(r) = \frac{r}{q} \frac{dq}{dr}, \quad (1.3)$$

where R_0 is the tokamak major radius. Some of the aforementioned geometric and magnetic variables are illustrated in figure 1.2.

Present-day tokamaks are equipped with various supplementary actuation schemes for additional heating and current drive. These include neutral beam injection (NBI),

and absorption of ion cyclotron waves (ICW), electron cyclotron waves (ECW) and lower hybrid waves (LHW) into the plasma. This thesis will mainly focus on the current drive effect of ECW, which is known as electron cyclotron current drive (ECCD).

ECCD involves the injection of an electromagnetic wave with a frequency ω into the plasma which is resonant with the electron cyclotron frequency ω_{ce} , i.e. $\omega = n\omega_{ce}$, where $\omega_{ce} = eB_\phi/m_e$, n is the harmonic number, e is the charge of an electron and m_e is its mass. Since $B_\phi \propto \frac{1}{R}$, where R denotes a distance to the centre of the torus, ω_{ce} depends on R and hence the energy of the wave is absorbed at a specific deposition location. This results in a driven current (and heating) at the same location.

The performance of a tokamak plasma is often expressed in terms of the normalized plasma pressure β (the ratio of the internal plasma pressure to the external pressure of the magnetic field). In a fusion reactor this pressure should be high in order to reach ignition. Unfortunately, high pressure plasmas are susceptible to various instabilities which can deteriorate the plasma performance [5]. One of these instabilities is the *sawtooth instability*, or sawtooth oscillation, which is the central topic of this thesis.

1.3 The sawtooth instability

The sawtooth instability is a periodic phenomenon which leads to a reorganization of the plasma core [6–8]. A typical sawtooth cycle comprises a slow ‘ramp’ of the plasma temperature and pressure, followed by a rapid ‘crash’, as illustrated in the electron cyclotron emission (ECE) measurements from the TEXTOR tokamak shown in figure 1.3. During the crash energy and particles in the hot plasma centre are mixed with colder outer regions, leading to a flattening of the temperature and pressure profiles. Afterwards, the profiles slowly restore again, and the cycle restarts. Consequently, measurements close to the plasma centre display upward ramps and downward crashes (channels 1 and 2), while more outward measurements display the inverse behaviour (channels 4 and 5). The location where the crash changes sign, i.e. where the temperature is roughly constant, is called the inversion radius (channel 3).

1.3.1 The physics of the sawtooth

The sawtooth instability manifests itself in the plasma core, and is directly related to the presence of a $q = 1$ surface. Although the physics of sawtooth is not fully understood, it is believed that the sawtooth crash is triggered by the $m = n = 1$ internal kink mode, which is a magnetohydrodynamic (MHD) instability leading to the kinking of the magnetic surfaces [9]. This internal kink mode can manifest itself as an *ideal* or as a *resistive* internal kink mode. This thesis only focuses on the latter, which is the most common type.

The onset of the resistive kink mode has been modelled by Porcelli *et al* [10], which in most cases can be simplified to a critical shear condition. This implies that a sawtooth crash occurs whenever the magnetic shear on the $q = 1$ surface exceeds a

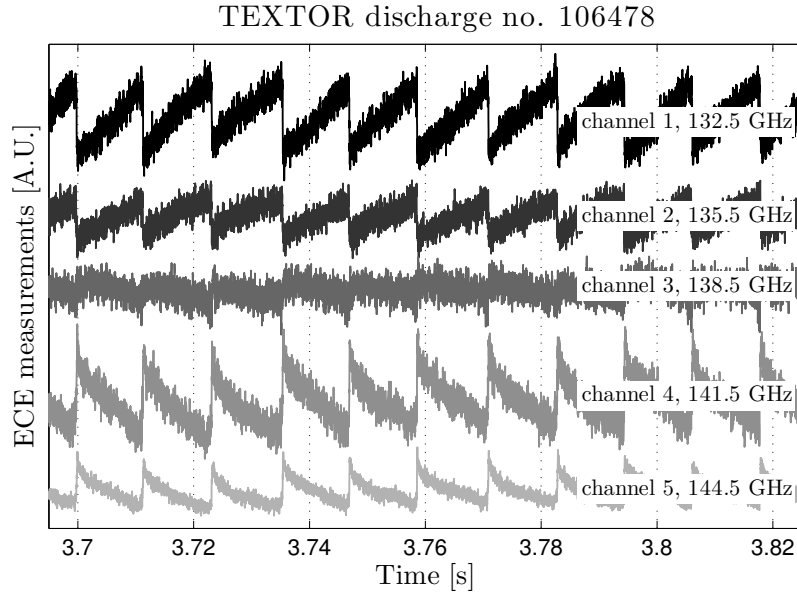


Figure 1.3: Raw line-of-sight ECE data from TEXTOR discharge no. 106478. The channel frequency indicates the measurement location; smaller frequencies measure closer to the plasma centre.

certain threshold value s_{crit} . What happens at the crash itself is still subject of debate. A well known model is the one by Kadomtsev [11], which is based on the magnetic reconnection of flux surfaces around the $q = 1$ surface. As such it describes the creation and rapid growth of a magnetic island, which eventually ‘replaces’ the plasma core. Although there is experimental evidence against this model, and several extensions and alternatives have been proposed [8, 12, 13], e.g. based on high- n ballooning modes [14, 15], it is still a commonly used crash model in simulations, due to its elegance and consistency with resistive MHD calculations. In this thesis a combination of the models by Porcelli and Kadomtsev will be used to analyse the sawtooth behaviour.

1.3.2 The relevance of the sawtooth period

By itself the sawtooth instability is not considered to be particularly harmful to the plasma. However, its influence on other plasma processes and instabilities makes it very relevant. It has been shown that sawtooth crashes can trigger edge localized modes (ELMs) [16], which can produce large heat loads on the vessel wall. More importantly, sawtooth crashes can provide the seed for the development of neoclassical tearing modes (NTMs) [17, 18], which are accompanied by a reduction of energy confinement and can even lead to a disruption. It should be noted that it is not so much the amplitude of the magnetic perturbation at the crash that provides this seed. Experiments have revealed that there is a much stronger correlation between the sawtooth *period* and the occurrence of NTMs [19, 20]; long sawteeth are likely to trigger NTMs, even for low β discharges. Hence, it is often desirable to have small sawtooth periods in order to limit the growth of seed islands for NTMs [21].

Moreover, the mixing effect of the sawtooth instability drives many transport processes in the plasma core, which can be beneficial. The sawtooth period affects the concentration of α particles (energetic helium), influences the exhaust of thermal helium ash and impurities from the plasma core [22] and can possibly regulate the refuelling of deuterium and tritium into the core. As such, the sawtooth can influence the fusion burn rate. Instead of fully suppressing the sawtooth instability, it is therefore desirable to have control over its period, in order to be able to optimize between its benefits and drawbacks.

Control of the sawtooth period will especially be important on future fusion reactors like ITER, the world's largest fusion test reactor currently being built in Cadarache (France). Since fast particles have been shown to lengthen the period of the sawtooth [23, 24], it is expected that the fusion-born α particles on ITER will lead to very long sawtooth periods [25, 26], thereby triggering NTMs, which possibly results in a disruption. Hence, on such devices there is a clear need for tools and methodologies to shorten the sawtooth period.

1.3.3 Sawtooth period actuators

Identifying suitable actuators for the sawtooth period has a long history, see [9] and references therein. Various different current drive and heating schemes have experimentally been explored to either lengthen or shorten the sawtooth period [27]. These actuators aim to either alter the magnetic shear around the $q = 1$ surface, or affect the orbits of energetic ions with respect to the $q = 1$ surface. As such, the period has been influenced by NBI [28–31], ion cyclotron resonance heating (ICRH) [23, 32, 33] and ECCD [34–37]. The latter has been shown to be particularly effective, yielding a highly localized current drive near $q = 1$, thereby allowing shortening of the period with a relatively small amount of power. Both ICRH and ECCD are envisaged to be used for sawtooth control on ITER. In this thesis we only focus on ECCD and its effect on the magnetic shear.

1.4 The sawtooth period control problem

The publications mentioned in section 1.3.3 mainly address the open-loop response of the period to specific actuator settings. The first closed-loop sawtooth period control experiments utilizing the ECCD actuator, as schematically depicted in figure 1.4, have been reported in [38–42], although a systematic design of the required feedback controller has not been presented. Moreover, a rigorous analysis of the dynamics of the sawtooth period, whereupon such a controller should be based, is still lacking.

Complementing these developments, this thesis focuses on the derivation of control strategies for the sawtooth period, such that the period is forced to and maintained around a certain desired value. To this end, the behaviour of the period is represented in a discrete-time framework, its (dynamic) input–output behaviour is analysed and

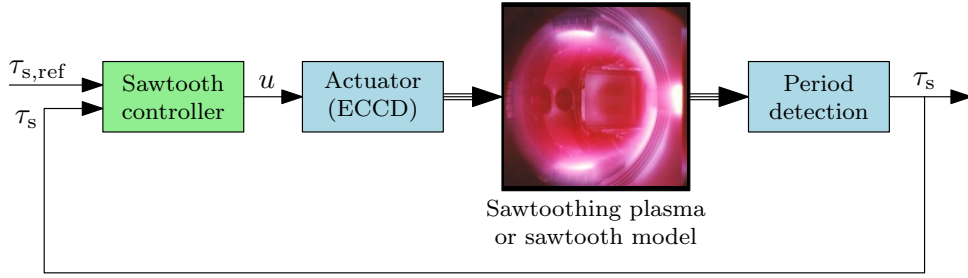


Figure 1.4: Schematic representation of the feedback control loop for the sawtooth period.

subsequent control schemes are deduced, both in a closed-loop and open-loop approach. In this work a combined Kadomtsev–Porcelli model is used as a case study.

Any controller design should start with a formulation of the requirements. What is the required accuracy, how fast does the period need to converge to the desired value, how large are the uncertainties of the system, which disturbances are present and how much should they be attenuated, etc. Unfortunately, for the sawtooth control problem the answers to most of these questions are still unknown, or at least difficult to define. It is uncertain how long typical sawteeth will be on ITER, and which periods will trigger NTMs. It is uncertain which disturbances will be present, and under which conditions a sawtooth controller should operate. As of yet, burning plasmas have never been achieved in a tokamak, hence, their behaviour is still unsure. Although much can be extrapolated from physics models, the true requirements for exhaust and refuelling in burning plasmas, as for their repercussions on the specifications for the sawtooth period, will have to follow from future ITER experiments. At present, the fusion community is simply not able to define what to expect from a sawtooth period controller, and under which circumstances it should work.

In the absence of requirements, this thesis will therefore show what control engineering is actually capable of. First, closed-loop control of the period is discussed, as depicted in figure 1.4. This encompasses the control-oriented modelling of the sawtooth plasma, and the subsequent design of a sawtooth controller which computes an input signal u for the ECCD actuator (e.g. required gyrotron power and/or deposition location) based on measurements of the sawtooth period τ_s , such that this period tracks a desired value $\tau_{s,ref}$ (i.e. $\tau_s \approx \tau_{s,ref}$). Three different feedback controller design approaches are discussed, each having a different objective, namely

- low complexity,
- high performance,
- high robustness.

In the first approach the controller is designed using standard linear control theory. Its simplicity makes it easily applicable to sawtooth models and tokamak experiments, but although its parameters are optimized, its closed-loop performance is limited. The closed-loop performance is largely improved in the second design approach, i.e. the steady-state error (the difference between τ_s and the desired $\tau_{s,ref}$ in steady state) and

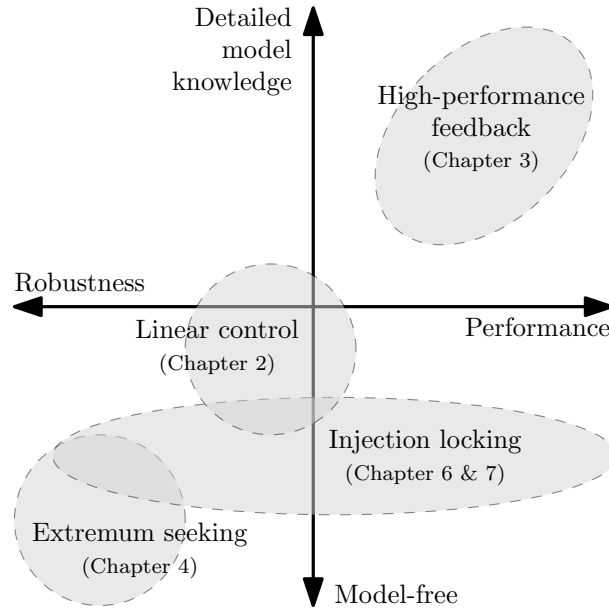


Figure 1.5: Schematic overview of the controllers presented in this thesis, in terms of their performance, robustness and required knowledge of the sawtooth dynamics.

the settling time (time it takes until $\tau_s \approx \tau_{s,\text{ref}}$) are minimized. This high-performance approach requires accurate knowledge of the sawtooth dynamics and assumes it to be (nearly) time-invariant. As such, this strategy is applicable to future fusion reactors, where plasmas are reproducible, the sawtooth dynamics is known or can be accurately measured and high performance is of uttermost importance to optimize the fusion power. In contrast, experimental devices, like present-day tokamaks, have different requirements. In the context of scientific plasma research, the operational conditions under which a sawtooth controller should work can be highly uncertain and subject to many different types of disturbances. As such, these devices call for a robust control strategy, while the closed-loop performance is only of secondary importance. This is the third approach presented in this thesis, called extremum seeking control. This strategy needs a minimum amount of information and is therefore directly applicable to any sawtooth model or tokamak experiment.

Each of the above feedback controllers require real-time sensing of the sawtooth period. This period τ_s has to be extracted from the available diagnostics (like ECE or soft x-ray measurements). To this end an accurate and robust period detection algorithm is presented in this thesis, which is applicable in real-time.

As an alternative to the aforementioned feedback control strategies, this thesis also presents a special type of open-loop sawtooth period control. In this injection locking technique the intrinsic dynamics of the sawtooth is employed to synchronize the sawtooth period with the input frequency. This methodology combines high performance with high robustness, and might therefore be applicable to both experimental devices and fusion reactors.

In conclusion, this thesis covers a wide spectrum of different sawtooth controllers.

Each controller is based on a different amount of knowledge of the sawtooth dynamics, yielding different levels of performance and robustness. A schematic representation of these approaches, and the chapters they are discussed in, is shown in figure 1.5.

1.5 Overview of this thesis

Chapter 2 introduces the Kadomtsev–Porcelli sawtooth model which has been derived and implemented during this research, and which is used throughout this thesis as a case study. This chapter presents a routine to identify the sawtooth period dynamics, and discusses the design of standard linear feedback controllers based on this knowledge. This chapter has recently been published in *Nuclear Fusion*.

Possible performance improvements of this methodology are presented in chapter 3. As such, it discusses a specific non-linear controller design, the utilization of other inputs and a subsequent multiple-input-multiple-output (MIMO) controller design. Opposed to this approach, chapter 4 discusses a highly robust feedback controller design, based on online gradient estimation and optimization. Both chapters have been submitted (separately) for publication in a *Nuclear Fusion* special issue.

In chapter 5 the period detection algorithm, which is required by the above feedback controllers, is presented. This algorithm is based on efficient multiresolution wavelet filtering, and has been tested on actual TEXTOR measurements. This chapter is based on a publication which recently appeared in *Fusion Engineering and Design*.

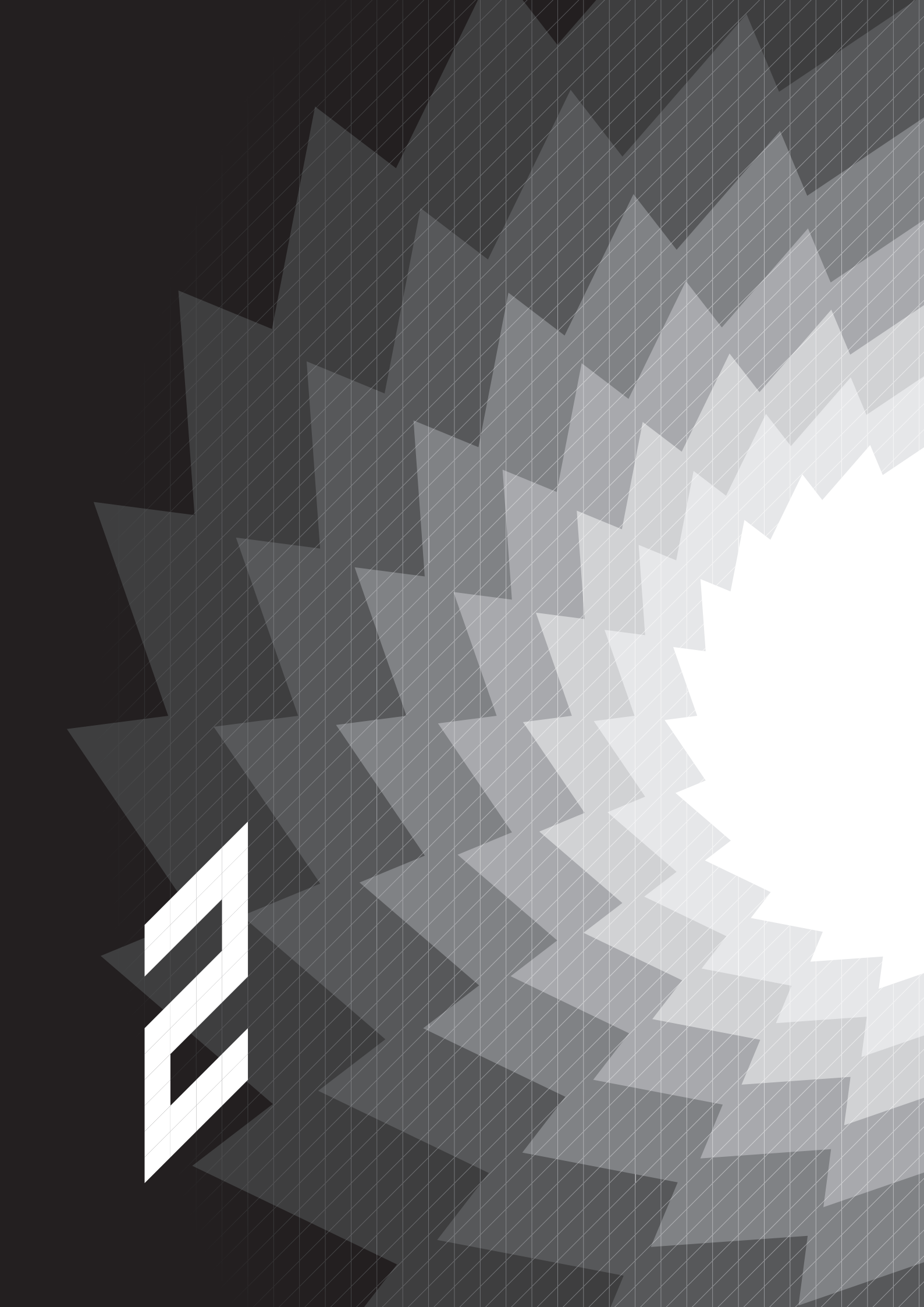
Chapter 6 discusses the use of modulated current drives to control the sawtooth period. This injection locking technique is applied to the Kadomtsev–Porcelli sawtooth model, on which results a simple open-loop controller is based. This chapter has recently been published in *Nuclear Fusion*. Experimental locking results are reported in chapter 7, which show good agreement with the simulations. The results in this chapter are taken from a paper which has been submitted to *Physical Review Letters*.

Finally, the important conclusions from the above chapters, as well as recommendations for further research, are summarized in chapter 8.

References

- [1] Pironti A. and Walker M.L. 2005 *IEEE Contr. Syst. Mag.* **25**(5) 24
- [2] Schultz K.R. 2006 *IEEE Contr. Syst. Mag.* **26**(2) 32
- [3] Lawson J.D. 1957 *Proc. Phys. Soc. B* **70**(1) 6
- [4] Wesson J.A. and Campbell D.J. 2004 *Tokamaks* 3rd edn. (Oxford: Oxford University Press)
- [5] Walker M.L. *et al.* 2006 *IEEE Contr. Syst. Mag.* **26**(2) 35
- [6] von Goeler S. *et al.* 1974 *Phys. Rev. Lett.* **33**(20) 1201
- [7] Vershkov V.A. and Mirnov S.V. 1974 *Nucl. Fusion* **14**(3) 383
- [8] Hastie R.J. 1997 *Astrophys. Space Sci.* **256**(1) 177
- [9] Chapman I.T. 2011 *Plasma Phys. Control. Fusion* **53**(1) 013001
- [10] Porcelli F. *et al.* 1996 *Plasma Phys. Control. Fusion* **38**(12) 2163

-
- [11] Kadomtsev B.B. 1975 *Sov. J. Plasma Phys.* **1**(5) 389
 - [12] Gimblett C.G. and Hastie R.J. 1994 *Plasma Phys. Control. Fusion* **36**(9) 1439
 - [13] Sykes A. and Wesson J.A. 1976 *Phys. Rev. Lett.* **37**(3) 140
 - [14] Park W. *et al.* 1991 *Phys. Fluids B* **3**(3) 507
 - [15] Nishimura Y. *et al.* 1999 *Phys. Plasmas* **6**(12) 4685
 - [16] Nave M.F.F. *et al.* 1995 *Nucl. Fusion* **35**(4) 409
 - [17] Sauter O. *et al.* 2002 *Phys. Rev. Lett.* **88**(10) 105001
 - [18] Gude A. *et al.* 1999 *Nucl. Fusion* **39**(1) 127
 - [19] Chapman I.T. *et al.* 2010 *Nucl. Fusion* **50**(10) 102001
 - [20] Buttery R. *et al.* 2004 *Nucl. Fusion* **44**(5) 678
 - [21] Westerhof E. *et al.* 2002 *Nucl. Fusion* **42**(11) 1324
 - [22] Nave M.F.F. *et al.* 2003 *Nucl. Fusion* **43**(10) 1204
 - [23] Campbell D.J. *et al.* 1988 *Phys. Rev. Lett.* **60**(21) 2148
 - [24] Chapman I.T. *et al.* 2009 *Nucl. Fusion* **49**(3) 035006
 - [25] Nave M.F.F. *et al.* 2002 *Nucl. Fusion* **42**(3) 281
 - [26] Chapman I.T. *et al.* 2007 *Plasma Phys. Control. Fusion* **49**(12B) B385
 - [27] Graves J.P. *et al.* 2005 *Plasma Phys. Control. Fusion* **47**(12B) B121
 - [28] Chapman I.T. *et al.* 2008 *Plasma Phys. Control. Fusion* **50**(4) 045006
 - [29] Nave M.F.F. *et al.* 2006 *Phys. Plasmas* **13**(1) 014503
 - [30] Chapman I.T. *et al.* 2008 *Nucl. Fusion* **48**(3) 035004
 - [31] Chapman I.T. *et al.* 2009 *Phys. Plasmas* **16**(7) 072506
 - [32] Graves J.P. *et al.* 2009 *Phys. Rev. Lett.* **102**(6) 065005
 - [33] Eriksson L.G. *et al.* 2006 *Nucl. Fusion* **46**(10) S951
 - [34] Westerhof E. *et al.* 2003 *Nucl. Fusion* **43**(11) 1371
 - [35] Mück A. *et al.* 2005 *Plasma Phys. Control. Fusion* **47**(10) 1633
 - [36] Angioni C. *et al.* 2003 *Nucl. Fusion* **43**(6) 455
 - [37] Ikeda Y. *et al.* 2002 *Nucl. Fusion* **42**(4) 375
 - [38] Lennholm M. *et al.* 2009 *Phys. Rev. Lett.* **102**(11) 115004
 - [39] Lennholm M. *et al.* 2009 *Fusion Sci. Technol.* **55**(1) 45
 - [40] Paley J.I. *et al.* 2009 *Nucl. Fusion* **49**(8) 085017
 - [41] Paley J.I. *et al.* 2009 *Plasma Phys. Control. Fusion* **51**(5) 055010
 - [42] Paley J.I. *et al.* 2009 *Plasma Phys. Control. Fusion* **51**(12) 124041



Systematic design of a sawtooth period feedback controller using a Kadomtsev–Porcelli sawtooth model

G. Witvoet^{a,b,c}, M.R. de Baar^{a,b}, E. Westerhof^b, M. Steinbuch^a
and N.J. Doelman^c

^a Eindhoven University of Technology

^b FOM-Institute for Plasma Physics Rijnhuizen

^c TNO Technical Sciences



Abstract

A systematic methodology for structured design of feedback controllers for the sawtooth period is presented, based on dedicated identification of the sawtooth dynamics. Therefore, a combined Kadomtsev–Porcelli model of a sawtoothing plasma actuated by an electron cyclotron current drive system has been set-up. This is used to derive the linearized input–output relations (transfer functions) from the varying deposition location of the electron cyclotron waves (ECW) to the sawtooth period. These transfer functions are derived around a large collection of operating points. Assessment of these control-relevant transfer functions shows that a sawtooth period controller requires an integral (I) action to guarantee closed-loop stability with zero steady-state error. Additional proportional-integral (PI) action can be applied to further increase the closed-loop performance. The parameters of both the I and PII controllers have been optimized in terms of stability, performance and robustness. Moreover, the effect of the mechanical ECW launcher on the closed-loop performance is studied for realistic cases. It is shown that the launcher dynamics seriously affects the achievable closed-loop performance in present-day experiments.

2.1 Introduction

The sawtooth is an instability cycle that leads to a repetitive reorganization of the plasma core [1–3]. The instability regulates the exhaust of Helium and α particles [4] and the influx of deuterium and tritium in a fusion reactor. The sawtooth is also associated with the triggering of neoclassical tearing modes (NTMs) well below the ideal β -limit [5,6], significantly reducing the operational performance of a reactor. The conflicting requirements for the processes of refuelling and exhaust, NTM avoidance, and α -confinement motivate the need for controlling the sawtooth behaviour, in particular the sawtooth period.

The sawtooth occurs when the $m = 1$ internal kink mode is driven unstable, the physics of which is associated with both the magnetic shear on the $q = 1$ surface [7] and the orbits of energetic ions with respect to the $q = 1$ surface [8–11]. It has been shown that the magnetic shear around the $q = 1$ surface can be actuated by electron cyclotron (EC) waves [12–14] and ion cyclotron (IC) waves [15], while the fast particle orbits can be affected by IC waves [11] and directional neutral beam injection (NBI) [10,16]. The above mentioned papers mainly address the open-loop response of the kink mode to specific actuator settings under various conditions. Actual closed-loop experiments, as illustrated by the feedback interconnection in figure 2.1, in which a real-time feedback controller is employed to achieve a prescribed sawtooth period, have only been carried out on Tore Supra [17,18] and TCV [19–21]. However, a systematic design of such a feedback controller, based upon a rigorous analysis of the dynamics of the sawtoothing plasma or sawtooth model, is still lacking. Such an approach is essential to guarantee closed-loop stability and convergence speed of the sawtooth period *a priori*. A systematic design approach would enable the design of a high performance controller, which will provide inputs to the plasma such that the prescribed sawtooth period can be achieved as quickly as possible, given the constraints of the plasma, while meeting the requirements in terms of robustness and accuracy.

In this paper we will provide such an analysis and controller design strategy based on linear discrete-time control theory [22,23], as an extension of the work previously presented in [24]. This methodology is applied to the case study of a sawtooth

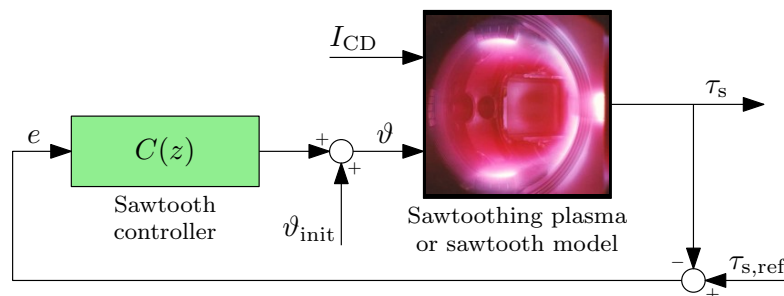


Figure 2.1: Closed-loop block scheme, where a sawtooth model or sawtoothing plasma is feedback-connected with a to-be-designed controller.

model based on magnetic diffusion, the sawtooth trigger model of Porcelli [7], and the reconnection model of Kadomtsev [25]. The actuation is modelled as a perturbation of the magnetic shear on and around the $q = 1$ surface by means of a local EC driven current, where the deposition location (indicated by the rotation angle of the electron cyclotron current drive (ECCD) mirror) forms the input. Sawteeth are normally sensed by detecting the crashes on ECE or soft x-ray channels [26], hence the output of the model is the time between subsequent crashes. The resulting low complexity combined Kadomtsev–Porcelli model is sufficient for controller design, as it manages to reproduce the typical input–output behaviour of the sawtooth, where the period is shortened or lengthened depending on the ECCD deposition location [13, 14].

In principle, the chosen inputs could be a combination of coupled power, deposition location and current drive efficiency. In this paper, however, we restrict ourselves to deposition location inputs. The reasons for this are threefold. First, the power input for fixed deposition location allows for uni-directional sawtooth control only, implying that smaller than ohmic periods cannot be achieved whenever the deposition is fixed on a location outside $q = 1$. In contrast, changing the deposition location allows both shortening and lengthening of the period. Second, the variation of the deposition location stems from a mechanical system, i.e. a steerable launcher (as on TEXTOR, TCV and Tore Supra), which is also used for real-time feedback control of NTMs [27]. This launcher is the slowest and most restrictive element of the closed loop. Therefore, an assessment of the launcher dynamics on the overall control performance is relevant. Finally, although present-day gyrotrons can vary their power over a large range, a real-time power variation or modulation can cause a significant energy dissipation in the gyrotron and its power supply and is therefore not a preferred control input.

The proposed analysis and design method makes use of a control-relevant identification technique, which uses the sawtooth model as a black-box input–output system and systematically investigates its dynamic behaviour within a specific operating regime. The identified dynamics is captured in a collection of discrete-time linear transfer functions using approximate realization techniques [28], describing the relation between the input (EC mirror angle) and output (sawtooth period) from one sawtooth crash to another. These transfer functions allow frequency domain representations, which enable a dedicated structured controller design and guarantee convergence to any desired period within the considered operating regime. It is important to note that this method is straightforwardly applicable to more complex numerical models and real-time experiments as well.

Based on the proposed analysis, it is shown that an integral (I) action is sufficient to guarantee closed-loop stability with zero steady-state error on the period. Postulating that the closed-loop performance should be improved even further while assuming stability and robustness constraints, a single proportional-double-integral (PII) controller is then designed and tested in a simulation with the original model.

Next, the influence of realistic actuator dynamics (i.e. limited speed of the ECCD mirror launcher) and time delays due to crash detection algorithms on the identified

sawtooth dynamics is investigated. It is shown that the relatively slow dynamics of current ECCD launchers on, e.g. TEXTOR and TCV creates a large restriction on the achievable closed-loop performance of the sawtooth instability. Furthermore, the importance of fast crash detection is addressed, yielding similar conclusions.

This paper is organized as follows. Section 2.2 introduces the combined Kadomtsev–Porcelli sawtooth model we will use as a case study throughout this paper, and its implementation in a real-time simulation environment. Section 2.3 discusses the theory of discrete-time systems, explains the proposed identification method and presents the identified sawtooth dynamics. The controller design based on these results is described and tested in section 2.4, after which section 2.5 discusses the influence of slow actuation and detection. Conclusions, future work and discussions are mentioned in section 2.6.

2.2 The sawtooth model

In this paper we will use a model-based approach to identify the input–output behaviour of the period of the sawtooth instability, upon which we will base our controller design. A control-oriented model should capture the relevant static and dynamic input–output behaviour of a system with a minimal amount of complexity. Therefore, our model (a continuation of the work in [29]) is solely based on the evolution of the poloidal magnetic field $B_\theta(r, t)$ over the radial coordinate r and time t . For large aspect-ratio tokamaks the toroidal magnetic field B_ϕ can be assumed constant, so that the poloidal field B_θ uniquely defines the safety factor q and magnetic shear s [30], since

$$q(r, t) = \frac{rB_\phi}{R_0B_\theta} \quad \text{and} \quad s(r, t) = \frac{r}{q} \frac{dq}{dr} = 1 - \frac{r}{B_\theta} \frac{dB_\theta}{dr}, \quad (2.1)$$

where R_0 is the tokamak major radius. Moreover, we focus entirely on the effect of the EC current drive location (input) on the sawtooth period (output). The effect of heating is simplified assuming steady-state temperature profiles (see below). In essence, these represent the time-averaged temperature profiles during the sawtooth cycle.

Although the model is in principle widely applicable, in this paper its geometric parameters are compatible with the TEXTOR dimensions, and values of various other variables are typical for this tokamak. Various parameters were chosen and fixed in order to reproduce realistic TEXTOR sawtooth periods for discharges with large counter-current NBI [16]. Consequently the effect of the EC heating on the sawtooth cycle is indeed small in comparison with the effect of the EC current drive.

2.2.1 Kadomtsev–Porcelli model description

The poloidal magnetic field $B_\theta(r, t)$ is assumed to evolve in two different ways:

- (i) between crashes it diffuses normally following Maxwell’s equations;
- (ii) at a crash it reconnects infinitely fast according to Kadomtsev’s reconnection model.

The trigger for a sawtooth crash is the onset of the $m = 1$ internal kink mode. This onset can be expressed in terms of conditions on the plasma potential energy functional $\delta\hat{W}$. The model of Porcelli [7] uses this $\delta\hat{W}$ to propose sawtooth triggering conditions (2.2a) and (2.2b) for both the ideal and resistive kink mode, in terms of their growth rate γ , the ion diamagnetic frequency ω_{*i} , the Alfvén time τ_A , the normalized ion Larmor radius $\hat{\rho}$ and a numerical scaling factor c_* :

$$\delta\hat{W} < -0.5\omega_{*i}\tau_A \quad (2.2a)$$

$$-0.5\omega_{*i}\tau_A < \delta\hat{W} < \hat{\rho} \quad \text{and} \quad \omega_{*i} < c_*\gamma. \quad (2.2b)$$

In this paper we focus on the resistive kink mode (2.2b), where magnetic reconnection takes place in a narrow resistive layer around the $q = 1$ surface. In this situation the condition $\delta\hat{W} < \hat{\rho}$ is normally fulfilled and the sawtooth trigger condition $\omega_{*i} < c_*\gamma$ can be transformed into a critical shear condition [7], since the growth rate γ depends on the shear at the $q = 1$ surface. Hence, in our model a crash (ii) will occur whenever

$$s_1 = s(r_{q=1}) \geq s_{\text{crit}} = \text{constant}, \quad (2.3)$$

where $r_{q=1}$ denotes the location of the outermost $q = 1$ surface, so $q(r_{q=1}) = 1$. In Porcelli's model the critical shear s_{crit} depends on many parameters and can be time dependent, but here we assume it to be constant (typically 0.133) in order to minimize the complexity of the model. The reconnection will be defined such that B_θ will diffuse for some time after every crash, until the crash criterion is met again.

Magnetic diffusion

The inter-crash behaviour of the magnetic field \mathbf{B} is described by the magnetic diffusion equation

$$\frac{\partial \mathbf{B}}{\partial t} = -\nabla \times \left(\frac{\eta}{\mu_0} \nabla \times \mathbf{B} - \eta \mathbf{J}_{\text{CD}} \right) \quad \text{if } s_1 < s_{\text{crit}}, \quad (2.4)$$

where \mathbf{J}_{CD} denotes the additional EC current drive, and η and μ_0 denote the plasma resistivity and permeability respectively. Assuming toroidal and poloidal axi-symmetry for a large aspect-ratio circular tokamak like TEXTOR, this equation can be reduced to a 1D partial differential equation (PDE) for the state $B_\theta(r, t)$

$$\frac{\partial}{\partial t} B_\theta = \frac{\partial}{\partial r} \left(\frac{\eta}{\mu_0 r} \left(B_\theta + r \frac{\partial}{\partial r} B_\theta \right) - \eta J_{\text{CD}} \right) \quad \text{if } s_1 < s_{\text{crit}}, \quad (2.5)$$

where J_{CD} is the toroidal component of the EC current drive. The boundary conditions for (2.5) are defined by symmetry and the total plasma current I_p at the tokamak minor radius a , hence $B_\theta(0, t) = 0$ and $B_\theta(a, t) = \frac{\mu_0 I_p}{2\pi a}$. Furthermore, we assume Spitzer resistivity [30] so that

$$\eta = 1.65 \times 10^{-9} \ln \Lambda Z_{\text{eff}} T_e^{-3/2}, \quad (2.6)$$

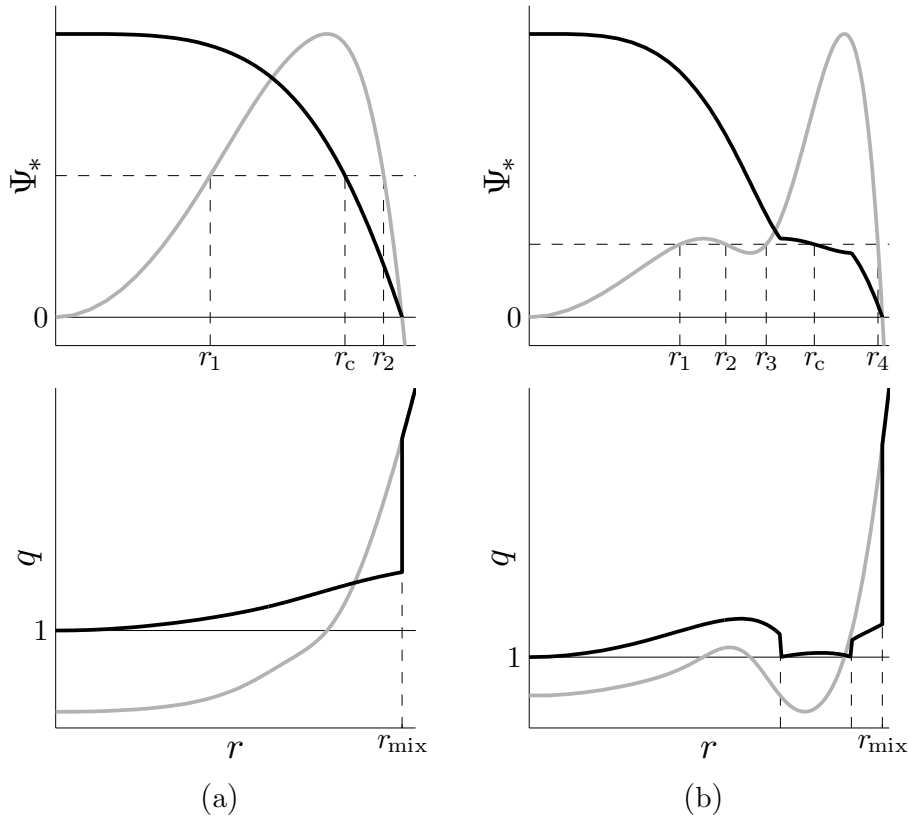


Figure 2.2: Pre-crash (grey) and post-crash (black) profiles for the helical flux Ψ_* and safety factor q according to the Kadomtsev reconnection model; (a) with a single $q = 1$ surface before the crash, where $r_c^2 = r_2^2 - r_1^2$; and (b) with three distinct $q = 1$ surfaces before the sawtooth crash, where $r_c^2 = r_4^2 - r_3^2 + r_2^2 - r_1^2$.

where the effective ion-charge $Z_{\text{eff}} \approx 1.5$ and the Coulomb logarithm $\ln \Lambda \approx 17$. Since the energy confinement time is much smaller than the time scale of magnetic diffusion, the influence of the time evolution of the electron temperature T_e on the sawtooth period is neglected. Hence, T_e is assumed to be time-invariant and is chosen such that the equilibrium of (2.5), i.e. the solution of $\partial B_\theta / \partial t = 0$ with $J_{\text{CD}} = 0$, yields

$$q_{\text{eq}}(r) = q_{0,\text{eq}} + (q_a - q_{0,\text{eq}}) \left(\frac{r}{a} \right)^2, \quad \text{with } q_{0,\text{eq}} = \frac{q_a}{1 + q_a}, \quad (2.7)$$

as the equilibrium q -profile. Hence, we have that

$$T_e(r) = T_0 \left[1 + q_a \left(\frac{r}{a} \right)^2 \right]^{-4/3}, \quad (2.8)$$

where $q_a = q(a)$ and the central temperature $T_0 = 2$ keV.

Kadomtsev crashes

Compared with the time scale of the magnetic diffusion equation (2.5) the collapse phase of the sawtooth cycle (initiated by the reconnection process) is generally extremely fast [2,3]. In our model the state B_θ is therefore immediately altered whenever

a crash occurs (i.e. when (2.3) is met), and is computed as a function of the state before the crash as described by the full reconnection model of Kadomtsev [3, 7, 25]. Kadomtsev's model assumes that flux surfaces with equal helical flux Ψ_* reconnect, while conserving toroidal flux (i.e. conserving cross-sectional area between the surfaces). This helical flux is determined by the state B_θ since

$$\Psi_*(r) = \int_0^r [B_\theta(\tilde{r}) - \tilde{r}B_\phi/R_0] d\tilde{r}. \quad (2.9)$$

For monotonic q -profiles Kadomtsev's description is well-defined, as is illustrated in figure 2.2(a). In this situation there is a unique $r_2 > r_{q=1}$ for every $r_1 < r_{q=1}$ such that $\Psi_*(r_1) = \Psi_*(r_2)$. Hence, the flux surfaces at r_1 and r_2 reconnect such that the helical flux after the crash $\Psi_*^c(r_c) = \Psi_*(r_1) = \Psi_*(r_2)$ with $r_c^2 = r_2^2 - r_1^2$. Consequently, each pre-crash q -profile yields a single corresponding post-crash profile.

However, when there are multiple $q = 1$ surfaces just before a sawtooth crash the full reconnection Kadomtsev model is somewhat ambiguous. For example, when there is a considerable amount of current drive close to the plasma centre, the q -profile can be a non-monotonic function of r , resulting in a flux function $\Psi_*(r)$ with multiple extrema. Figure 2.2(b) shows an actual profile from our model where there are four flux surfaces with the same Ψ_* . In this case we need to define explicitly how these surfaces reconnect. In this paper we propose to use a scheme of reconnections, explained in figure 2.3. We assume that at a single sawtooth crash there is a sequence of Kadomtsev reconnections around each of the pre-crash $q = 1$ surfaces. This eventually yields a monotonically decreasing post-crash flux function $\Psi_*^c(r)$ as shown in black in figure 2.3(c). This corresponds to a q -profile with $q \geq 1$ for all r , as figure 2.2(b) also shows. Consequently, after a small amount of time dt after the crash we have that $r_{q=1} \approx 0$ and $s_1 \approx 0$, so B_θ will indeed always diffuse after a crash.

This proposed reconnection scheme shows similarities with the method of Archimedes to compute surface and volume integrals using infinitesimal small rings. As such one can show that this scheme works for any Ψ_* -profile with multiple extrema, regardless of its actual shape, as long as one of its maxima has a flux larger than $\Psi_*(0)$. The Archimedes–Kadomtsev reconnection boils down to a relatively simple algorithm for the post-crash flux function $\Psi_*^c(r)$. If we define r_{i-} as all pre-crash surfaces with $d\Psi_*/dr < 0$ and r_{j+} as all surfaces with $d\Psi_*/dr > 0$, then

$$\Psi_*^c(r_c) = \Psi_*(r_{i-}) = \Psi_*(r_{j+}), \quad \text{where } r_c^2 = \sum_i r_{i-}^2 - \sum_j r_{j+}^2. \quad (2.10)$$

In the case where there are three $q = 1$ surfaces, as in figure 2.2(b), this implies that $\Psi_*^c(r_c) = \Psi_*(r_1) = \dots = \Psi_*(r_4)$, where $r_c^2 = r_4^2 - r_3^2 + r_2^2 - r_1^2$. Reconnection will occur for all surfaces with non-unique values of the helical flux. This defines the mixing radius r_{mix} , which can be expressed mathematically as

$$r_{\text{mix}} = \left\{ r : r > r_{q=1}, \Psi_*(r) = \min_{0 \leq \tilde{r} \leq r_{q=1}} \Psi_*(\tilde{r}) \right\}. \quad (2.11)$$

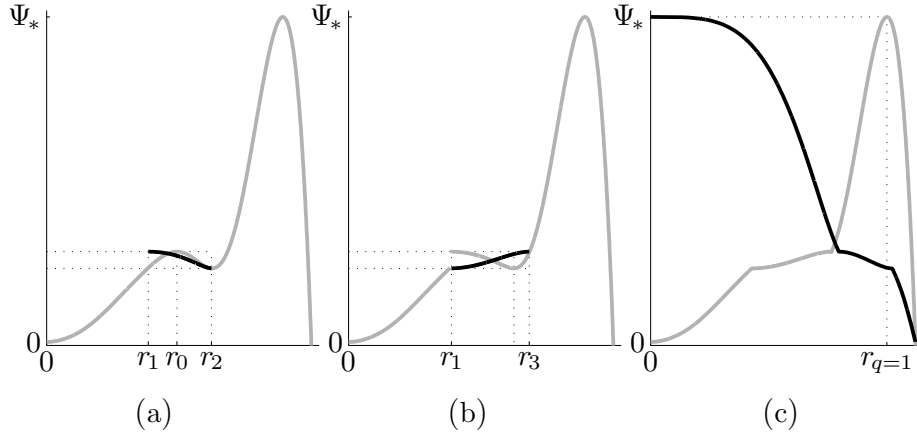


Figure 2.3: Helical flux profiles before (grey) and after (black) subsequent reconnections at a single sawtooth crash when multiple pre-crash $q = 1$ surfaces are present. (a) First a Kadomtsev reconnection takes place around r_0 (the innermost $q = 1$ surface), between r_1 and r_2 , resulting in a discontinuity in Ψ_* on r_1 ; (b) this discontinuity is removed by assuming an immediate subsequent reconnection around r_2 (the second $q = 1$ surface), between r_1 and r_3 ; (c) now the resulting flux function is continuous and has a unique maximum at $r_{q=1}$ such that a full Kadomtsev reconnection yields the final post-crash flux function indicated in black.

Given the definitions in (2.10) and (2.11) we can now formally define what happens with the state B_θ at a crash:

$$B_\theta(r, t^+) = \begin{cases} B_\theta(r, t^-) & \text{for } r \geq r_{\text{mix}} \\ \frac{d}{dr}\Psi_*^c(r) + \frac{1}{R_0}rB_\phi & \text{for } r < r_{\text{mix}} \end{cases} \quad \text{if } s_1 \geq s_{\text{crit}}. \quad (2.12)$$

Note that since the post-crash flux function $\Psi_*^c(r)$ is not necessarily a smooth function, the post-crash q -profile can have multiple discontinuities (or current layers) in addition to the usual one at r_{mix} , as indicated by the dashed lines at the bottom of figure 2.2(b).

Model input and output

Any control-oriented model should have at least one input and one output. Ideally, an output should be some measure of the behaviour of the system, such that it can be used to indicate a deviation from a desired situation or setpoint. Here the sawtooth period is of particular interest, as it determines the size of the $q = 1$ surface at the moment of the crash, which has a direct impact on the triggering of NTMs and the exhaust of α -particles and helium. Hence, we choose the time between subsequent sawtooth crashes as the output, and label this as the sawtooth period τ_s .

An input must be able to change the system behaviour such that it is noticeable in the output. It is known that ECCD has such an effect on the sawtooth period, i.e. the amount and deposition location of driven current strongly influences the steady-state sawtooth period within a plasma. For example, co-current depositions inside

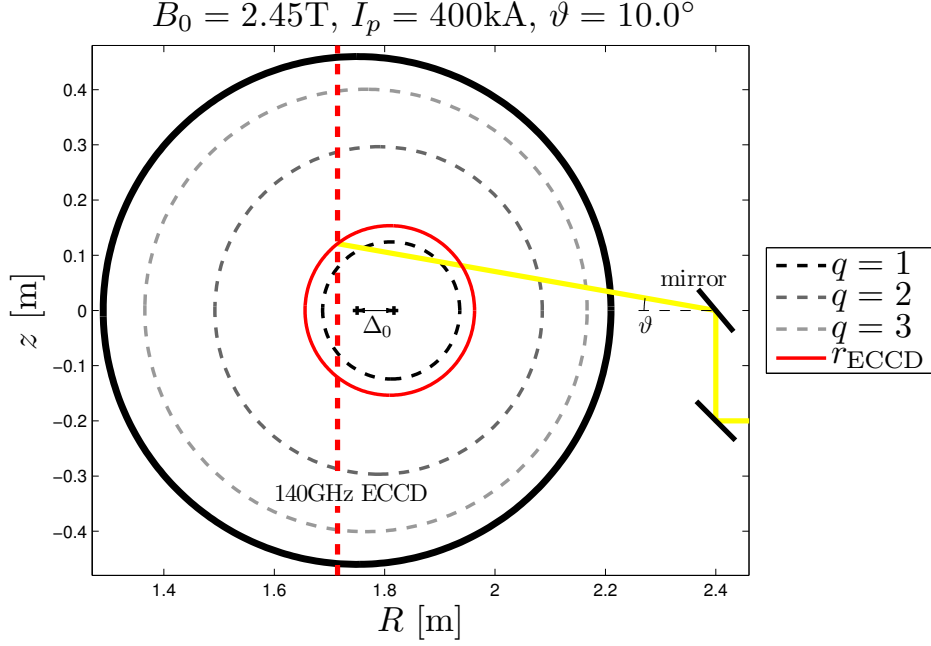


Figure 2.4: Poloidal cross-section of TEXTOR, showing the ECCD deposition location.

$q = 1$ shorten the period, whereas depositions outside $q = 1$ lengthen it. This effect is modelled by means of J_{CD} in (2.5), which we will now further specify.

The driven current is modelled as a Gaussian distribution over r , hence,

$$J_{\text{CD}} = J_0 \exp\left(-\frac{(r - r_{\text{ECCD}})^2}{w_{\text{CD}}^2}\right), \quad (2.13)$$

where w_{CD} is the deposition width (here 16 mm). On TEXTOR, the deposition location r_{ECCD} is determined by the poloidal deflection angle ϑ of the EC beam [31,32], as shown in the poloidal cross-section in figure 2.4. Here it is calculated algebraically by solving

$$r_{\text{ECCD}}^2 = z_{\text{ECCD}}^2 + (R_{\text{ECCD}} - R_0 - \Delta(r_{\text{ECCD}}))^2 \quad (2.14)$$

for r_{ECCD} , using the relations for electron gyration frequency (2.15a), mirror vertical angle (2.15b) and Shafranov shift (2.15c):

$$R_{\text{ECCD}} = \frac{1}{2\pi} \cdot \frac{2eR_0B_0}{f_{\text{ECCD}}m_e}, \quad (2.15a)$$

$$z_{\text{ECCD}} = (R_{\text{mirror}} - R_{\text{ECCD}}) \cdot \tan(\vartheta), \quad (2.15b)$$

$$\Delta(r_{\text{ECCD}}) = \Delta_0 \left(1 - \left(\frac{r_{\text{ECCD}}}{a}\right)^2\right). \quad (2.15c)$$

Here $\Delta(r_{\text{ECCD}})$ denotes the radial displacement of the deposition surface, assuming a parabolic profile of the Shafranov shift $\Delta(r) = \Delta_0(1 - (r/a)^2)$, where Δ_0 is the displacement of the magnetic axis. Furthermore, R_{ECCD} is the absorption location of the EC beam with frequency f_{ECCD} and z_{ECCD} is the vertical deposition location. Note that the effect of Doppler shifts on the input–output behaviour of the model

is neglected. The above algebraic relations map J_{CD} into two inputs for our model, namely the beam angle ϑ and the total driven current I_{CD} (i.e. the surface integral of J_{CD} in (2.13) which determines J_0). For the rest of this paper we will focus on the effect of ϑ and keep I_{CD} at a fixed value. The joint usage of both inputs is part of future research.

The model for B_θ as defined in (2.5) and (2.12) is known in control engineering as an *infinite dimensional impulsive dynamical system* [33]:

- it is *infinite dimensional* since (2.5) is a PDE, which is equivalent to an ordinary differential equation (ODE) with an infinite amount of states;
- it is *impulsive* since (2.12) describes infinitely fast jumps in the state B_θ ;
- it is *dynamical* since changes in the input will result in future changes of output; the system has an amount of ‘memory’ in terms of the state B_θ .

Unfortunately, dedicated controller design routines for these types of systems do not exist yet. In this paper, we therefore rely on standard control tools like linearization techniques of the input–output behaviour and classical feedback control theory to derive suitable controllers. This will also enable us to provide deeper insight into the underlying dynamics and will give analysis results with respect to the performance limitations. These techniques are further discussed in section 2.3.2 and 2.4.1.

2.2.2 Numerical implementation

The above described mathematical model has been implemented numerically into Matlab[®] Simulink[®], which is a dedicated simulation environment for dynamical systems. One of the motivations to use Simulink is its large flexibility; because of its modular graphical structure various dynamical systems can be combined by connecting their input and/or output channels. As such it is possible to combine any model with any controller, generate arbitrary input signals, and perform closed-loop simulations. Furthermore, Simulink comes with optimized differential equation solvers thanks to which it is generally fast and accurate.

An infinite dimensional impulsive dynamical system cannot be implemented using standard Simulink building blocks, but has to be written in a numerical code embedded in a Simulink C-code S-function [34]. To this end, (2.5) has been discretized using a central finite difference method over the spatial coordinate r in 250 points, yielding an ODE with 250 states $B_{\theta,i}$. A variable time step solver computes the time evolution of this ODE, yielding $B_{\theta,i}$ and q_i at all 250 points at every time step. Using cubic interpolation and root finding, $r_{q=1}$ and s_1 are then approximated. A zero-crossing event function finds the exact time t_1 when $s_1 = s_{\text{crit}}$, and forces the solver to compute the pre-crash states at t_1 . These states $B_{\theta,i}$ are then redefined according to (2.12), which involves trapezoidal integration, sorting, cubic interpolation and differentiation. Afterwards, the solver computes the time evolution of the ODE again, given the new

‘initial conditions’ for $B_{\theta,i}$. The time at which the state jumps occur is logged and used to determine the actual period, which is sent as output.

The discretization grid over r is dense around $r_{q=1}$ and r_{mix} , and more coarse towards the plasma edge. The grid is extremely dense around the current layer at r_{mix} , in order to approximate its large diffusion as well as possible and minimize discretization effects there. Since r_{mix} can change with every crash, this spatial grid is recalculated after every crash and $B_{\theta,i}$ is interpolated cubically around these new points. Simulations have shown that this approach indeed minimizes numerical oscillations.

The constructed C-code sawtooth model has a Simulink interface with two inputs (mirror angle ϑ and current drive I_{CD}) and a single output (period τ_s). As such it can easily be incorporated in a Simulink closed-loop scheme, illustrated in figure 2.1, where the difference between the period and a desired setpoint is sent to a controller, which computes an update of the mirror angle and sends it back to the model. In this paper I_{CD} is not part of the closed loop and is held constant. Moreover, note that our model outputs the actual period after every crash, whereas in practice a real-time crash detection and period estimation routine based on ECE or soft x-ray signals is required [26]. The effect of such an algorithm is further discussed in section 2.5.2.

The implemented model presented here has several advantages over, e.g. comprehensive numerical codes. It duplicates the typical input–output behaviour of the ECW actuated sawtooth instability, while keeping the complexity to a minimum. Therefore, it is able to compute multiple seconds of sawtooth data with high temporal resolution in less than a minute on an average computer. Furthermore, it is extremely flexible in two ways. First, it facilitates the interconnection of inputs and outputs, allowing creation of feedback loops in an intuitive way. Second, parameters or input signals can be changed as the simulation runs. This flexibility facilitates a useful controller design and testing platform.

2.3 Control-oriented system analysis

The model for the sawtooth instability as described above will be used as a case study to derive appropriate sawtooth period controllers, based on its dynamic input–output behaviour. The proposed approach is a black-box one, where we consider the implementation of the model in Simulink as the ‘real system’. We assume that the underlying model is unknown, and we only have specific data of the input and output signals available. We will show that we can then make estimations of the statics and dynamics of the system, on which we will base our controller design in section 2.4. Although in this paper the methodology is applied to a simulation model, it should be mentioned that this black-box approach can be applied to a wide variety of unknown systems, including processes in actual tokamak experiments.

2.3.1 Steady-state response and DC-gain

Previous publications [12, 13, 20] have shown that ECCD has a characteristic effect on the sawtooth period. Co-current ECW depositions inside $q = 1$ shorten the sawtooth period, whereas ECW depositions outside $q = 1$ lengthen it. We will use these steady-state observations to benchmark our simulation model. In all cases we will use the following parameters: toroidal field $B_\phi = 2.45$ T, plasma current $I_p = 400$ kA, driven current $I_{CD} = 2$ kA and Shafranov shift in the centre $\Delta_0 = 2$ cm.

To obtain the steady-state or static system response of our model, a large amount of simulations were performed. Each simulation was continued until a steady state was reached for a certain fixed mirror angle, i.e. until the output (sawtooth period) did not change anymore. Repeating this for a wide range of angles yields the results on the left of figure 2.5. Indeed, this figure shows that compared with the ohmic period of 15 ms, depositions close to the plasma centre (i.e. for small ϑ) shorten the sawtooth period to a little more than 3 ms, whereas more outward depositions lengthen it up to 30 ms (which are typical values for TEXTOR). The transition is around the $q = 1$ surface. These results are in good agreement with previous publications [13, 14, 29]. Hence, the ECCD actuated current diffusion mechanism of our model is sufficient to capture the basic sawtooth behaviour. Note that a very small amount of additional current (I_{CD} is only 0.5% of the plasma current I_p) is already able to alter the period up to one order of magnitude (from 3 to 30 ms).

The static input–output map in figure 2.5(a) can be relevant for feedforward purposes, but is in itself not useful to base a feedback controller design on. This requires information on the local behaviour of the system, like the DC-gain for each operating point ϑ , which can be derived from figure 2.5(a). This DC-gain, or low-frequency gain, denotes the change in steady-state output $\Delta\tau_s$ for a change $\Delta\vartheta$ in the input, in the limit case where $\Delta\vartheta \rightarrow 0$. Since the input–output map is smooth this can be done by taking its derivative over ϑ . The result is shown on the right of figure 2.5. Note that the system behaves non-linearly, in the sense that the magnitude of the DC-gain depends heavily on the operating point ϑ , but also changes sign twice. This makes it generally hard to define a single controller which can stabilize over the whole operating range (here $0^\circ < \vartheta < 15^\circ$). In this paper we will therefore focus our analysis and controller design on the specific operating range $0^\circ < \vartheta \leq 6.28^\circ$, indicated in blue in figure 2.5. This region comes with periods smaller than ohmic (between 3.1 and 14.8 ms), which is in agreement with the statement that small sawteeth are required to avoid the triggering of NTMs [35] and prevent impurity accumulation [4].

It is interesting to note that the static behaviour of our model seems to be influenced by the amount of $q = 1$ surfaces present. There are multiple $q = 1$ surfaces when $4.84^\circ < \vartheta < 6.58^\circ$, indicated by the shaded area in figure 2.5, and a single one otherwise. When multiple $q = 1$ arise, the DC-gain seems to drop quite rapidly with increasing ϑ . We will see in the next section that the dynamics is also different in this case.

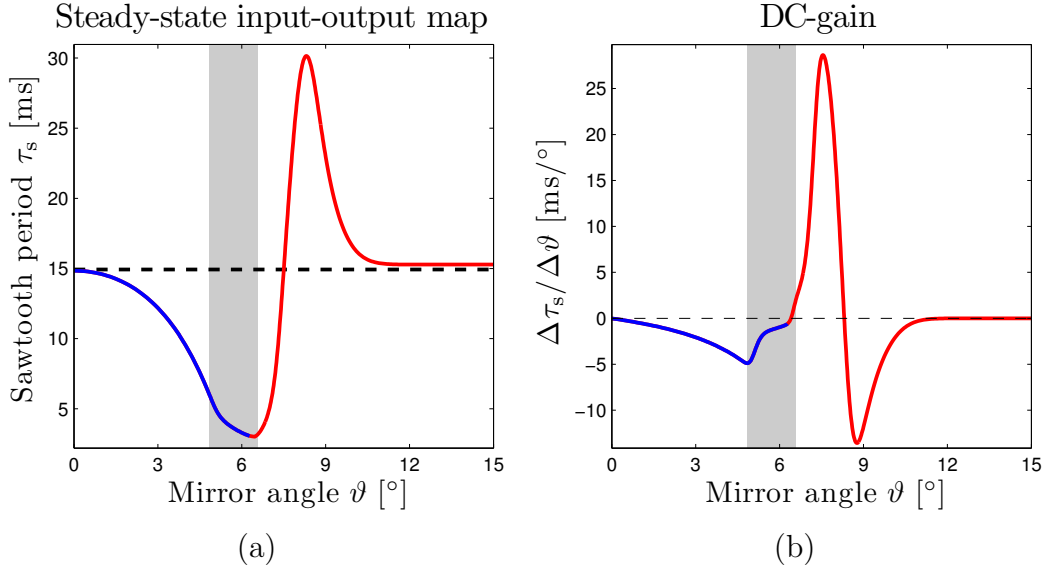


Figure 2.5: Static responses of the sawtooth model: (a) the input–output map, showing the steady-state period τ_s as a function of the mirror angle ϑ ; and (b) the derived DC-gain, i.e. the static change in period for a small change in mirror angle. The blue part indicates our specific region of interest, the shaded region is where there are multiple $q = 1$ surfaces present.

2.3.2 Sawtooth dynamics

The results in figure 2.5 do not contain any information on how fast changes in τ_s can occur. However, these underlying time scales or dynamics play an essential role in controller design, since they determine the controller structure and can possibly limit the achievable closed-loop performance. This section describes how we can make estimations of this dynamics using a black-box approach.

Discrete-time systems

First, we have to define how to represent this dynamics, as this is far from trivial. The system input is continuous in time, since the mirror angle ϑ takes values for any $t \in \mathbb{R}$. In contrast, the system output is discrete in time, since the period τ_s only changes when a crash has occurred. For this reason we will label our system as a discrete-time system. This implies that we restrict the input to change only at a crash and remain constant in between crashes. This is valid since a controller will only update its control signal when it receives a new measurement (i.e. at a crash), keeping the required mirror angle constant otherwise.

In this discrete-time framework [22, 23] the dynamics of the system is described by expressing the output τ_s at a certain crash number k in terms of outputs τ_s and inputs ϑ at previous crashes. The crash number k thus replaces the real time t , so that the response of the system is only described at the crashes, regardless of the time between crashes. Mathematically, this implies that we assume that the dynamic

sawtooth behaviour can be written as a so-called *difference equation*, i.e.

$$\tau_s(k) = f(\vartheta(k), \vartheta(k-1), \vartheta(k-2), \dots, \tau_s(k-1), \tau_s(k-2), \dots), \quad (2.16)$$

where f is some unknown function. When such a system is linear and of finite order, as is assumed later on in case of small perturbations, (2.16) takes the form

$$\begin{aligned} \tau_s(k) = & b_0\vartheta(k) + b_1\vartheta(k-1) + b_2\vartheta(k-2) + \dots + b_m\vartheta(k-m) \\ & - a_1\tau_s(k-1) - a_2\tau_s(k-2) - \dots - a_n\tau_s(k-n). \end{aligned}$$

Previous values of a signal are often described by the shift operator z , which is defined by the relation $w(k-1) = z^{-1}w(k)$. For linear systems this allows us to define the transfer function $H(z)$ of the system as

$$H(z) = \frac{b_0 + b_1z^{-1} + b_2z^{-2} + \dots + b_mz^{-m}}{1 + a_1z^{-1} + a_2z^{-2} + \dots + a_nz^{-n}}, \quad (2.17)$$

where $\max(m, n)$ is the order of the system. It should be noted that the ‘crash domain’ or ‘event driven’ representation of the sawtooth cycle in (2.17) is often associated with a constant time between two samples (crashes), which is essentially not true in our situation. However, the results in section 2.4 will show that for small perturbations this approach is still valid, thereby enabling us to use frequency domain techniques for controller design. Providing mathematical proof for this is part of current research.

Approximate realizations

Although the global behaviour of the sawtooth system is highly non-linear (but smooth), its local behaviour around an arbitrary operating point $(\vartheta_i, \tau_{s,i})$, where i is the operating point identifier, may well be approximated linearly. Such local linearizations are valid when the dynamic response $\Delta\tau_s(k)$ due to small perturbations $\Delta\vartheta(k)$ is approximately linear, and the time between samples k is approximately constant. Linearity means that the superposition principle holds, i.e. a perturbation $\alpha\Delta\vartheta(k)$ yields a response $\alpha\Delta\tau_s(k)$. For our specific model this is indeed the case, as long as the perturbation signal $\Delta\vartheta(k)$ is small enough. Moreover, in that case $\Delta\tau_s(k)$ is small compared with $\tau_{s,i}$, so indeed the sampling time can be assumed constant.

Local linearization boils down to finding transfer functions $H_i(z)$ around each operating point $(\vartheta_i, \tau_{s,i})$ which describe the time-dependent behaviour of $\Delta\tau_s(k)$ due to a chosen perturbation signal $\Delta\vartheta(k)$. Here we use approximate (or minimal) realization techniques [28], which rely on stepwise perturbation signals, to obtain these $H_i(z)$.

For each angle ϑ_i two simulations are performed, with positive and negative step inputs. In the former the mirror angle is fixed at $\vartheta_i - \Delta\vartheta$, and when a steady state is reached this angle is changed stepwise to ϑ_i , immediately after a crash. The change in output $\Delta\tau_s$ at every subsequent crash k is monitored. The latter simulation is in opposite direction, with a step from $\vartheta_i + \Delta\vartheta$ to ϑ_i . The two responses are scaled by a factor $1/\Delta\vartheta$ and averaged to obtain a single normalized 1° unit step response sequence

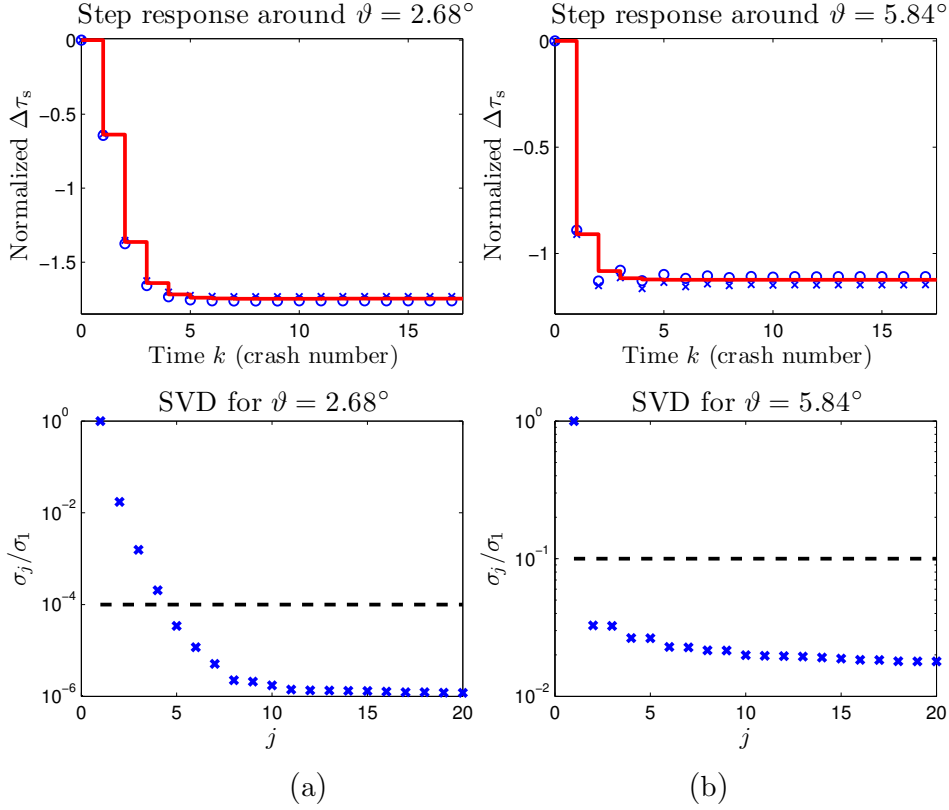


Figure 2.6: Example step responses and the corresponding Hankel singular values, for two different operating points: (a) $\vartheta = 2.68^\circ$ (single $q = 1$ surface); and (b) $\vartheta = 5.84^\circ$ (three $q = 1$ surfaces). The applied steps were very small (0.04°) but the responses in the upper plot were normalized to a unit step; \times and \circ denote positive and negative steps, respectively, the solid red line shows the response of a model of (a) fourth order or (b) first order.

$\Delta\bar{\tau}_s(k)$. In both simulations we use small perturbations, in this case $\Delta\vartheta = 0.04^\circ$. The top of figure 2.6 shows simulations for two different operating points: $\vartheta_i = 2.68^\circ$ (single $q = 1$) and $\vartheta_i = 5.84^\circ$ (three $q = 1$); positive step responses are indicated by \times , negative ones by \circ . The validity of the superposition principle (and thus the linearity assumption) is confirmed by the strong resemblance of the positive and negative responses.

The normalized step response sequence $\Delta\bar{\tau}_s(k)$ for $k = 0, 1, 2, \dots$ is put in a so-called block Hankel matrix H_E of the form

$$H_E = \begin{bmatrix} \delta_{1,0} & \delta_{2,0} & \delta_{3,0} & \delta_{4,0} & \cdots \\ \delta_{2,1} & \delta_{3,1} & \delta_{4,1} & \cdots & \cdots \\ \delta_{3,2} & \delta_{4,2} & \cdots & \cdots & \cdots \\ \delta_{4,3} & \vdots & \vdots & \ddots & \cdots \\ \vdots & \vdots & \vdots & \ddots & \ddots \end{bmatrix}, \quad (2.18)$$

where $\delta_{l,m} = \Delta\bar{\tau}_s(l) - \Delta\bar{\tau}_s(m)$, whose singular value decomposition $H_E = USV^T$ [36] is then computed. The Hankel singular values in the diagonal matrix S , shown on the

bottom of figure 2.6, are ordered $\sigma_1 \geq \dots \geq \sigma_j \geq \sigma_{j+1} \geq \dots \geq 0$ and can be used to choose the appropriate order of the linear transfer function $H_i(z)$, as the relative error of a j th order linearization is given by σ_{j+1}/σ_1 . For situations where there is a single $q = 1$ surface we decide to have a very small relative error of at most 10^{-4} , which is obtained by the fourth singular value, as shown on the bottom left of figure 2.6. Hence, for all $0^\circ < \vartheta_i \leq 4.84^\circ$ we will approximate the local dynamics by a fourth order linear transfer function.

However, the dynamic behaviour turns out to be different in the region where $4.84^\circ < \vartheta_i \leq 6.28^\circ$, coinciding with the presence of multiple $q = 1$ surfaces. The bottom right of figure 2.6 shows that the relative error then hardly decreases for orders larger than 1. Increasing the estimation order will thus be useless, as the dynamics is clearly dominated by a first order behaviour. Hence, for all $4.84^\circ < \vartheta_i \leq 6.28^\circ$, which we will label the multiple $q = 1$ case, we will use a first order approximation. Note that the resulting relative error is now in the order of 10^{-1} , which is partly because of some numerical noise due to the presence of multiple current layers.

The actual transfer functions are found by computing the approximate (minimal) realization [28] of each response $\Delta\bar{\tau}_s(k)$ in terms of the local state space matrices A_i , B_i , C_i and D_i at the considered operating point i . Given the selected order n , these are calculated using H_E and the reduced matrices S_n , U_n and V_n , obtained by selecting only $\sigma_1, \dots, \sigma_n$ from S and the corresponding rows and columns of U and V :

$$A_i = S_n^{-\frac{1}{2}} U_n^T H_A V_n S_n^{-\frac{1}{2}}, \quad (2.19a)$$

$$B_i = S_n^{-\frac{1}{2}} U_n^T H_B, \quad (2.19b)$$

$$C_i = H_C V_n S_n^{-\frac{1}{2}}, \quad (2.19c)$$

$$D_i = \Delta\bar{\tau}_s(0). \quad (2.19d)$$

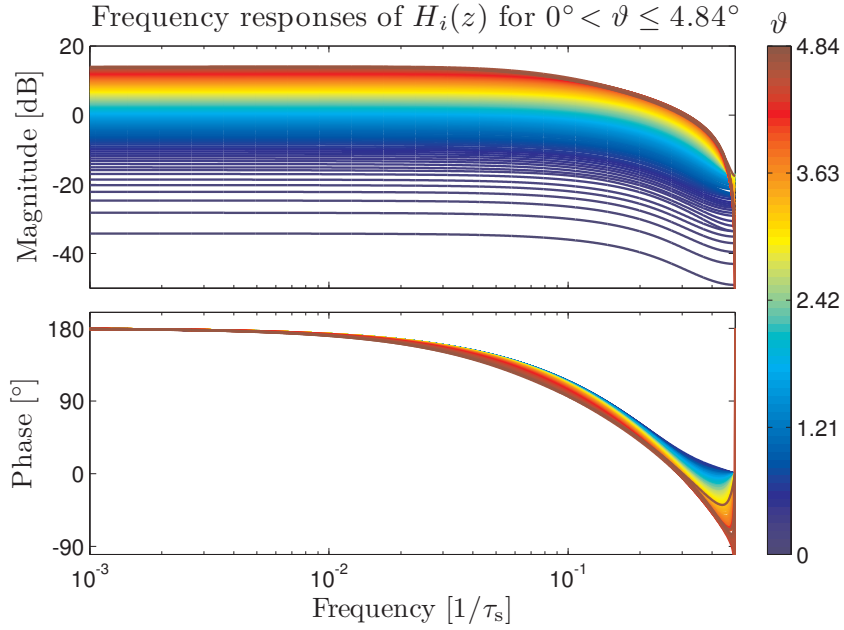
Here, the matrix $H_A = \bar{H}_E$ is the shifted Hankel matrix, i.e. the one time step k upwards shifted equivalent of H_E . Furthermore, H_B and H_C are the first column and row of H_E , respectively. The n th order linear transfer function $H_i(z)$ is then defined as

$$H_i(z) = C_i (zI - A_i)^{-1} B_i + D_i. \quad (2.20)$$

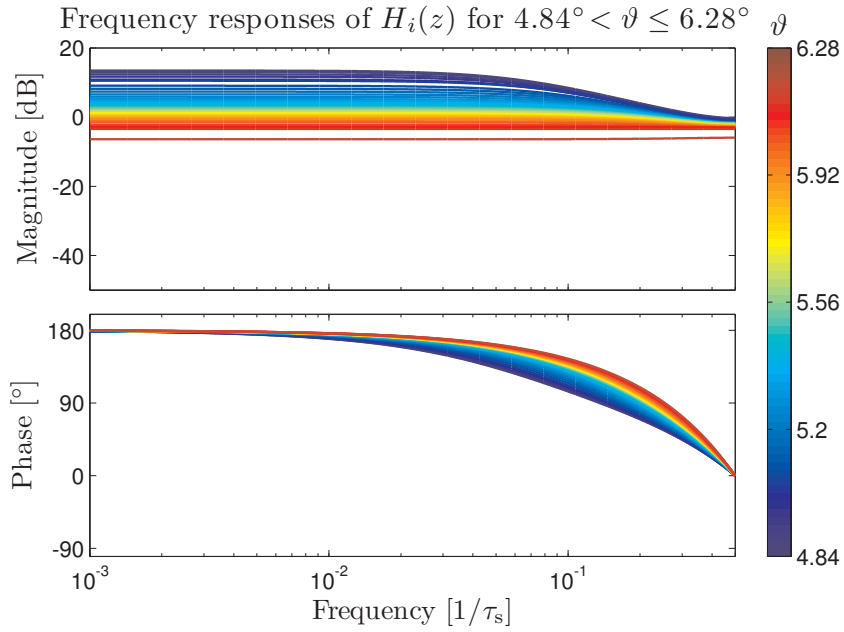
Specific time responses of the approximations are depicted by the red lines in the upper plots of figure 2.6, indeed showing good agreement with the measured data. Since we have used normalized step responses $\Delta\bar{\tau}_s(k)$, the unit of each $H_i(z)$ is [ms/°].

Frequency response data

The linear plants $H_i(z)$ have a unique frequency response function which can be represented in a Bode diagram. Such a diagram shows the amplification and phase shift of the output due to periodic input signals, with which the response to any input signal can be reconstructed. Figure 2.7 shows the frequency responses of the identified $H_i(z)$ for a large collection of operating points; the single $q = 1$ case on the left, the



(a)



(b)

Figure 2.7: Frequency responses of the identified plants $H_i(z)$: (a) when there is only one $q = 1$ surface, i.e. $0^\circ < \vartheta \leq 4.84^\circ$ (using fourth order fits); and (b) when there are multiple $q = 1$ surfaces, i.e. $4.84^\circ < \vartheta \leq 6.28^\circ$ (using first order fits).

multiple $q = 1$ case on the right. The frequency axis is defined as ‘per period’, or $1/\tau_s$, as our system is sampled only at a sawtooth crash. The gain (or magnitude) for low frequencies indeed matches the DC-gain results illustrated in figure 2.5. Both figure 2.5 and 2.7 show that the DC-gain increases with increasing ϑ_i (i.e. decreasing sawtooth

period), up to about $\vartheta_i = 4.84^\circ$; larger angles coincide with multiple $q = 1$, and the DC-gain drops with increasing ϑ_i .

From figure 2.7 some observations on the sawtooth behaviour can be made. First of all, all plants are stable, as expected. Second, all plants make a total phase drop of 180° (or more), which indicates a sample delay inside the system. This is logical, as a perturbation on the input signal at crash k will not be visible in the output until crash $k+1$. Next, nearly all plants act as low-pass filters, meaning that the system suppresses high frequent signals. There is, however, a clear difference between the single $q = 1$ and multiple $q = 1$ case, as this low-pass effect is stronger for the former (high frequent suppression of 20 dB or more) than for the latter (high frequent suppression of 15 dB or less). In the latter case the frequency spectrum is almost flat for most operating points, which implies that the system is nearly static: it takes just one crash to go from one steady state to another. Consequently, the phase in figure 2.7(b) is larger than in figure 2.7(a) for nearly all frequencies. As we will show in section 2.4, this implies that finding a controller for operating points $4.84^\circ < \vartheta_i \leq 6.28^\circ$ is easier than for $0^\circ < \vartheta_i \leq 4.84^\circ$, which may be counter-intuitive because of the more complex underlying physics due to the presence of multiple $q = 1$ surfaces.

As a final remark, note that the small mirror angle perturbations of 0.04° that we have used might be infeasible on an actual tokamak, since the influence on the period might be unmeasurable. In these situations larger perturbations can be applied, at the price of less accuracy of the obtained linear models.

2.4 Controller design and simulation results

In this section we will derive a controller $C(z)$ for the whole operating range $0^\circ < \vartheta \leq 6.28^\circ$, based on the frequency responses shown in figure 2.7. First we will discuss the classical frequency domain techniques [22, 23] which will be used in this design. Next, two different controllers are designed and then tested in simulation.

2.4.1 Design principles

Classical frequency domain controller design relies on some basic principles. Consider the general feedback loop depicted in figure 2.8, with a fixed plant $H(z)$ and a to-be-designed controller $C(z)$. The closed-loop output signals e and y will depend on both the input signal r and the controller $C(z)$, since

$$e = \frac{1}{1 + H(z)C(z)} \cdot r \quad \text{and} \quad y = \frac{H(z)C(z)}{1 + H(z)C(z)} \cdot r. \quad (2.21)$$

Generally, the goal of a controller is to obtain $y \approx r$ and thus $e \approx 0$, which implies that $C(z)$ needs to be as large as possible. This principle is called *high-gain feedback*. In particular, to achieve zero steady-state error ($e = 0$ for constant non-zero r) one needs an infinite gain at zero frequency. High gain often comes with a high *bandwidth*: the frequency where the open loop $H(z)C(z)$ crosses 0 dB is relatively large.

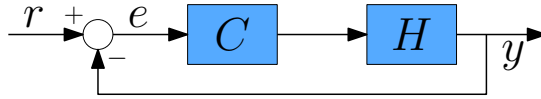


Figure 2.8: Classical feedback loop, where the controller $C(z)$ manipulates the plant $H(z)$ such that $r \approx y$ and $e \approx 0$.

However, depending on the dynamics of $H(z)$ a large gain can also yield an unstable closed loop. Stability of the closed-loop transfer functions in (2.21) is determined by the location of their poles, which are the solutions to $1 + H(z)C(z) = 0$ or $H(z)C(z) = -1$. This relation between the *open-loop* transfer function $H(z)C(z)$ and the point $(-1, 0)$ forms the basis of the Nyquist stability criterion [22]. Without going into detail here, this criterion states that the closed loop will be stable if and only if the graph of the open-loop frequency response $H(z)C(z)$ in the complex plane (also called Nyquist plot) has the point $(-1, 0)$ at its left. Translated in terms of Bode diagrams, this implies that the phase at each frequency where $H(z)C(z) = 1$ should be larger than -180° (and smaller than 0°) to have a stable closed loop.

Since the point $(-1, 0)$ forms the boundary between stability and instability, a certain ‘distance’ from this point is often desirable to be robust against uncertainties or system disturbances. In control engineering practice often a so-called *modulus margin* of 2 (i.e. 6 dB) is taken, corresponding to a minimal ‘distance’ of $\frac{1}{2}$ from $(-1, 0)$. In that case the closed loop will remain stable even if the gains increase up to a factor of 2.

All of the above described principles of performance, stability and robustness have a direct link with the frequency domain, which will thus play an essential role in the sawtooth controller design of the next section.

2.4.2 Controller design for the sawtooth model

Our controller design will be based on the linear plants with single $q = 1$, shown in figure 2.7(a), as these plants are more challenging to control (we will show that the multiple $q = 1$ case can easily be handled by the same controller). The design goal is to find a single controller $C(z)$ such that each open-loop frequency response $H_i(z)C(z)$ meets the above discussed requirements of stability and robustness, while having a good as possible performance, i.e. a large as possible controller gain.

Based on the considerations presented in section 2.4.1 and the results shown in figure 2.7, one can conclude that a suitable controller for the sawtooth instability requires at least three building blocks:

- a negative sign to guarantee local stability (phase roughly between -180° and 0°);
- an integrating action (infinite gain for zero frequency) to remove steady-state errors;
- an appropriate gain to meet the modulus margin and maximize performance.

Such a discrete-time integral (I) controller is defined as

$$C(z) = -I_1 \cdot \frac{z+1}{2(z-1)}, \quad (2.22)$$

or written as a difference equation

$$\Delta\vartheta(k) = \Delta\vartheta(k-1) - \frac{I_1}{2} [e(k) + e(k-1)], \quad (2.23)$$

with the error $e(k) = \tau_{s,\text{ref}}(k) - \tau_s(k)$, and the reference value (or setpoint) of the sawtooth period $\tau_{s,\text{ref}}(k)$. To increase closed-loop performance the integral gain I_1 was maximized while maintaining the robustness requirement, yielding $I_1 = 0.074$. The resulting Bode and Nyquist plots of the frequency responses of $H_i(z)C(z)$ are shown in figure 2.9. The Nyquist plot shows that each open loop is indeed stable and just outside the modulus margin disc around $(-1, 0)$. This indicates that, given the controller structure in (2.22), the performance (in terms of the gain I_1) cannot be increased further without violating the modulus margin. The Bode diagram shows that the obtained bandwidth lies between $2.3 \times 10^{-4} \frac{1}{\tau_s}$ for small angles ϑ_i and $5.3 \times 10^{-2} \frac{1}{\tau_s}$ for larger ϑ_i , as indicated by the vertical dashed lines. Hence, it takes more crashes to stabilize around large sawtooth periods (e.g. 14.5 ms) than around small ones (e.g. 3.5 ms), since the DC-gain of $H_i(z)$ is much larger for small periods. Consequently, expressed in real time t convergence to small period setpoints is much faster than to large period setpoints.

The closed-loop performance can be improved if we choose a different controller structure. The phase at high frequencies can be improved by adding a proportional term P to the controller, allowing the bandwidth and controller gain I_1 to increase. Furthermore, we can trade in low-frequency phase for more gain by including a second integral part in the controller. As such we obtain a so-called PII-controller of the form

$$C(z) = -I_2 \cdot \frac{(z+1)^2}{4(z-1)^2} - I_1 \cdot \frac{z+1}{2(z-1)} - P, \quad (2.24)$$

whose equivalent difference equation is given by

$$\begin{aligned} \Delta\vartheta(k) = & 2 \cdot \Delta\vartheta(k-1) - \Delta\vartheta(k-2) - \left[\frac{1}{4}I_2 + \frac{1}{2}I_1 + P\right] \cdot e(k) \\ & - \left[\frac{1}{2}I_2 - 2P\right] \cdot e(k-1) - \left[\frac{1}{4}I_2 - \frac{1}{2}I_1 + P\right] \cdot e(k-2). \end{aligned} \quad (2.25)$$

Again pushing the performance limits, we optimized the three controller parameters to obtain $I_2 = 0.0019$, $I_1 = 0.17$ and $P = 0.21$. The corresponding Bode and Nyquist plots are depicted in figure 2.10. Indeed, the performance has improved: the controller gain I_1 has increased by a factor 2.3, and the low-frequency gain has increased even further by means of the second integral action I_2 . This is also expressed by an increase in bandwidth, which is now between 1.0×10^{-3} and $1.1 \times 10^{-1} \frac{1}{\tau_s}$ (i.e. convergence is roughly between 9 crashes for small periods and 950 for large ones). Therefore, the controller

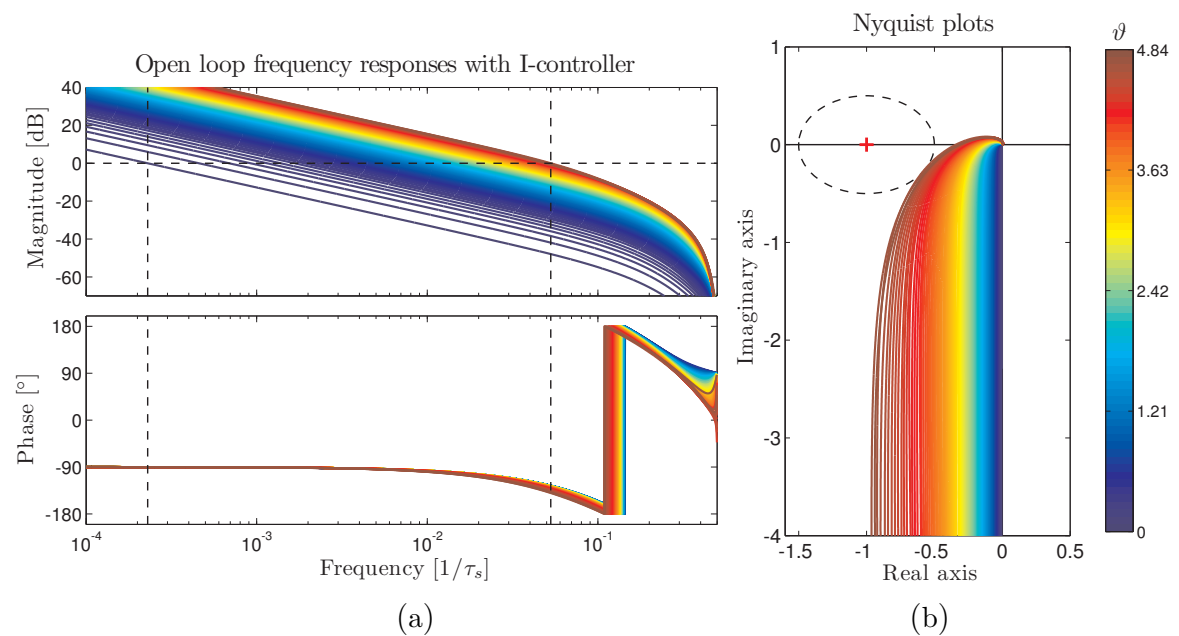


Figure 2.9: Representations of the open loops $C(z) \cdot H_i(z)$ for all identified plants with single $q = 1$ surface, using an integral controller $C(z)$: (a) the frequency response functions (Bode); and (b) Nyquist plots.

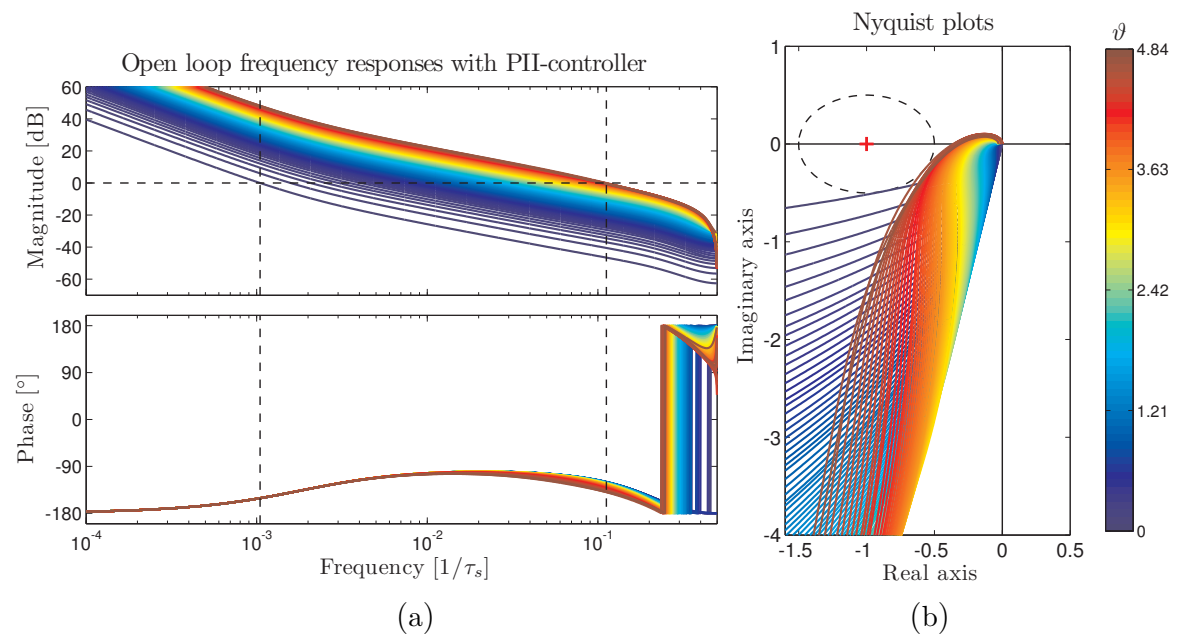


Figure 2.10: Representations of the open loops $C(z) \cdot H_i(z)$ with single $q = 1$ surface using a PII-controller: (a) in frequency domain; and (b) Nyquist plots.

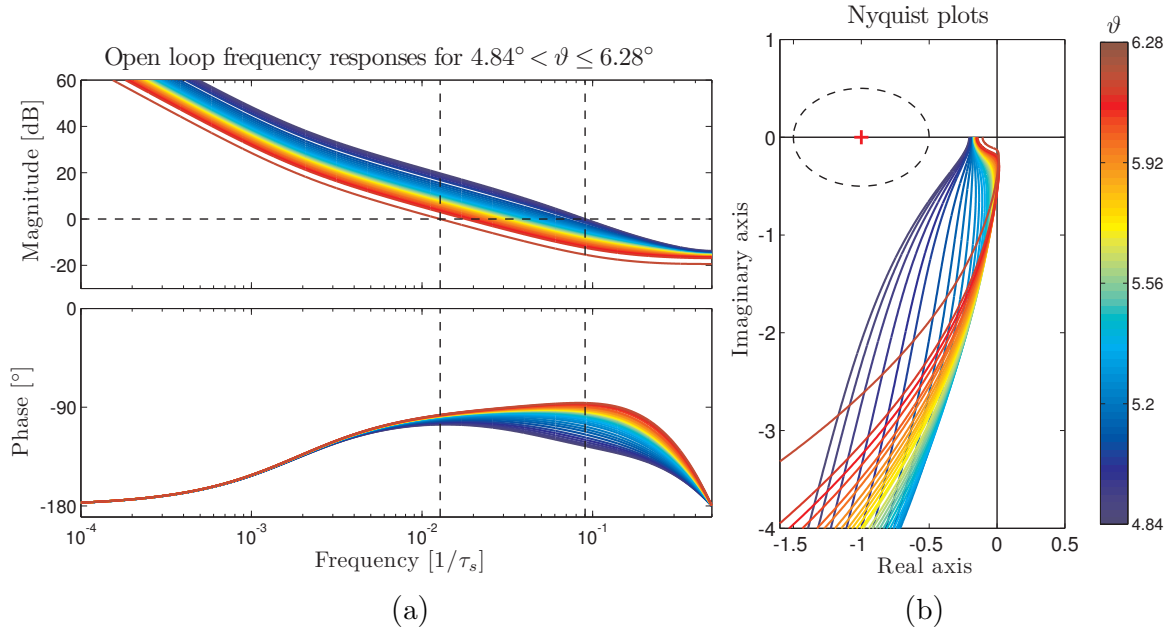


Figure 2.11: Open-loop representations for $4.84^\circ < \vartheta \leq 6.28^\circ$ (having multiple $q = 1$ surfaces) using the same PII-controller as in figure 2.10. The Bode diagram in (a) shows that the performance is fairly high (large bandwidth and gain); the Nyquist plot in (b) shows that all closed loops are robustly stable.

in (2.24) yields shorter settling times and better tracking results in time domain, as we will show in section 2.4.3. The Nyquist plots again show that the controller gain cannot increase without violating the requirements and is thus optimal for the given controller structure (2.24). Note how these plots ‘curl around’ the modulus margin disc, illustrating the classical trade-off in control engineering between performance and robustness.

Next we apply the PII-controller in (2.24) to the region where the q -profile is known to have multiple $q = 1$ surfaces. The resulting open-loop diagrams are shown in figure 2.11. As expected the controller $C(z)$ successfully stabilizes all plants $H_i(z)$ and easily meets the robustness requirement as the Nyquist plots stay away from the modulus margin disc. The frequency domain performance is also quite impressive with a bandwidth between 1.3×10^{-2} and $9.0 \times 10^{-2} \frac{1}{\tau_s}$ and large low-frequency gains. Roughly speaking, twice as large periods τ_s will now converge in seven times less crashes; in contrast to figure 2.10, larger periods will thus stabilize slightly faster than smaller ones.

Notice that in none of the controller design steps presented above we needed explicit information on the underlying physics. From a control point of view only the input–output behaviour of a system is really relevant. Complex underlying physics, such as complicated magnetic reconnections and the presence of multiple current layers, do not necessarily pose problems. In fact, the input–output behaviour in the region corresponding to more complex physics turned out to be beneficial for controller design, as shown in figure 2.11. It is, however, questionable whether this behaviour is actually

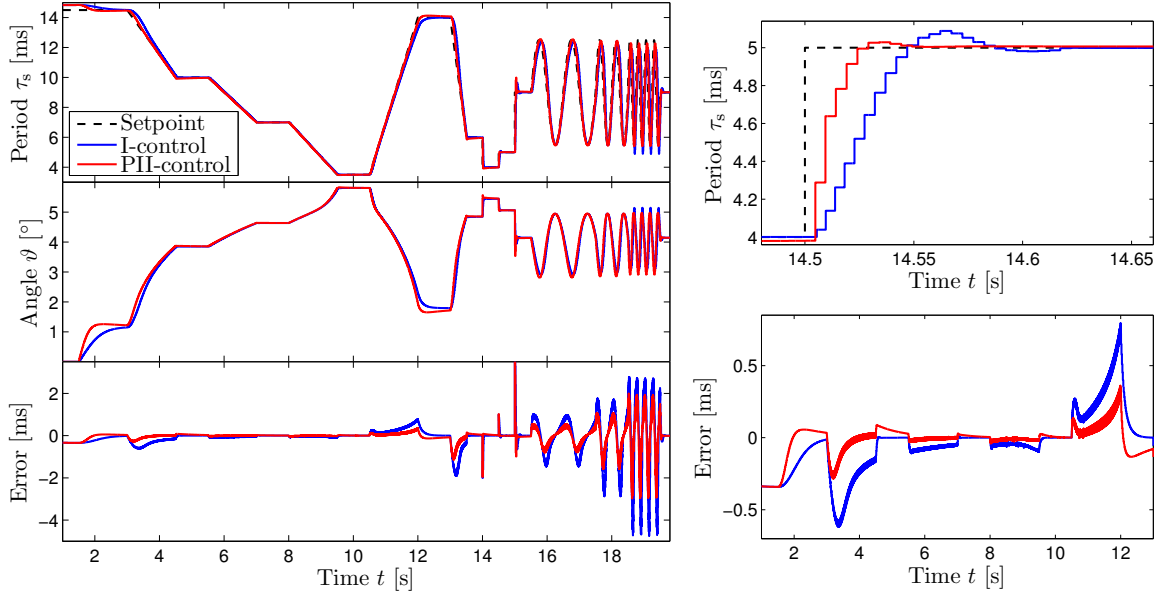


Figure 2.12: Simulink time-domain simulations with the full sawtooth model and the controllers in (2.22) and (2.24) in blue and red, respectively, using a slow and fast changing setpoint for the period. The top right is a zoom of the top left plot, showing a specific step response; the bottom right shows a zoom of the first 13 s (slow setpoint) of the error.

due to these physics or accidentally coincides with it.

At this point we should remark that the proposed method of linearization and linear controller design can only guarantee stability *locally*, i.e. our controllers are only guaranteed to work if the desired period is constant (or changing very slowly) and close to the initial period. However, the simulations in the next section will show that in our case the designed controllers also work for larger and faster input signals.

2.4.3 Time domain results

To prove the applicability of the derived controllers they are tested in the time domain. To this aim we connect each controller separately in a feedback loop with the full non-linear sawtooth model, as was depicted in figure 2.1. The setpoint or reference for the sawtooth period $\tau_{s,\text{ref}}$ in these simulations is chosen to be both slow and fast changing:

- starting from 14.5 ms, first going linearly to 10 ms, 7 ms and 3.5 ms slowly;
- then going back linearly to 14 ms somewhat faster, and going to 6 ms even faster;
- next going to 4 ms, 5 ms and 9 ms stepwise (i.e. infinitely fast);
- then oscillating with 1 Hz, 2 Hz and 4 Hz, respectively.

The closed-loop responses are shown in figure 2.12, depicting the I-controlled case in blue and the PII-controlled one in red. Generally, both controllers obtain excellent tracking results, yielding exactly the desired period. The PII-controller outperforms the I-controller though, as it converges faster, tracks the oscillating part of the setpoint

better, and yields an error which is roughly twice as small. Although *a priori* stability guarantees could only be given locally, i.e. for slowly changing setpoints and initial mirror angles ϑ_{init} close to the desired ones, figure 2.12 shows that our approach obtains fast convergence in all situations, even for fast changing setpoints. The error is, however, the smallest for the slow part of the setpoint, i.e. the first 13 s of the simulation, where the I-controller yields errors smaller than 0.8 ms, and the PII-controller obtains errors of 0.35 ms or less. As the setpoint changes faster, from 1 to 2 to 4 Hz, the error grows up to about 5 ms. Moreover, note that in both the slow and fast changing part the error is the largest when the desired period is the largest. This is in accordance with our previous observation that the DC-gain decreases with increasing sawtooth period. Consequently, for large periods the open-loop gain $H_i(z)C(z)$ is smaller and hence its closed-loop performance in terms of the convergence speed is worse. This effect of slow convergence for large periods is inherent to the sawtooth behaviour in this part of the operating range (the blue region in figure 2.5), and will always be present if we use a single $C(z)$ to control all periods. This could be improved using different controllers for different operating points, which is outside the scope of this paper.

The simulations show that the closed loop is indeed asymptotically stable in the whole operating regime we considered. The output τ_s converges to any desired value $3.1 \leq \tau_{s,\text{ref}} \leq 14.8$ ms, regardless of the initial mirror angle $0^\circ \leq \vartheta_{\text{init}} \leq 6.28^\circ$. This is due to the integrating action, which is an essential part of the sawtooth controllers. As (2.23) shows, a discrete-time integrator computes its output $\Delta\vartheta$ by summing all its inputs e over time k . So as long as the period deviates from the desired value, the controllers gradually change the mirror angle. The angle $\vartheta(k)$ will only remain constant when $e(k) = e(k-1) = 0$. Both controllers do not need any explicit knowledge of the sawtooth system in terms of, e.g. the static steady-state behaviour (by means of a lookup table as in [20]) or the inversion radius to achieve this perfect tracking. Therefore, such integrating controllers are inherently robust. Hence, it is very likely that the derived controllers can still achieve perfect tracking results when the sawtooth behaviour changes due to external disturbances or other processes inside the plasma (such as the presence of fast particles). However, this will probably only be true as long as the system operates in the region to the left of the minimum in figure 2.5(a). When operating at very small sawtooth periods, a small disturbance might push the system to the neighbouring region where the sign of the system changes, making the closed loop locally unstable, and possibly causing ϑ and τ_s to grow. In these situations, stability depends on the desired period in relation to the size and direction of the disturbances. Further investigation of these robustness issues is part of current research.

2.5 Influence of mirror launcher and period detection

The attentive reader will note that in the above simulations we were able to

- adjust the EC mirror angle infinitely fast;

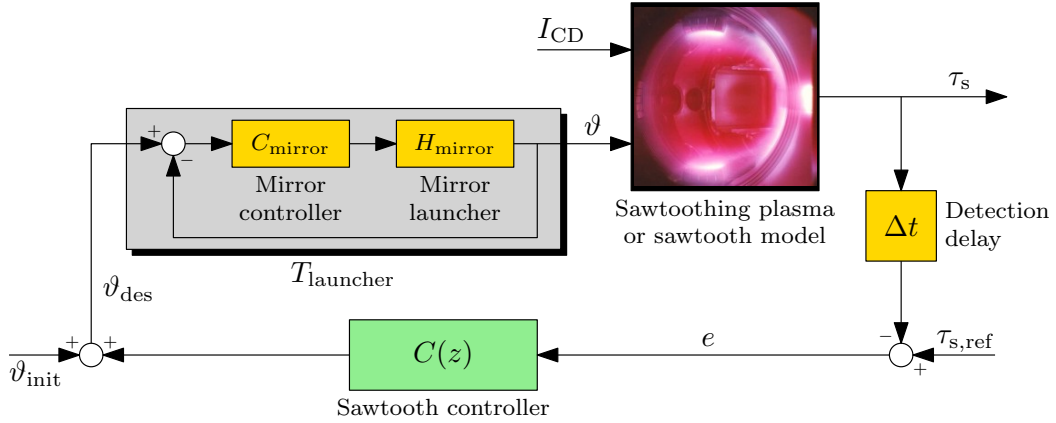


Figure 2.13: Schematic simulation block scheme, including a model for the closed-loop controlled mirror launcher and a sawtooth detection time delay.

- detect crashes instantaneously, hence measure the sawtooth period without any computational delay.

In practice the speed of actuation and detection is limited, but the above suggested methodology for identification and controller design is still applicable in those situations. In figure 2.13 the launcher dynamics is incorporated as a linear feedback loop (in continuous time) [27] and the detection algorithm as a static delay (shift in time) on the sawtooth period signal. The total system as seen by the controller, which should thus be identified, is now the combination of mirror launcher, sawtoothing plasma and detection delay. Consequently, slow actuation and detection changes the controller design and results in a closed-loop performance degradation. This section will illustrate this by discussing the effects of slow actuation and detection separately.

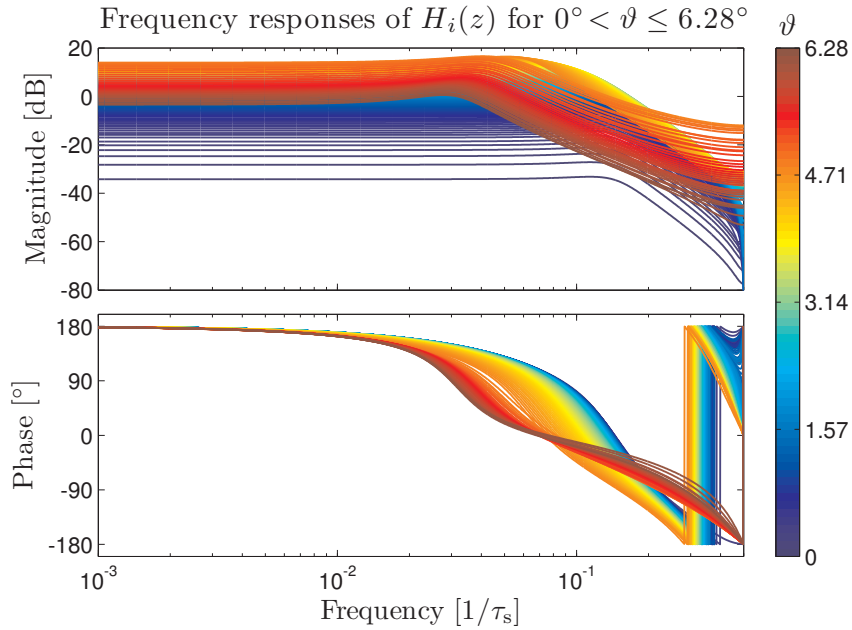
2.5.1 Poloidal mirror launcher

The poloidal angle of the ECCD mirror is commonly altered by means of a mechanical launcher installation connected to it, which is in turn feedback controlled (see figure 2.13). The speed of this closed loop is restricted by the mechanical design of the launcher and the corresponding controller. Roughly speaking, a launcher will track inputs with frequencies up to its open-loop bandwidth f_c quite well (i.e. $\vartheta = \vartheta_{des}$), but will hardly respond to larger frequencies. Unfortunately, most reported bandwidths, like 6.6 Hz on TCXV [19] and 12 Hz on TEXTOR [27], are rather low.

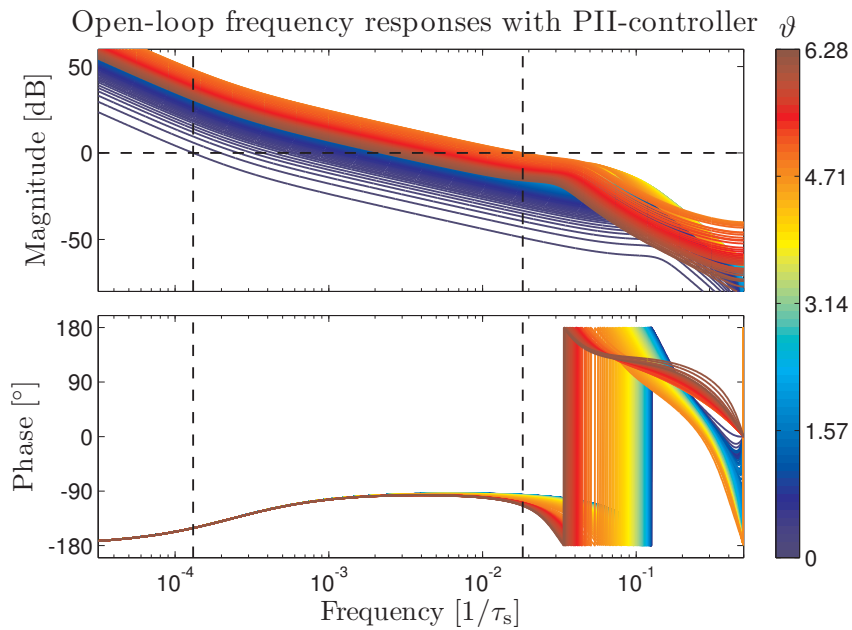
To illustrate the effect of such low bandwidths on the achievable closed-loop sawtooth performance, we model the launcher closed loop $T_{launcher}(s)$ as a continuous-time low-pass filter with cut-off frequency $f_c = 10$ Hz and damping $\beta = 0.35$, i.e.

$$T_{launcher}(s) = \frac{H_{mirror}C_{mirror}}{1 + H_{mirror}C_{mirror}} = \frac{(2\pi f_c)^2}{s^2 + 2\beta(2\pi f_c)s + (2\pi f_c)^2}, \quad (2.26)$$

with s the Laplace variable. Next, we repeat the identification procedure of section 2.3.2 on the interconnection of the sawtooth model and $T_{launcher}(s)$. The resulting estimated



(a)



(b)

Figure 2.14: Bode diagrams of the frequency responses including the mirror launcher dynamics: (a) of all identified systems $H_i(z)$ (third order for single $q = 1$ case, second order for multiple $q = 1$); and (b) of the open loops $C(z)H_i(z)$ after optimization of the PII-controller.

$H_i(z)$ are depicted in figure 2.14(a), again showing slightly different behaviour for operating points coinciding with multiple $q = 1$ surfaces (red curves). More importantly, all $H_i(z)$ are now dominated by the launcher dynamics, as the frequency responses can

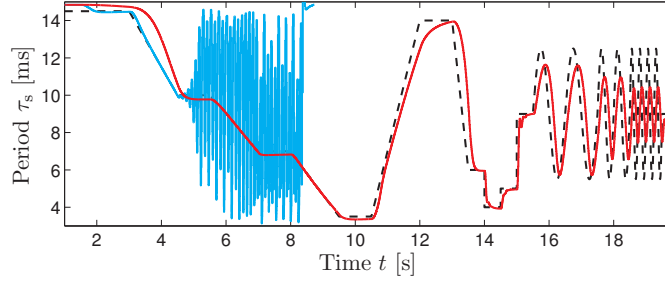


Figure 2.15: Closed-loop Simulink simulations including launcher model. The PII-controller of section 2.4.2 (cyan) yields unstable behaviour, which is corrected by the PII-controller of section 2.5.1 (red). Tracking of the setpoint (dashed) is worse than before, which is due to the slow mirror launcher dynamics.

be approximated by a combination of the low-pass filter in (2.26), varying DC-gain and an extra crash delay. Since $T_{\text{launcher}}(s)$ is sampled every sawtooth period τ_s , which is again approximately constant for the small perturbations of the identification analysis, the low-pass cut-off frequency f_c has a different normalized equivalent of $f_c \cdot \tau_s$ for each $H_i(z)$. Since in our region of interest we have $3.1 \leq \tau_s \leq 14.8$ ms, the cut-off frequency varies between $3.1 \times 10^{-2} \frac{1}{\tau_s}$ and $1.48 \times 10^{-1} \frac{1}{\tau_s}$, as can be seen in figure 2.14(a).

Consequently, the 180° phase drop at the cut-off also varies over a wide frequency range. This is very restrictive in controller design, as a single linear controller $C(z)$ can then never achieve a bandwidth higher than the lowest cut-off $f_c \cdot \tau_{s,\min}$. Now optimizing the PII parameters in (2.24) to achieve maximal performance (satisfying the stability and robustness constraints) for the new $H_i(z)$, we obtain $I_2 = 3.1 \times 10^{-5}$, $I_1 = 0.021$ and $P = 0.040$. The corresponding open-loop frequency responses are shown in figure 2.14(b). The closed-loop performance is indeed worse than in section 2.4.2, since the gain I_1 is a factor 8 lower and the bandwidth is now between 1.3×10^{-4} and $1.8 \times 10^{-2} \frac{1}{\tau_s}$, corresponding to convergence rates roughly between 55 and 7600 crashes.

This performance degradation is underlined by the time-domain simulations of figure 2.15, showing worse tracking behaviour than in figure 2.12. Again, performance is best for slow small-valued setpoints for the sawtooth period. To prove that the PII-controller of section 2.4.2 is no longer suitable, its response in a closed loop with slow launcher dynamics is also shown. Initially this controller performs very well, but as the period decreases the response becomes unstable at some point, oscillating for about 4 s until the simulation is terminated. We can identify exactly when this happens using the Nyquist plots of the open loops consisting of the identified plants in figure 2.14(a) and the controller of section 2.4.2. These plots will show that the open loop crosses the point $(-1, 0)$ when $\vartheta_i \geq 3.24^\circ$, i.e. when $\tau_{s,\text{ref}} \leq 11.66$ ms. This can be confirmed by simple time domain simulations: the closed loop is just stable for $\tau_{s,\text{ref}} = 11.7$ ms, whereas for $\tau_{s,\text{ref}} = 11.6$ ms the response is indeed unstable.

We have seen that mirror launcher steering mechanisms can be very restrictive on sawtooth control performance, even for current state-of-the-art mechanisms [19,

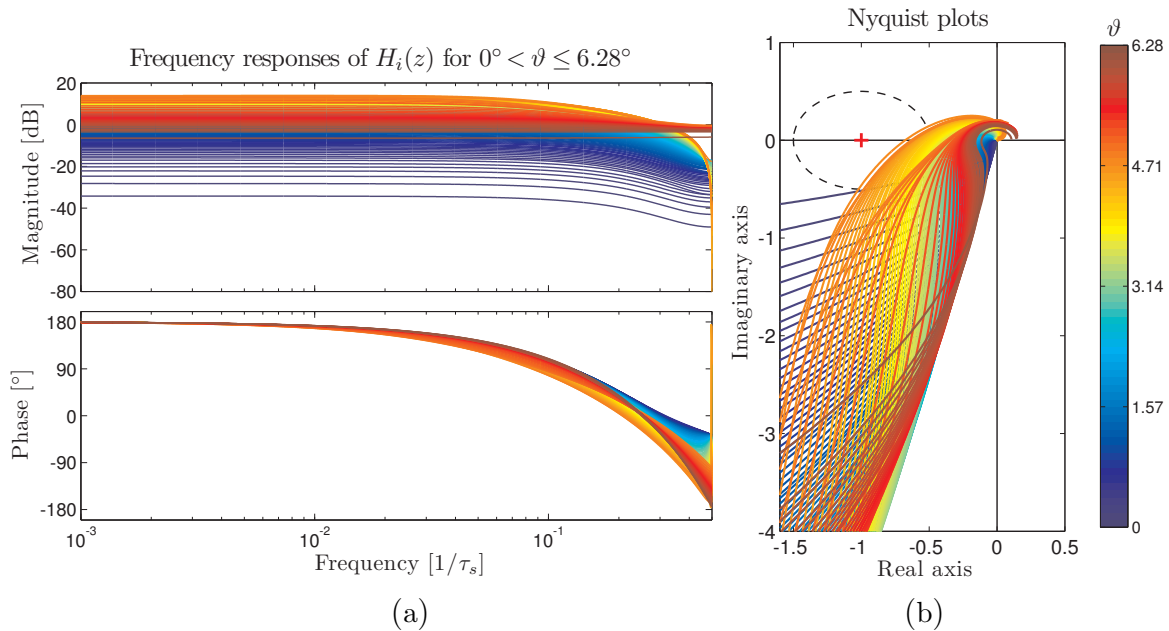


Figure 2.16: Illustration of the influence of a detection delay (here 3 ms). (a) Delay introduces a high frequency phase drop in the Bode diagram of all $H_i(z)$, which increases with decreasing τ_s ; (b) this causes the Nyquist plot of the open loop with the PII-controller of section 2.4.2 to loose robustness, although stability is maintained.

27]. This is true whenever its bandwidth pops up in the identified plants $H_i(z)$, so whenever $f_c \cdot \tau_{s,\min} < 0.5$. If slow closed-loop responses are acceptable, the analysis in section 2.3 can be reduced to just the identification of the DC-gain of the sawtooth (e.g. by means of a slow sweep of the mirror), as the remaining dynamics of $H_i(z)$ consists of the known discretized closed-loop launcher dynamics and an additional delay of one crash. However, in the likely situation that this yields unsatisfactory responses, the obvious solution is to increase the launcher bandwidth f_c , which sometimes requires a complete redesign of its mechanics. The design should be such that the launcher installation responds faster than the smallest possible sawtooth period. Alternatively, launcher tracking responses can be improved using feedforward control, as has been done on TEXTOR [27], which anticipates for the launcher's inertia and friction. The possibilities of feedforward control on present-day launchers as on TEXTOR and Tore Supra are limited, however, due to large non-linear friction components and mechanical hysteresis.

2.5.2 Sawtooth detection algorithm

Commonly used diagnostic systems to observe sawteeth include ECE temperature measurements and soft x-ray channels. Obtaining the sawtooth period from these measurements in real-time requires detection of the sawtooth crashes. This usually requires low-pass or band-pass filtering of the ECE or soft x-ray signals to discriminate between crash and noise [17]. However, this introduces time delays in the feedback loop

as crashes are observed Δt milliseconds after they actually occurred. Generally, more robust algorithms (less prone to fake or missed detections) involve larger delays Δt .

The effect of this Δt is dependent on the period $\tau_{s,i}$ at a certain operating point and can be expressed mathematically as the frequency response function

$$D(f) = \exp(-j2\pi f \cdot \Delta t / \tau_{s,i}). \quad (2.27)$$

The corresponding phase satisfies $\angle D(f) \propto -f \Delta t / \tau_{s,i}$, so it decreases linearly with increasing frequency f . The same phase drop will pop up in $H_i(z)$ when the sawtooth model is combined with a static delay as in figure 2.13. Figure 2.16(a) depicts a specific example with a constant $\Delta t = 3$ ms. This 3 ms is an estimation of the worst case time delay when using advanced wavelet based edge detection techniques on TEXTOR data [26]. This technique has proven to be extremely robust, yielding at most 3 ms of delay for hard-to-detect crashes and being even faster otherwise. Even such a small delay can have a large influence, as figure 2.16(a) shows that the phase drop can increase up to 180° for operating points with small sawtooth periods (the delay is then a whole period, since $\Delta t \approx \tau_{s,i}$). The consequence for the closed loop is illustrated in the open loop Nyquist plot of figure 2.16(b), using the same PII controller as in section 2.4.2. All operating points are still stable, but the plots are much closer to $(-1, 0)$, yielding a less robust closed loop and more oscillatory behaviour. The operating points having the worst performance and robustness are the ones whose open loop now enter the modulus margin disc, in this case $3.92^\circ < \vartheta_i < 5.0^\circ$, corresponding to sawtooth periods between 5.3 and 9.8 ms. Note that operating points with very small periods, for which $\Delta t \approx \tau_{s,i}$, perform even better, as these points show much better gain-phase behaviour in the frequency domain. Moreover, local instability does not occur until the delay is increased up to 6 ms.

The performance and robustness degradation as in figure 2.16(b) is often unacceptable and thus requires a redesign of the controller, which will yield a worse closed-loop performance. To minimize this effect the amount of delay should always be kept to a minimum, preferably such that $\Delta t \ll \tau_{s,\min}$.

Sometimes the sawtooth period signal itself is low-pass filtered to reduce the erratic effects which can be present. A commonly used filter [20] is the n th order running average filter¹, which can be written as

$$A(z) = (1 + z^{-1} + z^{-2} + \dots + z^{-n}) / n. \quad (2.28)$$

Higher n yields a smoother period signal, but also introduces a phase delay of $f \cdot n \cdot 180^\circ$. Other low-pass filters show similar behaviour, losing phase as n and f increase. Obviously, this places an even larger restriction on the achievable sawtooth bandwidth than a constant Δt . From a control point of view low-pass filters should be tuned

¹The running average filter only suppresses frequency $1/(n+1)$ and all its higher harmonics, and as such it is not very suited to suppress general high frequent noise. It is better to use Butterworth or Chebyshev filters for this purpose.

specifically for the disturbances which are present in the closed loop, while keeping its order n to a minimum, or else should be avoided.

2.6 Conclusions, future work and discussion

In this paper we have derived a low complexity sawtooth model, based on the Kadomtsev reconnection model and the critical shear condition of Porcelli, and implemented it in the real-time simulation environment of Matlab[®] Simulink[®]. This model successfully mimics the basic and well-known effect of co-current ECCD deposition on the sawtooth period: shortening the period for depositions inside $q = 1$ and lengthening it otherwise.

This implemented model was then used as a case study for systematic analysis and structured controller design for the sawtooth instability. Identification simulations were performed to gain insight into the dynamics around various operating points. This analysis revealed that the sawtooth model acts as a low-pass filter, although its behaviour for on-axis deposition locations is quite different from more outward depositions. The transition seemed to correspond with the transition from single $q = 1$ situations to the case with multiple $q = 1$ surfaces. Based on the identified frequency response functions both an I- and a PII-controller was designed, maximizing the closed-loop performance while satisfying stability and robustness specifications. Time simulations showed its success for both slow and fast changing setpoints; as expected convergence is much faster for small period setpoints than for large ones.

Next, the influence of slow actuation and detection was investigated. The launcher installations on current day tokamaks are relatively slow, making their dynamics dominant over the sawtooth dynamics themselves. On the one hand this can simplify analysis, as only the sawtooth DC-gain and the closed-loop launcher dynamics are relevant for controller design. On the other hand it calls for a redesign of the launcher mechanics, as it restricts the achievable closed-loop performance to a large extent.

The analysis and design approach in this paper relies on a representation of the sawtooth cycle in the discrete-time crash domain, although the time between samples (crashes) is variable. The usefulness of this approach is evident from the obtained results, but a rigorous mathematical proof of its validity is an important topic of future research. Furthermore, the work in this paper focused on a specific operating regime of the sawtooth instability, namely small deposition angles ϑ , corresponding to depositions close to the plasma centre, yielding periods smaller than ohmic. In future research the focus should be broadened in order to derive a controller for the whole operating range of the ECCD mirror. Possible research directions include hybrid controller switching techniques or extremum seeking algorithms.

Moreover, this work only considers the nominal case where various plasma parameters remain constant and disturbances are hardly present. Future work will involve an investigation of changing plasma conditions on the identified plants, an identification of plasma disturbance dynamics, and the influence of these issues on controller design and closed-loop performance. Also, the possibility of using other control inputs (like

gyrotron power) will be investigated.

Finally, the suggested approach of identification and structured controller design can and will be applied to other models and systems. A particular example is the application to numerical transport codes (like CRONOS) with a sawtooth triggering module, to investigate whether more complex underlying physics changes the sawtooth dynamics and how this can possibly influence controller design. Such codes will enable research on the effect of ECRH on the profile evolution of T_e and q and the resulting dynamics of the sawtooth period. With regard to the ITER baseline design the influence of fast particles will be of particular interest, as the prevention of long sawteeth due to the stabilizing effect of fusion-born α particles is an important issue. Moreover, applying the proposed approach on actual tokamak plasmas certainly deserves further attention.

The feasibility of controlling the sawtooth period in burning plasmas, like on ITER, is still a current subject of debate. Some argue that the α heating and corresponding sawtooth period lengthening will be so dominant that the effect of ECCD on the sawtooth period will be negligible. However, the ability to control the period towards very specific values or value ranges will be of uttermost importance on ITER. Even in the presence of fast particles the period should be small enough to avoid NTM triggering and to prevent accumulation of helium in the plasma core, but should also be large enough to ensure the continuation of the fusion reaction by allowing the fusion-born energetic α particles to transfer their energy to the plasma. The ability to show this for a relatively simple ECCD actuated sawtooth model, as in this paper, is an essential step in this direction. If we cannot prove systematic control over the period for simple models, it will certainly be impossible on ITER.

Acknowledgments

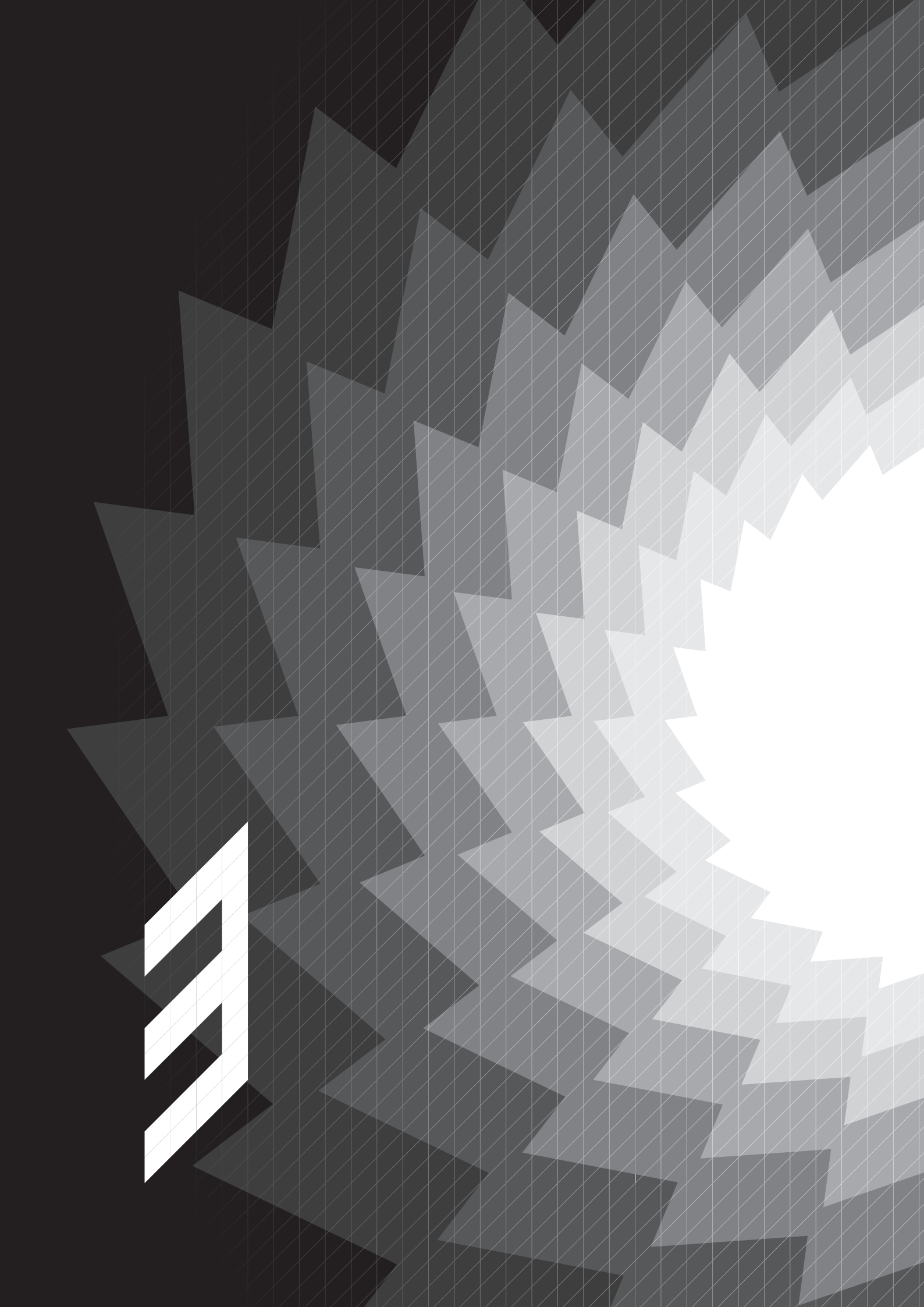
The authors would like to thank Hugo de Blank for his contribution to section 2.2.1, and Prof. Okko Bosgra for his inspirational thoughts on section 2.3.2.

The work in this paper has been performed in the framework of the NWO-RFBR Centre of Excellence (grant 047.018.002) on Fusion Physics and Technology. This work, supported by NWO, ITER-NL and the European Communities under the contract of the Association EURATOM/FOM, was carried out within the framework of the European Fusion Programme. The views and opinions expressed herein do not necessarily reflect those of the European Commission.

References

- [1] von Goeler S. *et al.* 1974 *Phys. Rev. Lett.* **33**(20) 1201
- [2] Hastie R.J. 1997 *Astrophys. Space Sci.* **256**(1) 177
- [3] Chapman I.T. 2011 *Plasma Phys. Control. Fusion* **53**(1) 013001

- [4] Nave M.F.F. *et al.* 2003 *Nucl. Fusion* **43**(10) 1204
- [5] Sauter O. *et al.* 2002 *Phys. Rev. Lett.* **88**(10) 105001
- [6] Gude A. *et al.* 2002 *Nucl. Fusion* **42**(7) 833
- [7] Porcelli F. *et al.* 1996 *Plasma Phys. Control. Fusion* **38**(12) 2163
- [8] Campbell D.J. *et al.* 1988 *Phys. Rev. Lett.* **60**(21) 2148
- [9] Chapman I.T. *et al.* 2009 *Nucl. Fusion* **49**(3) 035006
- [10] Chapman I.T. *et al.* 2007 *Plasma Phys. Control. Fusion* **49**(12B) B385
- [11] Graves J.P. *et al.* 2009 *Phys. Rev. Lett.* **102**(6) 065005
- [12] Mück A. *et al.* 2005 *Plasma Phys. Control. Fusion* **47**(10) 1633
- [13] Angioni C. *et al.* 2003 *Nucl. Fusion* **43**(6) 455
- [14] Merkulov A. *et al.* 2004 *Proc. of Joint Varenna-Lausanne Int. Workshop on Theory of Fusion Plasmas* (Varenna, Italy) 279
- [15] Eriksson L.G. *et al.* 2006 *Nucl. Fusion* **46**(10) S951
- [16] Chapman I.T. *et al.* 2008 *Nucl. Fusion* **48**(3) 035004
- [17] Lennholm M. *et al.* 2009 *Fusion Sci. Technol.* **55**(1) 45
- [18] Lennholm M. *et al.* 2009 *Phys. Rev. Lett.* **102**(11) 115004
- [19] Paley J.I. *et al.* 2009 *Nucl. Fusion* **49**(8) 085017
- [20] Paley J.I. *et al.* 2009 *Plasma Phys. Control. Fusion* **51**(5) 055010
- [21] Paley J.I. *et al.* 2009 *Plasma Phys. Control. Fusion* **51**(12) 124041
- [22] Åström K.J. and Wittenmark B. 1997 *Computer-Controlled Systems: Theory and Design* 3rd edn. (Englewood Cliffs, NJ: Prentice Hall)
- [23] Franklin G.F. *et al.* 1998 *Digital control of dynamic systems* 3rd edn. (Menlo Park, CA: Addison-Wesley)
- [24] Witvoet G. *et al.* 2010 *Proc 16th Joint Workshop on Electron Cyclotron Emission and Electron Cyclotron Resonance Heating* (Sanya, China) 390–395
- [25] Kadomtsev B.B. 1975 *Sov. J. Plasma Phys.* **1**(5) 389
- [26] van Berkel M. *et al.* 2011 *Fusion Eng. Des.* in press
- [27] Hennen B.A. *et al.* 2010 *Plasma Phys. Control. Fusion* **52**(10) 104006
- [28] de Schutter B. 2000 *J. Comput. Appl. Math.* **121**(1-2) 331
- [29] Witvoet G. *et al.* 2010 *Proc. 2010 Amer. Contr. Conf.* (Baltimore, MD, USA) 1979–1984
- [30] Wesson J.A. and Campbell D.J. 2004 *Tokamaks* 3rd edn. (Oxford: Oxford University Press)
- [31] Westerhof E. *et al.* 2003 *Nucl. Fusion* **43**(11) 1371
- [32] Oosterbeek J.W. *et al.* 2008 *Rev. Sci. Instrum.* **79**(9) 093503
- [33] Haddad W.M. *et al.* 2006 *Impulsive and hybrid dynamical systems* (Princeton, NJ: Princeton University Press)
- [34] The MathWorks, Inc. 2007 *Writing S-Functions* Version 6.6
- [35] Westerhof E. *et al.* 2002 *Nucl. Fusion* **42**(11) 1324
- [36] Horn R.A. and Johnson C.R. 1985 *Matrix Analysis* (Cambridge University Press)



CHAPTER 3

Sawtooth period control strategies and designs for improved performance

G. Witvoet^{a,b,c}, M. Steinbuch^a, M.R. de Baar^{a,b}, N.J. Doelman^c
and E. Westerhof^b

^a Eindhoven University of Technology

^b FOM-Institute for Plasma Physics Rijnhuizen

^c TNO Technical Sciences



Abstract

The sawtooth instability is associated with the triggering of neoclassical tearing modes, core fuelling, α -confinement and the exhaust of thermal helium. Sawtooth control is therefore important for optimal reactor performance in ELMy H-modes. Control schemes for the sawtooth period have been published in literature, but the systematic design of high-performance controllers (yielding accurate and fast convergent responses) has not been addressed. In this work, three control strategies for high performance sawtooth control are presented using electron cyclotron current drive (ECCD). Both degrees of freedom of the ECCD actuator will be explored and combined with advanced controller designs. First, the ECCD deposition location is used as a control variable, for which a gain-scheduled feedback controller and static feedforward control is derived. Second, the use of the driven current as a control variable is explored, and a simple controller is designed based on the identified dynamics. In the third approach both control variables are joined in an overall controller design, which enables the combination of high-performance control of the sawtooth period with control of the gyrotron power. Time-domain simulations with a combined Kadomtsev–Porcelli sawtooth model show that each strategy obtains a better closed-loop performance than standard linear feedback techniques on merely the deposition location.

3.1 Introduction

The sawtooth is a repetitive reorganization cycle of the plasma core [1,2], which is able to trigger neoclassical tearing modes (NTMs) well below the ideal β -limit [3,4]. These NTMs are accompanied by a reduction of energy confinement, and can lead to plasma disruptions. In a fusion reactor the sawtooth can also regulate the exhaust of Helium and α particles [5] and the influx of Deuterium and Tritium. The sawtooth period appears to be the most significant factor influencing these processes of α -confinement, refuelling and NTM avoidance [6], which motivates the need to control this period.

It has been shown experimentally that the sawtooth period can be manipulated by either neutral beam injection (NBI) [7,8], ion cyclotron (IC) waves [9–11], or electron cyclotron (EC) waves [12–14]. The latter is particularly effective, as EC waves can drive highly localized currents near the $q = 1$ surface, thereby altering the magnetic shear at this surface, a quantity which is associated with the onset of the sawtooth crash [15]. As such, the period can either be lengthened or shortened, subject to the deposition location and direction of the EC current drive (ECCD).

Control over the sawtooth period, in which the period is forced to and maintained at any desired value, requires the use of feedback loops. Experiments on Tore Supra [16,17] and TCV [18,19] have demonstrated the possibilities of closed-loop sawtooth period control, by changing the ECCD deposition location in real-time via a steerable EC mirror launcher. A systematic analysis of the sawtooth dynamics and consequent structured controller design for this situation has been developed in [20]. The linear controllers considered in this design are relatively robust against plasma uncertainties and variations within the bounds of the considered operating regime, and are therefore a natural choice for present-day experimental devices.

However, the results in [20] also revealed that linearly controlled sawteeth yield different convergence rates for different operating points, where the spread in these rates can be enormous. Moreover, when the EC mirror launcher is slow compared to the shortest sawtooth, as is the case on most present-day tokamaks [21,22], convergence rates can go up to thousands of crashes, yielding relatively large closed-loop errors. Hence, a high robustness leads to a degraded performance, which is an example of the classical performance–robustness trade-off in control engineering. Under reactor-like conditions such a poor performance will be unacceptable. It motivates the development of alternative control strategies to improve the closed-loop performance, i.e. to achieve faster convergence to desired sawtooth periods and smaller closed-loop errors. This can be achieved by taking more explicit knowledge of the sawtooth dynamics into the controller design. Note that this requires operation in a predictable and reproducible plasma regime, which coincides with the operational regime of a fusion reactor.

In this paper we will provide three of such alternative control strategies, and apply these to a numerical Kadomtsev–Porcelli diffusion model of the sawtooth instability [15,23]. These strategies take advantage of the capabilities of the ECCD actuator, exploring both the EC mirror angle and the driven current as control variables. First,

we consider sawtooth control via the EC mirror angle, and show how the limitations imposed by a slow mirror launcher can be overcome by using a gain-scheduled feedback controller [24] and additional static feedforward control. The design of the feedback controller makes use of easy-to-compute approximations of the sawtooth dynamics, which are shown to be sufficiently accurate. Second, we propose to use the amount of driven current (or gyrotron power) as an actuator, which is motivated by the generally extremely fast dynamics of the gyrotron. We will identify the corresponding sawtooth dynamics using approximate realization techniques [25], and show that this dynamics is such that a simple integral controller can yield an excellent performance. Third, we introduce the notion of multiple-input-multiple-output (MIMO) control, and design a feedback controller using sequential loop closing [26, 27]. This approach combines high-performance control of the sawtooth period via the driven current with a robust control loop for the requested gyrotron power via the EC mirror angle. MIMO control is expected to be an essential tool to maximize the energy efficiency of the sawtooth controller. Each of the controllers is designed in the frequency domain and optimized with respect to stability, robustness, and performance, as discussed in [20]. Moreover, time-domain comparisons will show that each strategy indeed has a better performance than the previously mentioned linear feedback approach on the EC mirror angle only.

This paper is organized as follows. Section 3.2 introduces the Kadomtsev–Porcelli sawtooth model which is used throughout this paper, as well as the representation of its dynamics and approximations thereof. Section 3.3 treats the three performance-improving control strategies and designs, and concludes with some remarks on stability. Finally, conclusions and discussion are mentioned in section 3.4.

3.2 The sawtooth model and its dynamic representation

The control strategies derived in this paper will be applied to a physics-based sawtooth model which has extensively been described in [20] and has also been used in [28]. In this section we will shortly summarize the main aspects of this model, and recapitulate how to denote its dynamics in the discrete-time domain. Finally, we will discuss how the sawtooth dynamics identification routine as presented in [20] can be simplified when the launcher of the EC beam mirror is much slower than the sawtooth itself, and thus dominates the overall dynamic response.

3.2.1 A Kadomtsev–Porcelli diffusion model

The considered sawtooth model aims to reproduce realistic input–output behaviour with as little complexity as needed, hence focusing only on the dominant dynamics of the sawtooth. It revolves around three physics models: the magnetic diffusion equation, the crash criterion of the Porcelli model [15], and the Kadomtsev reconnection model [23]. It can be written as a set of equations for the poloidal magnetic field B_θ

as a function of time t and space r [20]:

$$\frac{\partial}{\partial t} B_\theta = \frac{\partial}{\partial r} \left(\frac{\eta}{\mu_0 r} \left(B_\theta + r \frac{\partial}{\partial r} B_\theta \right) - \eta J_{\text{CD}} \right) \quad \text{if } s_1 < s_{\text{crit}}, \quad (3.1a)$$

$$B_\theta(r, t^+) = \begin{cases} B_\theta(r, t^-) & \text{for } r \geq r_{\text{mix}} \\ \frac{d}{dr} \Psi_*^c(r) + \frac{1}{R_0} r B_\phi & \text{for } r < r_{\text{mix}} \end{cases} \quad \text{if } s_1 \geq s_{\text{crit}}, \quad (3.1b)$$

with boundary conditions $B_\theta(0, t) = 0$ and $B_\theta(a, t) = \frac{\mu_0 I_p}{2\pi a}$. Here $s_1 = s(r_{q=1})$ denotes the magnetic shear at the surface where the safety factor q equals 1, which is compared to a constant critical shear threshold value s_{crit} ; and r_{mix} is the mixing radius, i.e. the radius up to which the flux surfaces reconnect during the crash. The post-crash helical flux function $\Psi_*^c(r)$ depends on the helical flux $\Psi_*(r)$ before the crash, defined as

$$\Psi_*(r) = \int_0^r [B_\theta(\tilde{r}) - \tilde{r} B_\phi / R_0] d\tilde{r}, \quad (3.2)$$

and can be calculated using an Archimedes–Kadomtsev approach [20], i.e.

$$\Psi_*^c(r_c) = \Psi_*(r_{i-}) = \Psi_*(r_{j+}), \quad \text{where } r_c^2 = \sum_i r_{i-}^2 - \sum_j r_{j+}^2. \quad (3.3)$$

Here r_{i-} are all pre-crash surfaces with $d\Psi_*/dr < 0$ and r_{j+} are all pre-crash surfaces with $d\Psi_*/dr > 0$. Moreover, η is the plasma resistivity, μ_0 is the vacuum magnetic permeability, B_ϕ is the toroidal magnetic field (taken constant by virtue of a large aspect-ratio), I_p is the plasma current and a and R_0 are the tokamak minor and major radius respectively.

This model has been embedded in a specially written C-code and implemented into the Matlab[®] Simulink[®] simulation environment. In this implementation the sawtooth period can be determined with a precision of nearly 10^{-6} ms,¹ which enables a reliable assessment of the sawtooth dynamics. Although this implemented model is applicable to various tokamaks, in this paper typical dimensions and parameters are specifically chosen to represent TEXTOR, yielding an ohmic sawtooth period of 14.9 ms.

The behaviour between the input (actuator) and output (variable to be controlled) of a system is of great importance for controller design. In our model the non-inductive current J_{CD} represents the actuator. Assuming a constant deposition width, this J_{CD} is characterized by the total driven current I_{CD} and its deposition location. The latter is determined by the poloidal deflection angle ϑ of the EC beam, imposed by the EC mirror rotation. Details on the calculation of J_{CD} can be found in [20]; here it suffices to remark that the deposition location moves outwards with increasing $|\vartheta|$ and is closest to the plasma centre when $\vartheta = 0^\circ$. The inputs to the model are thus I_{CD} and ϑ ; these are the actuator settings which are used as control variables. The output of the model is the sawtooth period τ_s , i.e. the time between two subsequent crashes (3.1b).

¹In fact, the variable-step solver has been set to use a relative and absolute tolerance of 10^{-9} , which forces the numerical error on the crash instant to be less than 10^{-6} ms.

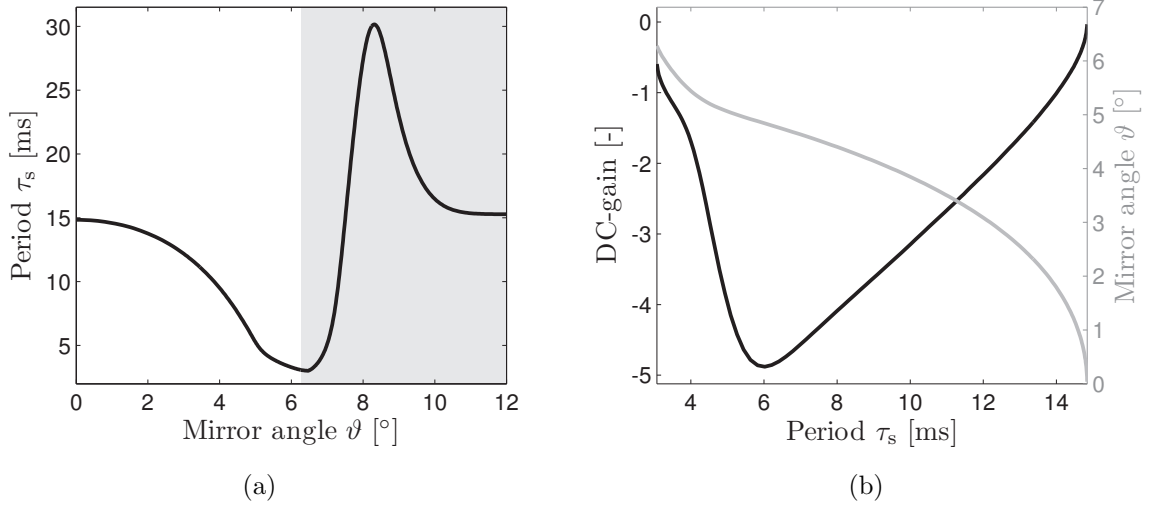


Figure 3.1: Static characteristics of the sawtooth model (3.1a)–(3.1b) using $I_{\text{CD}} = 2$ kA; (a) the steady-state input–output map, i.e, the sawtooth period τ_s for a constant input ϑ as $t \rightarrow \infty$; and (b) representation of the input–output map as a function of τ_s for $0^\circ \leq \vartheta \leq 6.28^\circ$ (grey) and the corresponding DC-gain $\Delta\tau_s/\Delta\vartheta$ (black).

In this paper both inputs I_{CD} and ϑ will be examined for use in a controller design, but first the mirror angle ϑ will be considered as a control variable while I_{CD} remains constant. This is quite common as most studies on control of the sawtooth period rely on this methodology [17, 18, 20]. Figure 3.1(a) depicts the steady-state input–output map of the model for this configuration, showing the behaviour of the sawtooth period to changing deposition locations; depositions inside $q = 1$ shorten the period, whereas depositions outside $q = 1$ lengthen it [12–14, 20]. Note that the slope of figure 3.1(a) changes sign: an increase in ϑ can either increase or decrease τ_s , depending on the specific value of ϑ . This makes it generally hard to derive a single controller for the whole operating range. As in [20] we therefore focus on $0^\circ \leq \vartheta \leq 6.28^\circ$, i.e. the non-shaded part of figure 3.1(a), where the periods are smaller than ohmic. Note that likewise shortening of the sawtooth period is considered to be necessary to avoid NTM triggering [29]. The black line in figure 3.1(b) shows the DC-gain as a function of the steady-state period τ_s for this specific region; it denotes the change in steady-state output $\Delta\tau_s$ for a small change $\Delta\vartheta$ in the input, which is thus the slope $\Delta\tau_s/\Delta\vartheta$ of figure 3.1(a). This DC-gain, which we label $d(\tau_s)$, is relevant for the feedback controller design in section 3.3.1. The grey line in figure 3.1(b) depicts the input–output map for the considered region as a function of the steady-state sawtooth period τ_s . This line will be used as the feedforward controller $\vartheta_{\text{ff}} = h(\tau_{s,\text{ref}})$ in section 3.3.1.

3.2.2 Sawtooth dynamics in the discrete-time domain

Feedback controller design requires knowledge of the sawtooth dynamics underneath the static map of figure 3.1, i.e. the time dependence (or transient) of the sawtooth

period as it changes from one operating point to another. The sawtooth period can only be observed by detecting a sawtooth crash, hence the measurements of the period are discrete in time. A sawtooth feedback controller will only react when it receives a new sawtooth period measurement, likewise the input (in this case ϑ) will only change at a crash and remains constant in between. The sawtooth dynamics can thus be described as a discrete-time system [20, 30], where the output τ_s at a certain crash number k is expressed in terms of outputs τ_s and inputs ϑ at previous crashes:

$$\tau_s(k) = f(\vartheta(k), \vartheta(k-1), \vartheta(k-2), \dots, \tau_s(k-1), \tau_s(k-2), \dots). \quad (3.4)$$

Unfortunately, the function f is unknown, even if a model as in (3.1a)–(3.1b) is available. One can however make local linear approximations of f based on small perturbations around specific operating points $(\vartheta_i, \tau_{s,i})$ in figure 3.1. Using approximate realization techniques [25], as has been thoroughly described in [20], the dynamic response of the sawtooth period due to these small perturbations can be translated into state space matrices A_i , B_i , C_i , and D_i , which define a linear discrete-time rational transfer function

$$H_i(z) = C_i(zI - A_i)^{-1}B_i + D_i \quad (3.5)$$

for each specific steady-state operating point $(\vartheta_i, \tau_{s,i})$, where i is the operating point identifier and z is the shift operator, defined as $w(k-1) = z^{-1}w(k)$. The frequency responses of these $H_i(z)$ give insight in the dynamic behaviour of the sawtooth and can directly be used in a controller design.

3.2.3 Approximation for slow mirror launchers

The results in [20] also showed that the presence of a relatively slow mechanical launcher, which alters the poloidal angle of the EC mirror, can change the estimated transfer functions $H_i(z)$ significantly. When the settling time of the launcher is slower than the shortest sawtooth, its dynamics dominates the frequency response of the sawtooth and limits the achievable closed-loop performance. On the other hand, a priori knowledge of the launcher dynamics in these situations can simplify the aforementioned control-relevant identification of $H_i(z)$. The sawtooth dynamics $H_i(z)$ around a certain steady-state period $\tau_{s,i}$ can then be approximated by

$$H_i(z) = d(\tau_{s,i}) \cdot T(z, \tau_{s,i}) \cdot z^{-1}, \quad (3.6)$$

i.e. the product of the DC-gain $d(\tau_{s,i})$, the discretized launcher dynamics $T(z, \tau_{s,i})$, and an additional delay z^{-1} . In this paper the function $d(\tau_{s,i})$ is the black curve in figure 3.1(b), whereas in a tokamak experiment $d(\tau_{s,i})$ can be estimated by slowly sweeping the EC mirror and calculating $\Delta\tau_s/\Delta\vartheta$. The additional delay is natural, since a change in ϑ at crash k will only be visible in the next period $\tau_s(k+1)$.

The term $T(z, \tau_{s,i})$ can be calculated beforehand using standard discretization techniques [30]. We assume that the launcher is feedback controlled and its resulting

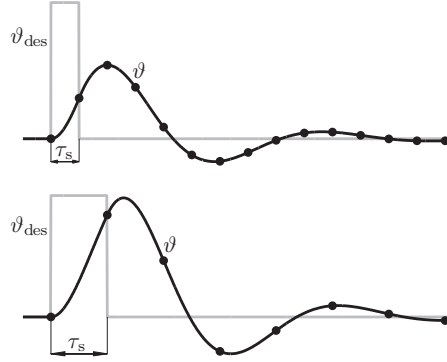


Figure 3.2: Illustration of the launcher response to a zero-order-hold input for two different sawtooth periods τ_s .

closed-loop behaviour T_{launcher} is known (either by first-principle modelling or dynamic measurements) and can be approximated by a second-order low-pass filter

$$T_{\text{launcher}}(s) = \frac{(2\pi f_c)^2}{s^2 + 2\beta(2\pi f_c)s + (2\pi f_c)^2}, \quad (3.7)$$

with cut-off frequency $f_c = 10$ Hz and damping $\beta = 0.35$; these values are based on reported bandwidths on TEXTOR [21] and TCV [22]. Although the launcher operates in continuous time, as indicated by the Laplace variable s , it is embedded in a discrete-time control loop; it receives a desired angle ϑ_{des} from the controller, which is only updated at a crash. Between crashes this ϑ_{des} remains constant, which is better known as a zero-order-hold operation (ZOH). The time between updates is variable, as the period τ_s changes. Hence, the dynamic response of the launcher in the discrete-time domain, i.e. in terms of the shift operator z , depends on the specific operating point. This is illustrated in figure 3.2, which shows the launcher response (black line) to an impulse in the discrete-time domain for two different τ_s . Due to the ZOH the launcher perceives this impulse as two subsequent steps which are a time τ_s apart (grey line). For each τ_s this results in a slightly different real-time launcher response (black line), which thereto is only considered at the crashes a time τ_s apart (black dots). Consequently, the launcher response as a function of the crash k depends on the sawtooth period, and settles in less crashes when τ_s is large.

The sequence of points in figure 3.2 defines the impulse response of the launcher $T(z, \tau_s)$ in the discrete-time domain and follows directly from the known transfer function $T_{\text{launcher}}(s)$ and period τ_s . For a closed loop as given in (3.7) the representation in z is a standard result [30], and for a specific operating point $\tau_{s,i}$ is of the form

$$T(z, \tau_{s,i}) = \frac{E(\tau_{s,i})z + F(\tau_{s,i})}{z^2 + G(\tau_{s,i})z + H(\tau_{s,i})}, \quad (3.8)$$

where E , F , G , and H are algebraic functions of $\tau_{s,i}$. For sufficiently fast launchers, i.e. for $f_c \cdot \tau_{s,\text{min}} < 0.5$ and reasonable damping β (e.g. $0.3 < \beta < 0.8$), the responses in figure 3.2 become pure impulses and hence $T(z, \tau_s) \approx z^{-1}$. Note that in such situations

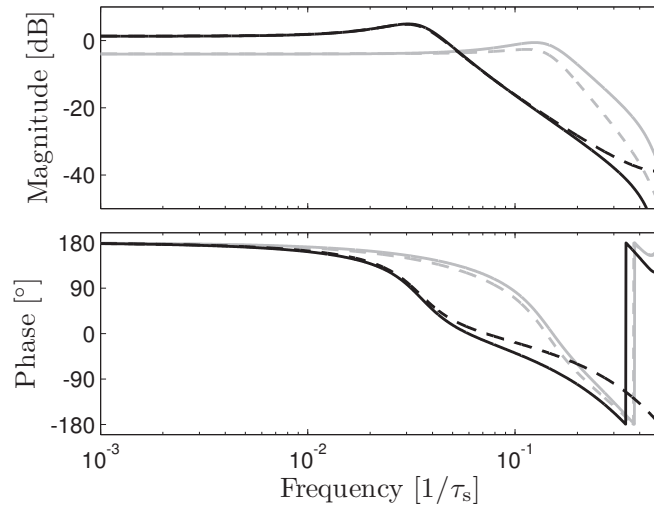


Figure 3.3: Comparison between the approximated sawtooth dynamics (solid) according to (3.6) and the measured sawtooth dynamics (dashed) reported in [20], for two different operating points: $\tau_{s,i} \approx 3.5$ ms (black) and $\tau_{s,i} \approx 14.5$ ms (grey).

the dynamics of the sawtooth itself is dominant, and the routine described in [20] is again required to identify the sawtooth dynamics.

The quality of the proposed simplification is demonstrated in figure 3.3, where the frequency responses of the complete identification routine from [20] (dashed) are compared to the ones from the approximation in (3.6) (solid) for two different sawtooth periods. Both magnitude and phase are approximated very well up to the resonance f_c . For higher frequencies there are some discrepancies. The controller designs in this paper are however relatively insensitive to these errors, as will be shown in section 3.3.1, since the obtained bandwidths will always be smaller than f_c .

3.3 Performance improving control strategies

Controller designs for the sawtooth instability are necessary to achieve and maintain any desired (small) sawtooth period, even in the presence of disturbances or uncertainties. The performance of such controllers is expressed in terms of how fast and accurate it achieves this goal. A high-performance sawtooth controller $C(z)$ should force the period from an initial value to a desired one as fast as possible, with zero steady-state error and very little overshoot. In the frequency domain these specifications translate to a large bandwidth (frequency where the open loop $C(z)H_i(z)$ crosses the 0 dB line), a large controller gain (typically infinite gain at frequency zero to prevent steady-state errors), and sufficiently large stability margins [20].

The achievable performance depends on the dynamics of the system and the chosen controller structure. In [20] a proportional-double-integral (PII)-controller was designed to control all operating points in the range $3.1 \leq \tau_s \leq 14.8$ ms via the angle of the EC mirror. Taking the limitations of the mirror launcher into account, based

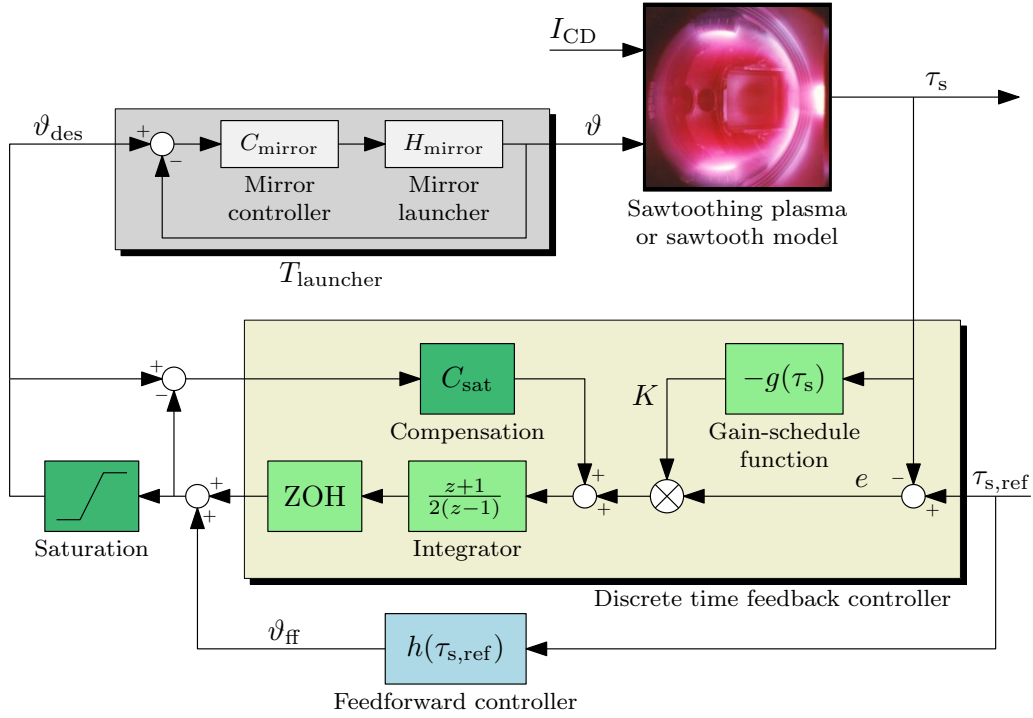


Figure 3.4: Complete control scheme, showing the feedback and feedforward controllers and the saturation compensation.

on realistic TEXTOR settings, this yielded bandwidths between $1.3 \times 10^{-4} \frac{1}{\tau_s}$ for large periods (15 ms) and $1.8 \times 10^{-2} \frac{1}{\tau_s}$ for small ones (6 ms). Since the convergence rate or settling time (in number of crashes) is roughly the inverse of this bandwidth, small periods settle on a desired value within 0.4 s, whereas large ones can take up to 20 s or more.

In this section we will discuss various strategies to improve this performance. First the application of more advanced feedback and feedforward techniques for controlling the period by means of the deposition location is discussed, using the approximations of section 3.2.3 and given the same launcher limitations as in [20]. Next, we will show the advantages of using the second input, the total driven current I_{CD} , as the control variable. Finally, the utilization of both ϑ and I_{CD} in a controller design is touched upon, after which the section concludes with some remarks on global stability.

3.3.1 Gain-scheduling and feedforward control on the mirror angle ϑ

In the context of linear control theory the DC-gain of a to-be-controlled system is ideally constant. However, choosing the ECCD deposition location, or EC mirror angle ϑ , as a control variable results in a large spread in the DC-gain of the system, as shown in figure 3.1(b). The identifications in [20] have shown that this leads to large variations in the frequency responses around the considered operating points. Designing a single linear controller which works for each operating point thus implies making concessions and leads to the aforementioned spread in bandwidths and significant settling times.

To overcome this limitation we propose to use a more advanced controller structure, which essentially consists of two parts: a feedback controller with an operating point dependent gain and a feedforward controller. The complete closed loop is depicted in figure 3.4. It shows a sawtoothing plasma, or in our case the sawtooth model as described in section 3.2.1, which has two inputs: a constant current drive I_{CD} and the EC mirror angle ϑ . The mirror is feedback controlled, where we assume that T_{launcher} is as in (3.7), in order to bring ϑ to a reference value ϑ_{des} , requested by the sawtooth controller. The ZOH block holds the discrete-time outputs of the controller to create a continuous-time signal for the launcher, as mentioned in section 3.2.3.

The feedback part of the sawtooth controller is essentially a discrete-time integrator

$$C(z) = K \cdot \frac{z + 1}{2(z - 1)}, \quad (3.9)$$

also known as I-controller, which is equivalent to the control action

$$\Delta\vartheta(k) = \Delta\vartheta(k - 1) + \frac{K}{2} (e(k) + e(k - 1)), \quad (3.10)$$

where e is the input to the controller and $\Delta\vartheta$ its output. In [20] it was shown that such an I-controller is sufficient to control the sawtooth period. This result will be further elaborated in this paper. By scheduling the gain K dependent on the current output τ_s , i.e. $K = -g(\tau_s)$, we can choose large controller gains whenever the DC-gain is small, and force fast convergence over the whole operating range. This type of controller is referred to as a *gain-scheduled controller* [24].

Here we choose the gain-schedule function $g(\tau_s)$ to be a continuous function of τ_s . To find $g(\tau_s)$ we optimize the controller gain K for each individual frequency response $H_i(z)$, as defined by the approximation for slow launcher dynamics given in (3.6), and thus obtain different K_i for different operating points $\tau_{s,i}$. We follow the same design rules as in [20], but now for each $H_i(z)$ individually:

Stability: The representation of the open-loop frequency response $C(z)H_i(z)$ in the complex plane (Nyquist plot) should have the point $(-1, 0)$ at its left.

Robustness: The modulus margin should be at most 2, i.e. in the Nyquist plot the ‘distance’ from the instability boundary $(-1, 0)$ should be at least $\frac{1}{2}$; this is required to be robust against disturbances and uncertainties and to prevent large overshoots.

Performance: Subject to the above constraints, the bandwidth should be as high as possible, i.e. the controller gain K should be maximized.

The resulting open-loop designs $C(z)H_i(z)$ are shown in figure 3.5. The Nyquist plots in figure 3.5(a) show that each individual operating point is indeed stable and exactly satisfies the robustness margin. The Bode diagrams in figure 3.5(b) show that the resulting performance is much better than when using a PII-controller with

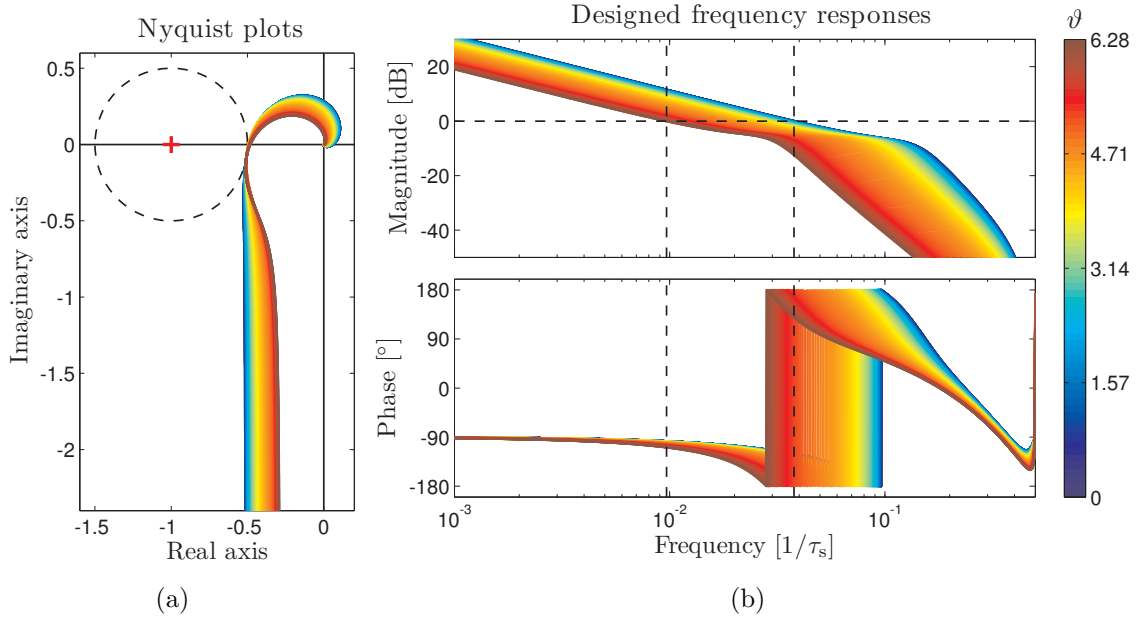


Figure 3.5: Representations of the open loops $C(z)H_i(z)$, using the approximations of $H_i(z)$ from section 3.2.3 and an optimized controller gain K_i for each operating point $(\vartheta_i, \tau_{s,i})$: (a) the Nyquist plots prove local stability and robustness for each individual $C(z)H_i(z)$; and (b) the Bode diagrams show relatively large bandwidths, even in the presence of slow launcher dynamics.

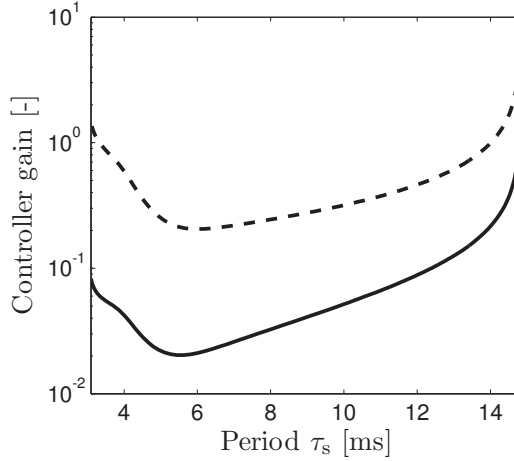


Figure 3.6: The gain-schedule function $g(\tau_{s,i})$, i.e. the controller gain K_i as a function of the steady-state sawtooth period τ_s (solid). For comparison the inverse of the sawtooth DC-gain, i.e. $-1/d(\tau_{s,i})$, is also shown (dashed).

constant parameters; the bandwidth has increased to values between $9.7 \times 10^{-3} \frac{1}{\tau_s}$ and $3.8 \times 10^{-2} \frac{1}{\tau_s}$, implying convergence rates between 26 and 103 crashes. Note that the highest bandwidths now correspond to the largest sawtooth periods. Roughly speaking, four times larger periods converge four times as fast, hence the settling time will roughly be the same for each operating point $\tau_{s,i}$ (around 0.35 s).

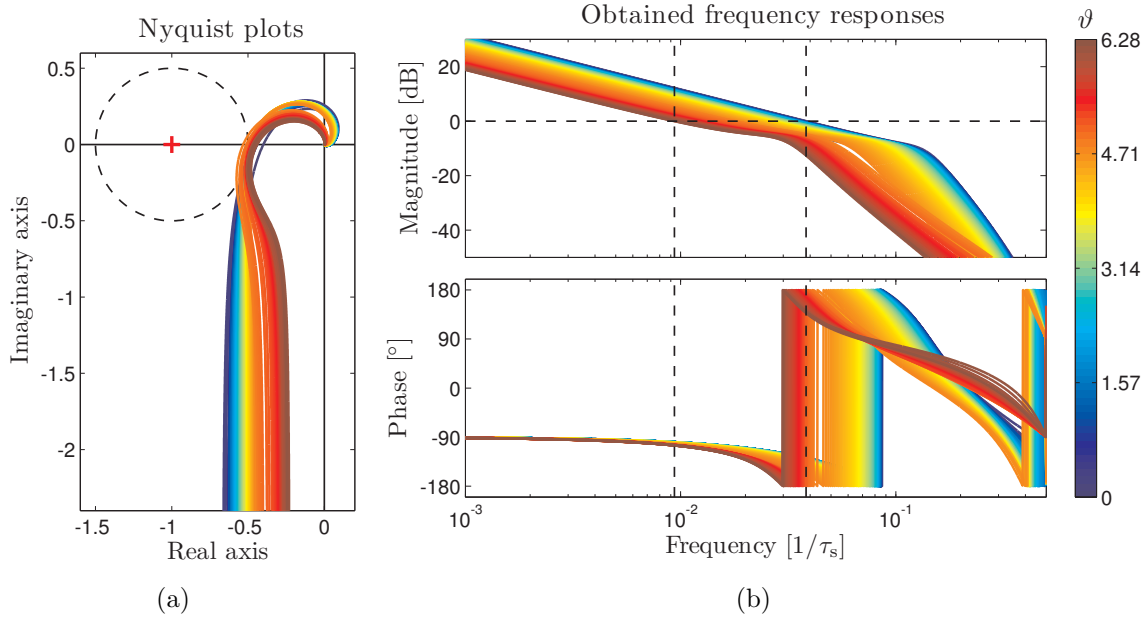


Figure 3.7: Representations of the open loops $C(z)H_i(z)$, using real measurements of $H_i(z)$ and a gain-scheduled I-controller according to figure 3.6: (a) the Nyquist plots show a violation of the modulus margin of at most 10%; and (b) the Bode diagrams show that the performance (in terms of bandwidth) is comparable to figure 3.5(b).

When the designed controller gains K_i are plotted as a function of the corresponding steady-state sawtooth period, the gain-schedule function $K = -g(\tau_s)$ can be obtained. This function $g(\tau_s)$ is depicted by the solid line in figure 3.6. The dashed line shows the inverse of the DC-gain of the system, which has a similar shape and thus proves that the controller gain K essentially compensates for the variation in this DC-gain. Additionally, there is a small trend in the ratio between the two lines due to the sawtooth dynamics, or specifically the closed-loop launcher dynamics. The limited speed of the launcher is more restrictive for small periods than for large ones, which leads to relatively smaller gains for small periods, as explained in section 3.2.3.

Notice that the controller is designed on approximations of the sawtooth dynamics, using merely the DC-gain, the discretized launcher dynamics and an additional delay. To prove the validity of these approximations for controller design, the same gain-scheduled controller has been applied to the identified models presented in [20]. The resulting open-loop frequency responses are shown in figure 3.7. The slight discrepancies with figure 3.5 are negligible: each frequency response is stable, there is only a slight violation of the robustness constraint for τ_s between 5 and 6 ms (the modulus margin is at most 2.2 instead of 2), and the obtained bandwidths are comparable (between $9.4 \times 10^{-3} \frac{1}{\tau_s}$ and $3.8 \times 10^{-2} \frac{1}{\tau_s}$). From figure 3.7 we can thus conclude that the slow launcher approximation in section 3.2.3 is accurate enough for feedback controller design, and that the designed gain-scheduled controller indeed meets our requirements.

The overall performance of the sawtooth control loop can be improved even further by including feedforward control, indicated by the blue block in figure 3.4. A feedforward controller pre-computes the required mirror angle based on the desired sawtooth period and its time-evolution, and should ideally be the inverse of the global sawtooth dynamics. Unfortunately, the actual discrete-time sawtooth dynamics in (3.4) is unknown, and the approximations $H_i(z)$ are only local, so the optimal dynamic feedforward controller is hard to find. However, the identifications in [20] and figure 3.3 have shown that up to a frequency $f_c \cdot \tau_{s,i}$ the frequency response of the sawtooth is nearly constant. This justifies the use of static feedforward control. It is known that for low frequencies the sawtooth behaves like the black line in figure 3.1(a); the feedforward controller $\vartheta_{\text{ff}} = h(\tau_{s,\text{ref}})$ should then be the inverse of this steady-state characteristic, i.e. the grey line in figure 3.1(b).

The static feedforward control described above has been used for sawtooth period control before. It is quite common to first slowly sweep the ECCD beam through the plasma to estimate the steady-state input–output map and then fix the mirror angle to a value corresponding to a desired sawtooth period. Such feedforward strategies rely heavily on knowledge of the sawtooth response; when the steady-state map is inaccurately estimated or changes over time, the predefined feedforward function $h(\tau_{s,\text{ref}})$ will yield erroneous or undesired sawtooth periods. It is for this reason that we advocate the combination of feedforward and feedback: the feedback loop compensates for potential discrepancies and forces the period to the desired value, without any steady-state error. Since feedforward control is essentially an open-loop control strategy, it does not influence the local closed-loop stability, even when $h(\tau_{s,\text{ref}})$ is highly inaccurate. An accurately tuned $h(\tau_{s,\text{ref}})$ can however easily increase the convergence speed of the closed loop, which is why feedforward is still considered here.

The feedback and feedforward controllers are specifically designed for the regime $0^\circ < \vartheta \leq 6.28^\circ$, a regime where the DC-gain has a constant sign and the steady-state map has a unique inverse $h(\tau_{s,\text{ref}})$. When the sawtooth system operates in a neighbouring regime, the closed loop could become unstable. Since the DC-gain of the sawtooth then changes sign, the I-controller could push the mirror angle in the wrong direction. To prevent this the desired mirror angle ϑ_{des} computed by the controller is saturated at 0° and 6.28° , as is also indicated in figure 3.4. Additionally, when ϑ_{des} hits these hard bounds, the integrator is pushed in the opposite direction by a compensation gain C_{sat} , to prevent integrator wind-up and to force the mirror angle back inside the operating regime. This approach is similar to standard anti-windup schemes [31], where normally $C_{\text{sat}} \geq 1$. Here we choose $C_{\text{sat}} = 10$.

The total controller, i.e. the gain-scheduled feedback, the static feedforward, and the saturation compensation, has been implemented in Simulink and combined with the original sawtooth model described in section 3.2.1 and the slow launcher described in section 3.2.3. Figure 3.8 shows a time-domain simulation of the closed loop in red. The top plot shows that the reference period (black) is being tracked very well throughout the whole operating regime. The bottom plot shows that the error is at

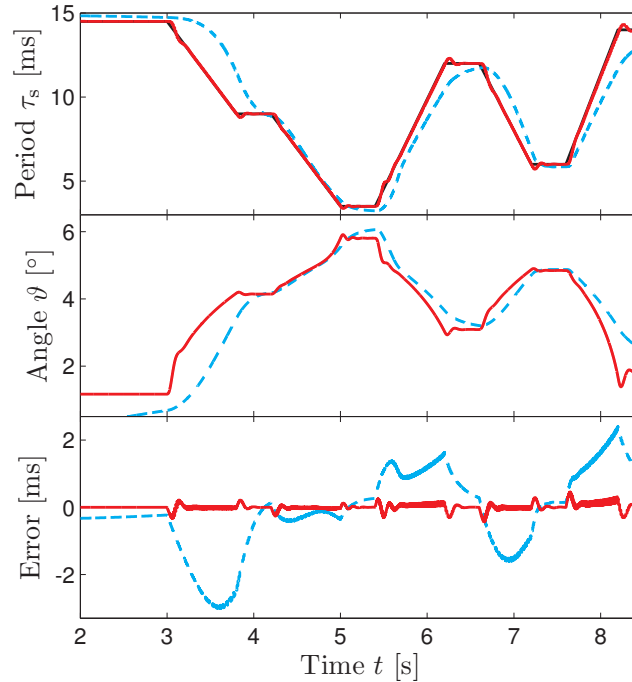


Figure 3.8: Tracking simulations of the sawtooth model actuated by a slow launcher; in combination with the constant PII-controller (dashed cyan) of [20], and with the high-performance controller (red) discussed in section 3.3.1. Note that the red line in the top plot nearly coincides with the requested period (depicted in black).

most 0.45 ms at the transitions of the reference (due to overshoot), and is nearly zero elsewhere. For comparison, figure 3.8 also shows the closed-loop response with the constant PII-controller of [20]. The new controller clearly yields a major performance improvement: it yields much smaller errors and is equally fast for both long and short sawtooth periods.

Figure 3.9 illustrates the use of the aforementioned saturation compensation. It shows the response of the sawtooth system when the desired period changes stepwise from 14.5 to 5 ms. Since this step introduces a large error, the feedback loop requests a very large mirror angle (grey line) which saturates at 6.28° . Still, the actual mirror angle ϑ overshoots to nearly 7.8° . Consequently, the sawtooth system slides into the neighbouring regime of figure 3.1(a) with steep positive slope, yielding a rapid increase of the sawtooth period after its initial decrease. However, after 0.1 s the saturation compensation manages to pull both ϑ_{des} and ϑ back into the stable operating regime, after which the sawtooth period eventually settles at the required 5 ms, with $\vartheta = 5.1^\circ$.

We have shown that the sawtooth period can be controlled with a high performance, i.e. with high accuracy and fast settling times for each desired period $\tau_{s,\text{ref}}$, even in the presence of a relatively slow EC mirror launcher. The key to this success is the inclusion of explicit knowledge of the sawtooth system into the controller design:

- the gain-scheduled feedback relies on precise knowledge of the launcher dynamics

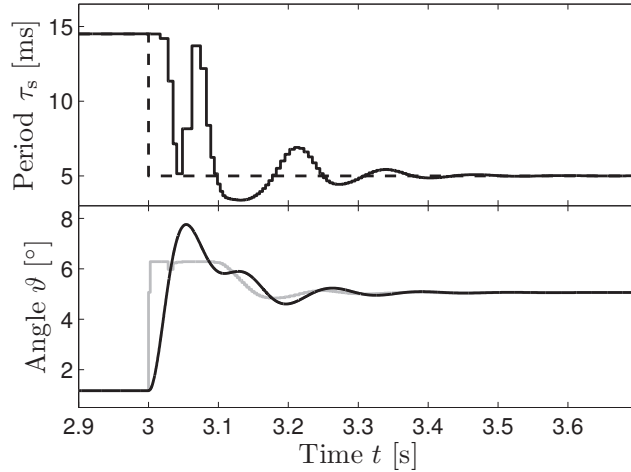


Figure 3.9: Closed loop step response using the high-performance controller. The top plot shows the reference (dashed) and the obtained sawtooth period (solid), the bottom plot shows both the requested angle ϑ_{des} (grey) and the actual mirror angle ϑ (black).

and the DC-gain $d(\tau_{s,i})$ of the sawtooth system;

- the static feedforward relies on knowledge of the steady-state input–output map;
- the saturation compensation relies on knowledge of the bounds of the stable operating regime.

Such high-performance control strategies are feasible when the plasma is reproducible, i.e. when uncertainties in the steady-state map and the DC-gain are relatively small, which is expected to be the case under reactor-like conditions. In any other situation the estimations for $h(\tau_{s,\text{ref}})$ and $d(\tau_{s,i})$ might be erroneous, which could lead to a deterioration of the closed-loop performance or even to instability. In other words, such strategies are less robust. This illustrates the typical trade-off in control engineering between performance and robustness.

3.3.2 Feedback control on the driven current I_{CD}

In the previous section advanced feedback and feedforward controllers were required to compensate for the relatively slow actuator for ϑ (the EC mirror launcher) and achieve an improved closed-loop performance. Alternatively, one could choose a different control variable with different actuator dynamics. In our case this is the total driven current I_{CD} (or equivalently, the gyrotron power), i.e. the second input to the sawtooth model. This section will explore the possibilities of using this I_{CD} as a control variable.

The effect of I_{CD} on the steady-state input–output map is shown in figure 3.10: as I_{CD} increases, the steady-state map in figure 3.1(a) is amplified with respect to the ohmic sawtooth period. This dependency is not exactly linear, since the location of the $q = 1$ surface, and hence the values of ϑ where the minimal and maximal periods occur, change with the size of I_{CD} . However, in our region of interest (small ϑ corresponding to small periods τ_s), the decrease in τ_s with increasing I_{CD} and fixed ϑ seems relatively

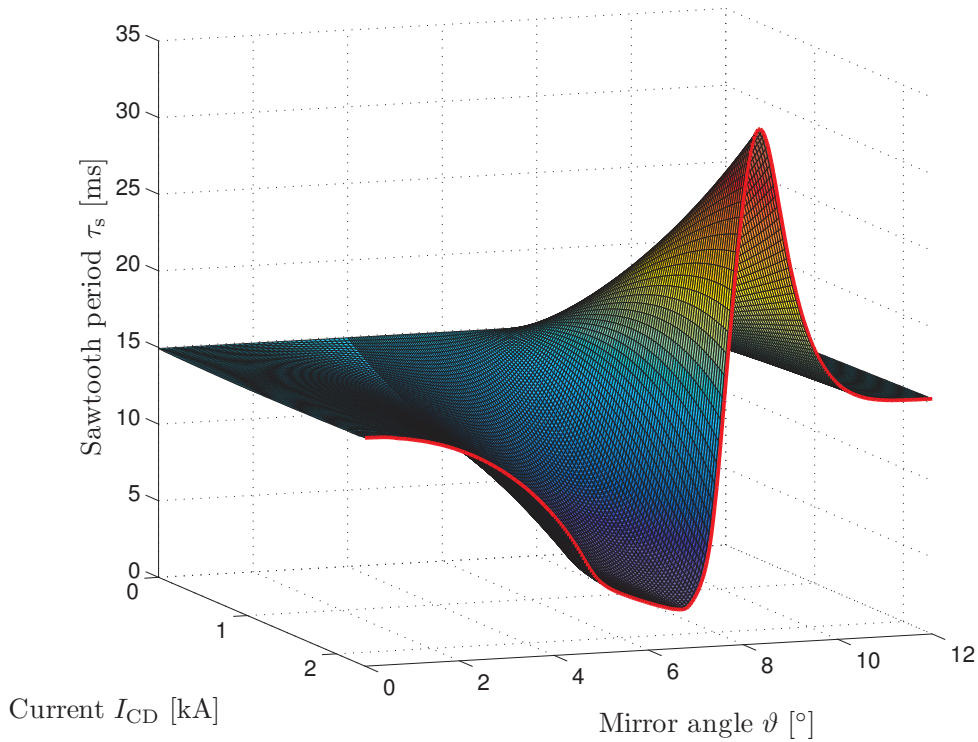


Figure 3.10: Steady-state input–output map of the sawtooth period, as a function of both mirror angle ϑ and total driven current I_{CD} . Each point on the map represents a simulation where ϑ and I_{CD} are fixed, after which the sawtooth model converges to a constant sawtooth period (deposition width is constant at 16 mm).

constant. As a consequence, the spread in the DC-gain in this region is fairly small, much smaller than in the angle-actuated case. From a control perspective this is an advantage, since it suggests that gain-scheduling might not be necessary to control the period.

More importantly, the control variable I_{CD} is not limited by slow actuator dynamics. Current state-of-the-art gyrotrons can change their power level extremely fast, much faster than the shortest sawtooth. Hence, gyrotron dynamics do not influence the discrete-time sawtooth dynamics and can thus be ignored.

The feedback controller design should be based on the transfer functions from input I_{CD} to output τ_s of the sawtooth system. To this end we fix the mirror angle at some arbitrary value inside our region of interest (here $\vartheta = 4.5^\circ$), and apply the identification routine described in [20]. For each operating point $I_{CD,i}$ step simulations are performed: the driven current is set to a value $I_{CD,i} - \Delta I_{CD}$ or $I_{CD,i} + \Delta I_{CD}$, and is changed stepwise (synchronized at the next crash) to $I_{CD,i}$ when the sawtooth model reaches a steady state. The resulting change in period $\Delta\tau_s(k)$, where k is the crash number and $k = 0$ at the time of the step, is monitored and scaled by a factor $1/\Delta I_{CD}$ to obtain a normalized step response sequence $\Delta\bar{\tau}_s(k)$ for $k = 0, 1, 2, \dots$. Next, this sequence is put in a Hankel matrix H_E , an appropriate approximation order is selected based on the singular value decomposition of this H_E (here: fifth order), and the state space matrices A_i, B_i, C_i

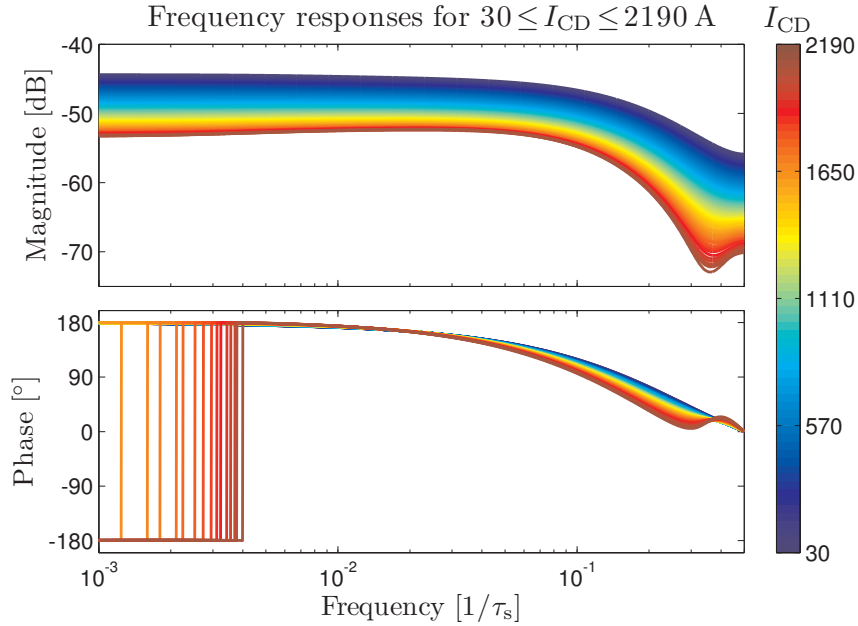


Figure 3.11: Identified frequency responses of the sawtooth dynamics from input I_{CD} to output τ_s , with $\vartheta = 4.5^\circ$.

and D_i are computed. The transfer functions $H_i(z)$ are then defined by (3.5). Here a perturbation $\Delta I_{CD} = 30$ A is chosen, which is small enough to satisfy the underlying linearity assumption. More details on this identification routine can be found in [20, 25].

The frequency responses of the obtained transfer functions $H_i(z)$, for a large collection of operating points $30 \leq I_{CD,i} \leq 2190$ A, are shown in figure 3.11. Similar to the results reported in [20], where ϑ was used as input, these transfer functions behave like a low-pass filter, suppressing high-frequency oscillations in I_{CD} . More importantly, as predicted by figure 3.10, the spread in the low-frequency DC-gain is much smaller: in figure 3.11 the variation in DC-gain is less than 10 dB, whereas for ϑ inputs it is more than 40 dB. A single I-controller as in (3.9) with a constant negative gain is therefore expected to yield a satisfactory performance throughout the whole operating range.

The tuning of the constant controller gain K is such that the closed-loop performance is optimized (i.e. $|K|$ is maximized), while maintaining the stability and robustness constraints for each open-loop frequency response $C(z)H_i(z)$. As such we obtained $K = -100$. The resulting open-loop frequency responses are shown in figure 3.12; the Nyquist plots proof local stability and robustness, whereas the Bode diagrams show that the bandwidth is between $3.7 \times 10^{-2} \frac{1}{\tau_s}$ and $7.8 \times 10^{-2} \frac{1}{\tau_s}$. This corresponds to convergence rates of approximately 13 crashes for long sawteeth (around 15 ms) to about 27 crashes for short ones (around 7 ms). Roughly speaking, in real-time each desired period $\tau_{s,\text{ref}}$ will therefore be tracked equally fast, i.e. in less than 0.2 s.

To demonstrate this statement figure 3.13 shows a closed-loop simulation using the designed I-controller in red. As the desired period $\tau_{s,\text{ref}}$ (black) decreases from

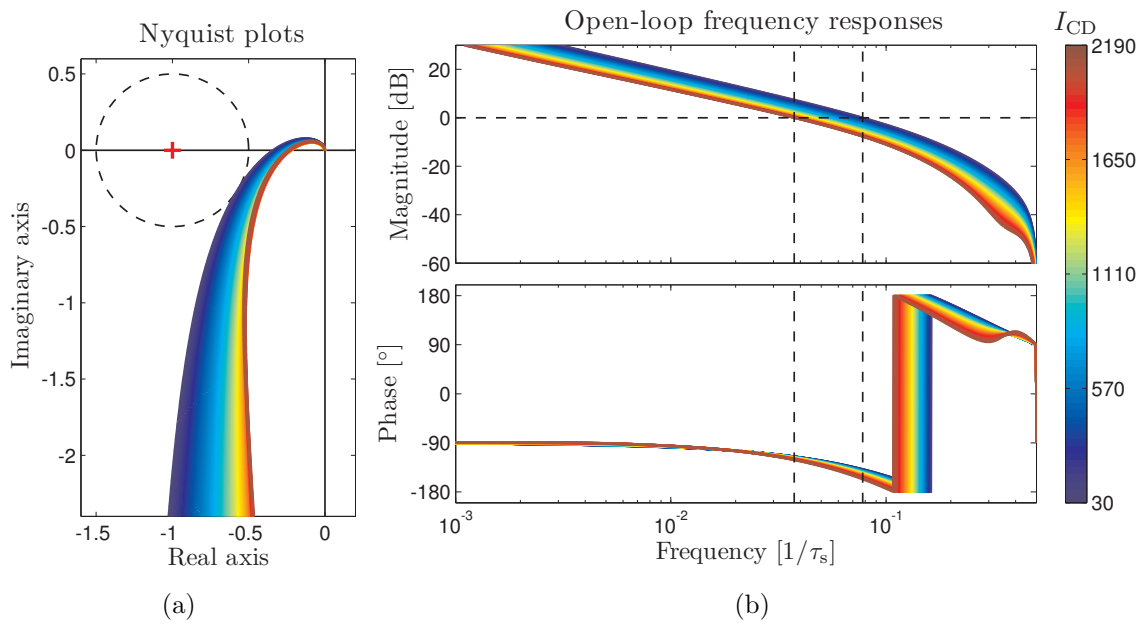


Figure 3.12: Representations of the open loop $C(z)H_i(z)$, with $H_i(z)$ as in figure 3.11 and using an I-controller $C(z)$ with constant gain $K = -100$.

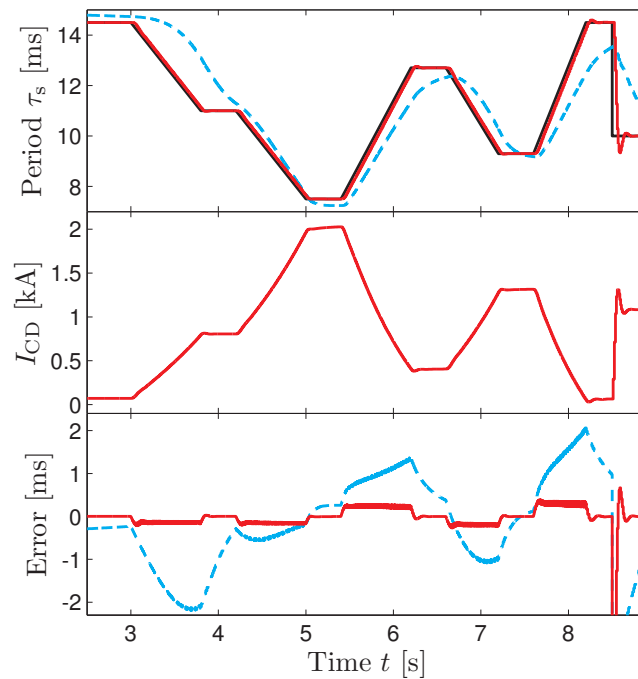


Figure 3.13: Closed-loop tracking simulations with the sawtooth model: using a PII-controller on the mirror angle ϑ , subject to slow launcher dynamics (dashed cyan); and using an I-controller on the driven current I_{CD} (red).

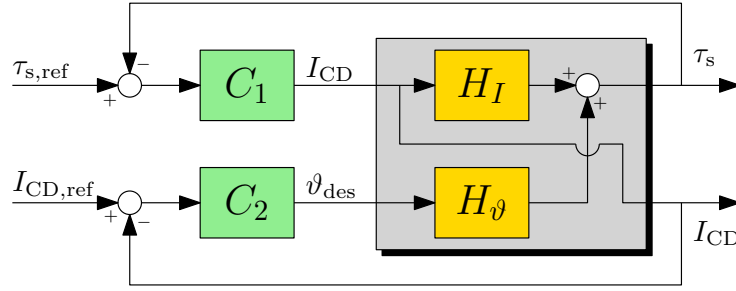


Figure 3.14: Multiple-input-multiple-output (MIMO) control scheme to control both the sawtooth period τ_s and the driven current I_{CD} .

ohmic to 7.5 ms, the driven current I_{CD} increases to about 2 kA. Since the response of the sawtooth system to this change in I_{CD} is very fast, the tracking error remains small: at most 0.3 ms in the first part, and 0.66 ms overshoot during the step in the reference. This is again a major performance improvement compared to the constant PII-controller on the mirror angle ϑ as presented in [20], depicted in cyan in figure 3.13.

Choosing I_{CD} as control variable has advantages in terms of performance and robustness. Due to the fast gyrotron dynamics and the small variation in DC-gain, we were able to achieve slightly better performance than in section 3.3.1, while using just a simple I-controller with a constant gain. In fact, a gain-scheduled integrator would have yielded only a marginal additional performance improvement. Hence, a constant controller is more desirable in this case, as it requires less explicit knowledge of the system and is therefore more robust.

Note that the amount of driven current I_{CD} needed to achieve a certain period τ_s strongly depends on the fixed mirror angle ϑ . This motivates the use of both inputs ϑ and I_{CD} in a single controller design, which will be introduced in the next section.

3.3.3 MIMO feedback control on both ϑ and I_{CD}

So far it has been shown that the period τ_s can be controlled by either ϑ or I_{CD} , where control via I_{CD} yields a better performance with a simpler controller. Under reactor-like conditions it could be desirable to control, or perhaps optimize, this driven current I_{CD} (or gyrotron power) as well. In that case, the sawtooth control problem involves multiple objectives utilizing multiple actuators, which is an example of a multiple-input-multiple-output (MIMO) problem in control engineering.

The design of the MIMO controller will be introduced by considering a specific disturbance rejection problem: the sawtooth should be kept at a specific desired operating point, in this case $\tau_{s,ref} = 7.6$ ms and $I_{CD,ref} = 2$ kA, despite the presence of disturbances. To this end we define our system as depicted by the grey box in figure 3.14, with two inputs (I_{CD} and the desired mirror angle ϑ_{des}) and two outputs (τ_s and I_{CD}). The block H_{ϑ} denotes the transfer function from ϑ_{des} to τ_s as defined by (3.6) with $\tau_{s,i} = 7.6$ ms (hence, including the feedback controlled mirror launcher as depicted in figure 3.4), and H_I is the transfer function from I_{CD} to τ_s represented

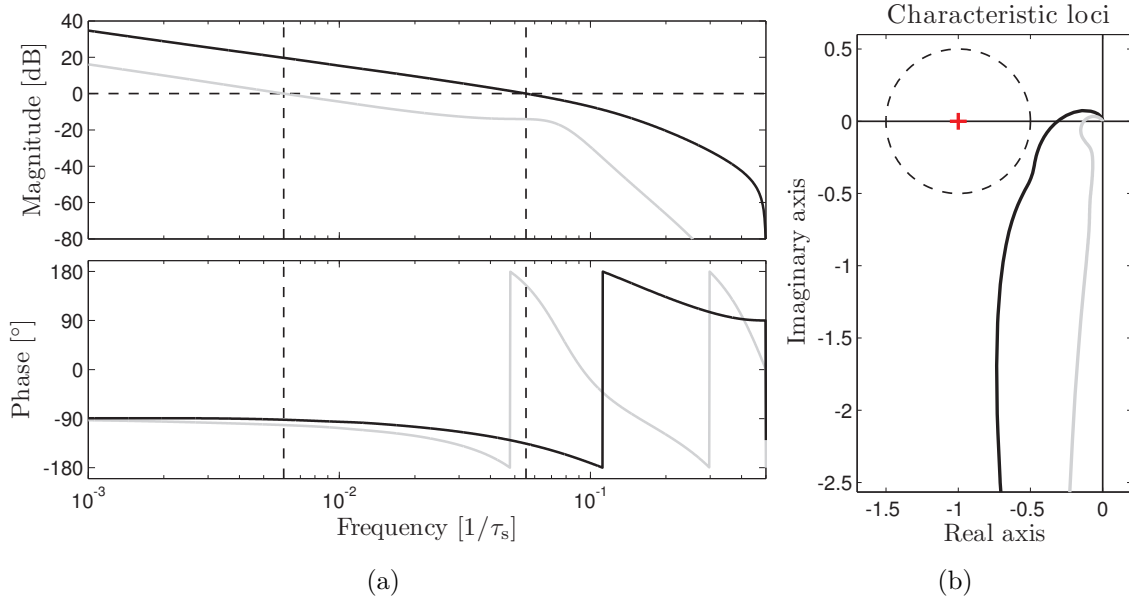


Figure 3.15: (a) Open loop frequency responses of the sequentially closed loops: the first loop C_1H_1 (black) and second loop C_2H_2 (grey). (b) The two characteristic loci of the MIMO open loop defined in (3.13).

by the line in figure 3.11 corresponding to $I_{CD} = 2$ kA. Moreover, we introduce two separate feedback loops: a fast loop to control τ_s via I_{CD} , and a slower loop to control I_{CD} via ϑ_{des} . The controller for each loop is designed with a technique called *sequential loop closing* [26,27]. In the first step we assume that $C_2 = 0$ and design a controller C_1 for the first transfer function $H_1 = H_I$, i.e. for the fastest time-scale of the sawtooth system. Like in section 3.3.2 an I-controller is sufficient for this purpose, whose gain is maximized for performance while satisfying the stability and robustness constraints. In the first step we then obtain

$$H_1(z) = H_I(z) \quad \longrightarrow \quad C_1(z) = -152 \cdot \frac{z+1}{2(z-1)}, \quad (3.11)$$

resulting in the open-loop frequency response $C_1(z)H_1(z)$ depicted in black in figure 3.15(a). Once this first feedback loop is closed, the second controller C_2 observes a system which is a combination of H_I , H_ϑ , and C_1 . In the second step this system H_2 is computed explicitly, after which C_2 is designed to control it. The performance requirement on this second loop is much less critical, since I_{CD} does not necessarily need to converge very fast. Hence, this loop is not pushed against its performance limits, but C_2 is designed with a large robustness margin and an open-loop bandwidth of $6 \times 10^{-3} \frac{1}{\tau_s}$ (approximately an order lower than the first loop). The second step then yields

$$H_2(z) = -\frac{C_1H_\vartheta}{1+C_1H_I} \quad \longrightarrow \quad C_2(z) = -2.1 \times 10^{-5} \cdot \frac{z+1}{2(z-1)}, \quad (3.12)$$

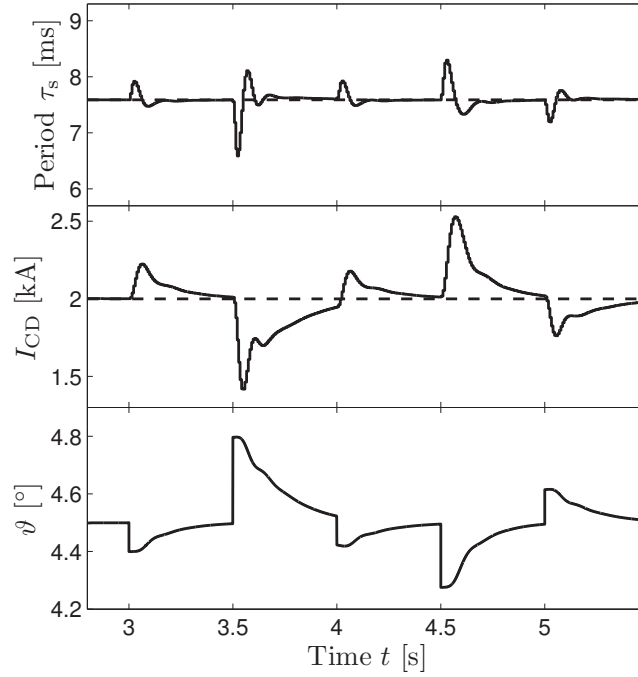


Figure 3.16: Closed-loop MIMO simulation with stepwise disturbances on ϑ , showing successful stabilization on $\tau_s = 7.6$ ms and $I_{CD} = 2$ kA.

of which the open-loop frequency response $C_2(z)H_2(z)$ is shown in grey in figure 3.15(a). Although the closing of the second loop can again alter the first feedback loop, it can be shown that the overall MIMO closed loop will remain stable [26, 27]. Moreover, since the second loop is designed with a large margin, it is very likely that the total MIMO system still satisfies the robustness constraint. To verify this we calculate the 2×2 MIMO open loop transfer function

$$H_{\text{MIMO}} \cdot C_{\text{MIMO}} = \begin{bmatrix} H_I & H_\vartheta \\ 1 & 0 \end{bmatrix} \cdot \begin{bmatrix} C_1 & 0 \\ 0 & C_2 \end{bmatrix} = \begin{bmatrix} H_I C_1 & H_\vartheta C_2 \\ C_1 & 0 \end{bmatrix}, \quad (3.13)$$

and compute its eigenvalues as a function of frequency. These eigenvalues are known as the *characteristic loci* [32], and when plotted in the complex plane they represent the MIMO equivalent for the Nyquist plot. The loci in figure 3.15(b) indeed confirm that our MIMO closed loop is stable and satisfies the robustness constraint.

Figure 3.16 shows a specific simulation result where the controllers C_1 and C_2 have been combined with the sawtooth model described in section 3.2.1. In this simulation the plasma starts at the desired operating point $\tau_s = 7.6$ ms and $I_{CD} = 2$ kA (with corresponding mirror angle $\vartheta = 4.5^\circ$), after which arbitrary stepwise disturbances on ϑ are applied at 3, 3.5, 4, 4.5 and 5 seconds. These disturbances can be interpreted as sudden shifts of the plasma position. The top plot shows that the sawtooth period immediately starts drifting away, but the driven current I_{CD} quickly responds to this and pushes the period back to the desired 7.6 ms on a short time-scale. On a much longer time-scale the mirror angle ϑ is then adjusted to bring I_{CD} back to its desired value. This is indeed in agreement with the MIMO controller design; C_1 has been

designed to control τ_s with a high performance utilizing the fast input I_{CD} , while C_2 closes a slower feedback loop to control I_{CD} with the mirror angle ϑ .

The extension of the above MIMO controller design to multiple operating points is relatively straightforward, but could be rather cumbersome. For each operating point both H_I and H_ϑ need to be identified. Then C_1 has to be designed to stabilize all possible H_I and C_2 has to stabilize all possible systems H_2 , which calls for a very robust (i.e. conservative) controller. In future research the use of adaptive MIMO controllers will be explored, e.g. to further increase the performance or to derive efficient controllers which control the period using a minimum of gyrotron power.

3.3.4 Proving global stability

All of the above controller designs make use of the local sawtooth dynamics observed in a small vicinity around a considered operating point. As such these controller designs can ensure *local* stability: the closed loop is guaranteed to be stable if the desired sawtooth period is constant or changing very slowly, and is close to the initial period. The presented simulations suggest that all closed loops are also *globally* stable, since the sawtooth period τ_s always tracks $\tau_{s,\text{ref}}$, regardless of the shape of $\tau_{s,\text{ref}}$. However, an explicit mathematical proof of this global stability still has to be found.

In control engineering stability is often proved by the construction of a so-called *Lyapunov function*, which is a positive definite energy function (it may or may not have a physical interpretation) of the internal states x of the system [33]. If one can find such a function $V(x) > 0$ and show that $\frac{dV}{dt}(x) = \frac{dV}{dx} \frac{dx}{dt} < 0$, where $\frac{dx}{dt}$ represents the dynamics of the system, every single solution $x(t)$ of the system is guaranteed to converge in the direction of decreasing energy (towards $V = 0$ at $x = 0$) and hence the system is inherently stable. In practice it is quite common to use quadratic Lyapunov functions $V(x) = x^T P x$, for which efficient numerical search algorithms exist.

As for the sawtooth, an arbitrary solution or response may evolve according to any of the identified local dynamics. Hence, one needs to find a single Lyapunov function $V(x) > 0$ which yields $\frac{dV}{dt}(x) < 0$ for all possible local dynamics, as this proves that the ‘energy’ of the response will decrease regardless of which dynamics the response actually follows. Without showing the details here, for most of the previously designed controllers and resulting closed loops we can indeed find a Lyapunov function, in this case a quadratic function $V(x) = x^T P x$, which satisfies these constraints. Although this is certainly a valuable result, it still does not prove global stability.

The key issue is that the sum of all local dynamics used in this analysis does not comprise the full dynamic response of the sawtooth instability, as each local dynamics is only valid in the vicinity of a steady-state operating point. The full dynamics is only described by the function f in (3.4), which should therefore be explicitly taken into account in the construction of $V(x)$. Unfortunately this f is unknown, hence a suitable Lyapunov function cannot be found. Future stability research should therefore focus on more advanced identification routines to approximate the full dynamics f .

3.4 Conclusions and discussion

In previous publications on feedback control of the sawtooth period [16, 19, 20, 22] the deposition location of the ECCD beam is used as the control variable. This location is determined by the reflection angle of the EC mirror, which can be altered in real-time by a mechanical launcher. The speed of this launcher is however limited; on most present-day tokamaks it is slower than the smallest possible sawtooth period. In [20] it was shown that this restricts the closed-loop performance achievable by standard linear controllers: convergence rates differ with each operating point and can typically be very slow, up to thousands of crashes.

In this paper we have derived alternative strategies to increase this performance, using a numerical Kadomtsev–Porcelli diffusion model as a case study. First, under the assumption of slow launcher dynamics, we have derived relatively simple approximations of the sawtooth dynamics in a specific sawtooth operating regime corresponding to smaller than ohmic periods. These approximations have been used in the design of a so-called gain-scheduled I-controller for the EC mirror angle. Moreover, a static feedforward controller has been derived based on the steady-state input–output map of the sawtooth. Additionally, a saturation compensation has been implemented to force the sawtooth system to remain inside the stable operating regime. Time simulations have shown that the closed loop performance is indeed much better than with a linear controller, as the errors are smaller and convergence rates are much faster.

Another approach is to use the total driven current (or gyrotron power) as the control variable. Current state-of-the-art gyrotrons are extremely fast, so their dynamics can be neglected. The sawtooth dynamics using this input has been identified, upon which a linear I-controller has been designed. The open-loop frequency responses show an increased performance compared to the mirror angle actuated case, which has been verified by time-domain simulations.

The amount of power needed to obtain a certain period in this alternative approach strongly depends on the given mirror angle, which motivates the assessment of MIMO control strategies. In this paper this approach is introduced by a specific MIMO controller design called sequential loop closing, where the driven current is used to control the sawtooth period with a high performance, and the mirror angle controls this driven current on a longer time-scale. In principle, such a MIMO approach can combine high performance with energy efficiency. A fast feedback loop on the driven current can force and maintain a desired period, after which a slow feedback loop on the mirror angle can decrease this driven current by pushing the sawtooth towards the minimum of the steady-state input–output map. When I_{CD} is such that this minimum coincides with the setpoint $\tau_{s,ref}$, the required gyrotron power is minimal. Note that the corresponding optimal angle weakly depends on $\tau_{s,ref}$, due to the shift of the $q = 1$ surface related to the associated change in I_{CD} . This gyrotron power optimization will require an adaptive control strategy like in [34]; the development of such adaptive MIMO controllers for the sawtooth period is part of current research.

Fusion reactors need to operate in predictable and reproducible plasma regimes, where the plasma behaviour is very well known and is controllable using the available actuators. Such precise knowledge of the plasma input–output behaviour enables the use of high-performance control strategies, which are essential to be able to maximize the fusion performance of the reactor. It is likely that such strategies will not only be necessary to control the sawtooth period, but also to control NTMs, edge localized modes (ELMs), resistive wall modes (RWMs), etc. It is therefore important to remark that the control strategies discussed in this paper, i.e. the gain-scheduling, feedforward, and MIMO techniques, together with the identification technique discussed in [20], can also be extrapolated to other control problems, both in simulations and experiments.

Finally, it should be noted that experimental tokamak devices, aimed at scientific plasma research, do not necessarily require high-performance controllers. Instead, such devices are designed to operate in various different plasma regimes and scenarios, where the uncertainties in the plasma are quite large. This calls for control strategies with high robustness. Development of such strategies is part of current research [34].

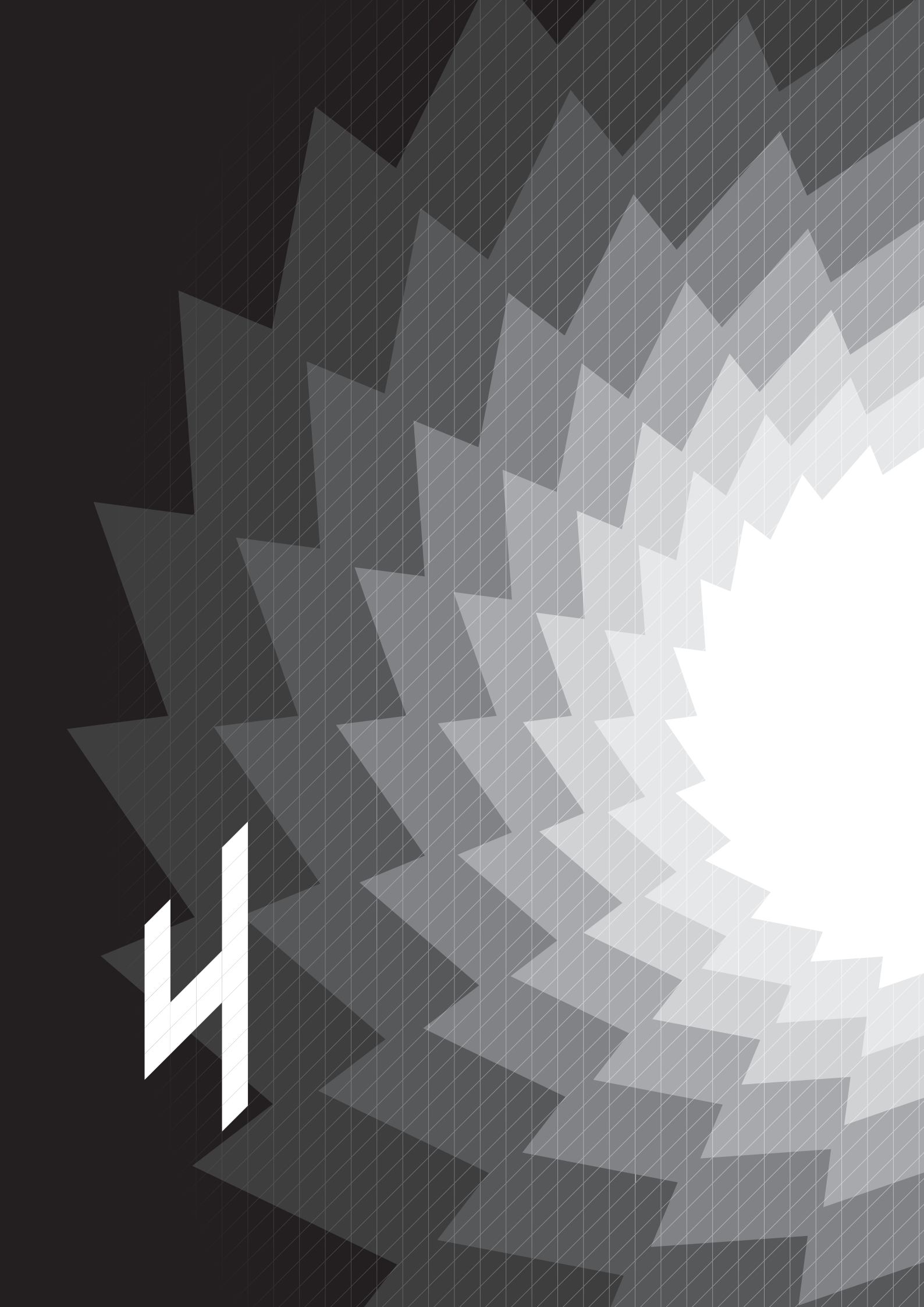
Acknowledgments

The work in this paper has been performed in the framework of the NWO-RFBR Centre of Excellence (grant 047.018.002) on Fusion Physics and Technology. This work, supported by NWO, ITER-NL and the European Communities under the contract of the Association EURATOM/FOM, was carried out within the framework of the European Fusion Programme. The views and opinions expressed herein do not necessarily reflect those of the European Commission.

References

- [1] von Goeler S. *et al.* 1974 *Phys. Rev. Lett.* **33**(20) 1201
- [2] Hastie R.J. 1997 *Astrophys. Space Sci.* **256**(1) 177
- [3] Sauter O. *et al.* 2002 *Phys. Rev. Lett.* **88**(10) 105001
- [4] Gude A. *et al.* 2002 *Nucl. Fusion* **42**(7) 833
- [5] Nave M.F.F. *et al.* 2003 *Nucl. Fusion* **43**(10) 1204
- [6] Chapman I.T. *et al.* 2010 *Nucl. Fusion* **50**(10) 102001
- [7] Chapman I.T. *et al.* 2008 *Plasma Phys. Control. Fusion* **50**(4) 045006
- [8] Chapman I.T. *et al.* 2008 *Nucl. Fusion* **48**(3) 035004
- [9] Eriksson L.G. *et al.* 2006 *Nucl. Fusion* **46**(10) S951
- [10] Graves J.P. *et al.* 2009 *Phys. Rev. Lett.* **102**(6) 065005
- [11] Lennholm M. *et al.* 2011 *Nucl. Fusion* **51**(7) 073032
- [12] Mück A. *et al.* 2005 *Plasma Phys. Control. Fusion* **47**(10) 1633
- [13] Angioni C. *et al.* 2003 *Nucl. Fusion* **43**(6) 455
- [14] Merkulov A. *et al.* 2004 *Proc. of Joint Varenna-Lausanne Int. Workshop on Theory of Fusion Plasmas* (Varenna, Italy) 279
- [15] Porcelli F. *et al.* 1996 *Plasma Phys. Control. Fusion* **38**(12) 2163
- [16] Lennholm M. *et al.* 2009 *Fusion Sci. Technol.* **55**(1) 45

-
- [17] Lennholm M. *et al.* 2009 *Phys. Rev. Lett.* **102**(11) 115004
 - [18] Paley J.I. *et al.* 2009 *Plasma Phys. Control. Fusion* **51**(5) 055010
 - [19] Paley J.I. *et al.* 2009 *Plasma Phys. Control. Fusion* **51**(12) 124041
 - [20] Witvoet G. *et al.* 2011 *Nucl. Fusion* **51**(7) 073024
 - [21] Hennen B.A. *et al.* 2010 *Plasma Phys. Control. Fusion* **52**(10) 104006
 - [22] Paley J.I. *et al.* 2009 *Nucl. Fusion* **49**(8) 085017
 - [23] Kadomtsev B.B. 1975 *Sov. J. Plasma Phys.* **1**(5) 389
 - [24] Rugh W.J. and Shamma J.S. 2000 *Automatica* **36**(10) 1401
 - [25] de Schutter B. 2000 *J. Comput. Appl. Math.* **121**(1-2) 331
 - [26] Mayne D.Q. 1973 *Automatica* **9**(2) 201
 - [27] Hovd M. and Skogestad S. 1994 *Automatica* **30**(10) 1601
 - [28] Witvoet G. *et al.* 2011 *Nucl. Fusion* **51**(10) 103043
 - [29] Westerhof E. *et al.* 2002 *Nucl. Fusion* **42**(11) 1324
 - [30] Franklin G.F. *et al.* 1998 *Digital control of dynamic systems* 3rd edn. (Menlo Park, CA: Addison-Wesley)
 - [31] Åström K.J. and Rundqwist L. 1989 *Proc. 1989 Amer. Contr. Conf.* (Pittsburgh, PA, USA) 1693–1698
 - [32] Skogestad S. and Postlethwaite I. 2005 *Multivariable Feedback Control: analysis and design* (Chichester, UK: John Wiley)
 - [33] Khalil H.K. 2002 *Nonlinear Systems* 3rd edn. (Upper Saddle River, NJ: Prentice Hall)
 - [34] Bolder J.J. *et al.* 2011 *Submitted to Nucl. Fusion*



Robust sawtooth period control based on adaptive online optimization

J.J. Bolder^a, G. Witvoet^{a,b,c}, M.R. de Baar^{a,b},
N. van de Wouw^a, M.A.M. Haring^a, E. Westerhof^b,
N.J. Doelman^c and M. Steinbuch^a

^a Eindhoven University of Technology

^b FOM-Institute for Plasma Physics Rijnhuizen

^c TNO Technical Sciences



Abstract

The systematic design of a robust adaptive control strategy for the sawtooth period using electron cyclotron current drive (ECCD) is presented. Recent developments in extremum seeking control (ESC) are employed to derive an optimized controller structure and offer practical tuning guidelines for its parameters. In this technique a cost function in terms of the desired sawtooth period is optimized online by changing the ECCD deposition location based on online estimations of the gradient of the cost function. The controller design does not require a detailed model of the sawtooth instability. Therefore the proposed ESC is widely applicable to any sawtoothing plasma or plasma simulation and is inherently robust against uncertainties or plasma variations. Moreover, it can handle a broad class of disturbances. This is demonstrated by time-domain simulations, which show successful tracking of time-varying sawtooth period references throughout the whole operating space, even in the presence of variations in plasma parameters, disturbances and slow mirror launcher dynamics. Due to its simplicity and robustness the proposed ESC is a valuable sawtooth control candidate for any experimental tokamak plasma, and may even be applicable to other fusion-related control problems.

4.1 Introduction

The sawtooth instability is a periodic redistribution of the plasma core [1–3]. On the one hand, its mixing effect provides a mechanism to regulate the exhaust of helium ash and α -particles [4], and the influx of deuterium and tritium in a fusion reactor. On the other hand, the sawtooth instability can trigger neoclassical tearing modes (NTMs), which in turn reduce the operational performance and could lead to disruptions [5, 6]. Sawtooth control, in particular control of the sawtooth period [7, 8], is necessary to avoid NTM triggering while concurrently refreshing the plasma core.

The onset of a sawtooth crash is often associated with the magnetic shear at the $q = 1$ surface [9]. The sawtooth period can therefore be affected by changing the shear around $q = 1$ through the injection of electron cyclotron (EC) waves, see [10–13] and references therein. By changing the deposition location of the resulting EC current drive (ECCD) relative to the $q = 1$ surface the shear can either be increased or decreased, leading to shorter or longer sawtooth periods, respectively. The ECCD deposition location is typically determined by the angle of an EC mirror. Sawteeth are usually observed using soft x-ray or electron cyclotron emission (ECE) measurements. The sawtooth period can be extracted from these measurements in several ways, e.g. using multiresolution wavelet analysis as discussed in [14].

The ECCD actuator has successfully been employed in a closed loop to control the sawtooth period on both TCV [15] and Tore Supra [16, 17] using classical linear controllers. A systematic design for such controllers has been presented in [18] based on structured analysis of the dynamics of the sawtooth period. This approach enabled *a priori* assessment of closed-loop stability, performance and robustness, which has been verified by simulations. Recently a similar methodology has been used to suggest performance improvement strategies [19], yielding faster convergence of the sawtooth period with high accuracy.

The above controller design strategies assume that the dynamics of the sawtooth period, i.e. its frequency response functions [18], and its statics, i.e. its steady-state input–output map, can be measured and remain approximately constant over time. This asks for reproducible and predictable plasmas. Under reactor-like conditions these requirements can easily be met, but under experimental circumstances plasma parameters are often uncertain or unknown. Variations in the profiles of, e.g. density, electron temperature, conductivity and impurity concentration, can cause the $q = 1$ surface to shift, and effects like scattering and EC beam deflections can alter the ECCD deposition location and width. Consequently, the input–output map and the underlying dynamics can change significantly, due to which the above mentioned controllers can become unstable. Hence, experimental devices require a sawtooth period controller which is robust against large variations, uncertainties and disturbances.

A first example of such a robust alternative has been presented in [20], showing experimental results from TCV using extremum seeking control [21]. The work in [20] is based on the specific controller structure from [22, 23], and maximizes the sawtooth

period without *a priori* knowledge of the ECCD deposition location which yields this maximum period. However, the controller parameters were reported to be difficult to select, and the practical relevance of maximizing the period is debatable.

Recent developments in control engineering [21, 24, 25] have shed new light on extremum seeking control (ESC), and have generalized and extended the work in [22, 23]. ESC is essentially an adaptive control strategy, which optimizes a certain cost function using an online estimation of its gradient. The results in [21, 24, 25] have shown that the ESC structure can be decomposed into separate subsystems, i.e. a cost function, a gradient estimator and an optimization routine. Each subsystem can be chosen and designed separately, which offers flexibility and allows for a systematic design and tuning of the extremum seeking controller. These insights thus offer solutions for the practical issues raised in [20], and allow for a dedicated optimization of ESC for the sawtooth period control problem.

In this paper we present such an extremum seeker design, tailored to the sawtooth period control problem based on these new developments [21, 25]. The controller is defined in the crash-driven discrete-time framework presented in [18] and uses a cost function which allows tracking of any desired sawtooth period. The gradient of this function is estimated online by means of an external perturbation on the EC mirror angle and subsequent dedicated filtering. A so-called sliding mode optimizer [26] uses this gradient to adjust the mirror angle with a constant rate towards the optimum, which coincides with the desired sawtooth period. Practical guidelines will be provided to tune the controller parameters, based on the required separation of time-scales between these subsystems of the extremum seeker [21].

This proposed adaptive control strategy is model-free, i.e. it does not rely on any mathematical or physical model of the sawtooth instability. Therefore, the controller is inherently robust, as it can be applied to any sawtooth simulation or sawtooth plasma. A Kadomtsev–Porcelli sawtooth model [18] is used as a case study to benchmark and test the controller. Simulation results affirm that the controller can track any time-varying sawtooth period reference, even when the plasma parameters change significantly, various types of disturbances and a detection delay are added, or slow EC mirror launcher dynamics is incorporated in the control loop. This demonstrates that ESC is indeed highly robust against uncertainties and disturbances, and is therefore readily applicable on experimental devices to control the sawtooth period. The high robustness does come at the expense of degraded closed-loop performance compared to the techniques in [18, 19]; the separation of time-scales prescribes low convergence speed and the external perturbation induces ongoing oscillations on the sawtooth period.

This paper is organized as follows, section 4.2 briefly discusses the considered sawtooth model and the sawtooth period control problem. In section 4.3, the basic principles of extremum seeking for sawtooth control are discussed. Controller structure design and tuning guidelines are elaborated on in section 4.4. Tests of the controller on the sawtooth model are presented in section 4.5 and possible performance improvements are suggested in section 4.6. Conclusions and discussion are addressed in section 4.7.

4.2 Control problem formulation

Since the highly robust control strategy for the sawtooth period presented in this paper is model-free, it is applicable to any sawtooth model or experimental sawtooth plasma. However, to illustrate the tuning of its controller parameters and to assess the resulting closed-loop behaviour, ESC will be applied to a specific sawtooth model in this paper, i.e. the one proposed in [18]. In this section this model is briefly recapitulated, and used to introduce the sawtooth period control problem.

4.2.1 Kadomtsev–Porcelli sawtooth model

The considered sawtooth model consists of three main elements: the magnetic diffusion equation, Porcelli’s criterion for triggering of the sawtooth crash [9] and the Kadomtsev reconnection model [27]. The model consists of a set of equations to describe the evolution of the poloidal magnetic field $B_\theta(r, t)$ as a function of time t and radius r

$$\frac{\partial}{\partial t} B_\theta = \frac{\partial}{\partial r} \left(\frac{\eta}{\mu_0 r} \left(B_\theta + r \frac{\partial}{\partial r} B_\theta \right) - \eta J_{\text{CD}} \right) \quad \text{if } s_1 < s_{\text{crit}}, \quad (4.1a)$$

$$B_\theta(r, t^+) = \begin{cases} B_\theta(r, t^-) & \text{for } r \geq r_{\text{mix}} \\ \frac{d}{dr} \Psi_*^c(r) + \frac{1}{R_0} r B_\phi & \text{for } r < r_{\text{mix}} \end{cases} \quad \text{if } s_1 \geq s_{\text{crit}}, \quad (4.1b)$$

with boundary conditions $B_\theta(0, t) = 0$ and $B_\theta(a, t) = \frac{\mu_0 I_p}{2\pi a}$. Here η is the plasma resistivity, μ_0 the magnetic permeability, R_0 the tokamak major radius, a its minor radius, B_ϕ the toroidal magnetic field and I_p the plasma current. Moreover, $s_1 = s(r_{q=1})$ is the magnetic shear at the surface where the safety factor q equals unity, where for large aspect ratio tokamaks $q(r, t) = \frac{r B_\phi}{R_0 B_\theta}$ and $s(r, t) = \frac{r}{q} \frac{dq}{dr}$. According to Porcelli’s model [9] a sawtooth crash is triggered if this s_1 exceeds a critical value s_{crit} , which is assumed to be constant here. At a sawtooth crash, the flux surfaces up to the mixing radius r_{mix} reconnect on a very short time-scale according to the model of Kadomtsev [27], represented by (4.1b). The magnetic field B_θ after a crash (at time t^+) follows from the post-crash helical flux function $\Psi_*^c(r)$, which depends on the pre-crash helical flux function $\Psi_*(r)$ at time t^- . This $\Psi_*^c(r)$ is calculated using the Archimedes-Kadomtsev approach proposed in [18], i.e.

$$\Psi_*^c(r_c) = \Psi_*(r_{i-}) = \Psi_*(r_{j+}), \quad \text{where } r_c^2 = \sum_i r_{i-}^2 - \sum_j r_{j+}^2, \quad (4.2)$$

where r_{i-} denotes the pre-crash surfaces with $d\Psi_*/dr < 0$, and r_{j+} the pre-crash surfaces with $d\Psi_*/dr > 0$. The output of the model is the time between two subsequent crashes (4.1b), which defines the sawtooth period τ_s .

The magnetic field B_θ , and thereby the period τ_s , can be influenced by the EC current drive profile J_{CD} in (4.1a). This profile is determined by the total driven current I_{CD} and the deposition location of the EC beam (assuming a constant deposition width). The latter is directly influenced by the EC mirror angle ϑ_a , which is considered

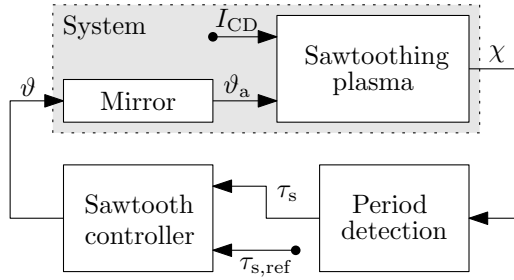


Figure 4.1: Sawtooth controller topology.

the input of the sawtooth model. The expression to determine J_{CD} from the current drive I_{CD} and the EC mirror angle ϑ_a is given in [18].

The model is implemented in a Matlab[®] Simulink[®] environment [18]. This gives great flexibility in the design and interconnection of systems and signals. The model parameters have been chosen according to the specifications of the TEXTOR tokamak [28], and tuned to yield a realistic ohmic sawtooth period of about 15 ms.

4.2.2 The sawtooth period control problem

A schematic representation of the sawtooth period control problem is shown in figure 4.1. The first input to the sawtooth plasma, or in our case the sawtooth model, is the EC driven current I_{CD} , which is in the same direction as the plasma current and is kept constant at $I_{CD} = 2$ kA. The second input is the mirror angle ϑ_a ; the requested mirror angle is denoted by ϑ , which is the control variable in this paper. The output of the sawtooth system is a set of measurements χ , e.g. soft x-rays or ECE, from which a sawtooth period τ_s is determined by a period detection algorithm [14]. The controller has two inputs: τ_s and a reference sawtooth period $\tau_{s,ref}$, which may be time-varying. The task of the controller is to steer the mirror such that τ_s converges to $\tau_{s,ref}$.

As we will later argue, our proposed control strategy operates on a time-scale that is slower than the time-scale of the sawtooth dynamics. This implies that the mirror adjustments are so slow that the sawtooth period is essentially always close to its steady-state value. For this reason the steady-state input–output behaviour of the sawtooth instability is of importance, which describes the relation between the mirror angle and the sawtooth period in steady-state, i.e. it depicts τ_s for a certain ϑ as $t \rightarrow \infty$. Figure 4.2 shows this input–output map for the sawtooth model described in section 4.2.1, which we will use as a case study throughout this paper. The ohmic period τ_Ω is indicated by the dashed line. Figure 4.2 thus shows that for mirror angles below 7.5° the sawtooth period shortens, and for larger angles the period is lengthened. This corresponds to injecting current either inside or outside the $q = 1$ surface, which is in agreement with [12, 13]. Note that the slope or gradient $d\tau_s/d\vartheta$ of the input–output map is not constant and even changes sign; for some values of ϑ an increase in mirror angle yields an increase of the period, whereas for other values of ϑ the period decreases. This shows the importance of the gradient for a controller design; in order

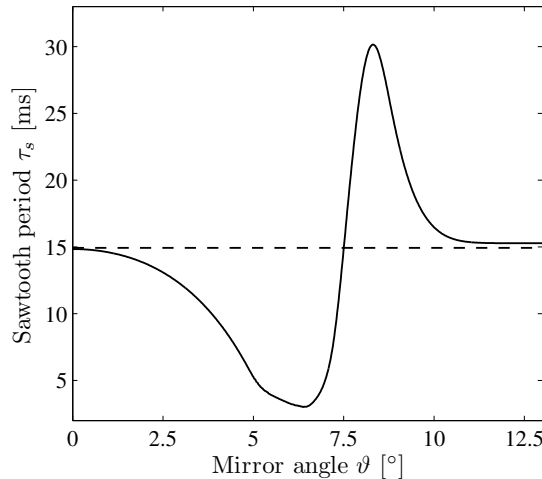


Figure 4.2: Steady-state map input–output map of the model presented in section 4.2.1 (solid) and the ohmic sawtooth period τ_Ω (dashed), for $B_\phi = 2.45$ T and $I_p = 400$ kA.

to steer the mirror in the right direction, the sign of $d\tau_s/d\vartheta$ has to be known.

Standard feedback control strategies as used in [15–18] or high-performance controllers as in [19] require the sign of the gradient to be constant, which limits their operating space, e.g. to $0^\circ \leq \vartheta \leq 6^\circ$. Moreover, they rely on knowledge of the gradient (also known as the DC-gain) and the underlying dynamics to ensure stability of the control loop. As mentioned in the introduction, this is a viable assumption under reactor-like conditions. However, on experimental tokamaks plasma parameters are often uncertain or time-varying, leading to large variations in the sawtooth dynamics, while the controller operating space generally needs to be large. Hence, such devices require more robust control approaches.

A good candidate is extremum seeking control, which does not rely on any *a priori* knowledge of the system. It only requires the existence of a stable steady-state input–output map, with a unique output τ_s for each fixed input ϑ [22, 29]; the curve in figure 4.2, of which each point is indeed stable [18], indicates that the considered sawtooth model meets this criterion. ESC identifies the gradient of the system online and is therefore able to cope with uncertainties of the input–output map. Consequently, it can be used throughout the entire operating space of the mirror. In this paper we will discuss the systematic design of an extremum seeking (ES) controller for the sawtooth period where the robustness against variations of the input–output map is specifically addressed.

4.3 Fundamentals of extremum seeking for sawtooth period control

ESC is an adaptive control strategy that uses online optimization techniques to slowly drive a process to a desired operating point which minimizes a cost function f . For sawtooth period control this implies that ESC finds the mirror angle ϑ that minimizes

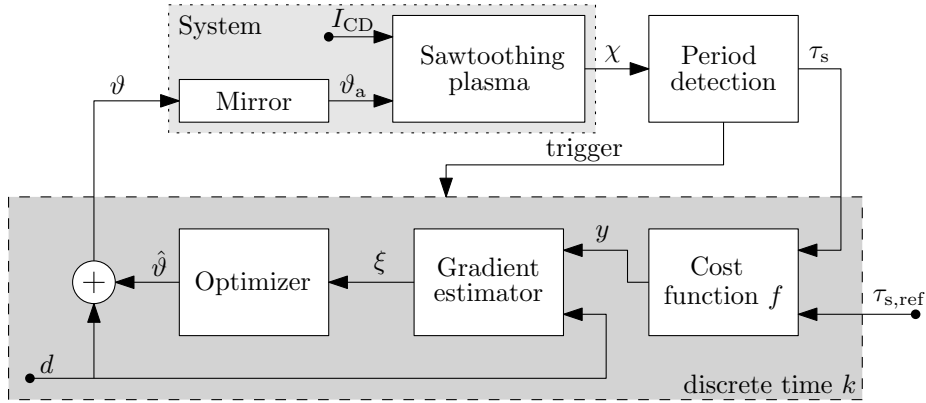


Figure 4.3: ESC topology for the sawtooth period, depicting the extremum seeking controller in the bottom grey box.

a certain function f such that the period τ_s matches a desired reference value.

The block scheme in figure 4.3 shows the ESC topology for the sawtooth period control problem. This closed loop operates in both continuous time (sawtooth process) and discrete time (controller). The sawtooth period, i.e. the variable to be controlled, only changes when a crash occurs. There are no measurements of the period between crashes, hence, controller updates of the angle ϑ are triggered by the period detection. Therefore, the controller operates in discrete time [30], with the interval between control updates being the most recent sawtooth period, which concurs with the approach taken in [18]. The variable k is the crash counter and is a measure of discrete time.

The ES controller consists of three subsystems: a cost function, a gradient estimator and an optimizer. The cost function should be such that its function value y is minimal if the measured sawtooth period τ_s is equal to the reference sawtooth period $\tau_{s,\text{ref}}$. The gradient estimator uses a perturbation signal d to estimate the gradients of the cost function with respect to the mirror angle ϑ . The optimizer uses this gradient estimate ξ to drive the estimate of the optimal mirror angle $\hat{\vartheta}$ to the minimizer ϑ^* of the cost function, which is typically unknown, under the assumption that the input–output map is not known exactly.

For this control strategy to function properly, it is desirable to maintain a separation of the time-scales that each subsystem operates in [25]. The cost function is static, and could thus be viewed as part of the sawtooth process. The estimation of the gradient can only be performed correctly if the dynamics of the sawtooth period has converged sufficiently close to the steady-state. The perturbation d used by the gradient estimator thus has to be slower than the slowest time-scale of the sawtooth dynamics. Some gradient estimators need settling time due to internal filtering, others rely on a slow optimizer in order to work; hence the optimizer operates at the longest time-scale. In summary there are three important time-scales [21, 25]:

1. the dynamics of the sawtooth period, including the cost function (fastest);
2. the perturbation for the gradient estimation (intermediate);
3. the optimization (slowest).

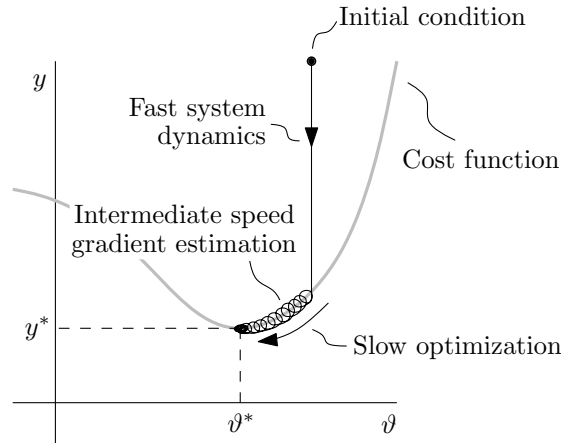


Figure 4.4: Output trajectory showing time-scale separation.

This time-scale separation can be visualized in figure 4.4, which is inspired by [21]. It shows an arbitrary steady-state map (combination of sawtooth system and cost function) in grey, with input ϑ and the value y of the cost function as output. The output quickly evolves from some initial condition to the steady-state map. The gradient estimation scans the cost function on an intermediate time-scale, and the optimization is performed on the slowest time-scale. The separation of time-scales allows us to design each subsystem separately, starting with the fastest system.

4.4 Extremum seeking controller design

This section discusses the working principles of the different ESC subsystems, as well as the accompanying design procedures. Moreover, implementation and tuning guidelines are proposed in section 4.4.4, and a supervisory control loop is discussed in section 4.4.5.

4.4.1 The cost function

The task of the extremum seeker is to find a mirror angle ϑ that minimizes a static cost function f . This minimum of the cost function should correspond to a desired operating point, i.e. when the sawtooth period τ_s matches a desired period or reference $\tau_{s,\text{ref}}$. Therefore we propose the cost function

$$f(\tau_s, \tau_{s,\text{ref}}) = (\tau_{s,\text{ref}} - \tau_s)^2, \quad (4.3)$$

which is zero when $\tau_s = \tau_{s,\text{ref}}$ and greater than zero otherwise. Figure 4.5 depicts this cost function as a function of the input ϑ in steady-state for $\tau_{s,\text{ref}} = 10$ ms, obtained by substituting the input–output map of figure 4.2 into (4.3). It shows multiple optima that minimize the cost function, since there are two possible mirror angles that can yield a sawtooth period of 10 ms. It is unknown *a priori* to which minimum the extremum seeker will converge. In section 4.5.1 it will be shown that the dynamic behaviour of the closed-loop system is very different at the two optimal mirror angles.

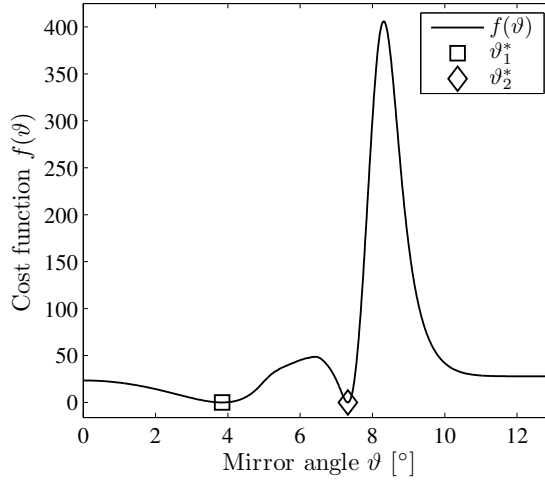


Figure 4.5: Steady-state cost function (4.3) evaluated for $\tau_{s,\text{ref}} = 10$ ms and the input–output map in figure 4.2. The optima ϑ_1^* , ϑ_2^* have been indicated with the markers.

Moreover, note that in a specific case where $\tau_{s,\text{ref}} > \tau_\Omega$ there will also be a local non-optimal minimum of the cost function at $\vartheta = 0^\circ$. In principle, ESC could converge to such a point. To avoid this a supervisor could be used, as discussed in section 4.4.5.

In practice the desired sawtooth period $\tau_{s,\text{ref}}$ may be time-varying, due to which the cost function may change. However, as long as this reference is varied on a slower time-scale than the one of the optimizer, the controller is able to track the moving minimum. In a previous application of ESC [20] the sawtooth period has been maximized. In our control framework this can be achieved by choosing the cost function $f(\tau_s) = -\tau_s$, or by choosing $\tau_{s,\text{ref}}$ in (4.3) greater than the maximum sawtooth period (i.e. > 30 ms).

4.4.2 Gradient estimator design

Numerical optimization algorithms often make use of the gradient of a cost function to find its minimum. A commonly used optimizer [21, 22, 29] is the first-order gradient descent method

$$\hat{\vartheta}(k) = \hat{\vartheta}(k-1) - \gamma \cdot \left. \frac{df}{d\vartheta} \right|_{\hat{\vartheta}(k-1)}, \quad (4.4)$$

where $\left. \frac{df}{d\vartheta} \right|_{\hat{\vartheta}(k)}$ is the gradient at crash k , i.e. the derivative of the cost function with respect to the control variable, in this case the mirror angle ϑ . The optimization rate is proportional to this gradient (scaled with a gain $\gamma > 0$); if the gradient is positive, the ϑ is decreased and vice versa, until the minimum is reached.

Since by assumption the input–output map is unknown, the gradient $\left. \frac{df}{d\vartheta} \right|_{\hat{\vartheta}(k)}$ has to be estimated online. To this end we first consider the minimal gradient estimator [29], depicted in grey in figure 4.6, whose working principle relies on using external perturbations on the input ϑ . In this scheme $y(k)$ is the value of the cost function, $\vartheta(k)$ its argument, $d(k)$ is an externally applied perturbation and $\xi(k)$ is the output variable. In accordance to the separation of time-scales we assume that the perturbation $d(k)$ is

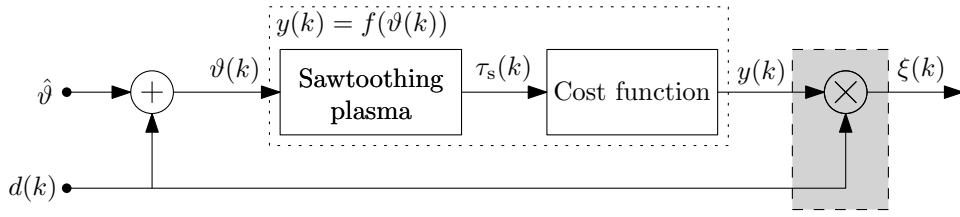


Figure 4.6: Topology of a minimal gradient estimator, indicated in grey.

slower than the sawtooth dynamics, so that the combination of the sawtooth system and the cost function can be approximated by a static function $f(\vartheta(k))$, like the one shown in figure 4.5. For the output of the scheme it then follows that

$$\xi(k) = d(k)f(\hat{\vartheta} + d(k)). \quad (4.5)$$

The perturbation $d(k)$ is chosen to be sinusoidal. This is a common choice in ESC, although other perturbations are also possible [31]. Let ω be the frequency and α the amplitude, so that $d(k) = \alpha \sin(\omega k)$, then the output becomes

$$\xi(k) = \alpha \sin(\omega k)f(\hat{\vartheta} + \alpha \sin(\omega k)). \quad (4.6)$$

A first-order Taylor expansion of $f(\vartheta(k))$ around the nominal input $\hat{\vartheta}$ yields

$$f(\hat{\vartheta} + \alpha \sin(\omega k)) \approx f(\hat{\vartheta}) + \alpha \sin(\omega k) \left. \frac{df}{d\vartheta} \right|_{\vartheta=\hat{\vartheta}} + \mathcal{O}(\alpha^2). \quad (4.7)$$

Assuming small α , and thereby neglecting the higher-order terms, substitution of this result in (4.6) then yields

$$\begin{aligned} \xi(k) &\approx \alpha \sin(\omega k)f(\hat{\vartheta}) + \alpha^2 \sin^2(\omega k) \left. \frac{df}{d\vartheta} \right|_{\vartheta=\hat{\vartheta}} \\ &= \alpha \sin(\omega k)f(\hat{\vartheta}) + \frac{\alpha^2}{2}(1 - \cos(2\omega k)) \left. \frac{df}{d\vartheta} \right|_{\vartheta=\hat{\vartheta}}. \end{aligned} \quad (4.8)$$

Hence, the instantaneous output $\xi(k)$ consists of a static component $\alpha^2/2$ times the gradient, plus additional oscillations due to the perturbation. However, note that the optimizer, which will use this $\xi(k)$, operates on a longer time-scale than the estimator; the oscillations will effectively average out over such a long time-frame, since

$$\lim_{K \rightarrow \infty} \frac{1}{K} \sum_{k=0}^K (\xi(k)) = \frac{\alpha^2}{2} \left. \frac{df}{d\vartheta} \right|_{\vartheta=\hat{\vartheta}}. \quad (4.9)$$

Hence, under the assumption of time-scale separation, the output $\xi(k)$ of figure 4.6 indeed provides an estimation of the gradient of the cost function (in an averaged sense) with a scaling of $2\alpha^{-2}$.

The accuracy of the gradient estimator in (4.5) and figure 4.6 is further improved by the inclusion of additional filters. In the closed loop the nominal operating point $\hat{\vartheta}$ and

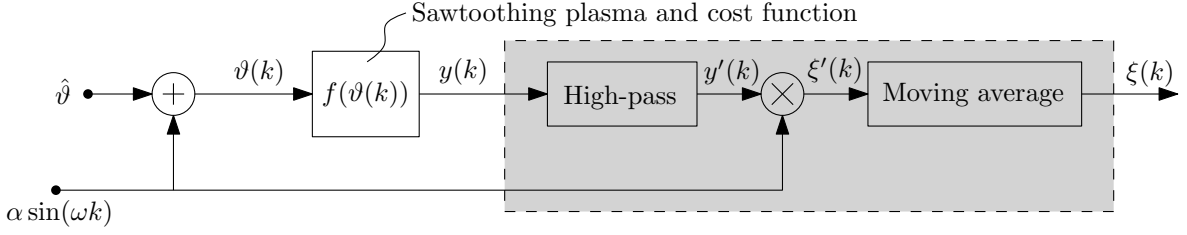


Figure 4.7: Block scheme of the proposed gradient estimator, indicated in grey.

thereby $f(\hat{\vartheta})$ are time varying. Consequently, the first term in (4.8) does not average out completely. Since $\hat{\vartheta}$ is varying slowly (with the speed of the optimizer), $f(\hat{\vartheta})$ can be attenuated by high-pass filtering the output of the cost function $y(k)$. The filtered signal $y'(k)$ then has an average close to zero, while the term $\alpha \sin(\omega k) \left. \frac{df}{d\vartheta} \right|_{\vartheta=\hat{\vartheta}}$ in (4.7) is retained. The inclusion of this filter naturally improves the gradient estimation, although ξ is still an approximation which is only valid in an averaged sense.

Additionally, a low-pass filter could be applied to the gradient estimation [21,22,25]. If such a filter is tuned to have a slow response, the oscillating terms in (4.8) are attenuated at the cost of additional delay. A more elegant approach is the application of a moving average filter. Note that $\xi(k)$ consists of sums of periodic signals of frequency $n\omega$ with $n = 1, 2, 3, \dots$. A moving average filter with a time window equal to the period time of the perturbation suppresses the exact same frequencies and thus removes all oscillating terms in (4.8). Let the perturbation frequency be $\omega = a\pi$ where $0 < a < 1$ and $2/a$ is a natural number. The perturbation then becomes

$$d(k) = \alpha \sin(a\pi k), \quad (4.10)$$

and a full period of the perturbation then involves $n = 2/a$ sawtooth crashes. Therefore, we propose the following moving average filter:

$$\xi(k) = \frac{1}{n} \sum_{j=1+k-n}^k \xi'(j), \quad (4.11)$$

with $\xi'(k)$ the unfiltered gradient estimate. A schematic representation of this extended gradient estimator, which is used in this paper, is shown in figure 4.7. The gradient estimate is formed by the output $\xi(k)$, which again has to be scaled by a factor $2\alpha^{-2}$.

The frequency of the perturbation separates the fast time-scale of the sawtooth dynamics from the slower time-scale of the gradient estimator. This frequency should be sufficiently low (belonging to the pass-band of the sawtooth dynamics [18]), such that the response of the sawtooth period to the perturbation is close to steady-state. On the other hand, a faster perturbation leads to faster convergence of the gradient estimator. The tuning of the perturbation frequency is discussed in section 4.4.4.

4.4.3 Optimizer design

The optimizer uses the estimation of the cost function gradient to change the mirror angle such that the cost function is minimized, such as the first-order gradient descent

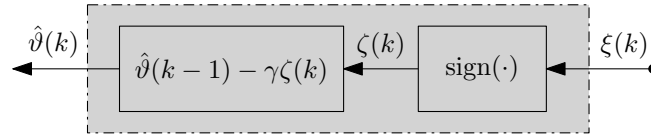


Figure 4.8: Sliding mode optimizer.

technique in (4.4). In this technique the gain γ scales the convergence rate of the optimizer, which depends on the estimated gradient. This implies that when the gradient is large, γ has to be small to ensure that the optimization is sufficiently slow. Unfortunately, in the sawtooth period control problem the gradient undergoes very large changes, as suggested by figure 4.2 and 4.5. If γ is tuned such that acceptable performance is achieved in the regions where the gradient is large, typically for mirror angles around 7.5° , the convergence speed is extremely slow in the regions with small gradients, typically for mirror angles $0^\circ \leq \vartheta \leq 6^\circ$. If the optimizer is tuned such that it is performing well in the region $0^\circ \leq \vartheta \leq 6^\circ$, it can actually be unstable in other regions, since the time-scale separation may not be guaranteed. This issue was encountered in [20] and ameliorated by scheduling the optimizer gain. However, this compromises robustness, since it requires information on the input–output behaviour of the sawtooth.

An alternative approach, specifically beneficial for high-order non-linear cost functions as in figure 4.5, is to make the convergence rate completely independent of the gradient by means of a so-called sliding mode optimizer [26]. This optimizer uses only the sign of the first-order gradient estimate, and steers the nominal mirror angle with constant velocity (in discrete time) towards the minimizer ϑ^* , i.e.

$$\hat{\vartheta}(k) = \hat{\vartheta}(k-1) - \gamma \text{sign}(\xi(k)). \quad (4.12)$$

The corresponding block scheme is shown in figure 4.8. There are three main advantages of this type of optimizer:

- the gradient does not affect the convergence rate, hence acceptable performance can be achieved throughout the entire operating range;
- it is more robust (with respect to convergence), since it requires only the sign of the gradient and thus allows for certain errors on the gradient estimation;
- the tuning of the optimizer gain is simplified considerably, as will be discussed in section 4.4.4.

A disadvantage of this approach, which is assumed to be allowed here, is that chatter of ϑ around the optimum will arise. Chatter is referred to as the unwanted bouncing or switching of variables, in this case the mirror angle ϑ , as shown in figure 4.9. The proposed optimizer is always optimizing $\hat{\vartheta}(k)$ with a fixed convergence rate determined by γ . As a result, when close to an optimum, the mirror angle (and with that the sawtooth period) will display an additional oscillation around the optimum, with a

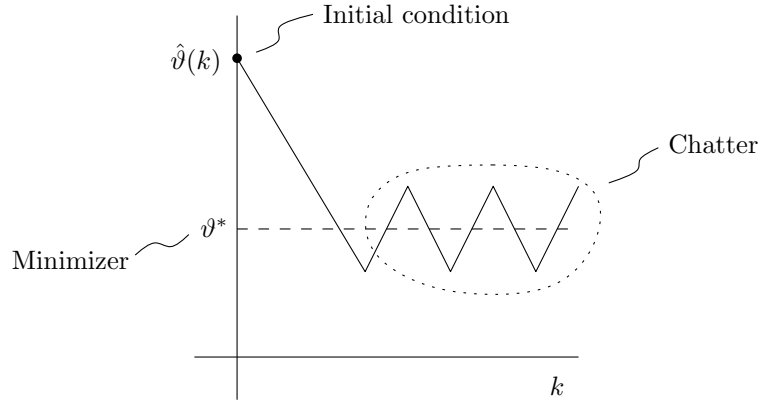


Figure 4.9: Illustration of chatter around an optimum.

lower frequency than the perturbation. This frequency is related to the settling time of the gradient estimate, and the slope of the trajectory of $\hat{\vartheta}(k)$ is equal to $\pm\gamma$. The chatter can be interpreted as a disturbance, but since its frequency is lower than the perturbation frequency, the correlation between perturbation and chatter is small. Hence, chatter does not influence the gradient estimate. The amplitude of the chatter is determined by the optimizer gain γ and the settling time of the optimizer, which is mainly determined by the perturbation frequency. A larger γ yields a larger chatter amplitude; the same holds for a larger settling time of the optimizer.

4.4.4 Overall control system and tuning of the controller parameters

This section discusses the complete closed-loop control system shown in figure 4.10, and presents guidelines for the tuning of the controller parameters. Note again that the mirror and the plasma operate in continuous time, whereas the controller is defined in discrete time. The transition from continuous to discrete time is done by the sawtooth period detection. Conversely, a ‘hold’ operation keeps $\vartheta(k)$ constant in between crashes to form the continuous-time signal $\vartheta(t)$.

Tuning of the gradient estimator

As discussed in section 4.4.2, the frequency of the perturbation $d(k)$ has to be sufficiently low such that the sawtooth period is close to steady-state at all time. In [18] it is shown that currently existing mirror launchers operate on a longer time-scale than the sawtooth period dynamics. The speed of the mirror launcher is largely characterized by the bandwidth of its own motion control system. Roughly speaking, the mirror launcher can follow frequencies up to the bandwidth quite well (so that $\vartheta_a \approx \vartheta$) but attenuates higher frequencies (so that $\vartheta_a \approx 0$). The bandwidth of the launcher thus determines the maximal perturbation frequency.

This bandwidth f_{bw} is specified in the continuous-time domain, while the proposed ESC operates in discrete time. The fastest perturbation frequency in continuous time occurs if the sampling interval of the controller is the shortest, i.e. when the sawtooth

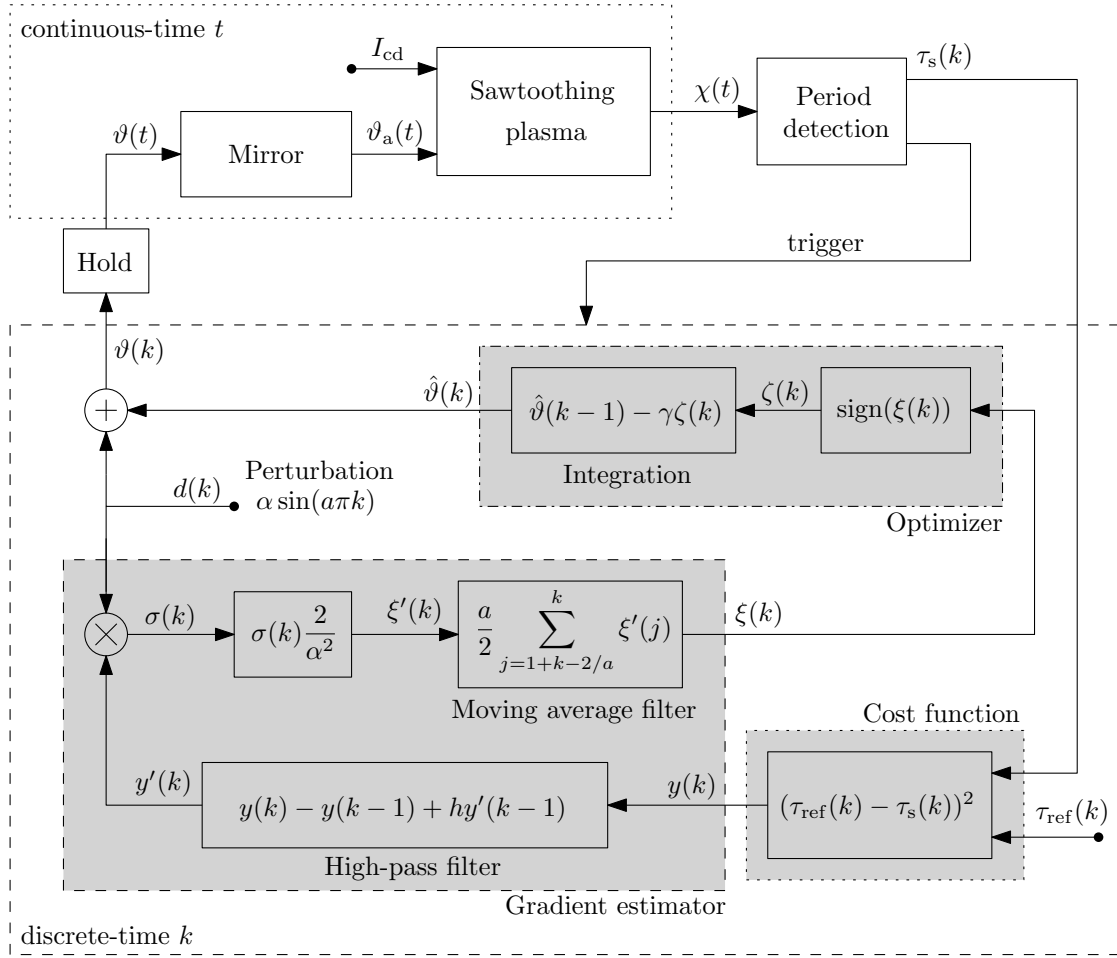


Figure 4.10: Complete closed loop with the ESC subsystems, i.e. the cost function, the gradient estimator, and the optimizer, marked grey.

period is the shortest. Hence, the perturbation frequency should be selected such that its continuous-time equivalent at the minimal sawtooth period is slightly lower than bandwidth of the launcher. Defining $\tau_{s,\min}$ as the smallest possible sawtooth period, the perturbation frequency a should thus satisfy

$$a \leq 2f_{\text{bw}} \cdot \tau_{s,\min}. \quad (4.13)$$

The earlier posed limits on parameter a still apply as well, i.e. $0 < a < 1$ and $2/a$ must be a natural number. With a realistic bandwidth f_{bw} of 10 Hz [18] and a minimal sawtooth period of 3.0 ms the perturbation frequency would be $a = 0.05 \text{ crash}^{-1}$. This perturbation frequency assures optimal performance of the gradient estimator, assuming that the mirror launcher dominates the sawtooth period dynamics.

In case the mirror launcher operates on a faster time-scale than the sawtooth dynamics, the selection of parameter a requires identification of the slowest time-scale of the sawtooth period. In that case the perturbation should belong to the pass-band of the sawtooth period dynamics. Stepwise identification experiments as described in [18] give information on the time-scale of the sawtooth period. The period of the

perturbation $d(k)$ should be larger than the settling time of such a step. In [18], a step around $\vartheta = 2.68^\circ$ has a settling time of 5 crashes. Taking a safety margin into account, a perturbation period of 10 crashes could be chosen. Simulations indeed showed that, in the case of an infinitely fast launcher, the perturbation frequency could be increased to $a = 0.2 \text{ crash}^{-1}$, corresponding to a 10 crashes period.

The amplitude α of the perturbation $d(k)$ must be chosen as small as possible, since larger α lead to larger estimation errors in (4.8). However, the minimal amplitude is often limited by practical considerations such as the presence of disturbances. When disturbances are large, the gradient estimator can become quite slow, as it then takes more time to average out the effect of these disturbances. This can be overcome by choosing a larger perturbation amplitude, to improve the signal-to-noise ratio of the gradient estimation $\xi(k)$. In a practical setup the positioning accuracy of the mirror is likely to pose a lower limit on the minimal perturbation amplitude. E.g. the mirror on TEXTOR has a maximal positioning error of 0.6° during maximal acceleration [32], and smaller positioning errors during normal motion. Therefore the perturbation amplitude is chosen $\alpha = 0.3^\circ$.

The high-pass filter in figure 4.10 is of a discrete-time first-order type. It has a single tuning parameter h which must satisfy $0 < h < 1$. The lower the value of h the more aggressive the filtering, i.e. for very low h the output of the filter would always be close to zero and a lot of the content of $y(k)$ is lost. It is therefore important to choose h close to 1. A practical value is $h = 0.9$.

Tuning of the optimizer

The optimizer gain γ is directly related to the optimization speed and should be tuned such that the optimizer is slower than the gradient estimator. If the gain is chosen too large, the optimizer tends to overshoot and miss the optimum since the gradient estimator is not able to determine the gradient accurately if the operating point is changing too fast. A pragmatic approach is to start with a small γ and increase the gain during experiments. Here it is assumed that the gradient estimator needs three perturbation periods to settle, i.e. $3 \cdot 2/a$ sawtooth crashes to obtain a proper gradient estimate, since the moving average filter has a memory of one perturbation period and the high-pass filter introduces some additional settling time. The estimated minimizer $\hat{\vartheta}(k)$ may not change too much in this time window. Figure 4.2 shows that the largest gradient is around $\vartheta \approx 7.5^\circ$, a region which is approximately 2° wide. We therefore assume that the mirror angle may vary about 0.5° during the settling of the gradient estimator. An initial guess for the optimizer gain is thus

$$\gamma = \frac{0.5}{6}a \text{ [}^\circ\text{/crash]}. \quad (4.14)$$

With $a = 0.2 \text{ crash}^{-1}$ (assuming an infinitely fast launcher) the initial guess is $\gamma = 0.017^\circ\text{/crash}$, in simulations we could choose $\gamma = 0.02^\circ\text{/crash}$.

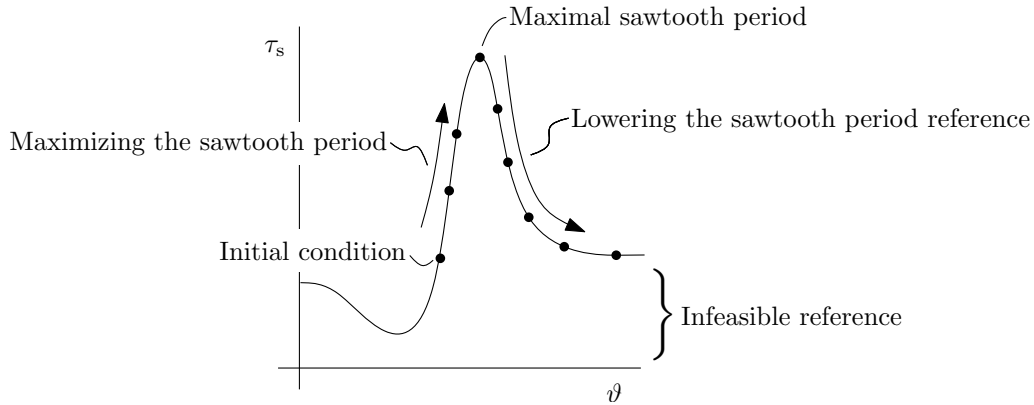


Figure 4.11: Unbounded mirror angle growth due to an infeasible reference.

4.4.5 Usage of a supervisor for practical issues

In most control implementations supervisory controllers are employed to detect and correct undesired closed-loop behaviour. For the sawtooth control problem a supervisor can be used to guard the low-level controller, i.e. the ESC, since the requested mirror angle could grow unbounded for certain specific reference trajectories.

This is illustrated in figure 4.11. If the sawtooth period is first maximized and then sequentially lowered, it is not *a priori* known in which direction the ESC will choose to evolve, i.e. either to the left or to the right of the maximum. If the ESC steers towards the right it is possible to have unbounded growth of the mirror angle if $\tau_{s,\text{ref}}$ becomes smaller than the ohmic sawtooth period. A supervisor can be used to detect such unbounded growth and steer the mirror back by using feedforward techniques.

Detection could be done by means of an additional gradient estimator, which estimates the gradient of the input–output map of figure 4.2 directly (instead of the gradient of the cost function). If the sign of this gradient is negative for mirror angles beyond the $q = 1$ surface, unbounded growth might occur, and the mirror needs to be steered back accordingly. Another solution is to simply limit the maximally allowed mirror angle. Similarly, a supervisor can prevent convergence to a non-optimal local minimum at $\vartheta = 0^\circ$, e.g. by steering the angle to an arbitrary value outside $q = 1$ whenever $\tau_{s,\text{ref}} > \tau_\Omega$. The actual design of a supervisory controller is out of scope for this paper, as all simulation results are obtained without the use of a supervisor.

4.5 Simulation results

To validate the effectiveness of the proposed ESC strategy, this section shows and discusses the following closed-loop simulations:

1. the tracking of sawtooth period reference trajectories in section 4.5.1;
2. testing the controller for robustness against varying plasma parameters and disturbances in section 4.5.2;
3. the impact of the mirror launcher dynamics on the performance in section 4.5.3.

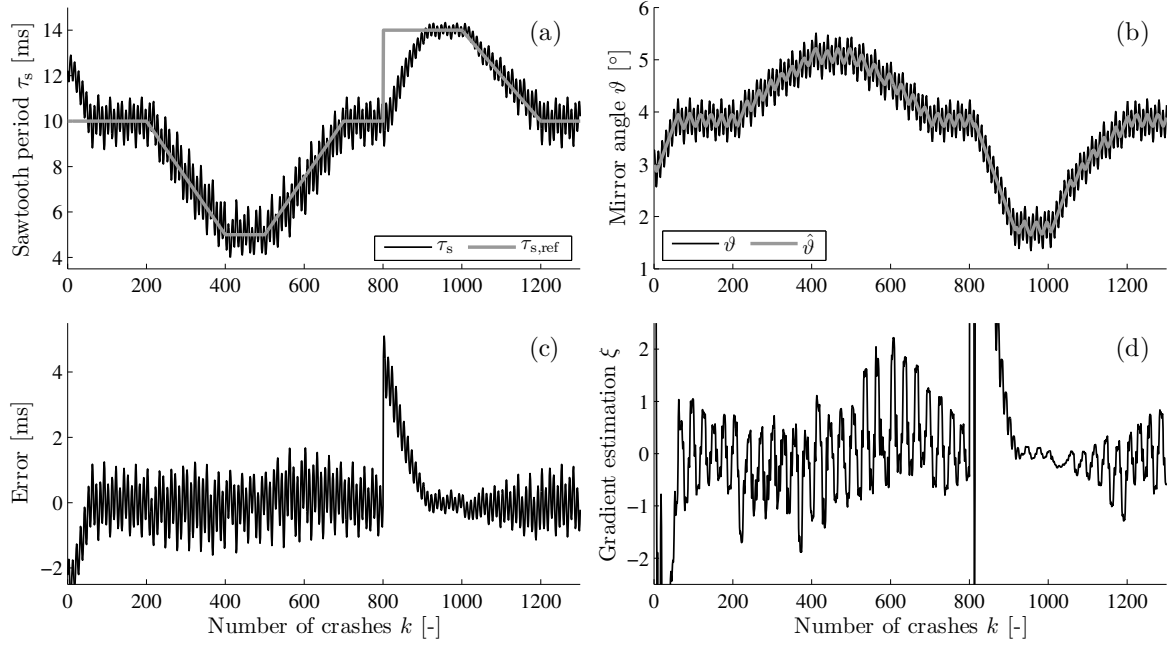


Figure 4.12: Simulation results of tracking small sawtooth period references: (a) the sawtooth period τ_s , (b) the mirror angle ϑ and estimated minimizer $\hat{\vartheta}$ which shows the chatter, (c) the tracking error $\tau_s - \tau_{s,ref}$ and (d) the gradient estimate.

For cases 1 and 2 the response of the mirror launcher to a requested angle is assumed to be infinitely fast compared to the sawtooth dynamics. The controller parameters are the same for all simulations in section 4.5.1 and section 4.5.2, in section 4.5.3 the tuning is adjusted to cope with the launcher dynamics.

4.5.1 Tracking of sawtooth period references

In the following results the EC driven current $I_{CD} = 2$ kA, the perturbation frequency $a = 0.2$ crash⁻¹, its amplitude $\alpha = 0.3^\circ$, the optimizer gain $\gamma = 0.02^\circ/\text{crash}$ and the high-pass filter parameter $h = 0.9$, as has been discussed in section 4.4.4.

Tracking small sawtooth periods

In the first simulation the initial mirror angle is chosen $\vartheta(k=0) = 3^\circ$ and the reference trajectory for the sawtooth period takes values between 5 and 14 ms, i.e. the controller operates on the left-hand-side of figure 4.2. The closed-loop results are shown in figure 4.12. The sawtooth period as a function of the elapsed sawtooth crashes is shown in figure 4.12(a), the reference is indicated with the thicker grey line. Figure 4.12(b) shows the mirror angle and the estimate of the minimizer $\hat{\vartheta}$, which shows the chatter due to the sliding mode optimizer. In figure 4.12(c), the error $\tau_s - \tau_{s,ref}$ is shown, which is the difference between the actual sawtooth period and the reference. The gradient estimate ξ is shown in figure 4.12(d). The reference starts at 10 ms, and is then gradually lowered to 5 ms. Then the reference sawtooth period is increased, first

linearly then in a stepwise fashion. The results show that there is a small transient from the initial condition. The controller achieves tracking of the requested sawtooth period with an error of slightly more than 1 ms when the reference is changing gradually. The controller successfully handles a step in the reference applied at $k = 800$ crashes; the settling takes place in about 100 crashes.

The oscillations on the sawtooth period are a result of the perturbation on ϑ and the chatter on $\hat{\vartheta}$ introduced by the sliding mode optimizer. Since the gradient of the input–output map is relatively small, the resulting oscillations on τ_s are small. In figure 4.12(b) the amplitude of the chatter is approximately equal to the perturbation $d(k)$.

The step in $\tau_{s,\text{ref}}$ leads to a large increase in the gradient estimation in figure 4.12(d). A first-order gradient descent optimizer (4.4) as in [20], whose optimization rate is proportional to the gradient, would have yielded a significant change in the mirror angle at this step. Such a change in ϑ can be risky, as it can instantly bring the sawtooth system to another operating region (e.g. the right-hand-side of figure 4.2), which can result in an unbounded growth of ϑ . In a specific incidental case, such a change in ϑ may also turn out just right, yielding an uncharacteristically fast convergence for ESC. An example can be found in [20], where the controller adapts within just one perturbation period to a rapid change in vertical position. In contrast, figure 4.12(b) shows that the sliding mode optimizer always alters ϑ linearly towards the new optimum. Hence, due to this constant optimization rate the sliding mode optimizer is more robust against large variations of the gradient.

Tracking large sawtooth periods

Figure 4.13 shows the simulation result where the initial mirror angle $\vartheta(k = 0) = 7.3^\circ$ and the reference takes values between 8 and 25 ms, including a step at $k = 800$ crashes. The controller operates in the middle region of figure 4.2, typically around a mirror angle of 7.5° . There is a small transient from the initial condition, after which the controller achieves good tracking. The step in the reference is handled successfully as well. Although the step is twice as large as the previous result, the settling time is only 30 crashes. This is because the gradient in this operating region is much larger than compared to the smaller sawteeth in figure 4.12. Hence, small changes in ϑ have a large effect on τ_s . So although the convergence rate in $^\circ/\text{crash}$ is fixed, τ_s converges much faster, since a much smaller change in mirror angle is required. However, the large gradient has also caused the oscillations on the sawtooth period to increase by a factor 5. To reduce these oscillations one could make the amplitude of the perturbation smaller in regions where the estimated gradient is large, e.g. by means of gain-scheduling as suggested in [20].

Tracking in different operating regions

In the previous two simulations the ESC operated in a single operating region where the sign of the gradient of the input–output map remained constant. The proposed

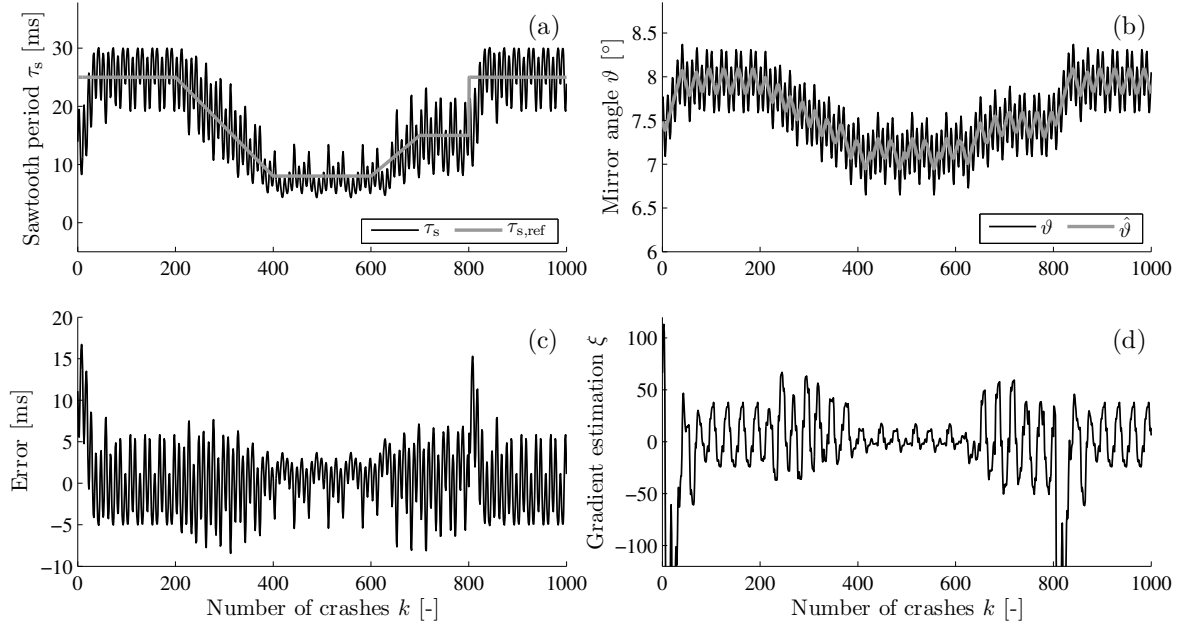


Figure 4.13: Simulation results of tracking large sawteeth: (a) the sawtooth period τ_s , (b) the mirror angle ϑ and estimated minimizer $\hat{\vartheta}$ with chatter present, (c) the tracking error $\tau_s - \tau_{s,ref}$ and (d) the gradient estimate ξ .

ESC is also capable of switching between such regions, and can thereby cover the whole operating region with a single controller. To demonstrate this, a simulation has been performed with an initial mirror angle $\vartheta(k=0) = 7.5^\circ$ and a sawtooth period reference which starts at 10 ms, gradually decreases to 5 ms and then rises again to 10 ms. The result is shown in figure 4.14, which indicates successful tracking of the reference period. Figure 4.14(a) shows that the sawtooth period makes a small jump around $k = 400$ crashes, i.e. when the controller jumps from the middle region (with large gradient) to the left-hand-side region (with smaller gradient). Apparently, the latter region is more attractive than the former. This can be explained by figure 4.14(c), which depicts the sawtooth period as a function of the mirror angle. The thickness of the band created by the trajectory of τ_s around the input–output map indicates the accuracy of the gradient estimate. For mirror angles $5.5^\circ \leq \vartheta \leq 6.5^\circ$ the band is very narrow, which implies that the sawtooth dynamics is very fast in this region (as has been shown in [18]). The gradient estimation is therefore very accurate, which makes this region very attractive. A wider band, as for $\vartheta > 6.5^\circ$, indicates a less accurate gradient estimation due to slow sawtooth dynamics. The trajectory of τ_s at $\vartheta \approx 6.7^\circ$ is actually perpendicular to the steady-state input–output map, thanks to which the controller crosses the minimum to the region around $\vartheta = 6^\circ$. Hence, the ESC converges to the smallest of the two angles corresponding to 5 ms, which is actually quite eligible since the oscillations on τ_s are much smaller there.

In our case the region with slow dynamics is surrounded by fast sawtooth dynamics. Hence, the somewhat erroneous gradient estimations in the slow region are intercepted

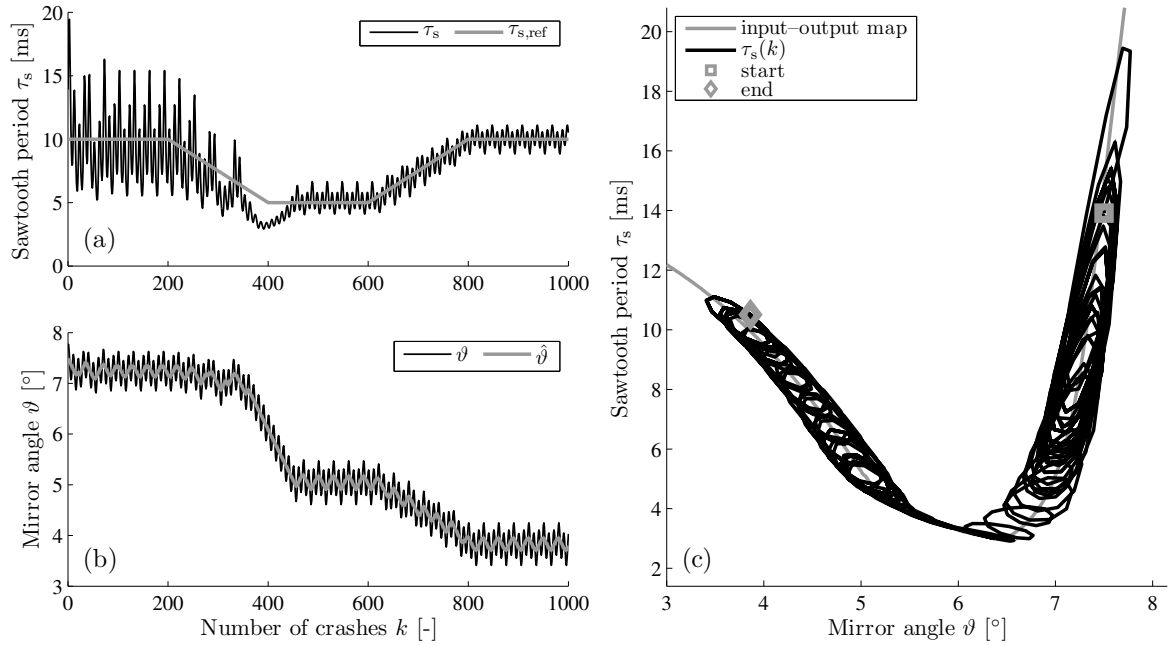


Figure 4.14: Simulation results of tracking 10 ms sawteeth in two different regions: (a) the sawtooth period τ_s , (b) the mirror angle ϑ and estimated minimizer $\hat{\vartheta}$ with chatter present and (c) the input–output map and sawtooth period as function of the mirror angle. The markers indicate the start and the end of the sawtooth period trajectory.

by the neighbouring fast dynamics, where the gradient is estimated correctly. It should be noted that the slow response around $\vartheta \approx 6.7^\circ$ and the fast one around $\vartheta \approx 6^\circ$ are predictions of the model in section 4.2.1, and may or may not occur in real experiments. In practice, one may encounter other phenomena that can have effects on the behaviour of the controller. The simulations show that ESC can handle such phenomena, as long as the separation of time-scales is satisfied.

4.5.2 Extremum seeking and robustness

For experimental devices controller robustness is an important issue. Robustness is considered as the ability of the controller to handle disturbances and uncertainties. The simulations in this section will indeed demonstrate the robustness of ESC; firstly, by considering variations of plasma parameters, and secondly, by disturbing the closed loop with noise and delay.

Robustness against varying plasma parameters

First, the robustness of ESC is demonstrated by applying the same controller to a sawtooth model with different parameters; the driven current I_{CD} is changed from 2 to 1.8 kA, the plasma current I_p from 400 to 350 kA and the toroidal magnetic field B_ϕ from 2.45 to 2.4 T. The simulation results are shown in figure 4.15, together with the previous results from figure 4.12. Figure 4.15(c) shows that the steady-state

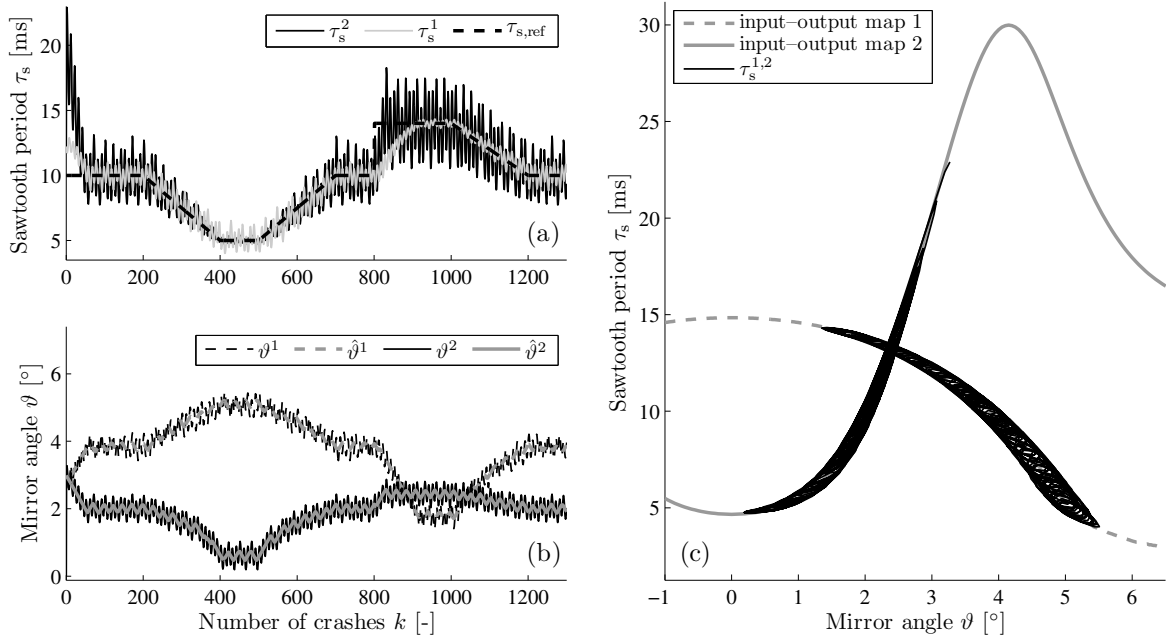


Figure 4.15: Simulation results with different plasma parameters ⁽²⁾, together with the original simulation indicated with ⁽¹⁾. The sawtooth period τ_s is shown in (a), the mirror angle ϑ and estimated minimizer $\hat{\vartheta}$ in (b) and the sawtooth period trajectory in (c). We see that in spite of a dramatic variation of the gradients, including a change of sign, the sawtooth controller still performs robustly.

input-output map has completely changed, due to the large shift of the $q = 1$ surface. Nevertheless, the reference is still successfully tracked. The oscillation on the sawtooth period at $\tau_s \approx 15$ ms is larger than before, since the gradient at this operating point is now larger. At $\tau_s \approx 5$ ms the oscillation is smaller, since that specific operating point now has a nearly zero gradient. The settling time after the step at 800 crashes is now much faster, which is again caused by the larger gradient at $\tau_s \approx 15$ ms.

A linear controller as used in [15, 16, 18] is not able to cope with such large parameter variations, as they change the sign of the gradient over a large portion of the operating space. ESC automatically adapts to such variations, even if these occur online, i.e. during a discharge. Such changes are similar to changes in the reference sawtooth period, since both introduce a sudden change in cost function. Hence, ESC is guaranteed to track these variations if they occur either on a slow enough time-scale, or stepwise with sufficient time between the steps (as in previous simulations). Note that if the parameter variations largely affect the sawtooth period dynamics, the time-scales of the controller subsystems might have to be adjusted.

Robustness against disturbances and detection delay

Real experiments are often subject to actuator and sensor noise. In the sawtooth control loop disturbances on the deposition location can occur, e.g. due to EC beam

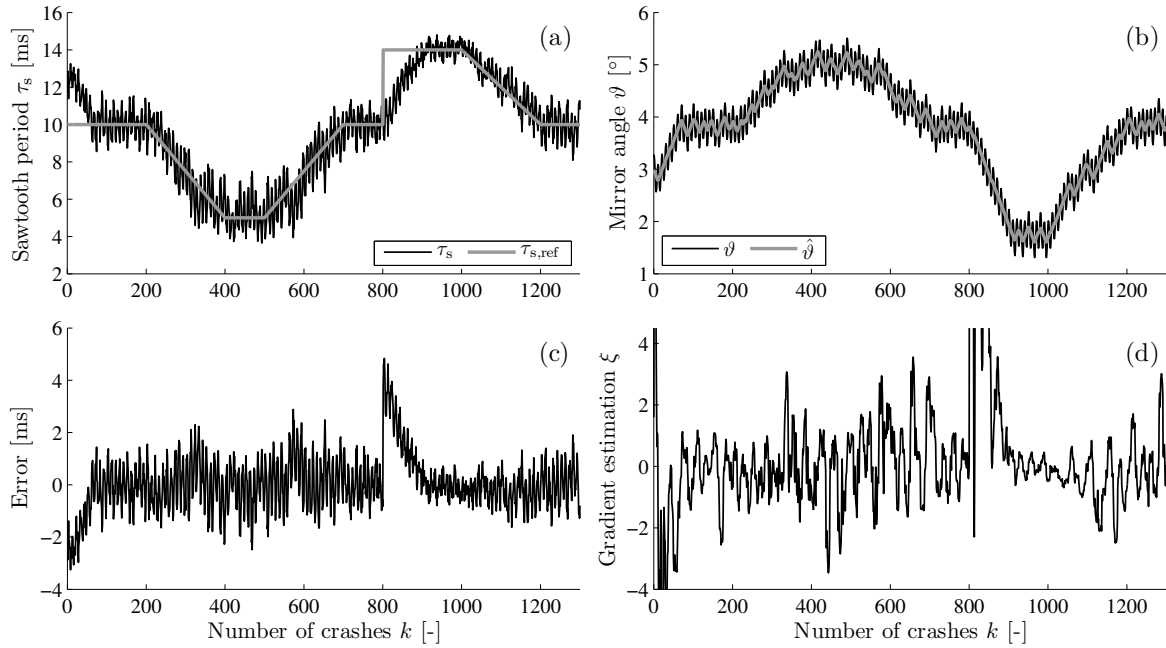


Figure 4.16: Simulation results with disturbances present: (a) the sawtooth period τ_s , (b) the mirror angle ϑ and estimated minimizer $\hat{\vartheta}$, (c) the tracking error $\tau_s - \tau_{s,\text{ref}}$ and (d) the gradient estimate ξ .

deflections or fluctuations of the plasma position and shape. Moreover, the EC current drive can exhibit noise due to vibrations in the gyrotron. On the sensor side a sawtooth crash detection is never flawless and will inevitably introduce delay and noise on the sawtooth period. To demonstrate that ESC can cope with these disturbances the following disturbances have been added in a repeat of the simulation depicted in figure 4.12:

- a $\pm 0.25^\circ$ uniform random noise on ϑ ;
- a ± 20 A uniform random noise on I_{CD} ;
- a ± 0.5 ms uniform random noise and an additional delay of 5 ms on τ_s .

The results depicted in figure 4.16 show that the controller still successfully tracks the reference and is thus robust for the added disturbances. In principle the 5 ms detection delay introduces a phase shift between the perturbation $d(k)$ and the resulting sawtooth period output $\tau_s(k)$, which influences the gradient estimate. However, here this phase shift is at most 1 crash, which is quite small compared to the perturbation period of 10 crashes. Moreover, the other disturbances on the gradient estimate are mostly attenuated by the moving average filter.

4.5.3 Impact of slow launcher dynamics

In the previous simulations the mirror launcher has been considered infinitely fast. In practice, this launcher is a closed-loop controlled mechanical device with a limited

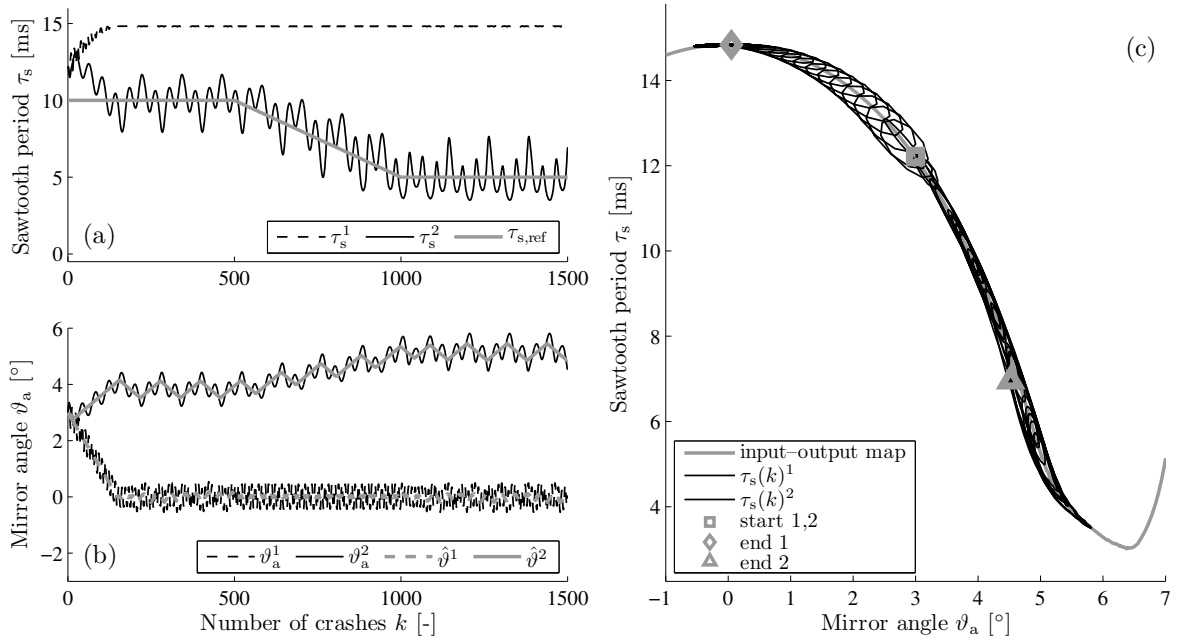


Figure 4.17: Simulation results with slow launcher dynamics, ⁽¹⁾ is with original tuning, ⁽²⁾ is with adjusted tuning: (a) the sawtooth period τ_s , (b) is the actual mirror angle ϑ_a and estimate of the minimizer $\hat{\vartheta}$, and (c) is the trajectory of τ_s on the steady-state input–output map. Markers indicate the start and end of these trajectories.

bandwidth, introducing dynamics between ϑ and the actual mirror angle ϑ_a . In this section its closed loop is modelled in the same fashion as in [18], i.e. by means of a second order low-pass filter with a cut-off frequency (bandwidth) of $f_{bw} = 10$ Hz and a damping of 0.35. With this model two simulations have been performed to investigate the influence of a slow launcher on the ESC: one with the original controller tuning, and one with adjusted tuning. The results are shown in figure 4.17. The reference starts at 10 ms and is lowered to 5 ms. The original tuning, indicated with ⁽¹⁾, fails as it maximizes the cost function instead, due to a wrong estimation of the sign of the gradient. Therefore, two controller parameters are adjusted. The perturbation frequency is lowered to the bandwidth of the launcher, as described in section 4.4.2, i.e. $a = 0.05$ crash⁻¹. Secondly, the optimizer gain γ is reduced to $\gamma = 0.01^\circ/\text{crash}$ to preserve the separation of time-scales. The results of the simulation with adjusted tuning are indicated with ⁽²⁾. It shows that functionality of the controller is restored. Note that the overall control loop is a factor two slower, hence the launcher appears to be a limiting factor in achievable performance.

With the adjusted tuning, the settling time of the gradient estimator has increased. This is visible in the chatter, which is of lower frequency. The gradient estimator is four times as slow as before, the optimizer gain has been reduced by a factor two. Consequently, the amplitude of the chatter has increased with a factor two.

4.6 Extremum seeking and performance

The above results clearly demonstrate the extremely high robustness of the extremum seeking controller. This robustness is inherent to the fact that ESC is completely model-free; it simply estimates the momentary behaviour of the sawtooth period online. An ESC approach is therefore very useful under experimental tokamak conditions, where the exact plasma parameters are somewhat uncertain or conditions may vary to a large extent. The disadvantage of ESC is its relatively low performance. The simulations have shown that convergence (or settling time) can take more than 100 crashes (i.e. more than 1 s in continuous time), and the sawtooth period will always oscillate around its desired value due to the applied perturbation $d(k)$ and the chatter. Consequently, steady-state errors are about ± 1 ms for small τ_s , but can increase up to ± 5 ms for larger τ_s . For comparison, linear feedback controllers as in [18] and high-performance approaches as in [19] obtain zero steady-state errors, and the latter typically converges within 0.2 to 0.35 s. Hence, under predictable reactor-like conditions such approaches might be more beneficial.

The above illustrates the classical trade-off between robustness and performance. It also indicates that the performance of ESC can be improved by including explicit knowledge of the sawtooth into the controller, at the expense of some robustness. In this section we briefly suggest three methods to achieve this.

4.6.1 Feedforward control

In situations where the steady-state input–output map of the sawtooth period is approximately constant and *a priori* known, this knowledge can be employed in advance to steer the mirror angle towards a value corresponding to a desired $\tau_{s,\text{ref}}$. This open-loop technique is called feedforward control, a widely used technique to improve closed-loop performance, such as in [19]. Feedforward control can easily be combined with ESC by using the input–output map of figure 4.2 as a look-up table for the mirror angle and adding this to the value of ϑ computed by the optimizer. This will improve the settling time to a large extent (up to the time-scale of the mirror launcher), but it does not affect the steady-state oscillations. The extremum seeker will still perturb and chatter to make sure the system remains at the optimum of the cost function.

Feedforward control yields the best results when the input–output map is known accurately. If the calculated feedforward angle is significantly wrong, it can be viewed as a disturbance or change in cost function. Since ESC is robust against such disturbances, it will compensate for the error in the feedforward, and still steer towards the desired sawtooth period. However, this does reduce the performance in terms of the settling time, possibly making it worse than without feedforward.

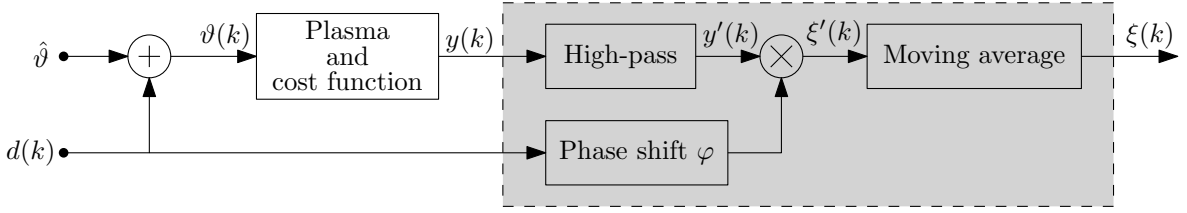


Figure 4.18: Gradient estimator topology with additional phase lag compensation.

4.6.2 Phase lag compensation

The sinusoidal perturbation on ϑ leads to an oscillation of the sawtooth period τ_s with the same base frequency as ϑ . For slow perturbations these signals are approximately in phase, but for higher frequencies the sawtooth (and launcher) dynamics can introduce a phase shift between ϑ and τ_s , which influences the accuracy of the gradient estimate. In case of a phase shift ψ it can be shown that the averaged gradient estimate becomes

$$\lim_{K \rightarrow \infty} \frac{1}{K} \sum_{k=0}^K (\xi(k)) = \cos(\psi) \cdot \frac{\alpha^2}{2} \left. \frac{df}{d\vartheta} \right|_{\vartheta=\hat{\vartheta}}. \quad (4.15)$$

Hence, a mismatch $\cos(\psi)$ is introduced, which can even lead to a wrong estimation of the sign of the gradient when $\psi \geq \pi/2$. This can be compensated for by phase-shifting the demodulation signal with an estimate of the phase lag [33] as shown in figure 4.18. Let φ be the phase shift in the demodulation signal. The gradient estimate then becomes

$$\lim_{K \rightarrow \infty} \frac{1}{K} \sum_{k=0}^K (\xi(k)) = \cos(\psi - \varphi) \cdot \frac{\alpha^2}{2} \left. \frac{df}{d\vartheta} \right|_{\vartheta=\hat{\vartheta}}.$$

Hence, if the demodulation phase shift φ equals the phase lag ψ , then the gradient estimate is not affected. Unfortunately, the phase lag introduced by the sawtooth dynamics varies with the sawtooth period. In this case φ should be chosen as the average phase lag, since $\varphi < \psi$ has the same effect on the gradient estimation as $\varphi > \psi$ (due to symmetry of the cosine function). Determining this average phase lag at the perturbation frequency requires dynamic identification experiments, as has been proposed in [18].

When the phase lag is compensated for, the perturbation frequency can be increased, yielding shorter settling times of the gradient estimator. Consequently, the optimizer gain can be increased, leading to faster convergence of the overall control loop.

4.6.3 Reducing the tracking error

Part of the oscillations on the error shown in the simulation results are introduced by chatter, which is a side effect of the chosen sliding mode optimizer. A common approach to eliminate chatter is the use of the saturation function (or a similar function like a hyperbolic tangent) instead of the sign function [34] in the optimizer (4.12). This

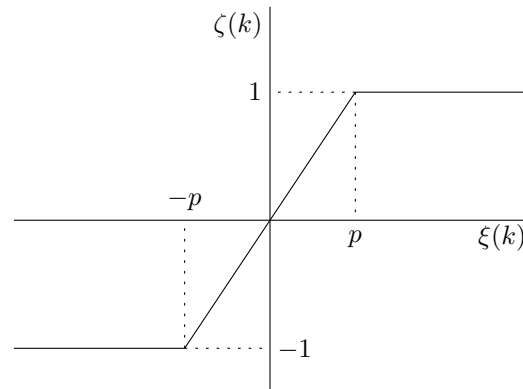


Figure 4.19: Saturation function and tuning parameter p .

way the optimization speed is constant when the estimated gradient is large, and proportional to the gradient when the gradient is small.

The saturation function depicted in figure 4.19 has limits $-1, 1$, as does the sign function, and has a parameter p that can be tuned to select at which value of the gradient to switch from sliding mode to first-order gradient descent. However, the simulation results in section 4.5.1 show that the gradient varies significantly with the operating point. If p is small compared to the gradient estimate, the optimizer would only operate like a sliding mode optimizer, and chatter would not be eliminated. If p is large compared to the gradient estimate, the optimizer only uses first-order gradient descent, which reduces robustness and affects the convergence speed. Hence, eliminating chatter improves the performance in terms of steady-state error, but at the expense of slower convergence and less robustness.

4.7 Conclusions

In this paper we have provided a structured design of a robust sawtooth period controller. The proposed extremum seeking controller is a special type of adaptive controller. Its working principle relies on online identification of the gradient of a cost function, which has a minimum at the desired sawtooth period, by a gradient estimator. The benefit of this control strategy is that it does not rely on any model describing the behaviour of the sawtooth period and is therefore highly robust. Moreover, in principle it can be implemented and tuned without any preceding identification experiments at all.

We have discussed each of the three building blocks of the controller, i.e. the cost function, the gradient estimator and the optimizer, and designed each one such that the sawtooth period is controlled with maximal robustness and acceptable performance. Furthermore, practical tuning guidelines for the controller parameters have been suggested, based on the required separation of time-scales between these subsystems, and several performance improvements have been introduced.

The behaviour of the extremum seeking controller has been assessed in a closed-

loop interconnection with a Kadomtsev-Porcelli sawtooth model. Simulation results demonstrated the tracking of sawtooth period references in different operating regimes. The controller is able to handle step-wise changes in the sawtooth period reference, changes in plasma parameters, additional crash detection delay and disturbances on both the actuator and sensor side. In each case the controller tracks the desired sawtooth period, which demonstrates its high robustness.

ESC does come with a non-zero steady-state error, as the sawtooth period is always oscillating around the reference value. This is partly caused by an external sinusoidal perturbation on the EC mirror angle, which is needed for the online estimation of the gradient of the cost function. Moreover, there is an additional chatter on the mirror angle, introduced by the sliding mode optimizer.

The high robustness against plasma uncertainties and disturbances makes ESC applicable to a wide variety of sawtooth models and real sawtoothing plasmas. ESC is a particularly interesting candidate to control sawteeth on experimental devices, where plasma variations are large and performance requirements are low. Under controlled plasma conditions where closed loop performance (in terms of convergence speed and steady-state error) is more important, such as under reactor-like conditions, high-performance sawtooth control strategies as in [19] are probably more suitable. Finally, the possible applications of the proposed controller are not limited to the sawtooth control problem only; ESC could be an interesting candidate for any problem in or around the tokamak with non-linearities, large model uncertainties or parameter variations.

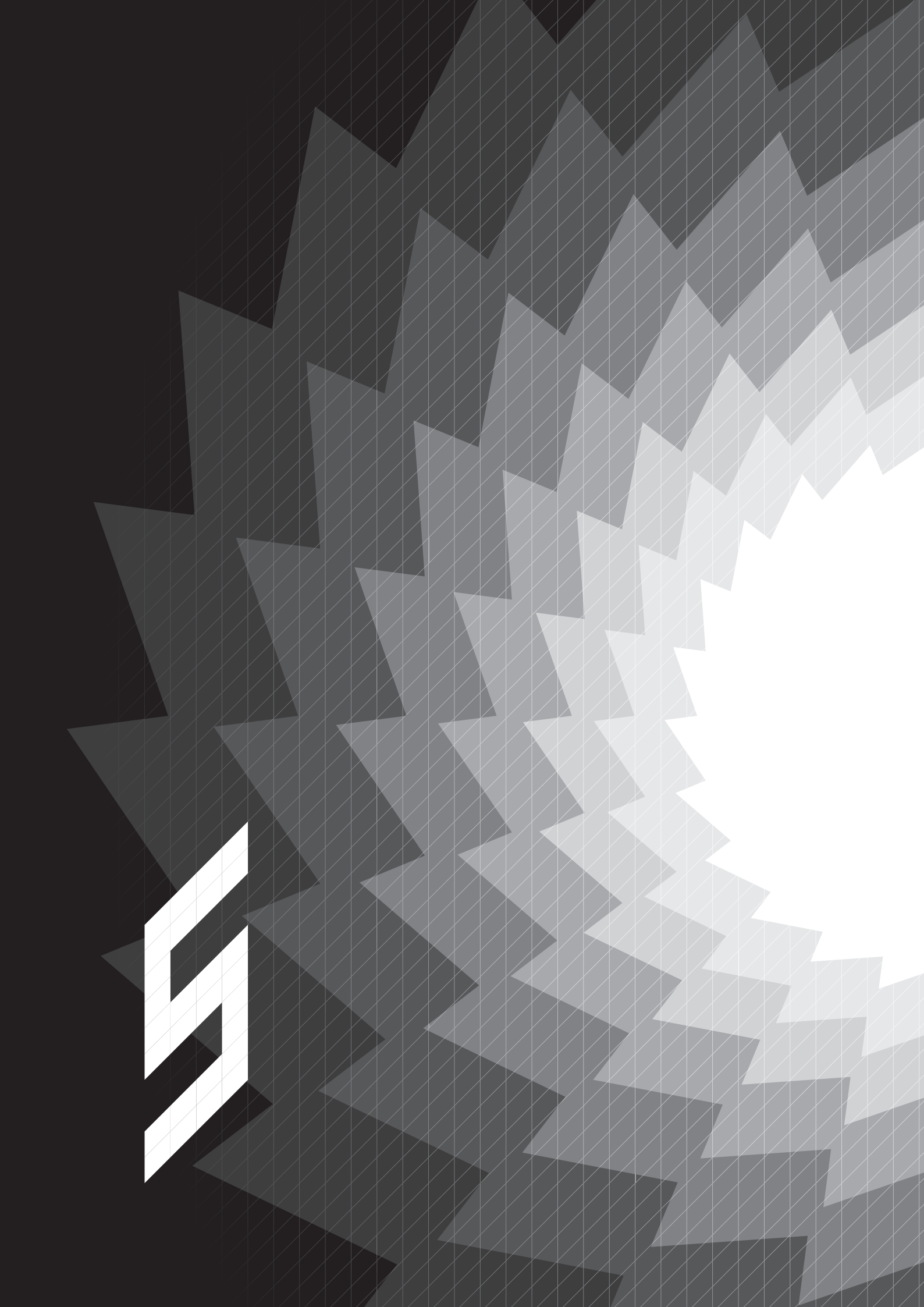
Acknowledgments

The work in this paper has been performed in the framework of the NWO-RFBR Center of Excellence (grant 047.018.002) on Fusion Physics and Technology. This work, supported by the NWO, ITER-NL and the European Communities under the contract of the Association EURATOM/FOM, was carried out within the framework of the European Fusion Programme. The views and opinions expressed herein do not necessarily reflect those of the European Commission.

References

- [1] von Goeler S. *et al.* 1974 *Phys. Rev. Lett.* **33**(20) 1201
- [2] Hastie R.J. 1997 *Astrophys. Space Sci.* **256**(1) 177
- [3] Wesson J.A. and Campbell D.J. 2004 *Tokamaks* 3rd edn. (Oxford: Oxford University Press)
- [4] Nave M.F.F. *et al.* 2003 *Nucl. Fusion* **43**(10) 1204
- [5] Sauter O. *et al.* 2002 *Phys. Rev. Lett.* **88**(10) 105001
- [6] Gude A. *et al.* 2002 *Nucl. Fusion* **42**(7) 833
- [7] Buttery R. *et al.* 2004 *Nucl. Fusion* **44**(5) 678
- [8] Chapman I.T. *et al.* 2010 *Nucl. Fusion* **50**(10) 102001

- [9] Porcelli F. *et al.* 1996 *Plasma Phys. Control. Fusion* **38**(12) 2163
- [10] Chapman I.T. 2011 *Plasma Phys. Control. Fusion* **53**(1) 013001
- [11] Mück A. *et al.* 2005 *Plasma Phys. Control. Fusion* **47**(10) 1633
- [12] Merkulov A. *et al.* 2004 *Proc. of Joint Varenna-Lausanne Int. Workshop on Theory of Fusion Plasmas* (Varenna, Italy) 279
- [13] Angioni C. *et al.* 2003 *Nucl. Fusion* **43**(6) 455
- [14] van Berkel M. *et al.* 2011 *Fusion Eng. Des.* in press
- [15] Paley J.I. *et al.* 2009 *Plasma Phys. Control. Fusion* **51**(5) 055010
- [16] Lennholm M. *et al.* 2009 *Fusion Sci. Technol.* **55**(1) 45
- [17] Lennholm M. *et al.* 2009 *Phys. Rev. Lett.* **102**(11) 115004
- [18] Witvoet G. *et al.* 2011 *Nucl. Fusion* **51**(7) 073024
- [19] Witvoet G. *et al.* 2011 *Accepted for publication in Nucl. Fusion*
- [20] Paley J.I. *et al.* 2009 *Plasma Phys. Control. Fusion* **51**(12) 124041
- [21] Tan Y. *et al.* 2010 *Proc. 29th Chinese Contr. Conf.* (Beijing, China) 14–26
- [22] Krstić M. and Wang H.H. 2000 *Automatica* **36**(4) 595
- [23] Krstić M. 2000 *Syst. Control Lett.* **39**(5) 313
- [24] Nešić D. 2009 *Eur. J. Control* **15**(3-4) 331
- [25] Nešić D. *et al.* 2010 *Proc. 49th Conf. Decis. Contr.* (Atlanta, GA, USA) 4625–4630
- [26] Pan Y. *et al.* 2003 *Int. J. Contr.* **76**(9-10) 968
- [27] Kadomtsev B.B. 1975 *Sov. J. Plasma Phys.* **1**(5) 389
- [28] Neubauer O. *et al.* 2005 *Fusion Sci. Technol.* **47**(2) 76
- [29] Tan Y. *et al.* 2006 *Automatica* **42**(6) 889
- [30] Choi J.Y. *et al.* 2002 *IEEE T. Automat. Contr.* **47**(2) 318
- [31] Tan Y. *et al.* 2008 *Automatica* **44**(5) 1446
- [32] Hennen B.A. *et al.* 2009 *Fusion Eng. Des.* **84**(2-6) 928
- [33] Elong E. *et al.* 2000 *Proc. 2000 Amer. Contr. Conf.* (Chicago, IL, USA) 428–432
- [34] Slotine J.J.E. and Li W. 1991 *Applied nonlinear control* (Englewood Cliffs, NJ: Prentice Hall)



CHAPTER 5

Real-time determination of the sawtooth period using multi-scale wavelet analysis



Abstract

Feedback control techniques for the sawtooth require real-time sensing of the sawtooth period. This data has to be extracted from diagnostic measurements, like electron cyclotron emission (ECE) or soft x-ray signals, via a sawtooth crash recognition algorithm. In this chapter we present a robust, low latency and high fidelity algorithm, which has been optimized for real-time sensing of the crashes. The algorithm is based on time-scale wavelet theory and edge-detection, and implemented in an efficient filterbank. Since the algorithm is based on a multi-scale analysis utilizing different sizes of the wavelets (scales), it enables distinction between different sizes of sawtooth crashes, resulting in an algorithm which is both robust and accurate. This chapter discusses the underlying wavelet theory, offers practical tuning guidelines and applies the algorithm to various types of sawtooth crashes from actual ECE measurements from the TEXTOR tokamak. The results show that the realized accuracy is well below the uncertainty of the crash period for most crashes. Although the presented crash detection method is only demonstrated for ECE measured TEXTOR sawteeth, it can in principle be applied to any periodic crash or phenomenon, existing in time-series data from any diagnostic measurement.

This chapter is based on the publication:
M. van Berkel, G. Witvoet, M.R. de Baar *et al.* 2011 *Fusion Engineering and Design*,
[doi:10.1016/j.fusengdes.2011.07.002](https://doi.org/10.1016/j.fusengdes.2011.07.002)

5.1 Introduction

Open-loop control of the sawtooth period has a long history, see [1] and references therein. Various sawtooth actuators have been experimentally identified and explored to either lengthen or shorten the sawtooth period [2]. These include neutral beam injection (NBI), ion cyclotron resonance heating (ICRH) and electron cyclotron current drive (ECCD), where the latter two are also envisaged to be used for sawtooth control on ITER.

Inclusion of the ECCD actuator in a feedback loop for the sawtooth period has been demonstrated on Tore Supra [3, 4] and TCV [5–7]. Structured system analyses and subsequent systematic controller designs utilizing this actuator have been derived in chapter 2, 3 and 4. Such closed-loop approaches to control the sawtooth period enable us to establish *a priori* stability bounds and to make sensible trade-offs between performance and robustness, as has been shown in these chapters. Hence, closed-loop control is highly desirable, as it can make the sawtooth period robust against large disturbances or plasma variations, and can increase the accuracy and convergence speed with which a desired period can be tracked.

Any feedback loop requires real-time sensing of the variable-to-be-controlled, which is in this case the sawtooth period. The period cannot be measured directly, but has to be extracted from available diagnostic signals, like temperature measurements from electron cyclotron emission (ECE) or soft x-ray channels, by means of a real-time detection algorithm. During a typical sawtooth cycle the profiles of current density and pressure evolve to a magneto-hydrodynamic unstable state, which is relaxed in a crash-like event. The cycles therefore feature a slow and a fast time-scale, where the slow time-scale is associated with the redistribution of the current and the replenishing of the stored energy, visible as a slow ramp of the plasma temperature. During the crash, i.e. the fast time-scale, the profiles of pressure and current density are reset, yielding a sudden collapse of the temperature, after which the cycle restarts. This crash is the typical signature of the sawtooth cycle; most sawtooth period determination algorithms are based on the detection of these crashes.

Various real-time period determination methods are reported in the papers on closed-loop sawtooth control. In [3] methods based on simple difference filter operations on ECE measurements are proposed. Although real-time applicable, this method lacks robustness, and fails in noisy signal environments. The noise-sensitivity can be improved by applying a band-pass filter such that part of the noise is suppressed [6], but this reduces the accuracy and generally introduces significant signal delays, which are detrimental for the performance of any control-loop [8]. Furthermore, various types of time–frequency methods based on Fourier analysis have been used, such as the Short Time Fourier Transform (STFT) [9], the Morlet Wavelet [10, 11] and instantaneous frequency methods [12, 13]. Although these time–frequency methods work well for off-line analysis, they study the global frequency behaviour of the sawtooth cycles, i.e. the period is generally inferred from a number of crashes. Consequently, the estimate

is averaged (i.e. not instantaneous) and in real-time delayed by a number of crashes, which can significantly reduce the performance of any control algorithm. In addition these methods are computational intensive.

The detrimental effect of the latency of the sawtooth period detection on the closed loop has been addressed in chapter 2. Moreover, a sawtooth period sensor needs to be reliable, since a missed or falsely detected crash can introduce large disturbances in the feedback loop. This motivates the development of an algorithm for high-fidelity, low latency identification of the sawtooth period. In this chapter we present a method to obtain such an algorithm based on the following requirements: (1) details in the shape of the signals should not affect the outcome of the method, i.e. the method should be able to deal with, e.g. pre-cursors and post-cursors; (2) the delay should be minimal and be within one or two periods; (3) the algorithm should be robust against noise, and applicable to various types of diagnostics; and (4) the period estimation should be accurate. The algorithm will be tested on experimental data from the six channel radiometer used in the in-line ECE-system in TEXTOR [14].

The proposed method is based on time-scale analysis generated by a B-spline wavelet [15]. This analysis is localized in time, so that the periodic behaviour of the sawtooth can be determined robustly, accurately and with less delay than currently used methods. The repetition rate is inferred from two subsequent crashes, instead of a large number of crashes, such that each individual period can be identified. The power of the method lies in the fact that it is a multi-scale analysis, i.e. it makes a coupling between the various scales (which are a measure of frequency) of the analysis. This will ensure that the location of the crash can be determined more accurately. In addition, these numerous scales will introduce robustness, without introducing extra delay. Furthermore, the algorithm has been implemented in real-time by means of an efficient filter bank algorithm.

This chapter will start with a description of the used methodology in section 5.2, where the basics of wavelet theory, together with the efficient implementation through filter banks, are explained. In section 5.3, the principles of the designed real-time algorithm are explained, where a special emphasis is put on the choice of the threshold. The results from the application of the algorithm to specific ECE measurements from TEXTOR are presented in section 5.4. Finally, in section 5.5 a summary and conclusions are presented.

5.2 Methodology

The core of our proposed algorithm is a multi-scale wavelet analysis of the available data, introduced in section 5.2.1 and 5.2.2. This is a vital tool to combine both robustness and accuracy into a single algorithm design for the detection of sawtooth crashes. A classic approach is the edge-detector given by Canny [16], discussed in section 5.2.3. In section 5.2.4 this edge-detector is adopted into the family of discrete wavelets such that it can be implemented in a real-time filter bank algorithm.

5.2.1 Multi-scale analysis

Current real-time algorithms for sawtooth period detection are comprised of a low-pass filter to reduce the noise, and a difference filter to estimate the derivative over time. The resulting band-pass filter yields large responses around sawtooth crashes; a threshold based algorithm can then approximate the time instant of the crash. However, sawtooth crashes can have significantly varying amplitudes, time-scales, pre-cursors and noise levels, which makes it impossible to detect each individual crash robustly with a single band-pass filter. In addition, whenever a good robustness is needed, the order of the band-pass filter (i.e. the time window over which it acts) generally has to be large, leading to a relatively large time delay.

A band-pass filter operation on a signal $y(t)$ is essentially a convolution of a certain fixed function $\psi(t)$ with this signal in the time domain, and can therefore be interpreted as a one-scale analysis. If a wide function $\psi(t)$ is chosen, the amplitude of the filtered response on a crash becomes large and thus easily detectable, but the localization of the crash in time becomes rather inaccurate. On the other hand, a narrow $\psi(t)$ yields a good localization but has a much smaller response. Hence, a one-scale analysis is subject to a natural uncertainty principle [16, 17], making it impossible to optimize between robustness and accuracy simultaneously using a single band-pass filter.

The solution is to use a multi-scale analysis, which can simultaneously achieve small delay, good accuracy and large robustness. In essence such an analysis incorporates different functions $\psi(t)$ (wavelets) simultaneously, combining wavelets with well localized responses and small delays (high accuracy) with wavelets with large responses on sawtooth crashes (large robustness). Such a multi-scale analysis is attained by the wavelet framework, a well structured signal processing technique which allows a very efficient implementation such that it can be used in real-time. The choice of wavelet typically depends on the specific signal and application; in this chapter the wavelet is specifically based on the ECE signal properties from TEXTOR.

5.2.2 Wavelets

Wavelets constitute a broad family of mathematical functions [17–19], which can be used for the analysis, denoising and compression of signals. Similar to the Fourier transform, which expresses the signal in terms of harmonic functions, a wavelet transform expresses the signal in terms of wavelets. Additionally, wavelets are localized in time, i.e. they are zero outside a certain time-interval (or support width), which allows for the analysis of non-stationary signal behaviour.

A wavelet $\psi(t)$ needs to fulfil a so-called weak admissibility condition [20]. In practice this condition implies that $\psi(t)$ has a zero average, i.e.

$$\int_{-\infty}^{+\infty} \psi(t) dt = 0. \quad (5.1)$$

The multi-scale analysis of a transform $W\{\cdot\}$ is formalized in the Continuous Wavelet Transform (CWT), where a signal $f(t)$ is convolved with different dilations $s \in \mathbb{R}^+$ and

translations $\tau \in \mathbb{R}$ of the same (mother) wavelet $\psi(t)$ [17], i.e.

$$F(\tau, s) = W \{f(t)\} = \langle f, \psi_{\tau, s} \rangle = \int_{-\infty}^{+\infty} f(t) \frac{1}{\sqrt{s}} \psi \left(\frac{t - \tau}{s} \right) dt. \quad (5.2)$$

The factor $s^{-1/2}$ ensures that $\|\psi_{\tau, s}\|_2 = 1$, and thus allows a comparison between the coefficients F at different dilations s . The convolution in (5.2) expresses the amount of overlap between the signal $f(t)$ and $\psi_{\tau, s}$ as the wavelet is dilated (stretched) with s and translated (shifted) with τ over the signal. In other words, if $f(t)$ and $\psi_{\tau, s}$ are alike, the resulting wavelet coefficients $F(\tau, s)$ are large.

The CWT of a signal $f(t)$ yields a two-dimensional function $F(\tau, s)$, which allows for an analysis of the localization τ over multiple dilations or scales s . These scales are closely related to the frequency content of the signal: wavelet coefficients of scales $s \approx 1$ (small time-window) mainly describe the high-frequent behaviour, i.e. the fine and local properties of the signal. The more coarse and low-frequent properties of the signal are described by the wavelet coefficients of larger scales $s \gg 1$ (large time-window). Hence, in contrast to the STFT, the resulting flexible time–frequency (or time–scale) window of wavelet transforms allows for the simultaneous analysis of high and low-frequent content [21]. Wavelets have a good localization in both time and frequency [22], although this is still bounded by the Heisenberg uncertainty principle [17], as is the case for the Fourier transform and the STFT. The success of a wavelet transform, in terms of the detection of features and recognition of patterns inside a signal, depends on the chosen wavelet [18, 19].

5.2.3 Canny edge-detection

A well known wavelet example is the Morlet wavelet. Within the fusion community it has been used to analyse, e.g. neoclassical tearing modes (NTMs) [23], edge localized modes (ELMs) [24–26] and sawteeth [10, 11]. The Morlet wavelet is proven to be good at detecting periodic behaviour over a longer time frame (i.e. over many crashes), because it is based on harmonic analysis. However, in this chapter we wish to detect each sawtooth crash individually. This requires recognition of specific features in the signal and thus implies the use of a different wavelet.

The choice of wavelet should be based on the properties of the considered signal. Here we wish to distinguish steep sawtooth crashes from the (often significant) noise in the ECE signals. Hence, the measurements $x[n]$ consist of the deterministic unscaled temperature inside the tokamak $u[n]$ and an additive noise part $v[n]$, i.e.

$$x[n] = u[n] + v[n]. \quad (5.3)$$

Here we assume that $v[n]$ is zero-mean Gaussian white noise with variance σ^2 . From the literature it is known that in ECE measurements the dominating noise is the so-called ‘thermal’ noise, which is indeed white and Gaussian [27]. This thermal noise dominates over all the other noise sources caused by the ECE diagnostic [28]. This

has also been experimentally verified, justifying the assumption that $v[n]$ is zero-mean Gaussian white noise.

Consequently, detection of sawtooth crashes in ECE signals is very similar to the detection of step-edges in signals flooded by white Gaussian noise. For this application Canny [16] has derived the optimal edge-detector, based on three criteria. These criteria are related to: (1) the Signal-to-Noise-Ratio (SNR), which determines how well the deterministic part can be distinguished from the noise; (2) the localization, which determines how well the position of the edge can be detected; and (3) the elimination of multiple responses on a single edge, such that an edge gives a local unique maximum at the position of the edge. These conflicting criteria (due to the Heisenberg uncertainty principle) were used by Canny in a numerical optimization process, which resulted in the first derivative of a Gaussian as the most suitable function (or wavelet) [16]. This function will therefore be used as the wavelet in our analysis, which allows detection of individual crashes and thus fast and accurate determination of the most recent sawtooth period.

Figure 5.1 shows the wavelet coefficients $F(\tau, s)$ of the CWT in (5.2) for two different ECE channels, using the first derivative of a Gaussian as the wavelet $\psi(t)$. This multiresolution analysis (a special case of multi-scale analysis [19]) reveals the sawtooth crashes as vertical dark ‘lines’, both for the clearly sawtoothed channel 3 (top) as for the noise-dominated channel 2 (bottom). These vertical detection ‘lines’ are wide for large dilations s and become narrower as the dilation of the wavelet decreases. For small s the wavelet is well localized, but also sensitive to the noise, yielding small coefficients due to the small SNR. A large dilation ($s \gg 1$) only shows a large response around large edges (i.e. crashes), but is much less localized, making it difficult to determine the exact location of the crash. The key result is that when a crash is detected for a large s , where it is clearly distinguishable, the maxima of the wavelet coefficients can be traced towards the lower scales, where the good localization of the maxima can be utilized to find the exact position of the crash. Hence, sawtooth crashes can be both well distinguished and well localized using this maxima chain [30] in the multiresolution framework.

5.2.4 Efficient implementation

The above described wavelet transform needs to be applied in a real-time detection algorithm, which requires an efficient implementation of the CWT. The calculation effort can significantly be reduced by choosing a dyadic dilation grid ($s = 2^m$). Still, this discrete implementation of the CWT requires $\mathcal{O}(N(\log_2(N))^2)$ operations, with N the total number of samples [17], which is still not very efficient. Therefore we suggest a Discrete Wavelet Transform (DWT), which is the discrete counterpart of the CWT. This DWT can be implemented very efficiently in a filter bank algorithm, depicted in figure 5.2, which has a computational effort of $\mathcal{O}(N \log_2(N))$ operations [17]. The suggested filter bank in figure 5.2 is slightly different from classic filter bank theory [17,21], but is equivalent to the method described in [30].

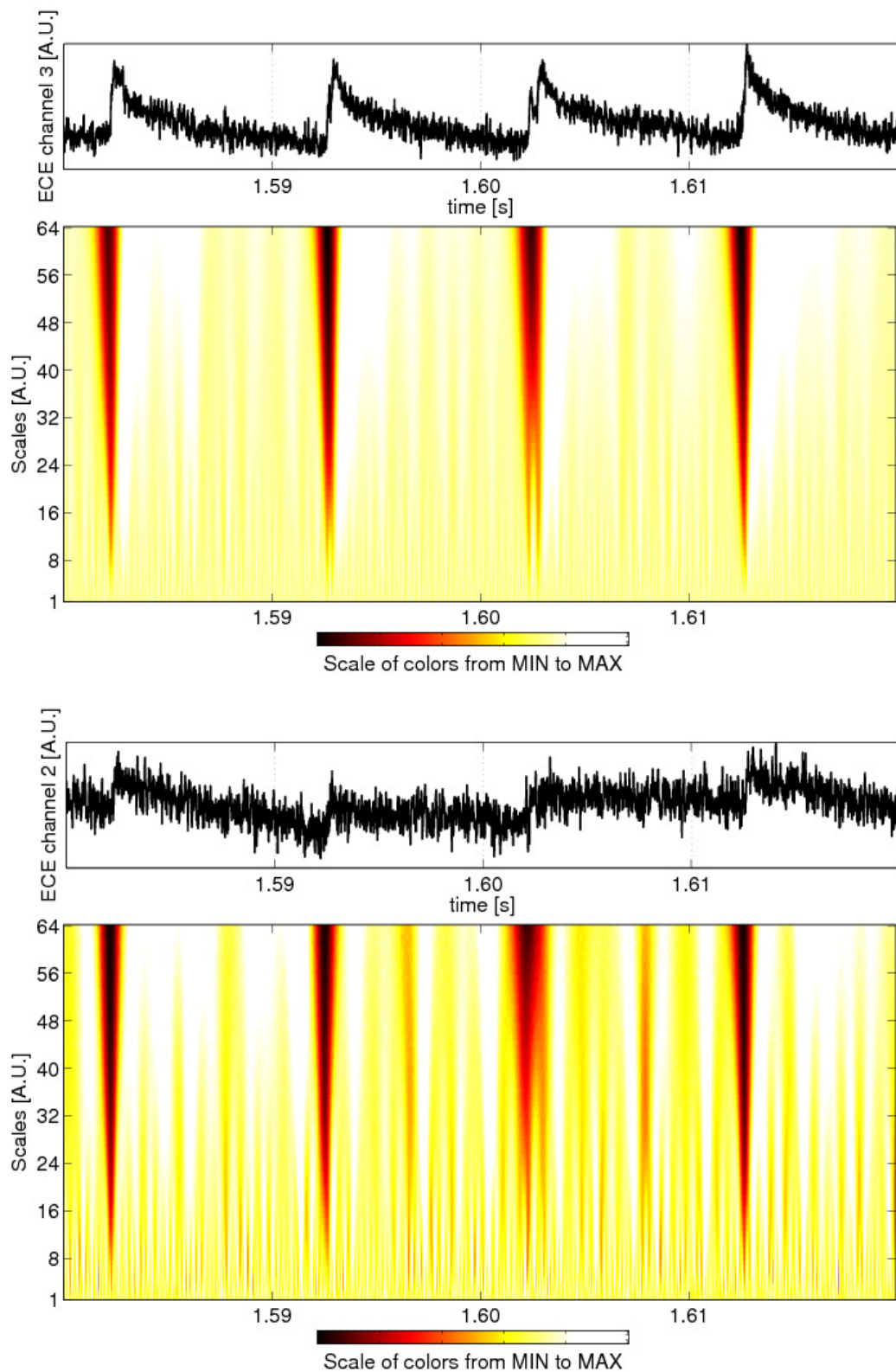


Figure 5.1: ECE line-of-sight receiver data of channel 3 (138.5 GHz) and channel 2 (135.5 GHz) of TEXTOR discharge no. 106482 measured around 1.6 s, and their CWT using the first derivative of the Gaussian, as defined in [29], for scales $s = 1$ to $s = 64$.

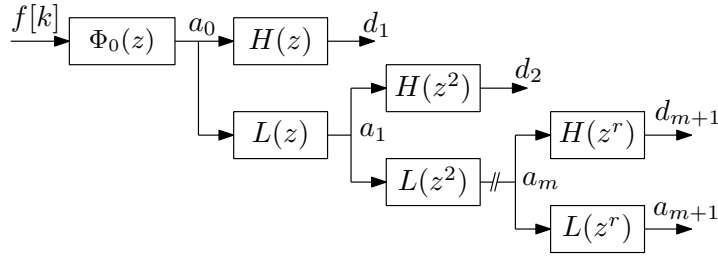


Figure 5.2: Dyadic filter bank to calculate the wavelet coefficients d_r , where $\Phi_0(z^{-1})$ is the initialization filter, $L(z^r)$ are the scaling filters and $H(z^r)$ are the wavelet filters, with $r = 2^{m-1}$.

A filter bank algorithm is based on two functions: the wavelet $\psi(t)$ and the scaling function $\phi(t)$. This scaling function $\phi(t)$ is not a wavelet since it does not satisfy the weak admissibility condition (5.1), i.e. $\int_{-\infty}^{+\infty} \phi(t) dt = 1$. The scaling function (father wavelet) transform and (mother) wavelet transform are defined as [31]:

$$a_m[n] = \langle f, \phi_{m,n} \rangle = \int_{-\infty}^{+\infty} f(t) 2^{-m/2} \phi(2^{-m}t - n) dt, \quad (5.4a)$$

$$d_m[n] = \langle f, \psi_{m,n} \rangle = \int_{-\infty}^{+\infty} f(t) 2^{-m/2} \psi(2^{-m}t - n) dt, \quad (5.4b)$$

with $m \in \mathbb{Z}$ the dilation parameter and $n \in \mathbb{Z}$ the translation parameter. The so-called approximation coefficients $a_m[n]$ and wavelet coefficients $d_m[n]$ are the result of a convolution between the signal $f(t)$ and the scaling function $\phi(t)$ or wavelet $\psi(t)$, respectively. In the DWT framework the scaling function and wavelet should fulfil two properties: (1) $\phi(t/2)$ can be written as a summation of different translations of $\phi(t)$, the so-called two-scale relationship, and (2) $\psi(t/2)$ can be written as a summation of different translations of $\phi(t)$ [17]. The first derivative of a Gaussian, chosen in the previous section, does not have a scaling function that fulfils these properties. Therefore an approximation of a Gaussian is made by means of a B-spline, which yields a scaling function $\phi(t)$ that does fit inside the filter bank framework [32]:

$$\phi(t) = \beta_p(t) = \frac{1}{p!} \sum_{q=0}^{p+1} \binom{p+1}{q} (-1)^q \left(t - q + \frac{p+1}{2} \right)_+^p. \quad (5.5)$$

This B-spline $\beta_p(t)$ is constructed by repeated convolutions of the box function, where

$$(t - \lambda)_+^p := \begin{cases} (t - \lambda)^p & \text{if } t \geq \lambda, \\ 0 & \text{if } t < \lambda. \end{cases} \quad (5.6)$$

The normalized version of (5.5) indeed converges with increasing order p to a Gaussian (for odd p). The two-scale relation for the B-spline is

$$\frac{1}{\sqrt{2}} \beta_p \left(\frac{t}{2} \right) = \sum_{n=-\infty}^{+\infty} l_p[n] \beta_p(t - n), \quad (5.7)$$

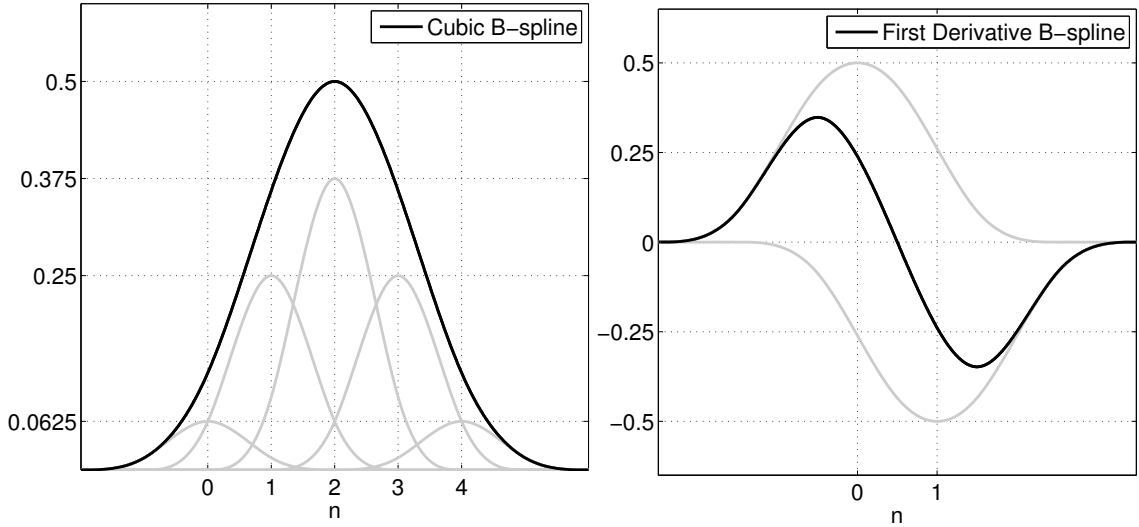


Figure 5.3: Cubic B-spline (left) and its first derivative (right), where the grey lines present the compressed B-splines used in (5.7) and (5.9).

which thus expresses the approximation coefficients of a coarse scale in terms of fine scales. Hence $l_p[n]$ defines a low-pass filter in the discrete-time \mathcal{Z} -domain (i.e. $X(z) = \sum_{n=-\infty}^{\infty} x[n]z^{-n}$), which can be used in the filter bank of figure 5.2:

$$L_p(z) = \frac{\sqrt{2}}{2^p} (1 + z^{-n})^{p+1}. \quad (5.8)$$

The order p is a design parameter; larger p give better approximations, but also larger filters $L_p(z)$ and a less accurate crash localization. For the considered ECE signals we choose a cubic B-spline ($p = 3$), which yields an approximation error less than 3% compared to a Gaussian. This choice is partly based on the high sample rate of the used ECE diagnostic (100 kHz); the crash then covers multiple samples, which allows for the use of relatively large filters at the smaller scales. When this is not the case, as for instance in soft x-ray measurements on TEXTOR (10 kHz) or Tore Supra ECE measurements [3] (1 kHz), the order p needs to be decreased, in these cases to $p = 1$ and $p = 0$. This adaptation is completely in line with the theory described in [16].

The desired wavelet, i.e. the first derivative of a Gaussian, can now be approximated by the difference of two shifted B-splines, which is the same as the derivative of a B-spline of order $p + 1$ [32]. Hence

$$\psi(t) = \frac{d\beta_{p+1}(t)}{dt} = \beta_p(t) - \beta_p(t - 1). \quad (5.9)$$

Consequently, the wavelet coefficients can be expressed in terms of the approximation coefficients, using $h[n] = [\frac{1}{2}, -\frac{1}{2}]$ and

$$\psi\left(\frac{t}{2}\right) = \sum_{n=0}^1 h[n] \beta_p(t - n), \quad (5.10)$$

which defines the high-pass filter $H(z)$ that is used in figure 5.2 (where an additional normalization factor $1/\sqrt{2}$ is used). Both (5.7) and (5.9), with the corresponding scaling and wavelet function, are represented graphically in figure 5.3.

The two-scale relationship (5.7) computes the approximation coefficients from scale m to scale $m + 1$. The coefficients a_0 belonging to the finest scale $m = 0$ can be approximated by the discretized version of (5.4a)

$$a_0[n] = \langle f, \phi_{0,n} \rangle \approx \sum_{k=-\infty}^{\infty} f[k] \phi_0[k - n], \quad (5.11)$$

where ϕ_0 defines a pre-filter operation $\Phi_0(z)$ on the samples of the measured signal $f[k]$, see figure 5.2. The number of samples encompassed by $\Phi_0(z)$ should generally be larger than the order p , so as to filter some noise and thereby get useful maxima even in the first scale. Therefore the B-spline (5.5) needs to be interpolated, yielding a symmetric filter $\Phi(z^{-1}) = \Phi(z)$. Alternatively, one could choose to use the sample points $f[k]$ as expansion coefficients $a_0[n]$, but then it will take multiple scales (and filter operations $L(z)$) to obtain the first useful maxima for detection.

The great advantage of the filter bank is that the wavelet coefficients are calculated by a cascade of filters, thereby significantly reducing the computational effort. The filter bank used in this chapter differs from a common filter bank, as it does not use downsampling; this yields a so-called *à trous algorithm* or Stationary Wavelet Transform (SWT) shown in figure 5.2. The SWT calculates the same wavelet coefficients as the standard filter bank, but also computes intermediate wavelet coefficients. This has a number of advantages: (1) in a real-time detection algorithm downsampling can induce extra delay (especially for $m \gg 1$), because the sample rate decreases with increasing scale m , which is thus prevented in a SWT; (2) it is time-invariant; (3) all signal information is retained. The only disadvantage is that the SWT is computationally less efficient, but still of $\mathcal{O}(N \log_2(N))$ [31], which is still much more efficient than the CWT, and easily applicable on current-day computers.

In a standard filter bank with downsampling every step in scale m comprises of the same filters $L(z)$ and $H(z)$, in agreement with the two-scale relations (5.7) and (5.9). When downsampling is removed, the filter coefficients should only operate on every 2^{m-1} th sample. Consequently, the filters need to be adapted to the scale m , yielding $L(z^r)$ and $H(z^r)$ with $r = 2^{m-1}$. In conclusion, the used SWT filter bank is completely defined by the pre-filter $\Phi_0(z)$ from (5.11), the low-pass filters $L(z^r)$ and the high-pass filters $H(z^r)$, all shown in figure 5.2.

A proper wavelet transform allows the analysed signal (i.e. the expansion coefficients a_0) to be reconstructed, since this implies that all signal information is retained during the decomposition into wavelet coefficients. A filter bank should fulfil two conditions to guarantee reconstruction, namely the anti-aliasing condition and the perfect reconstruction condition [22]. The former is irrelevant, since downsampling (which causes aliasing) is not used in our method. The perfect reconstruction can be derived from the illustration in figure 5.4; if we assume the low-pass reconstruction filter is identical

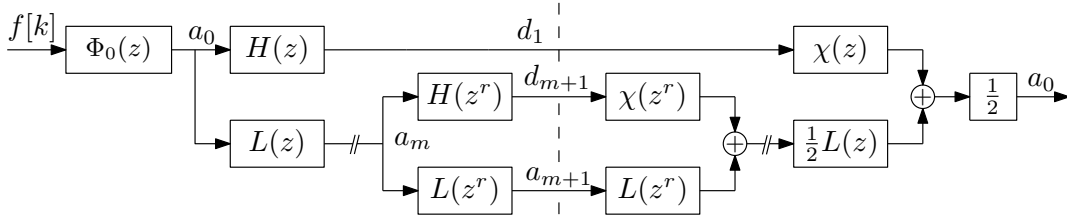


Figure 5.4: The complete dyadic filter bank showing the decomposition and reconstruction branches such that the expansion coefficients of the first scale a_0 can be reconstructed.

Table 5.1: Filter coefficients that generate the accompanying functions of the cubic B-spline.

n	$\Phi_0(z)/2$	$L(z)/\sqrt{2}$	$L(z^2)/\sqrt{2}$	$H(z)/\sqrt{2}$	$\Lambda(z)/\sqrt{2}$
0	0.0029	0.0625	0.0625	-0.5	0.0078
1	0.0234	0.2500	0	0.5	0.0703
2	0.0786	0.3750	0.2500		0.2109
3	0.1637	0.2500	0		0.7266
4	0.2314	0.0625	0.3750		-0.7266
5	0.2314		0		-0.2109
6	0.1637		0.2500		-0.0703
7	0.0786		0		-0.0078
8	0.0234		0.0625		
9	0.0029				

to the decomposition filter $L(z)$, this reads

$$L(z^r) L(z^r) + H(z^r) \Lambda(z^r) = 2z^{-l} \quad \text{with } l \in \mathbb{Z}. \quad (5.12)$$

Using the definitions of $L(z)$ and $H(z)$ the high-pass reconstruction filter $\Lambda(z)$ can then be derived for an arbitrary B-spline scaling function of order p [17], i.e.

$$\Lambda(z) = \frac{\sqrt{2}}{8} (-1 + z^{-1}) \sum_{n=0}^p (1 + 2z^{-1} + z^{-2})^n. \quad (5.13)$$

The reconstruction filters will not be used in this chapter, but their existence proofs that the filters $L(z)$ and $H(z)$ do not cause any loss of information. For completeness we remark that it is not possible to reconstruct the original signal $f[k]$ from the expansion coefficients a_0 . However, this is generally acceptable, since the pre-filter is chosen such that only high-frequent noise is lost during this filter operation.

The filters $L(z)$, $H(z)$, $\Phi(z)$ and $\Lambda(z)$ derived in this section completely describe the proposed wavelet transformation. All their numeric values are summarized in table 5.1. The largest scale used in this paper is $m = 9$, but it can be increased up to the point where the wavelet encompasses two sawtooth periods.

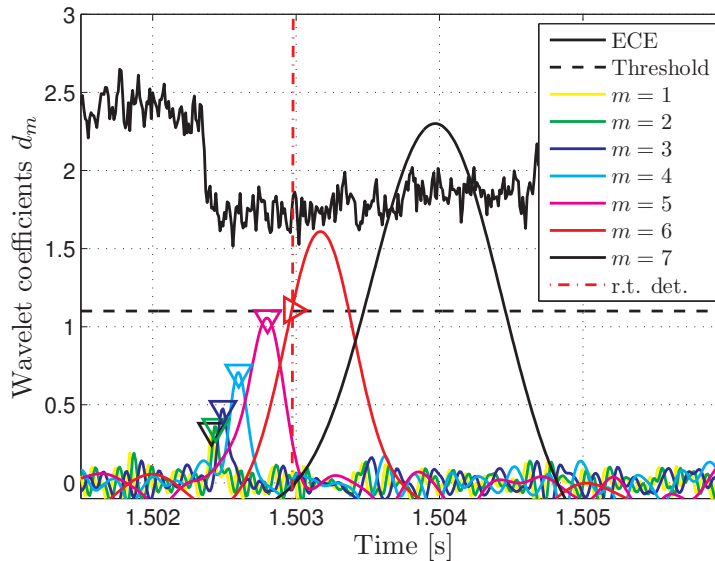


Figure 5.5: Real-time responses of the wavelet coefficients, from $m = 1$ (yellow) to $m = 7$ (black), on a sawtooth crash on ECE channel 1 (132.5 GHz) of discharge no. 106482. The red-coloured marker \triangleright is the point of detection (using a robust threshold, indicated by the horizontal dashed line), the other markers ∇ present the traced maxima, where the last one (black) shows the identified moment of the crash. The vertical dash-dot line shows when this crash has been detected in real-time (r.t. det.).

5.3 Real-time implementation

In this section a real-time algorithm is developed based on the wavelet transform introduced in the previous section. This consists of three parts: (1) development of a threshold for the crash-detection; (2) derivation of a maxima chain such that the period can be determined robustly and accurately; and (3) combining multiple channels in a single period estimation to increase reliability.

5.3.1 Crash detection

The real-time response of the designed filter bank to a specific measured sawtooth crash is depicted in figure 5.5. As predicted in section 5.2.1, this figure shows that the maxima of the wavelet coefficients for small dilations m are quite small and close to the noise level. The wavelet coefficients for higher scales m are much larger, but also introduce more delay, since their time-window (or the number of samples employed by their filters) is much larger. A sawtooth crash is detected whenever one of the wavelet coefficients exceeds a certain threshold value. As can be concluded from figure 5.5, a tight threshold is sensitive to the noise in the signal and can yield false crash detections, whereas a large threshold increases the delay of the detection.

The threshold should at least be chosen large enough to prevent detections on peaks of the wavelet coefficients that are actually a result of signal noise. As explained in section 5.2.3, the noise $v[n]$ entering the filter bank is of Gaussian nature, which implies

that the wavelet coefficients resulting from this noise are also Gaussian distributed. For such situations we can define a risk of detecting a false crash due to noise [33], and state that there is a very high probability that the noise remains just below a certain lower-bound on the threshold T_{\min} [17], defined as

$$T_{\min} = \sigma \sqrt{2 \log_e N}, \quad (5.14)$$

where σ^2 is the variance of the noise on the ECE signal, and N is the total amount of sample points in this signal. Note that T_{\min} increases with N , which reflects that the chance of taking points from the tail of the Gaussian distribution increases as the number of points increase.

In practice, the true variance of the noise in (5.14) is unknown. However, we can define an upper-bound on the variance of the noise present in each wavelet coefficient d_m using the 2-norm (or energy norm) of the scales. Every branch of the filter bank can be represented by an equivalent filter $W_m[n]$, where $\|W_m[n]\|_2 = 1$, i.e. the amount of signal energy in every branch is preserved. Moreover, we know that $\|v[n]\|_2 = \sigma^2$. Using the Cauchy–Schwarz inequality we then obtain

$$|\langle W_m, \mathcal{N} \rangle| \leq \|W_m[n]\|_2 \cdot \|v[n]\|_2 = \sigma^2, \quad (5.15)$$

where \mathcal{N} denotes the normal distribution with variance σ^2 responsible for the noise on the ECE signals. Hence, according to (5.15) there is no need for additional calculations to separate the noise from the ECE signal; instead the variance can be estimated based on the output of the first scale d_1 , which mainly consists of noise. However, since (5.15) only provides a lower-bound for the true variance σ^2 , the threshold should be chosen somewhat larger than T_{\min} in (5.14).

Apart from the noise, there can be other phenomena influencing the ECE measurements (like pre-cursors, changes in plasma temperature or density, or the presence of other instabilities), which thereby affect the wavelet coefficients d_m . In practice, the threshold should therefore be increased by a certain factor to improve the robustness of the detection. Here we use a threshold which is a factor 3 larger than T_{\min} , based on the analysis of a few experimental measurement sets. Figure 5.5 clearly shows that this threshold yields a significant margin above the noise level (≈ 0.2) and still allows detection of the crashes on the higher scales. Note that the threshold is adaptive in our algorithm, since the variance σ^2 on which it is based is estimated online.

5.3.2 Period determination

Sawtooth crashes can be detected robustly with our multi-scale analysis, but to assure a precise measurement of the period the location of the crash needs to be determined accurately as well. As discussed in section 5.2.2, this can be done by means of a maxima chain, where the maxima of the wavelet coefficients d_m , which indicate the middle of the crash, are traced from the higher to the lower scales. The maxima \bar{d}_m of the scales are found by a simple maximum detector, $d_m[i-1] < \bar{d}_m[i] > d_m[i+1]$, which are stored in a buffer with the size of the wavelet with the biggest dilation.

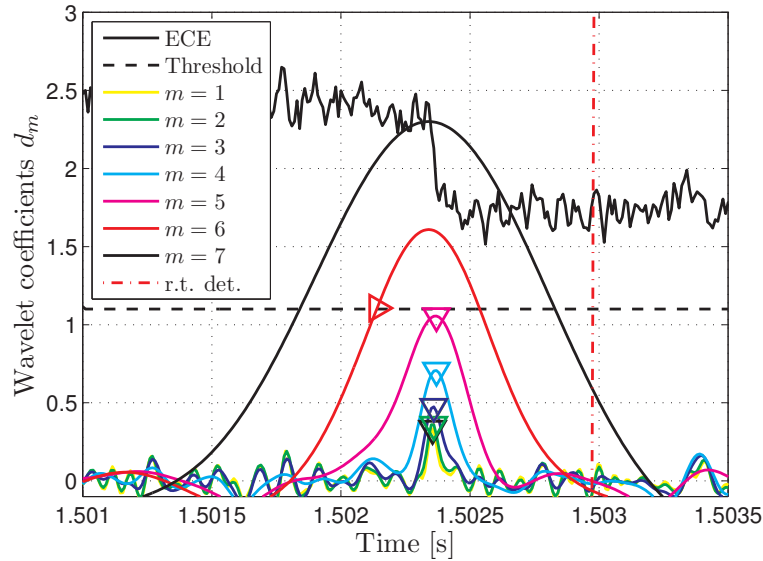


Figure 5.6: Non-causal response of the wavelet coefficients on the same sawtooth crash as shown in figure 5.5, where the maxima of the different scales are now aligned, allowing a good localization of the crash. The time instant of detection is represented by the dash-dot line (r.t. det), which corresponds to the point indicated by \triangleright on the non-causal scale $m = 6$.

Crashes are normally detected in the higher scales $m > 1$. Since the wavelet coefficients d_m at this scale are more delayed than d_{m-1} , we can detect a sawtooth crash at scale m , select the maximum at scale $m - 1$ (which belongs to the same crash) and then trace the stored maxima in the buffer back towards the smallest scale. To this end the wavelet responses need to be compensated for their delay (shifted back over time) to align the maxima for proper tracing. This delay is *a priori* known, since the product of all filters in one branch of the filter bank, which describe the wavelet, are anti-symmetric (linear-phase) FIR-filters. Consequently, the delay for every scale m is the length of the wavelet filter divided by two. The resulting non-causal responses of the wavelet coefficients are shown in figure 5.6, which demonstrates the precise localization of the crash by the smallest scale, in this case $m = 1$. The difference between the time instants of the last two consecutive crashes defines the sawtooth period.

It is not always possible to trace the maxima chain all the way to scale $m = 1$, as this scale is quite sensitive to noise. This can lead to more than one or no maxima in the vicinity of the crash for this scale, making an exact localization impossible. The maxima chain therefore stops at the smallest scale whose maximum can directly be traced back to the crash, which could be a scale $m > 1$.

The delay of the methods depends on when the crash is detected, i.e. which scale exceeds the threshold. Clear crashes in the ECE measurements have a very small delay (near 0.13 ms), whereas indistinct crashes have more delay (around 1.63 ms), with rare outliers to 6.43 ms for hard-to-distinguish crashes. For each ECE measurement the algorithm has been tested on, the delay is less than the sawtooth period. This is quite

acceptable for use in a feedback loop [8].

The advantage of the proposed maxima chain is that it combines robustness and accuracy: it returns an accurate period determination (on a small scale) as soon as a crash has been detected (on a robust larger scale). The obtained accuracy is independent of the detection scale and is generally in the order of a few samples (less than 0.1 ms). Moreover, since the chosen B-spline wavelet approximates the ideal edge detector [16], there is a clear theoretical basis to claim that the proposed wavelet algorithm will outperform any one-scale band-pass algorithm [3, 6].

5.3.3 Combining channels

The line-of-sight ECE-system of TEXTOR consists of six channels. Hence, it is possible to improve the wavelet algorithm by a smart combination of the different channels. However, not all channels are suitable: those near the inversion radius are often noisy and hardly display any crashes. Moreover, channel 6 (147.5 GHz) was malfunctioning during the selected TEXTOR shots, being prone to non-linearity and cross-talk [14].

The wavelet transform is applied in parallel to the remaining channels 1 to 5. By comparing these channels mutually false crashes, if any, can be suppressed, since a false crash normally only occurs on a single channel. To this end an evaluation block has been designed, which observes the crash time instants in real-time, and only if a crash has been detected by sufficient channels (here 2) near the same time instant, the mean over these instants is returned as the moment of the crash. If only one channel detects a (probably false) crash during some time interval, the detection is ignored and the specific channel is reset. Moreover, the threshold is disabled for some small amount of time after a detected crash, e.g. to prevent detection of post-cursors.

For each channel the large responses at a crash of the wavelet coefficients d_m on a scale $m \gg 1$ are related to the amplitude and the sign of the sawtooth crash. This also holds for a channel near the inversion radius, where the wavelet coefficients are too small to trigger a threshold, but still yield a distinguishable response on top of the noise level. The sign and amplitude of the wavelet coefficients on the different channels at a crash can be used to estimate the location of the inversion radius, i.e. by finding the zero-crossing of a function fitted through these coefficients.

5.4 Results

The sawteeth shown in the ECE measurements in figure 5.5 and 5.6 are quite basic. Our wavelet detection algorithm can handle these sawteeth with ease, even though the noise in the ECE signals is quite large. In this section we will show the performance of the algorithm on a variety of sawtooth crashes that are much harder to detect. To this end the algorithm has been implemented in the Matlab[®] Simulink[®] real-time testing environment. The used ECE data stems from channel 1 (132.5 GHz) of TEXTOR discharges no. 106482 and no. 107915. Additional results can be found in [34].

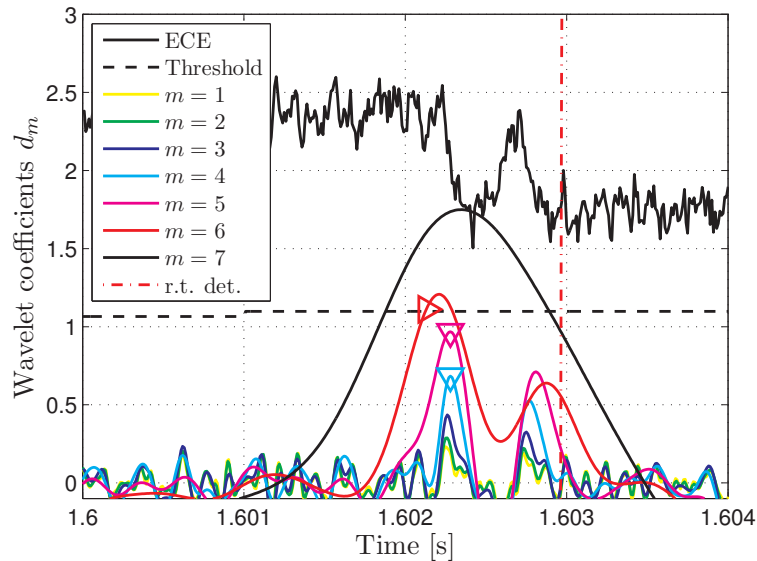


Figure 5.7: Non-causal responses on a double crash, where \triangleright denotes the point of detection and the vertical dash-dot line indicates the real-time detection moment of the crash (r.t. det.), for the 132.5 GHz ECE in discharge no. 106482.

5.4.1 Double crash

Figure 5.7 shows a specific example of a sawtooth where the reconnection seems to occur in two phases, yielding a sort of double crash. The lower scales (especially $m = 4$ and 5) detect the two falling edges separately, since the width of their corresponding wavelet is small (0.46 ms for $m = 4$). As the scale increases the two maxima of each wavelet coefficient come together, since the corresponding wavelet starts to encompass both edges (for $m = 6$ it is 1.66 ms wide). For even larger scales, in this case $m = 7$ (3.26 ms wide), the maxima of both edges overlap entirely and is thus treated as a single crash. In the example of figure 5.7 the first edge is the steepest, yielding the largest response of the wavelet coefficients. For this reason the maxima chain chooses this edge as the true crash, tracing it down to $m = 4$ for a precise estimation of its time instant. Note that such double crashes reduce the magnitude of the wavelet coefficients, especially at the lower scales, which implies that detection often takes place at the higher scales, yielding a larger delay for such crashes.

5.4.2 Crashes with pre-cursors

Figure 5.8 shows a classic sawtooth [35], where the crash is preceded by a pre-cursor. The algorithm still detects the crash accurately, even though the amplitude of the pre-cursor is just as large as the crash in this example. It can be seen that small sized wavelets, whose width is smaller than the period of the pre-cursor (like for $m = 2$ and $m = 3$), directly respond to the pre-cursor and therefore oscillate with the same frequency. Larger scales $m \geq 4$ encompass both the rising and falling ‘edge’ of the pre-cursor oscillations, smearing out their effect, leading to smaller coefficients around

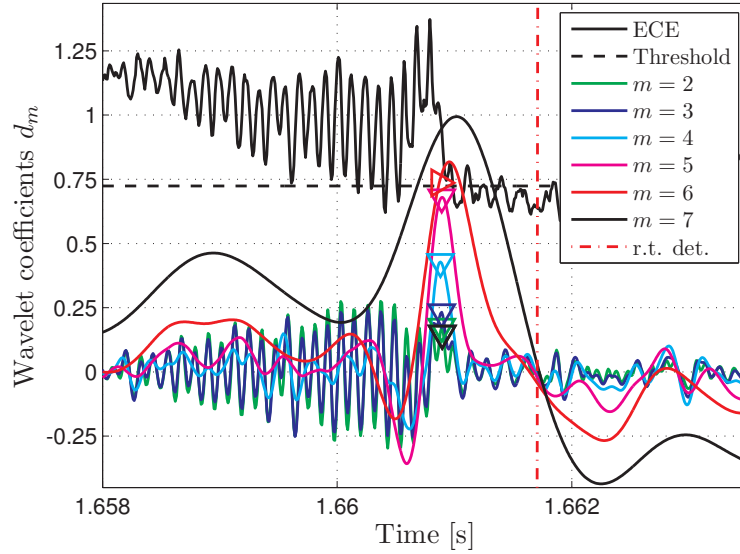


Figure 5.8: Non-causal responses on a crash with pre-cursor, showing only scales m from 2 to 7 (132.5 GHz channel, discharge no. 107915).

the pre-cursor. At $m = 6$ and $m = 7$ the wavelet only analyses the global course of the temperature (i.e. its low-frequent behaviour), thereby clearly recognizing the sharp transition at the crash. Note that these scales also recognize that the average temperature during the build-up of the pre-cursor slowly decreases and increases again. The crash is detected in $m = 6$ and the maximum chain is traced towards $m = 2$ to accurately determine the middle of the crash. Since the detection takes place in $m = 6$, the wavelet coefficients of $m = 7$ do not play a role in the detection (see figure 5.5), and are only shown for completeness (the same is true for figure 5.7). The detection delay is therefore 0.83 ms in this case.

Figure 5.9 depicts some surrounding sawteeth of the same discharge, showing another hard-to-detect crash around 1.63 s. Again, the amplitude of its pre-cursor is just as large as the crash, but the crash itself is less deep than the surrounding ones. Consequently, the scale $m = 6$, which detects all surrounding crashes, does not detect the crash at 1.63 s. It is very likely that a conventional one-scale method would miss this crash, but in our wavelet framework we can extend the amount of scales (up to a wavelet twice the size of the sawtooth period), at the expense of some additional calculation time (due to a larger filter bank size); as shown in figure 5.9 the crash can be detected by the scale $m = 9$.

Crashes that are only detected by (additional) higher scales are subject to a larger delay. In figure 5.9 the delay for the crash around 1.63 s is 6.43 ms ($m = 9$), whereas the delay for the surrounding crashes is just 0.83 ms, since these are detected at $m = 6$. The accuracy is not affected, since it is still possible to trace a maxima chain starting from $m = 9$. Note that the responses of very large scales, like $m = 9$, can also be large in the negative direction; tracking of the inversion radius (and hence the direction of the crash in each channel) is important in these cases to avoid false detections on these

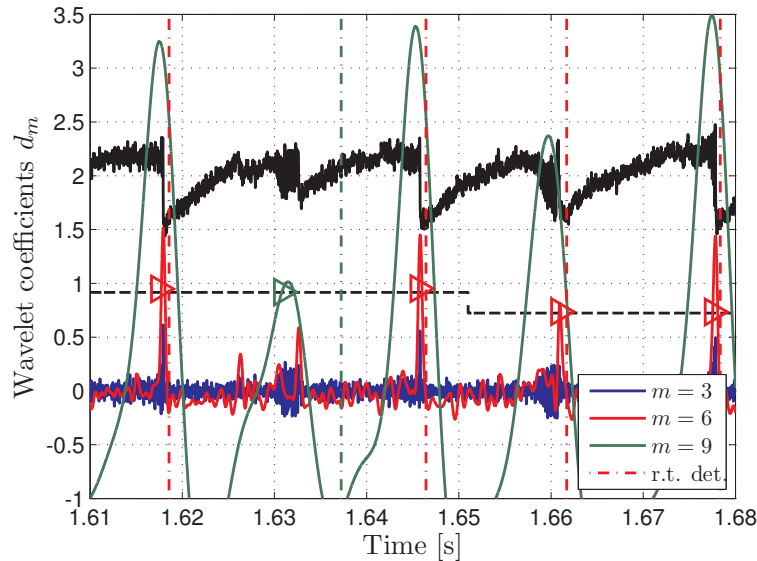


Figure 5.9: Non-causal responses of the wavelet coefficients for five subsequent crashes, some of which are preceded by a pre-cursor (132.5 GHz ECE, discharge no. 107915).

responses. Finally, note that figure 5.9 also illustrates the adaptive threshold: at 1.65 s the threshold is decreased, as the algorithm estimates that the variance of the noise has decreased.

5.4.3 Period of discharges no. 106482 and no. 107915

The real-time implemented wavelet algorithm has been tested on the raw ECE data from TEXTOR discharges no. 106482 and no. 107915. The results, in terms of the determined sawtooth period and estimated delay for each crash, are shown in figure 5.10 and 5.11, respectively. The delay has been calculated by the subtraction of the calculated time instant of the crash from the moment of detection. In the real-time implementation the filter bank operates on each of the ECE channels separately (up to scale $m = 7$), and the resulting wavelet coefficients are combined as described in section 5.3.3. This combination increases the robustness, since crashes missed on one channel are detected on another, and generally improves the delay.

The plasma conditions in discharge no. 106482 were approximately constant, yielding a nearly constant sawtooth period of about 10 ms throughout the discharge. Consequently, the delay is also roughly constant (about 0.7 ms), except for some small outliers due to some occasional difficult-to-detect crashes. In discharge no. 107915 the sawtooth period was deliberately influenced by the addition of NBI power. In the first part of the discharge, from 1 s to 2.2 s, the sawteeth are generally well conditioned (good SNR). Apart from some outliers due to an occasional pre-cursor, the delay is very small (around 0.2 ms). The period increases from 12 ms to 23 ms, due to the NBI switch-on at 1.5 s. Between 2 s and 3 s the ECE mirror angle changes linearly, due to which the inversion radius moves through the different ECE channels. Consequently,

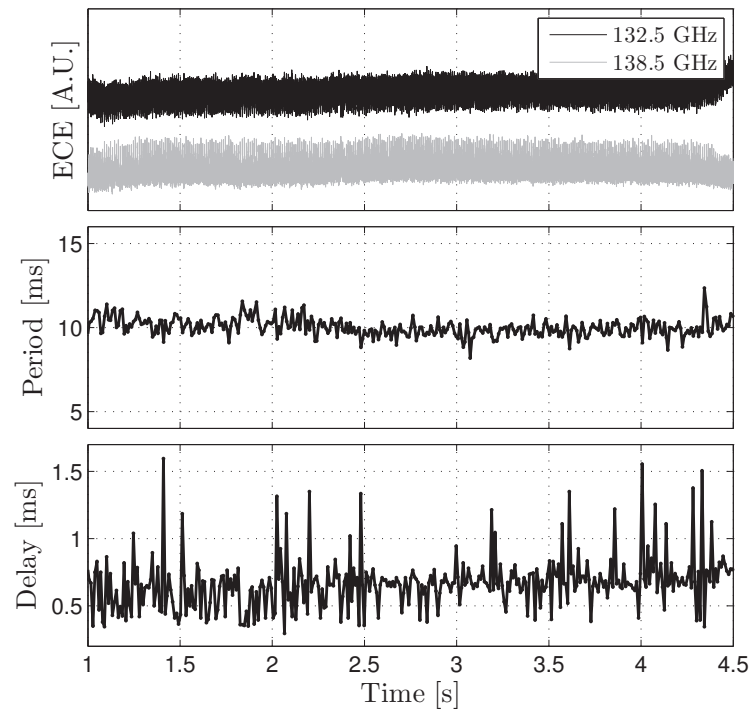


Figure 5.10: Real-time determined sawtooth period (middle) for TEXTOR discharge no. 106482, together with an estimate of the delay for each crash (bottom). The top plot shows two of the raw ECE measurements.

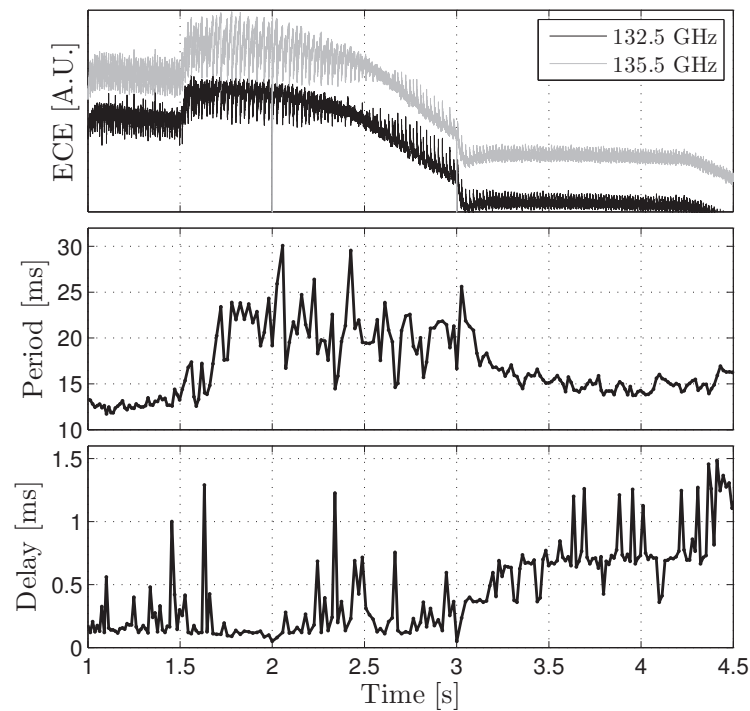


Figure 5.11: Real-time determined sawtooth period (middle) for discharge no. 107915. The top plot shows two ECE channels, the bottom plot displays an estimate of the delay.

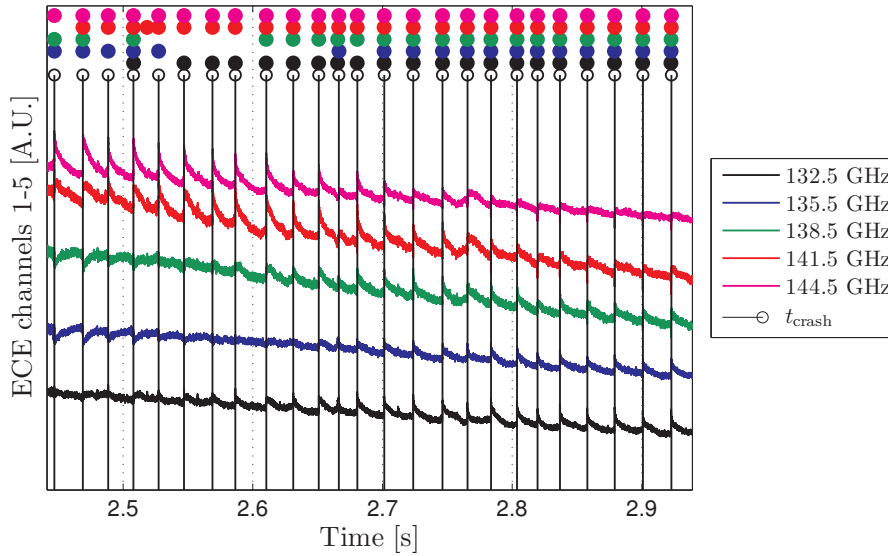


Figure 5.12: Sawteeth of discharge no. 107915, where a coloured \bullet represents a detection on a specific channel and the vertical lines depict the time instant of the crash as determined by the real-time algorithm.

the SNR decreases, resulting in somewhat larger detection delays. The same holds for the end of the discharge: the crashes are relatively small (the ECE channels measure far from $q = 1$), yielding a small SNR and thus large delay. The period is still accurately determined by the algorithm though, showing a decrease to about 14 ms due to the NBI switch-off at 3 s.

During NBI actuation the measured period is rather erratic, but the algorithm detects every single crash correctly, as demonstrated in figure 5.12. As the inversion radius changes, the detection fails on some individual channels, but the crash is always detected on at least two other channels. The algorithm is robust in the sense that false detections do not occur, due to the relatively large threshold of $3 \cdot T_{\min}$. Finally, note that the results show the advantage of our wavelet based edge-detection algorithm. It allows to identify each individual sawtooth period, whereas frequency based methods only return an average of the period over multiple sawtooth crashes.

5.4.4 Accuracy

The accuracy of our detection algorithm can be estimated in a regime with constant and well defined sawteeth, like discharge no. 106482. This can be done by comparing the calculated sawtooth period (i.e. the output of the algorithm) to the period estimates of the individual channels, as is represented in figure 5.13. This figure shows that the natural fluctuations of the period are more significant than the discrepancies between the individual channels. This can also be expressed quantitatively: the standard deviation of the calculated period is $\sigma_{\text{period}} = 0.51$ ms, whereas the differences between various ECE channels return $\sigma_{132.5-138.5} = 0.13$ ms, $\sigma_{132.5-141.5} = 0.22$ ms and

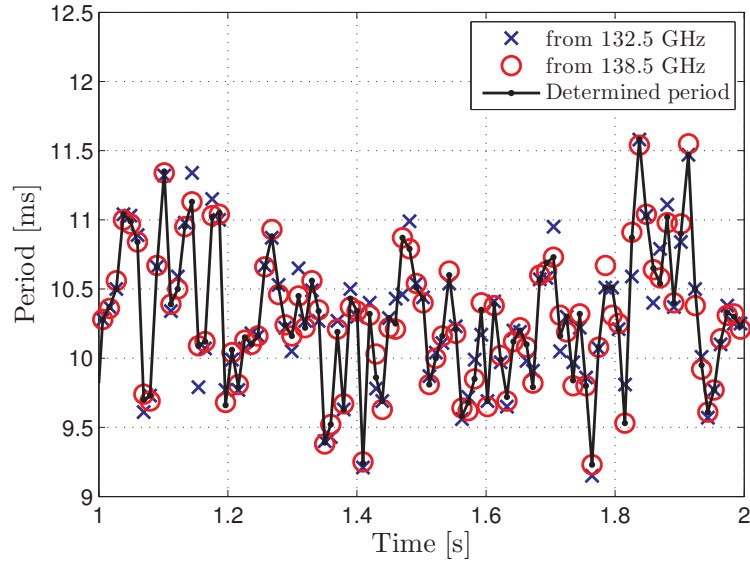


Figure 5.13: Period estimates of two individual ECE channels compared to the calculated period (i.e. the outcome of the algorithm) for discharge no. 106482.

$\sigma_{138.5-141.5} = 0.20$ ms, respectively. Hence, it can be concluded that the error on the period determination is much smaller than that of the natural fluctuations of the period itself, in some cases nearly a factor 4. As such there is no need to further improve the algorithm with respect to the accuracy.

5.5 Conclusions

In this chapter we have developed an algorithm for real-time detection of sawtooth crashes, which has shown to be both robust and accurate. The algorithm is based on time-scale wavelet theory, and is designed using an optimal edge-detector and its efficient B-spline approximation. This yields a multiresolution (or multi-scale) analysis of the sawtooth, which enables successful detection for a wide variety of sawtooth sizes and shapes, making this technique very robust. Thanks to a relatively large (i.e. robust) adaptive threshold value and a smart combination of the available ECE channels, the amount of missed or falsely detected crashes can be kept to a minimum. Moreover, a so-called maxima chain has been implemented, which allows tracing of the exact time instant of the crash towards the lowest and most accurate scales. By construction, the algorithm always detects a crash in the lowest possible scale, thereby minimizing the amount of delay for each individual crash. Consequently, in terms of robustness, accuracy and delay, this multi-scale technique is expected to outperform any conventional one-scale band-pass algorithm.

Thanks to an efficient implementation in a filter bank, the algorithm can easily be applied in real-time, Simulation results on actual TEXTOR ECE measurements, using the real-time Matlab[®] Simulink[®] environment, demonstrate that each period is accurately determined, even for indistinct or hard-to-detect sawteeth. The algorithm

always returns the latest individual sawtooth period, in contrast to the Morlet wavelet (which is hard to implement in real-time), that only returns an averaged period. Together with the small delay of the algorithm, this makes our approach an excellent candidate for use in a feedback control loop for the sawtooth period.

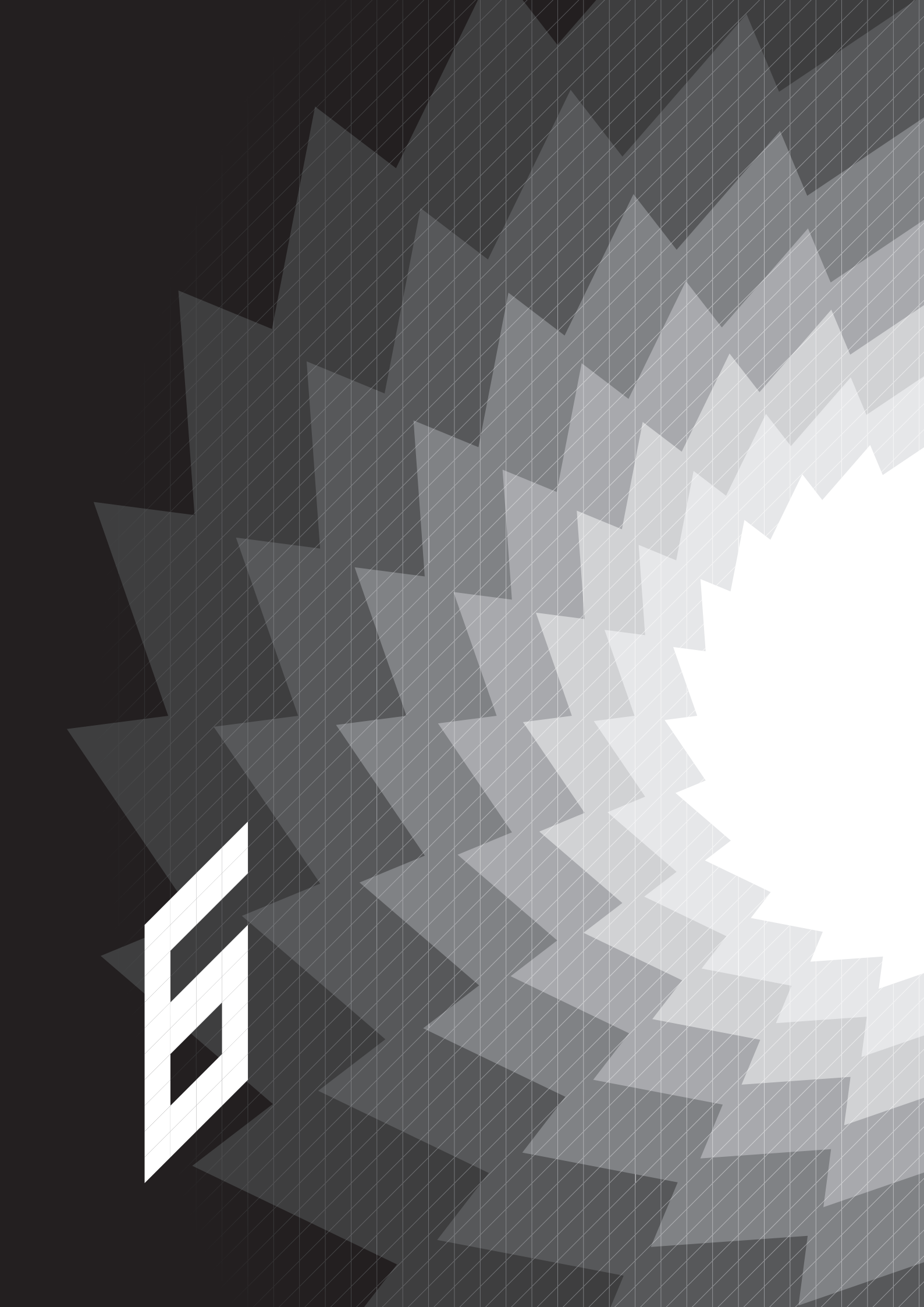
The presented algorithm has a large flexibility. There is design freedom in, e.g. the choice of the wavelet, the order of the B-spline, the number of scales and their step size, the pre-filter and the threshold value, thanks to which it can be adapted to many different applications. As such, it can be applied to any periodic crash or phenomenon, existing in any time series measurement. In future research the framework presented in this chapter can therefore be extrapolated to the detection and identification of other plasma processes, such as ELMs, NTMs or fishbones. Moreover, since different wavelets (or wavelet filter banks) can be run in parallel, it is also possible to discriminate between different types of periodic crashes. As such, wavelet analysis can be a useful tool to discriminate between, e.g. type-I and type-III ELMs, in a real-time control loop.

The presented algorithm provides the sawtooth period sensor which is required by the feedback controllers in chapter 2, 3 and 4. Hence, the final step in demonstrating its value for sawtooth period control, is by embedding the algorithm in an actual feedback loop on a tokamak, in connection with real-time diagnostics (such as ECE or soft x-ray) and a feedback controller. This implementation and subsequent sawtooth control experiments are part of current research.

References

- [1] Chapman I.T. 2011 *Plasma Phys. Control. Fusion* **53**(1) 013001
- [2] Graves J.P. *et al.* 2005 *Plasma Phys. Control. Fusion* **47**(12B) B121
- [3] Lennholm M. *et al.* 2009 *Fusion Sci. Technol.* **55**(1) 45
- [4] Lennholm M. *et al.* 2009 *Phys. Rev. Lett.* **102**(11) 115004
- [5] Paley J.I. *et al.* 2009 *Nucl. Fusion* **49**(8) 085017
- [6] Paley J.I. *et al.* 2009 *Plasma Phys. Control. Fusion* **51**(5) 055010
- [7] Paley J.I. *et al.* 2009 *Plasma Phys. Control. Fusion* **51**(12) 124041
- [8] Witvoet G. *et al.* 2011 *Nucl. Fusion* **51**(7) 073024
- [9] Bizarro J.P.S. and Figueiredo A.C.A. 2008 *Fusion Eng. Des.* **83**(2-3) 350
- [10] Hallatschek K. and Zilker M. 1998 *IEEE Trans. Nucl. Sci.* **45**(4 Part 1) 1872
- [11] Santoso S. *et al.* 1997 *Rev. Sci. Instrum.* **68**(1) 898
- [12] Bizarro J.P.S. and Figueiredo A.C.A. 1999 *Nucl. Fusion* **39**(1) 61
- [13] Figueiredo A.C.A. *et al.* 2004 *Rev. Sci. Instrum.* **75**(10) 4268
- [14] Oosterbeek J.W. *et al.* 2008 *Rev. Sci. Instrum.* **79**(9) 093503
- [15] Unser M. 1997 *Proc. SPIE* vol. 3169 (San Diego, CA, USA) 422–431
- [16] Canny J. 1986 *IEEE Trans. Pattern Anal. Mach. Intell.* **PAMI-8**(6) 679
- [17] Mallat S. 2009 *A wavelet tour of signal processing: the Sparse way* 3rd edn. (London: Academic Press)
- [18] Addison P.S. 2002 *The illustrated wavelet transform handbook: introductory theory and applications in science, engineering, medicine and finance* (Bristol: Institute of Physics)

-
- [19] Burrus C.S. *et al.* 1998 *Introduction to wavelets and wavelet transforms: a primer* (Upper Saddle River, NJ: Prentice Hall)
 - [20] Calderon A.P. 1964 *Studia Math* **24**(2) 113
 - [21] Chui C.K. 1992 *An introduction to wavelets* (San Diego, CA: Academic press)
 - [22] Strang G. and Nguyen T. 1996 *Wavelets and filter banks* (Wellesley, MA: Wellesley-Cambridge Press)
 - [23] Nave M.F.F. *et al.* 2003 *Nucl. Fusion* **43**(3) 179
 - [24] Poli F.M. *et al.* 2008 *Plasma Phys. Control. Fusion* **50**(9) 095009
 - [25] Kass T. *et al.* 1998 *Nucl. Fusion* **38**(1) 111
 - [26] Stober J. *et al.* 2001 *Nucl. Fusion* **41**(9) 1123
 - [27] Hartfuss H.J. *et al.* 1997 *Plasma Phys. Control. Fusion* **39**(11) 1693
 - [28] Cima G. *et al.* 1995 *Phys. Plasmas* **2**(3) 720
 - [29] Misiti M. *et al.* 2009 *Matlab Wavelet ToolboxTM User's Guide*
 - [30] Mallat S. and Zhong S. 1992 *IEEE Trans. Pattern Anal. Mach. Intell.* **14**(7) 710
 - [31] Daubechies I. 1992 *Ten Lectures on Wavelets* vol. 61 of *CMBMS-NSF Series in Applied Mathematics* (Philadelphia, PA: Siam publications)
 - [32] Unser M. 1999 *IEEE Signal Proc. Mag.* **16**(6) 22
 - [33] Donoho D.L. and Johnstone J.M. 1994 *Biometrika* **81**(3) 425
 - [34] van Berkel M. *et al.* 2011 *Fusion Eng. Des.* in press
 - [35] Hastie R.J. 1997 *Astrophys. Space Sci.* **256**(1) 177



CHAPTER 6

Numerical demonstration of injection locking of the sawtooth period by means of modulated EC current drive

G. Witvoet^{a,b}, M. Lauret^{a,b}, M.R. de Baar^{a,b}, E. Westerhof^b and M. Steinbuch^a

^a Eindhoven University of Technology

^b FOM-Institute for Plasma Physics Rijnhuizen



Abstract

In this paper the sawtooth period behaviour under periodic forcing by electron cyclotron waves is investigated. The deposition location is kept constant while the gyrotron power is modulated with a certain period and duty cycle. Extensive simulations on a representative dynamic sawtooth model show that when this modulation is properly chosen, the sawtooth period quickly synchronizes to the same period and remains locked at this value. It is shown that the range of modulation periods and duty cycles over which sawtooth period locking occurs depends on the deposition location, but is particularly large for depositions near the $q = 1$ surface. The simulation results reveal a novel approach to control the sawtooth period in open loop, based on injection locking, which is a well-known technique to control limit cycles of non-linear dynamic oscillators. The locking and convergence results are therefore used in a simple open-loop locking controller design, with which accurate sawtooth period tracking to any desired value is indeed demonstrated. Injection locking appears to let the sawtooth period converge to the modulation period quickly, partly because it does not suffer from slow EC mirror launcher dynamics. Moreover, simulations show that the method has a relatively large robustness against general uncertainties and disturbances. Hence, injection locking is expected to outperform conventional sawtooth control methods using a variable deposition location and constant gyrotron power. Finally, the recent result with sawtooth pacing is shown to be a special case of the general locking effect.

6.1 Introduction

The sawtooth oscillation is a periodic relaxation of the plasma surrounding the magnetic axis [1–3]. A typical sawtooth cycle comprises a slow rise in core plasma temperature, followed by a rapid crash, during which the core temperature is mixed with colder outer regions [4]. In a fusion reactor the sawtooth can regulate the exhaust of helium and α -particles [5] and the influx of deuterium and tritium. However, the sawtooth is also able to trigger neoclassical tearing modes (NTMs) well below the ideal β -limit [6, 7], especially when the sawtooth period is long [8] due to stabilization effects by, e.g. fast particles or auxiliary heating. These NTMs significantly reduce the operational performance of a reactor and can even lead to disruptions. The need for NTM avoidance [9] whilst simultaneously optimizing α -confinement, refuelling, and exhaust inside the fusion reactor motivate the control of the sawtooth behaviour. Control of the sawtooth period is a key area of research for which many techniques have been developed [10].

The sawtooth crash is associated with both the magnetic shear on the $q = 1$ surface [11] and the orbits of energetic ions with respect to the same surface [12–14]. Sawtooth period actuators typically attempt to influence either of these aspects. It has been shown that ion cyclotron (IC) waves are able to affect both the magnetic shear around $q = 1$ [15] and the orbits of fast ions [14], whereas the effect of directional neutral beam injection (NBI) is typically on the fast particle orbits [16, 17]. Probably the most promising sawtooth period actuator is electron cyclotron current drive (ECCD), which can modify the magnetic shear evolution quite effectively due to its highly localized deposition ability. The possibilities of ECCD actuation have been shown experimentally on, e.g. ASDEX Upgrade [18], TEXTOR [19], TCV [20] and references therein. Moreover, experiments carried out on Tore Supra [21, 22] and TCV [23–25] have demonstrated the feasibility of feedback control of the sawtooth period using the ECCD deposition location as control input. A systematic feedback control design based upon a rigorous system analysis for this input has recently been developed in [26]. Unfortunately, present-day mechanical EC mirror launchers, i.e. the systems responsible for changing the deposition location, are limited in speed and thereby restrict the achievable performance of the above feedback approaches, as has been proven in [26].

The above mentioned publications only consider continuous wave (CW) operation, where the gyrotron power remains constant in time and the period is altered by slowly changing the deposition location. However, recent experiments on TCV [27] have shown that the sawtooth period can also be forced by modulated EC waves. The results are potentially important and suggest an alternative sawtooth period control strategy, which may even have repercussions on the requirements of the control system for NTMs. However, the power modulation in these experiments was externally synchronized with the sawtooth crash by means of a real-time control loop. Although this specific modulation choice seems logical from a physics perspective, it is not necessarily the

optimal choice. This motivates the analysis of the sawtooth behaviour under generic EC modulations, from both a physics and system theoretic point of view.

In this paper we carry out this analysis, and thereby bring the periodic forcing or pacing of the sawtooth period by modulated EC waves in a broader perspective. To this end extensive simulations are performed, where the deposition location is held fixed, while the gyrotron power is on-off modulated relatively fast with a period in the same order of magnitude as the sawtooth period. This approach is in strong analogy to *injection locking* [28–30], a well-known technique in Circuit and System Theory to synchronize limit cycles of non-linear dynamic oscillators with the input frequency. Since the sawtooth is a relaxation oscillation whose dynamics typically exhibit both slow (ramp phase) and fast (crash phase) time-scales, it behaves quite similar to a certain subclass of such non-linear oscillators [31] and is therefore expected to be sensitive to injection locking. Indeed, it will be shown in simulation that under some conditions the sawtooth oscillation will lock to the modulated input, i.e. the period of the sawtooth becomes identical to the period of the power modulation. This synchronization of the sawtooth is completely autonomous, as the phase between ECCD modulation and sawtooth cycle is not explicitly prescribed. This is in contrast to [27], where the ECCD pulse always starts right after a crash. Hence, the locking results reveal a novel open-loop approach to control the sawtooth period to a desired value, by simply applying an EC power modulation with the same period. This way both shorter and longer than ohmic periods can be achieved, dependent on the fixed deposition location.

Sawtooth period locking has numerous advantages. First, it is an open-loop method, so locking of the period does not depend on any crash detection algorithm [32]. Second, it is generally very fast. It does not rely on an EC mirror launcher, which is typically slow compared with the sawtooth period, and the underlying dynamics is so fast that sawtooth locking often occurs within only a couple of crashes. Third, its performance can be quite robust. The locking range, i.e. the range of different ECCD modulations (characterized by its period and duty cycle) for which the sawtooth period actually locks, is quite large, especially when the deposition is close to the $q = 1$ surface. This causes locking ranges for different deposition locations to overlap, indicating that the period can remain locked at the desired value, even in the presence of a certain degree of deviations in plasma parameters which lead to such variations in the deposition location. Additionally, it can be more efficient than CW operation, as the modulated current drive can achieve comparable periods using (time-averaged) less power.

In this paper the model of the sawtooth oscillation described in [26] is used to analyse the locking behaviour of the sawtooth. The dynamic behaviour of this model is representative for actual sawteeth, as it is based on sawtooth physics in terms of the magnetic diffusion equation, the trigger model of Porcelli *et al* [11], and the reconnection model of Kadomtsev [4]. The temperature profile is assumed to be constant. The input of the model is the driven EC current, which is directly related to the gyrotron power. A wide range of different modulations, with different periods and

duty cycles, is applied to this model, yielding a large set of results in the form of locking ranges and corresponding convergence and phase information. These results show a clear structure in the locking behaviour, and illustrate how the sawtooth oscillation synchronizes with the ECCD modulation automatically. These results also reveal that sawtooth pacing [27] is indeed a special case of the more generic case of sawtooth period locking. Moreover, a comprehensive CRONOS [33] transport simulation is provided to validate the locking abilities of the sawtooth. Finally, the locking ranges are used in simple open-loop locking controller designs, which are demonstrated in time-domain simulations.

This paper is organized as follows. Section 6.2 shortly discusses the combined Kadomtsev–Porcelli sawtooth model and describes the simulations to investigate its injection locking behaviour. Section 6.3 then shows the obtained results for various situations, and confirms these with a CRONOS simulation. Based on these results some simple open-loop control routines are derived and tested in section 6.4. Conclusions and discussion are given in section 6.5.

6.2 Methodology

As mentioned in the introduction, this paper will focus on the effect of the EC driven current on the sawtooth period. In particular, it will be shown that a modulation of this EC current has a peculiar effect on the dynamics of the sawtooth, in the sense that the sawtooth period locks on the exact same period as the modulated EC current. This will later be used in an open-loop controller design.

This section will first shortly discuss the dynamic model for the sawtooth which will be used as a case study. Next, it will introduce the notion of *injection locking*, and will describe what type of open-loop simulations will be performed to analyse this locking phenomenon of the sawtooth period.

6.2.1 Dynamic model for the sawtooth behaviour

In our analysis, we use a relatively simple model for the sawtooth period, which was extensively described in [26]. This model focuses on the dominant dynamics of the sawtooth, which is a vital part of its input–output behaviour. The dynamics are centred around three building blocks: the magnetic diffusion equation, the crash criterion of the Porcelli model [11], and the Kadomtsev reconnection model [4]. As has been discussed in [26], the resulting sawtooth model can be written as a set of equations for the poloidal magnetic field B_θ as a function of time t and space r , having both slow and (infinitely) fast timescales:

$$\frac{\partial}{\partial t} B_\theta = \frac{\partial}{\partial r} \left(\frac{\eta}{\mu_0 r} \left(B_\theta + r \frac{\partial}{\partial r} B_\theta \right) - \eta J_{\text{CD}} \right) \quad \text{if } s_1 < s_{\text{crit}}, \quad (6.1a)$$

$$B_\theta(r, t^+) = \begin{cases} B_\theta(r, t^-) & \text{for } r \geq r_{\text{mix}} \\ \frac{d}{dr} \Psi_*^c(r) + \frac{1}{R_0} r B_\phi & \text{for } r < r_{\text{mix}} \end{cases} \quad \text{if } s_1 \geq s_{\text{crit}}, \quad (6.1b)$$

with boundary conditions $B_\theta(0, t) = 0$ and $B_\theta(a, t) = \frac{\mu_0 I_p}{2\pi a}$. Here $s_1 = s(r_{q=1})$ denotes the magnetic shear at the surface where the safety factor q equals 1, which is compared with a critical shear threshold value s_{crit} (which is chosen constant in this paper); r_{mix} is the mixing radius, i.e. the radius up to which the flux surfaces reconnect during the crash; and $\Psi_*^c(r)$ is the post-crash helical flux function. This function depends on the helical flux $\Psi_*(r)$ before the crash, defined as

$$\Psi_*(r) = \int_0^r [B_\theta(\tilde{r}) - \tilde{r}B_\phi/R_0] d\tilde{r}, \quad (6.2)$$

and can be calculated using the Archimedes–Kadomtsev approach presented in [26], i.e.

$$\Psi_*^c(r_c) = \Psi_*(r_{i-}) = \Psi_*(r_{j+}), \quad \text{where } r_c^2 = \sum_i r_{i-}^2 - \sum_j r_{j+}^2. \quad (6.3)$$

Here r_{i-} are all pre-crash surfaces with $d\Psi_*/dr < 0$ and r_{j+} are all pre-crash surfaces with $d\Psi_*/dr > 0$. Furthermore, η is the plasma resistivity, μ_0 is its magnetic permeability, B_ϕ is the toroidal magnetic field which is considered constant due to the large aspect-ratio assumption, I_p is the plasma current and a and R_0 are the tokamak minor and major radius, respectively.

The actuator is represented by the non-inductive driven current J_{CD} , whose profile is characterized by the total driven current I_{CD} and the deposition location (the deposition width is held constant at 16 mm). The deposition location is determined by the poloidal deflection angle ϑ of the EC beam, imposed by the rotation of the EC mirror. The inputs are thus I_{CD} and ϑ ; these are the actuator settings we can vary and use as control parameters. The analytic equations to calculate J_{CD} from these variables are given in [26]. The output of the model is the sawtooth period τ_s , the variable to be controlled, defined by the time between two subsequent crashes (6.1b).

The model has been implemented into Matlab[®] Simulink[®], by embedding a specially written C-code into an S-function [34]. This code has been written such that the model is solved with high spatial and temporal resolution to enable detailed analysis of the sawtooth dynamics. It uses a 250 point non-uniform discretization grid for the spatial coordinate r , which is very dense around $r_{q=1}$ and r_{mix} , and is redefined after every crash (such that it follows r_{mix}). Furthermore, it uses cubic interpolation techniques to accurately calculate $r_{q=1}$ and s_1 , and utilizes a zero-crossing event function to precisely determine when the trigger $s_1 = s_{\text{crit}}$ occurs. Thanks to the fast and accurate variable-step solvers which come with Simulink, the moment of a crash can then be located with a precision of nearly 10^{-6} ms. Furthermore, due to the large flexibility of Simulink, the model can be interconnected with other systems and the input signals $I_{\text{CD}}(t)$ and $\vartheta(t)$ can easily be defined. Typical dimensions and parameters in the model were specifically chosen to represent the TEXTOR tokamak, but in principle the model and its implementation are straightforwardly applicable to other machines also.

6.2.2 Injection locking

The identification routine and frequency domain results in [26] have shown that the sawtooth model defined in (6.1a)–(6.1b) indeed exhibits significant dynamic behaviour. Not only the evolution of B_θ between crashes in (6.1a) is time-dependent, the response from crash to crash also shows an amount of ‘memory’, presumably due to the fact that the post-crash profile depends on the profile before the crash, as represented in (6.3). The combination of its slow time-scale in (6.1a) and its (infinitely) fast one in (6.1b) cause the sawtooth to converge to a stable limit cycle with a certain free-running ohmic period (for $J_{CD} = 0$), which corresponds to around 15 ms for typical TEXTOR settings. The sawtooth instability is essentially a relaxation oscillation, whose structure and resulting behaviour shows large similarities to general non-linear oscillators [31], which are well known within the field of Electronic Circuits and System Theory. One of the most famous and elegant examples is the Van der Pol oscillator [28,31]

$$\frac{d^2}{dt^2}x + \mu(x^2 - 1) \frac{d}{dt}x + x = u. \quad (6.4)$$

For very large damping $\mu \gg 1$ this equation displays a relaxation oscillation; it exhibits both fast and slow time-scales, and for $u = 0$ displays a limit cycle with a certain free-running period $T_0 \sim \mathcal{O}(\mu)$. However, this limit cycle period can be altered by means of *injection locking* [28–30]: if a periodic input signal u is applied to the system, the oscillator will eventually synchronize or lock to this external signal, such that its output has the exact same period. For example when $u = A \sin(\omega t)$ the output x will oscillate with the same frequency ω . This locking occurs as long as the injected period is close to the free-running period; the range of periods for which locking occurs is called the *locking range*. Injection locking has been demonstrated on a wide variety of non-linear oscillators, including the Van der Pol oscillator.

The occurrence of limit cycles and injection locking is determined by the structure of the underlying dynamics of a system. Because both (6.1a)–(6.1b) and (6.4) display similar relaxation behaviour with both fast and slow dynamics, it is to be expected that the sawtooth instability is also sensitive to injection locking. In this paper this phenomenon will be investigated using the above discussed sawtooth model as a case study, which allows us to perform many extensive simulations to cover a wide range of the operating space. Since the model is constructed around the elementary dynamics of magnetic diffusion together with a fast reconnection scheme, it is expected that the obtained results can be extrapolated to a real tokamak experiment.

6.2.3 Description of the simulations

Injection locking requires the input of the sawtooth system to oscillate with periods comparable to or shorter than τ_s . On present-day tokamaks the deposition location, determined by the EC mirror angle ϑ , is therefore not suited for injection locking, as current state-of-the-art mirror launcher installations (like on TEXTOR [35] and TCV [23]) are unable to alter ϑ with such high speeds [26]. In contrast, gyrotron

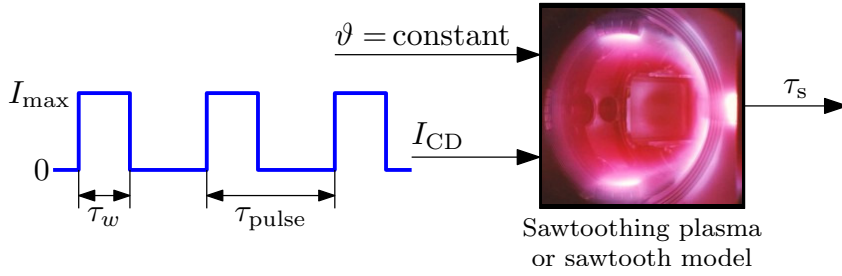


Figure 6.1: Schematic representation of the open-loop locking simulations.

power, or in our case the driven current I_{CD} , can be modulated at very high rates [35], resulting in relatively high-frequency on–off pulse trains, which are very suitable for locking experiments.

To investigate sawtooth period (injection) locking, we will use the open-loop approach as represented in figure 6.1. The mirror angle ϑ is held constant, at a value corresponding to a deposition either inside or outside the $q = 1$ surface, while the EC current drive is initially kept at $I_{CD} = 0$, allowing the system to converge to the ohmic period. Then, starting at an arbitrary (random) moment in time, the driven current I_{CD} (in the same direction as the plasma current) is on–off modulated. The modulation is in this case characterized by three parameters: the maximum current I_{max} (in this paper either 2 or 4 kA), the pulse period τ_{pulse} (in ms), and the duty cycle w or pulse width τ_w . This duty cycle w is expressed as a percentage of τ_{pulse} , i.e. $w = \tau_w / \tau_{pulse} \times 100\%$.

For a given combination of pulse parameters I_{max} , τ_{pulse} and w the output τ_s immediately after the start of the pulse is monitored. If this output converges to a constant period exactly equal to τ_{pulse} , we say that the sawtooth is locked for that specific combination of I_{max} , τ_{pulse} , and w . In that case the convergence speed and phase information are also stored. Since injection locking is a purely open-loop technique, the phase difference between pulse and sawtooth cycle during locking is not prescribed, but we will see that it takes on a particular fixed value by itself. In other words, the sawtooth system has complete freedom in how it ‘aligns’ with the pulse train; the start of a pulse could be at the start or the end of the sawtooth cycle, or anywhere in between. The output τ_s can also lock on subharmonics of the pulse period τ_{pulse} , in which case we say that the sawtooth is locked with periodicity τ_s / τ_{pulse} . In any other case there is no locking, as the sawtooth period will change continuously without stabilizing on a constant value. In these situations the modulated ECCD may result in some periodic cycling of the sawtooth period or even a completely erratic behaviour. Although these kind of behaviours can also be of interest, we will not further address them in this paper.

Sawtooth period locking is based on a temporary reduction or increase of the shear at $q = 1$ during the time the co-current EC power is switched on. Therefore, it has similarities with sawtooth pacing, a technique recently studied on TCV [27]. Sawtooth pacing utilizes the stabilizing effect of ECCD outside $q = 1$ to create longer than

ohmic periods. It uses a feedback loop to turn on the EC power right after a crash has been detected, thereby reducing the growth rate of s_1 . As soon as a certain pre-set time τ_{set} has passed, the EC power is turned off again, allowing a rapid increase of s_1 and the occurrence of a crash soon thereafter. Although the exact occurrence of the next crash depends on the growth rate of s_1 after the EC switch-off (in principle we only know that $\tau_s > \tau_{\text{set}}$), the experiments in [27] have shown that this strategy can predict τ_s with relatively high accuracy. This enables pre-emptive control of the NTM which will be triggered by this crash. However, the phase between pulse and sawtooth cycle is fixed, and the method depends heavily on the quality of the crash detection, since a missed crash will change the EC power modulation and the resulting sawtooth period drastically. Injection locking is different in multiple ways. First, the sawtooth period in case of locking is exactly known beforehand. Second, it does not depend on a crash detection algorithm, since it is an open-loop technique. Third, because the phase between pulse and cycle is not prescribed, the sawtooth has more degrees of freedom to lock on a certain period whenever the locking range is large, in which case it can be more robust and require less power. On the other hand, its feedback loop makes pacing more robust when the locking range is small. Finally, injection locking can handle both lengthening and shortening of the sawtooth period, as is shown in the next section.

6.3 Sawtooth locking results

In this section we will present the open-loop injection locking results for the sawtooth period. First, the nominal case where $I_{\text{max}} = 2$ kA will be discussed, showing that both lengthening and shortening of the period can be achieved. Next, the effect of a larger modulated current drive, in this case $I_{\text{max}} = 4$ kA, will be presented. Finally, a validation simulation using the CRONOS transport code will be presented. All model parameters are the same as in [26], i.e. $a = 0.46$ m, $R_0 = 1.75$ m, $B_\phi = 2.45$ T, $I_p = 400$ kA, and $s_{\text{crit}} = 0.133$, unless explicitly mentioned otherwise.

6.3.1 Locking on large sawtooth periods

We will first discuss the locking simulations which intend to lengthen the sawtooth period. Note that long sawtooth periods are often undesirable since they are associated with the triggering of NTMs. However, for a locked sawtooth this long period is exactly known beforehand, i.e. it is exactly known when the next crash occurs. In principle, one can then anticipate on the NTM trigger and control the NTM pre-emptively [27]. As the production of fast α particles is expected to generate large sawtooth periods on ITER [14], locking on specific large periods might therefore be useful for the ITER standard scenario to control NTMs.

To allow a fair comparison with the CW simulations presented in [26], the same amount of current drive is chosen, namely $I_{\text{max}} = 2$ kA. The mirror angle is fixed at the value $\vartheta = 8^\circ$, which is outside the $q = 1$ surface and close to the maximum (located

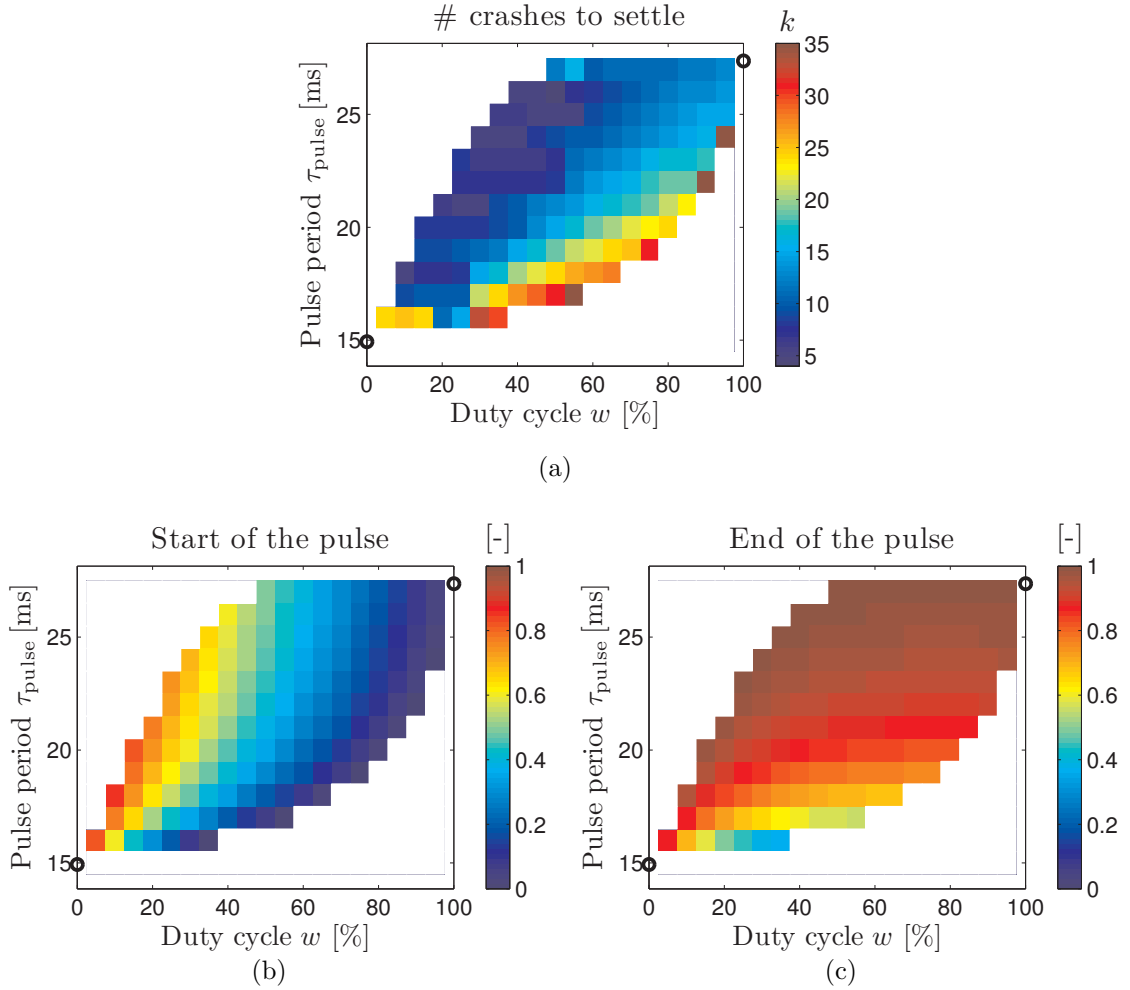


Figure 6.2: Sawtooth period locking range using a 2 kA pulse-modulated driven current and a fixed mirror angle $\vartheta = 8^\circ$, corresponding to EC depositions outside $q = 1$. (a) Convergence speed, expressed as number of crashes k until the sawtooth period τ_s settles at τ_{pulse} . (b), (c) Phase in locked situation, indicated by the start and end of the pulse relative to the previous sawtooth crash.

at $\vartheta = 8.3^\circ$) in the CW steady-state input–output map. The CW sawtooth period for these settings is 27.4 ms.

Next, various combinations of pulse period $15 \leq \tau_{\text{pulse}} \leq 30$ ms and duty cycle $0\% < w < 100\%$ have been applied to the sawtooth model, yielding a grid of locking results, which are summarized in figure 6.2. Each coloured pixel in this figure corresponds to a combination of τ_{pulse} and w for which the sawtooth period τ_s locks to τ_{pulse} . The black circles at 0% and 100% indicate the ohmic period (where $I_{\text{CD}} = 0$) and the 2 kA CW sawtooth period, respectively. The locking range covers a large area between those two points, so there is a wide range of allowable duty cycles w to lock at a certain period, given the chosen values of ϑ and I_{max} . Such a large locking range suggests that locking can be robust against various disturbances and uncertainties in the plasma, as we will discuss in section 6.3.3. Furthermore, figure 6.2 shows that nearly the same

period as for CW can be achieved using only half of the CW power: using a duty cycle of $w = 50\%$ the sawtooth can lock at $\tau_s = \tau_{\text{pulse}} = 27$ ms. Time-averaged this is the same amount of power as a 1 kA CW current drive, which would yield a steady-state period of only 21.0 ms for this ϑ (or at most 21.4 ms at $\vartheta = 8.2^\circ$). Hence, locking can be a very useful tool to reduce the overall power consumption of the sawtooth period control problem.

The colours in figure 6.2(a) indicate the speed of convergence. When we define τ_s to be settled at crash k as soon as it stays within 0.1% of the desired τ_{pulse} for all subsequent crashes, this figure shows how many sawtooth crashes k it takes before τ_s changes from the ohmic value to the desired τ_{pulse} , starting from the beginning of the current drive pulse. Apart from some outliers convergence is quite fast, generally needing at most 30 crashes to lock at a desired period. Moreover, if the period converges at all, the fastest responses occur for the smallest duty cycles w , in some cases needing only a handful of crashes. An example of such a fast response is depicted in blue in figure 6.3(a). This figure also illustrates what happens if the sawtooth does not lock. The red line shows that the sawtooth period itself then ends up in a kind of limit cycle, yielding an oscillatory response of the period. In the depicted example the period repeats every 5 crashes, but oscillations of 2 and 20 crashes have also been observed. The green line in figure 6.3(a) is a typical slow locking response of one of the outliers of figure 6.2(a). In such situations the sawtooth period first starts to oscillate as if no locking would occur, but as time continues the oscillation lengthens and the period τ_s moves in the direction of τ_{pulse} , until the period suddenly locks at τ_{pulse} .

Figures 6.2(b) and (c) give insight in the phase during locking, proving that there is a clear locking structure recognizable; the way that the period locks is smoothly dependent on the parameters τ_{pulse} and w . This phase φ expresses the alignment between the current drive pulse and the sawtooth cycle, and is defined as

$$\varphi_{\text{start}} = \frac{t_{\text{start}} - t_{\text{crash}}}{\tau_{\text{pulse}}}, \quad \varphi_{\text{end}} = \frac{t_{\text{end}} - t_{\text{crash}}}{\tau_{\text{pulse}}}, \quad (6.5)$$

where t_{start} and t_{end} are the start and end times of a specific pulse and t_{crash} is the time of the previous sawtooth crash. Except for some small values of τ_{pulse} , the sawtooth locks in such a way that a crash occurs just after the end of the pulse, i.e. $\varphi_{\text{end}} \approx 1$. The specific example in the top of figure 6.3(b), depicting the evolution of the shear at the $q = 1$ surface during convergence, illustrates this. It clearly shows that the sawtooth tries to ‘align’ itself to the power modulation, until the reduction of s_1 during the pulse is such that the period becomes exactly equal to τ_{pulse} and the sawtooth is in steady-state. The same is true for the bottom plot of figure 6.3(b), although in that case the requested period τ_{pulse} is much smaller and the sawtooth chooses to align such that the pulse is halfway in the sawtooth cycle. Note that the speed of convergence in figure 6.2(a) is hardly affected by the initial phase between the first pulse and the sawtooth cycle. There is a clear dependence on both τ_{pulse} and w , despite the fact that the modulation started randomly for each simulation. The speed is really dominated

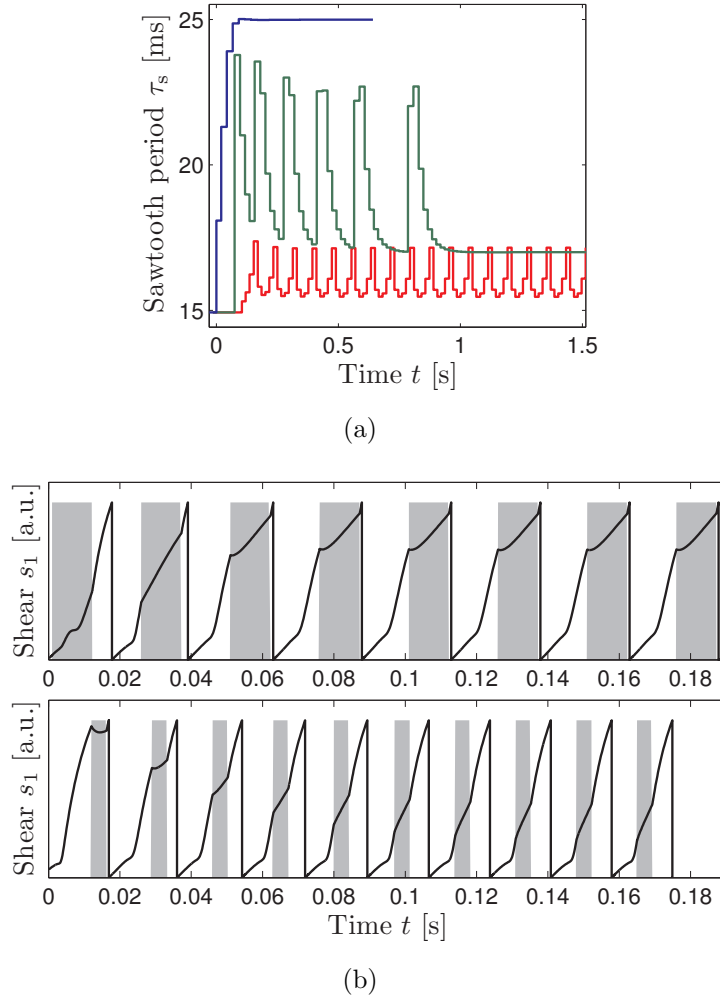


Figure 6.3: Simulation results with a 2 kA modulated current drive and $\vartheta = 8^\circ$: (a) time response of the sawtooth period in case of fast convergence (blue; $\tau_{\text{pulse}} = 25$ ms, $w = 45\%$), slow convergence (green; $\tau_{\text{pulse}} = 17$ ms, $w = 55\%$) and no locking at all (red; $\tau_{\text{pulse}} = 20$ ms, $w = 10\%$); (b) magnetic shear at the $q = 1$ surface for $\tau_{\text{pulse}} = 25$ ms, $w = 45\%$ (top) and $\tau_{\text{pulse}} = 17$ ms, $w = 25\%$ (bottom), illustrating how the sawtooth ‘aligns’ with the ECCD modulation. In (a) time has been shifted to permit easy viewing of the first sawtooth periods.

by the underlying sawtooth dynamics; even if initial phase and locked phase are the same, the q -profile needs some transient adaptation before the period is really locked.

Figure 6.2(b) also suggests a relation between the sawtooth pacing technique of [27] and sawtooth period locking. Since the start of the pulse in sawtooth pacing is always at 0, it should correspond to the outer right pixels of the locking range. We can verify this by performing sawtooth pacing simulations with the sawtooth model described in section 6.2.1. In these simulations the EC current is turned on when a crash has occurred and is switched off a pre-set time τ_{set} later. The results in figure 6.4(a) show that for each value of τ_{set} a different steady-state output τ_s is observed. The resulting steady-state duty cycles $w = \frac{\tau_{\text{set}}}{\tau_s} \times 100\%$ are depicted in figure 6.4(b), which indeed

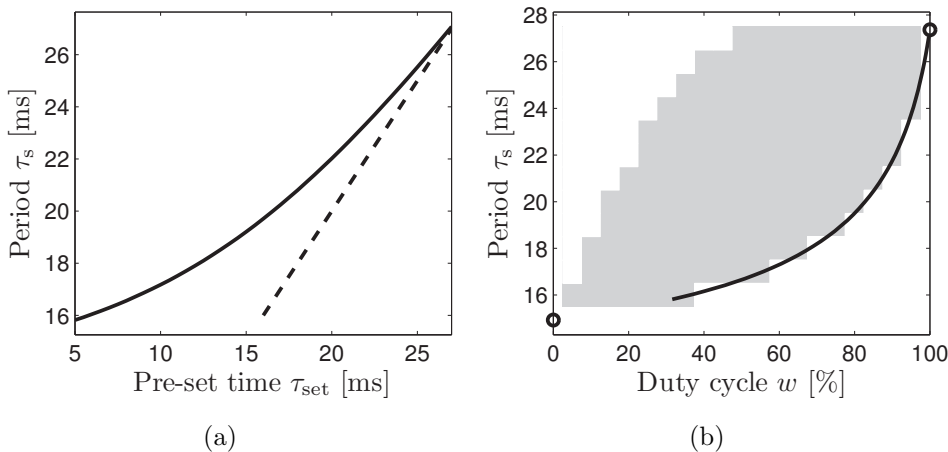


Figure 6.4: Sawtooth pacing [27] simulation results using $I_{\max} = 2$ kA and $\vartheta = 8^\circ$: (a) relation between the pre-set time τ_{set} and the obtained sawtooth period τ_s , and (b) the corresponding duty cycles $w = \frac{\tau_{\text{set}}}{\tau_s} \times 100\%$ (black) in relation to the previously obtained locking results (grey).

correspond to the outer right of the locking range. Hence, it is likely that sawtooth pacing is actually a special case or subset of sawtooth period locking. The latter has, however, more degrees of freedom with respect to the phase between modulation pulse and sawtooth cycle, yielding more flexibility in the choice of the duty cycle. Consequently, locking uses less gyrotron power than sawtooth pacing, since the former can achieve the same periods with smaller duty cycles.

6.3.2 Locking on small sawtooth periods

Next, the same type of locking simulations have been performed using a smaller mirror angle, in this case $\vartheta = 6^\circ$ corresponding to a deposition inside $q = 1$, in an attempt to shorten the sawtooth period. This value of ϑ is close to the minimum of the CW steady-state input–output map in [26], which is located at $\vartheta = 6.4^\circ$. Again, $I_{\max} = 2$ kA has been used.

The obtained locking range is depicted in the grid of figure 6.5, using various combinations of pulse period $3 \leq \tau_{\text{pulse}} \leq 15$ ms and duty cycle $0\% < w < 100\%$. Again, the black circles at 0% and 100% indicate the ohmic period of 15 ms and the CW sawtooth period of 3.3 ms, respectively. Compared with the previous results subharmonics do now appear, as figure 6.5(a) shows. For some combinations of τ_{pulse} and w the sawtooth period τ_s locks at an integer times τ_{pulse} . Consequently, the total locking range consists of ‘islands’ of different periodicity $\tau_s/\tau_{\text{pulse}}$. Roughly speaking these higher periodicity regions are essentially scaled versions of part of the periodicity 1 region; two 40% 5 ms pulses yield nearly the same sawtooth response as a 40% 10 ms pulse. This is confirmed by figures 6.5(b) to (d), which show that convergence speed and phase during locking is similar for each periodicity. Hence, these higher periodicities do not provide an additional operating space and will not be further addressed in

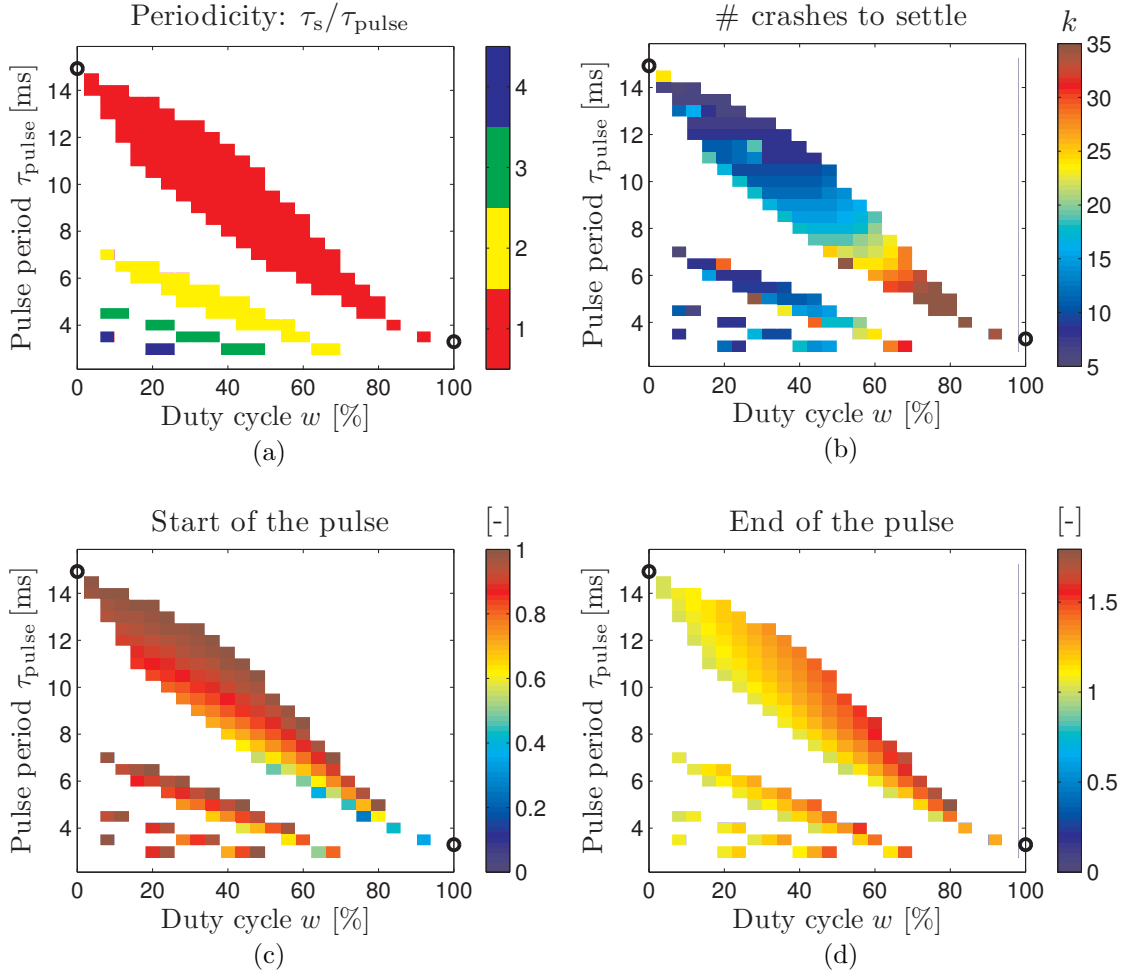


Figure 6.5: Sawtooth period locking range for $I_{\text{max}} = 2$ kA and $\vartheta = 6^\circ$, corresponding to EC depositions inside $q = 1$. (a) Periodicity of the locked sawtooth, i.e. the ratio between locked period τ_s and pulse period τ_{pulse} . (b) Convergence speed, expressed as number of crashes k until the sawtooth period τ_s settles. (c), (d) Phase in locked situation, expressed in relation to the previous sawtooth crash.

this section. We only focus on the locking range for periodicity 1, which is somewhat smaller than in figure 6.2. The selection of the appropriate duty cycle w for a desired period τ_{pulse} is thus more delicate in case of period shortening. Moreover, there is a clear relation between w and the locked period; smaller periods need larger duty cycles. Hence, it effectively takes more power to obtain smaller periods, as could be expected.

Apart from some very small τ_{pulse} and an occasional outlier, the speed of convergence is again quite fast. Figure 6.5(b) shows that locking generally occurs within 5 to 35 crashes, where the convergence speed clearly decreases with decreasing period τ_{pulse} ; it takes roughly 6 times as many crashes to settle on 3 times as small periods. Typical time responses of fast and slow locking cases, as well as responses where no locking occurs, are very similar to the results shown in figure 6.3(a).

The phase during locking is depicted in figures 6.5(c) and (d), where figure 6.5(d)

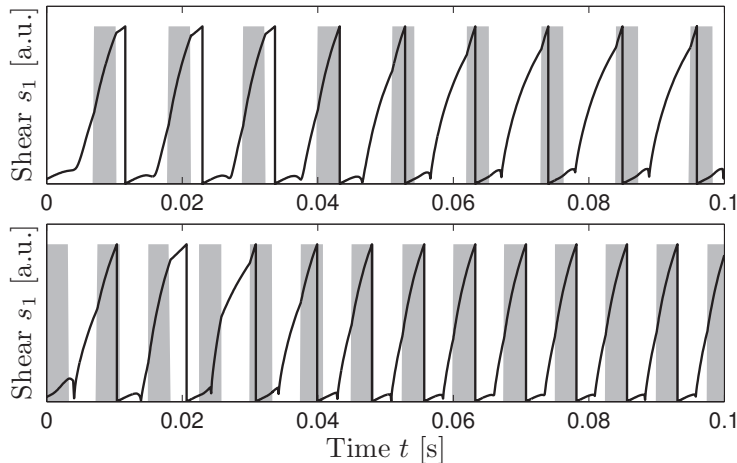


Figure 6.6: Specific locking results showing the evolution of the magnetic shear at $q = 1$ with a 2 kA modulated current drive and $\vartheta = 6^\circ$, for $\tau_{\text{pulse}} = 11$ ms, $w = 30\%$ (top) and for $\tau_{\text{pulse}} = 7.5$ ms, $w = 44\%$ (bottom).

shows that for every locked sawtooth the pulse ends after the next crash, i.e. $\varphi_{\text{end}} > 1$. Hence, for sawtooth period shortening, the sawtooth ‘aligns’ itself with the ECCD modulation such that the crash occurs *during* the current drive pulse. Moreover, the phase generally decreases with decreasing τ_{pulse} . This is illustrated by the evolution of the magnetic shear at $q = 1$ of the two examples in figure 6.6. In the top plot τ_{pulse} is relatively large (11 ms), so the pulse needs to increase the shear only slightly in a short time to obtain the desired period. As a result, the crash is aligned towards the start of the pulse. In the bottom plot τ_{pulse} is much smaller (7.5 ms), yielding an alignment where the crash is near the end of the pulse, so that s_1 is increased more and faster by the pulse. Note that this suggests that ECCD is mostly effective near the end of the sawtooth cycle.

These locking simulations can be repeated for various different mirror angles and corresponding EC deposition locations. A short overview of these results is given in figure 6.7, where the locking ranges for mirror angles 4° , 6° , 7° , 7.7° , 8° and 9° are related to the 2 kA CW steady-state map of the sawtooth model, which has been presented before in [26]. The important observation from this figure is that the locking ranges are the largest near the extrema of the CW map, i.e. for depositions close to the $q = 1$ surface. The locking ranges typically get narrower as the deposition location moves to either the plasma centre or the plasma edge. A possible explanation is that an on–off pulse at such depositions is low-pass filtered through the diffusive time-scale before it reaches the $q = 1$ surface, so that its influence on the shear s_1 at this surface is smoothed. A pulsed current drive with a maximum current I_{max} and duty cycle w will then effectively be the same as a CW current drive with a total current level of $I_{\text{CD}} = \frac{w}{100\%} \cdot I_{\text{max}}$. Consequently, the locking range reduces to a single line. To fully make use of the benefits of sawtooth period locking, one should thus try to operate close to $q = 1$ in the vicinities of the extrema.

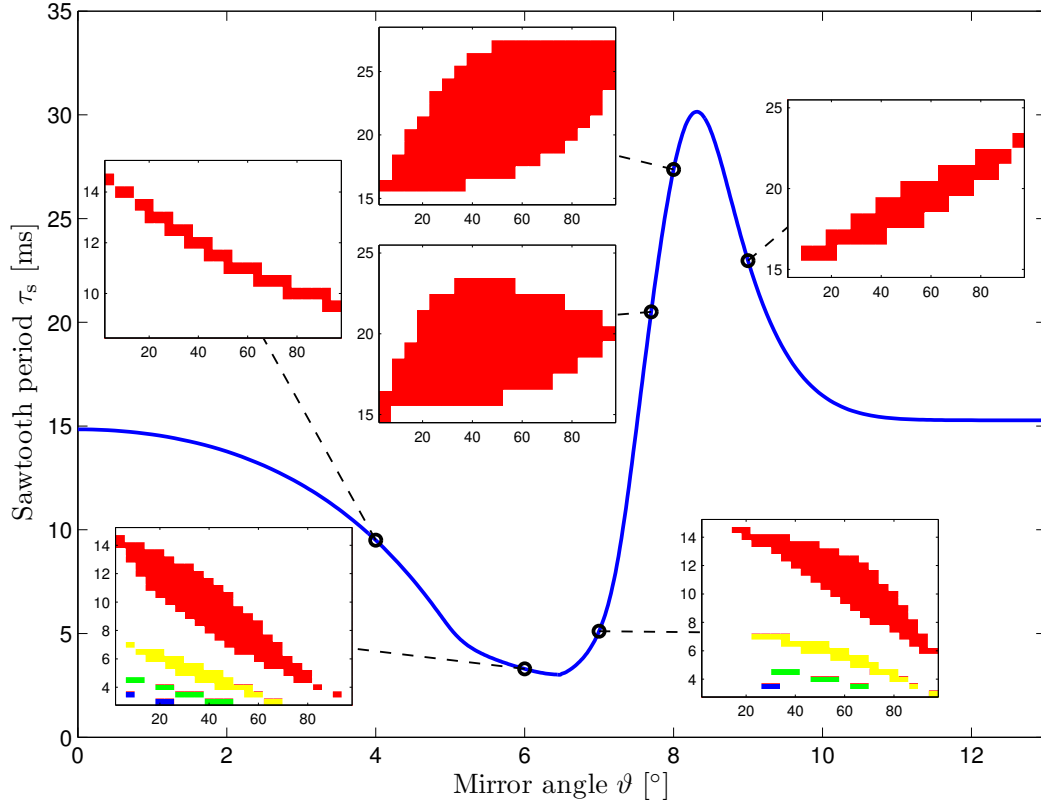


Figure 6.7: Overview of specific locking ranges in relation to the 2 kA continuous wave steady state input–output map. The coloured pixels indicate the periodicity of the locked periods. For CW the change in deposition location from $\tau_{s,\min}$ (at $\vartheta = 6.4^\circ$) to $\tau_{s,\max}$ (at $\vartheta = 8.4^\circ$) is about 20 mm, leading to a 7 mm change in the $q = 1$ location.

6.3.3 Injection locking and robustness

The size of the locking range is an important aspect of injection locking, since a large locking range indicates that the technique can be robust against perturbations and disturbances. This can be understood by considering figure 6.7 again. When the locking ranges are large, like at 7.7° and 8° in this figure, there is a relatively large overlap of the ranges between two specific ϑ , in this case $7.7^\circ \leq \vartheta \leq 8^\circ$. Hence, when the sawtooth is locked at a certain τ_{pulse} with a w somewhere in this overlapping region, it is likely to remain locked at the exact same period even if ϑ is time-varying within the same bounds. As such locking can accommodate variations in, e.g. deposition location, plasma shape or plasma position. A similar reasoning holds for other disturbances or changing plasma conditions also.

This robustness is demonstrated by the results in figure 6.8, where two open-loop strategies to obtain a 25 ms period are compared: using a CW ECCD of 1.6 kA (grey) and using a 25 ms 60% duty cycle ECCD modulation of 2 kA (black), both with $\vartheta = 8^\circ$. In the first simulation, depicted in figure 6.8(a), the plasma current I_p is slowly ramped down once the period is settled at the desired 25 ms. In the CW case the sawtooth period immediately starts to deviate and eventually drifts away, due

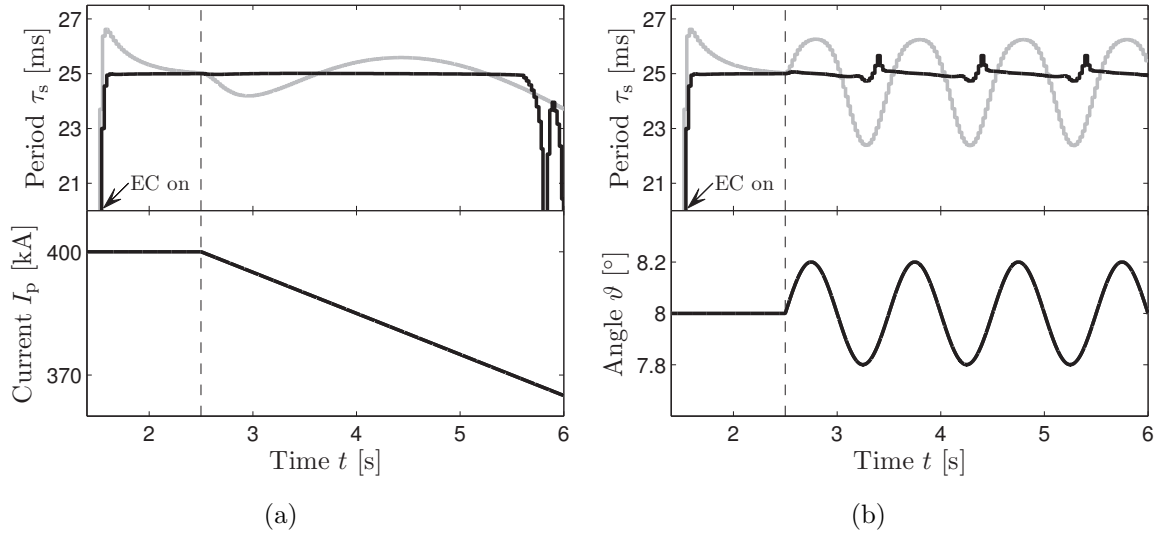


Figure 6.8: Simulation results illustrating the robustness of injection locking (black; with $I_{\max} = 2$ kA, $\tau_{\text{pulse}} = 25$ ms and $w = 60\%$) compared with CW operation (grey; with $I_{\text{CD}} = 1.6$ kA), during (a) a slow ramping down of the plasma current; and (b) an oscillation of the EC mirror angle.

to the corresponding change in the location of the $q = 1$ surface. In contrast, the modulated current drive retains locking at 25 ms over a large time span, until I_p drops below 370 kA. The $q = 1$ surface has moved 8 mm towards the plasma centre by then, which is half the size of the EC beam width (16 mm). Hence, injection locking has a more robust performance than open-loop CW operation, since it achieves a sawtooth period of exactly 25 ms regardless of the actual I_p (as long as it remains between 370 and 400 kA).

In figure 6.8(b) a 1 Hz sinusoidal disturbance is added to the EC mirror angle ϑ , to simulate the effect of an oscillating deposition location. In the CW case the sawtooth period starts to oscillate in phase with the disturbance, taking values between 22.4 and 26.2 ms. The response in the locked situation is quite different. Since the phase between pulse and sawtooth cycle is not constant, as was shown in figures 6.2(b) and (c), it needs to track the change in the deposition location. As a consequence, the period initially decreases slowly to align the crash closer to the end of the pulse, but then rapidly increases again when ϑ is at its minimum, forcing a ‘re-alignment’ where crash and end of the pulse are further apart. The sawtooth period thus displays a 1 Hz periodic response, but it essentially remains locked at a period between 24.7 and 25.7 ms, i.e. having much smaller variations than for the CW case. Note that both simulations in figure 6.8 also show that locking converges faster than CW operation, as the settling of the period after the ECCD switch-on at $t = 1.5$ s is much smaller.

Figure 6.9 shows a simulation where the noise on ϑ is high-frequency, which mimics the jitter often observed on the sawtooth period. A 1 kHz Gaussian disturbance with a standard deviation of $\sigma = 0.5^\circ$ was added to the nominal mirror angle $\vartheta = 8^\circ$

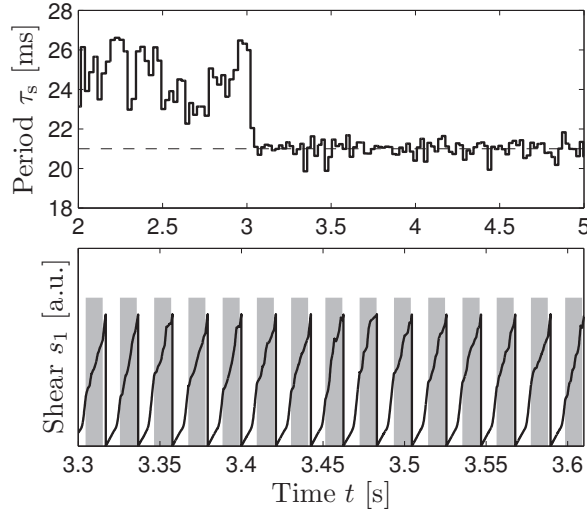


Figure 6.9: Simulation with a high-frequency noise on the nominal mirror angle $\vartheta = 8^\circ$. Initially I_{CD} is constant at 2 kA, from $t = 3$ s it is modulated with $\tau_{\text{pulse}} = 21$ ms and $w = 50\%$. Despite some small remaining jitter on the period (top plot), the sawtooth remains locked for the rest of the simulation, as is visualized by the bottom plot.

throughout the simulation. The top plot shows that with a 2 kA CW current drive (up to $t = 3$ s) the sawtooth period varies roughly between 23 and 27 ms. At $t = 3$ s the current drive is modulated with $\tau_{\text{pulse}} = 21$ ms and $w = 50\%$, after which the sawtooth quickly locks, thereby reducing the jitter and keeping τ_s between 20 and 22 ms. The sawtooth remains locked for the rest of the simulation despite the jitter, which is illustrated by the timing of the ECCD modulation compared with the evolution of the shear s_1 in the bottom figure. The phase remains approximately the same, implying that the sawtooth cycle and the modulation remain synchronized (not a single cycle is ‘slipped’).

6.3.4 Effect of a larger current drive

In CW operation a larger I_{CD} can either reduce or increase the shear at $q = 1$ more effectively, thereby yielding larger or smaller sawtooth periods. Moreover, a large EC driven current also influences the location of the $q = 1$ surface, which is important for locking. This motivated the choice to investigate the influence of I_{CD} on the locking results, by repeating the simulations of section 6.3.1 with a twice as large current drive.

Using $\vartheta = 8^\circ$ the results depicted in figure 6.10 were generated, which are comparable to the results in figure 6.2 in terms of convergence speed and phase. Figure 6.10(b) shows that the locking convergence is generally only a fraction slower, where smaller duty cycles w still tend to settle quicker than larger ones. Moreover, the phase between the modulation and a locked sawtooth cycle is also comparable, as figures 6.10(c) and (d) show that the alignment is again such that the pulse is near the end of a cycle.

There are also some clear differences. First, figure 6.10(a) shows that higher periodicity locking can occur. However, like in section 6.3.2, these higher periodicities

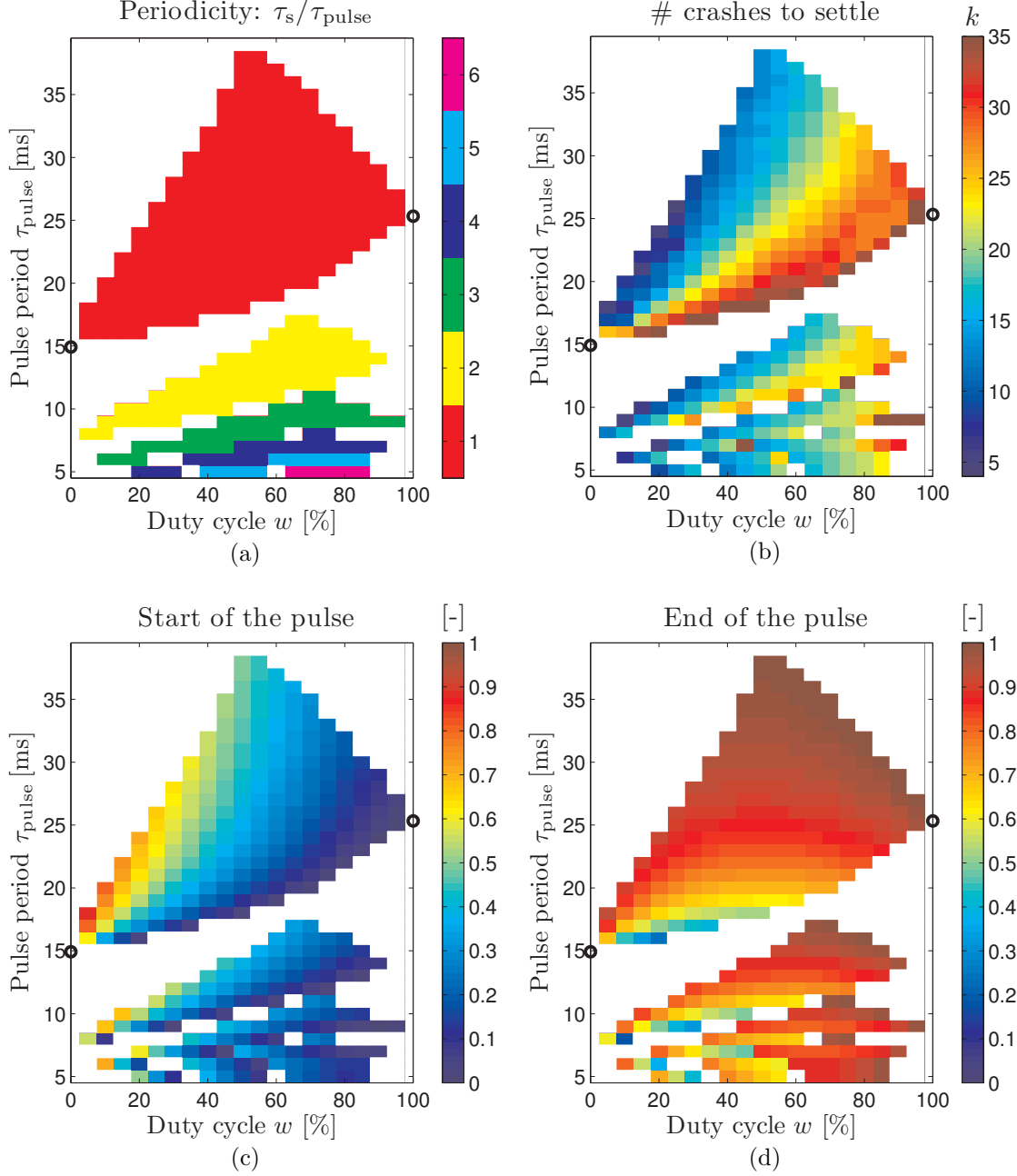


Figure 6.10: Sawtooth period locking range for $I_{\text{max}} = 4$ kA and $\vartheta = 8^\circ$, corresponding to EC depositions slightly outside $q = 1$. (a) Periodicity of the locked sawtooth. (b) Speed of convergence, expressed as number of crashes k until the sawtooth period τ_s settles. (c), (d) Start and end of the pulse relative to the previous sawtooth crash, indicating the phase in locked situation.

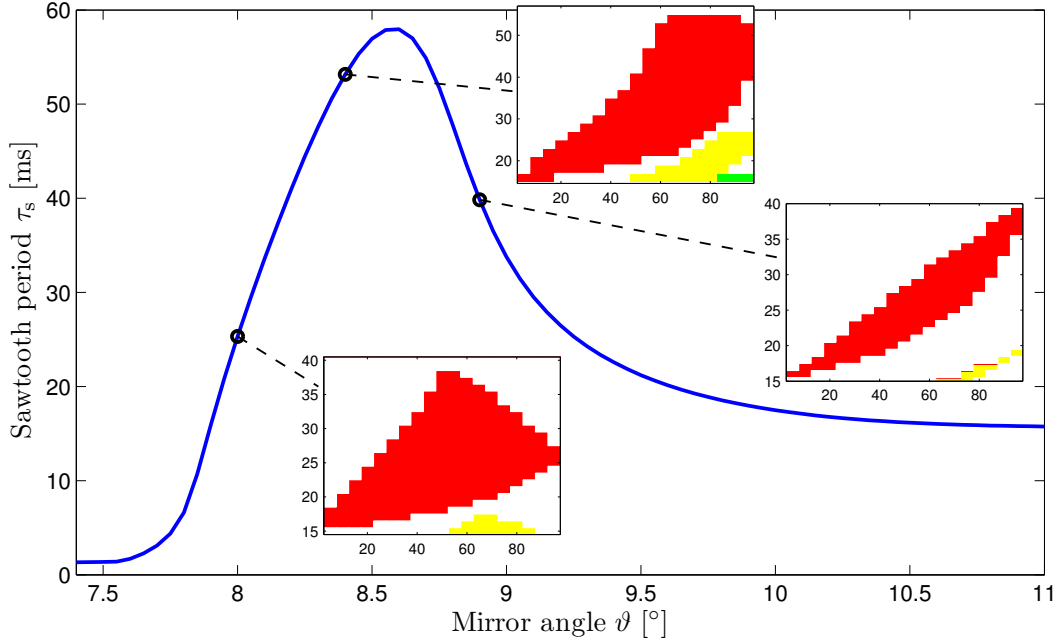


Figure 6.11: Overview of specific locking ranges in relation to part of the 4 kA CW steady state input–output map. The coloured pixels indicate the periodicity of the locked periods.

are essentially scaled versions of the periodicity 1 locking range and thus do not extend the operational space. Second, the locking range is much larger than in figure 6.2, even covering locked periods which are larger than the 4 kA CW period (25.3 ms) at this ϑ . The sawtooth can be locked to a period up to 38 ms using a 4 kA pulse with a 50% duty cycle, hence using effectively the same amount of power as a 2 kA CW current drive.

The shape of the locking range in figure 6.10 shows similarities with the result for $\vartheta = 7.7^\circ$ in figure 6.7, which suggests that the ECCD deposition is now closer to the $q = 1$ surface. This is confirmed by figure 6.11, in which a part of the 4 kA steady-state input–output map (with an expanded $q = 1$ surface) is compared with 4 kA locking simulations at 8° , 8.4° and 8.9° . The increase of I_{CD} has changed the shape of the locking ranges and generally made them somewhat larger; both the range of locked periods has increased, as the set of duty cycles w for which locking occurs. Moreover, the results indicate that periods larger than CW (for a specific ϑ) can only be achieved on the positive slope of the input–output map, i.e. close to $q = 1$ surface. It also appears that the maximum CW period forms an upperbound for the maximum locked period. However, locking can achieve this periods with duty cycles smaller than 100%, hence requiring less time-averaged power.

The large locking range in figure 6.10 follows from the fact that large current drives close to $q = 1$ have a strong effect on s_1 . This is illustrated by figure 6.12, which depicts the autonomous ‘alignment’ or synchronization of the sawtooth cycle with the fixed ECCD modulation. The example in the top plot shows that, when the sawtooth

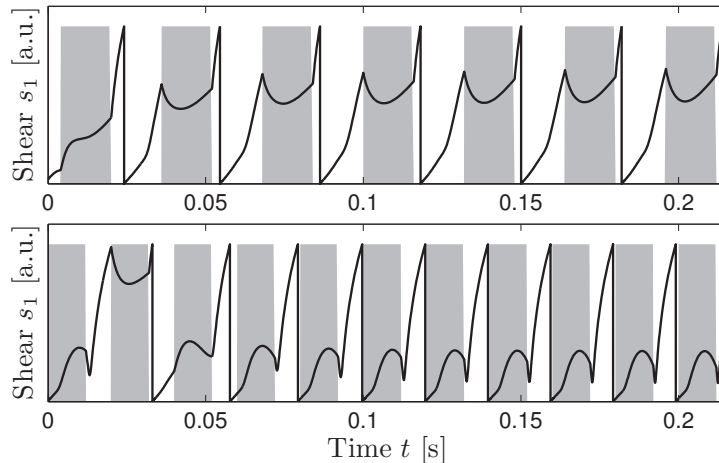


Figure 6.12: Evolution of the shear at $q = 1$ using a 4 kA modulated current drive and $\vartheta = 8^\circ$, for $\tau_{\text{pulse}} = 32$ ms, $w = 50\%$ (top) and $\tau_{\text{pulse}} = 20$ ms, $w = 60\%$ (bottom).

is locked, s_1 first evolves like in the ohmic case during the first 14 ms after a crash. Shortly before s_1 would reach the critical shear s_{crit} the 4 kA current drive starts, thanks to which s_1 is significantly reduced. The current drive succeeds in keeping it below the crash trigger, but as soon as the pulse ends the shear increases very rapidly, forcing a crash shortly afterwards. Hence, the phase for this relatively large period (32 ms) is such that the pulse is at the end of the sawtooth cycle, where it has the largest effect. For comparison, the bottom plot shows a simulation with a much smaller period (20 ms), where the pulse is located at the beginning of a locked sawtooth cycle.

6.3.5 Validation with a CRONOS simulation

Although a full understanding of the underlying physics is still missing, sawtooth period locking can almost certainly be attributed to the fact that the sawtooth is a dynamic relaxation oscillation: a magnetic process with both slow and fast time-scales as in (6.1a)–(6.1b), yielding a limit cycle with an adjustable period. The locking behaviour displayed in this paper is therefore not just an exclusive property of the used model, as more advanced sawtooth models, as well as experimental sawteeth, are expected to be dominated by similar magnetic dynamics. Hence, locking of the sawtooth period on the ECCD modulation period is likely to occur also in comprehensive transport codes or tokamak experiments. As a proof of principle, this section will discuss a specific simulation result using the CRONOS 1.5D transport solver [33].

In this particular CRONOS simulation the 1D transport equations for current diffusion, electron temperature and ion pressure are solved using the ‘`zkiautonew`’ transport model, a relatively fast model based on 0D energy confinement time scaling laws. Moreover, neoclassical transport is calculated by NCLASS, whereas the profiles for electron density (relatively flat around $r = 0$ to neglect the effect of sawtooth crashes), NBI heating (a 28 cm wide 2 MW Gaussian distribution centred at $r = 0$), and ECCD (a 12 mm wide 2 kA Gaussian distribution) are explicitly prescribed. The 2D

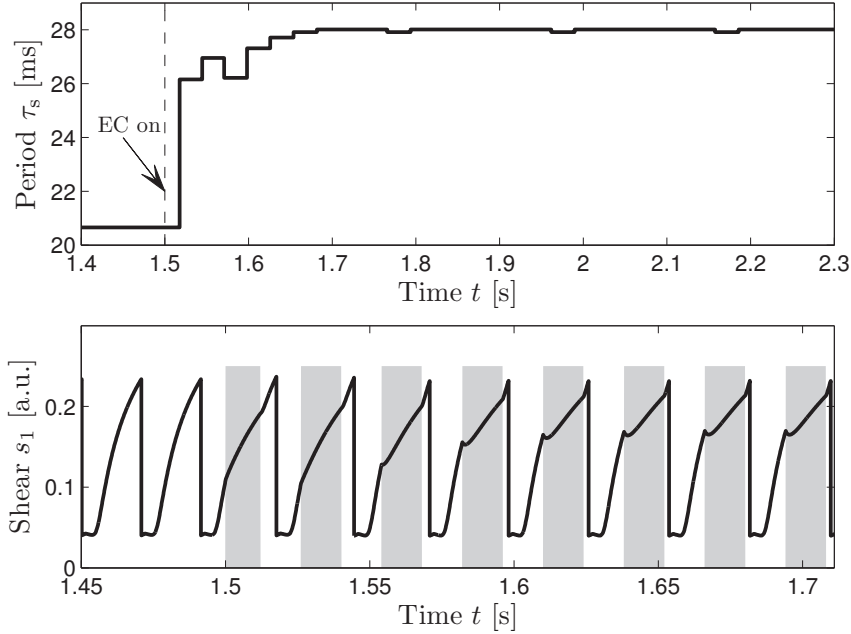


Figure 6.13: Injection locking result with the CRONOS transport code, using a 50% duty cycle ECCD modulation with a 28 ms period, starting at $t = 1.5$ s. The sawtooth period changes from its ohmic value to the prescribed 28 ms (top), locking within 7 crashes. The evolution of the shear at the $q = 1$ surface (bottom) resembles the top result in figure 6.3(b), showing a similar phase between pulse and sawtooth cycle.

magnetic equilibrium at every time step is calculated by the HELENA fixed boundary solver, which has been modified to the TEXTOR geometry. Sawtooth crashes are incorporated through the Porcelli reconnection module.

The CRONOS result in figure 6.13 indeed demonstrates the locking behaviour of the sawtooth in a comprehensive transport code. The sawtooth period is initially at its ohmic value, which is 20.7 ms in this case, where the $q = 1$ surface before the crash is located at a normalized radius of $\rho = r/a = 0.26$. From time $t = 1.5$ s onwards a 28 ms 50% duty cycle ECCD modulation of 2 kA is deposited at $\rho = 0.28$, so slightly outside $q = 1$. The top plot of figure 6.13 shows that the sawtooth period then indeed converges to this 28 ms within 7 crashes. The period remains locked for the rest of the simulation, even when some numerical disturbances occur at 1.77, 1.96, and 2.16 s. The bottom of figure 6.13 depicts the evolution of the shear at $q = 1$ during the first few crashes after ECCD switch-on, together with the applied ECCD pulses. This plot clearly resembles the previous results in figure 6.3(b): the growth rate of s_1 during the pulse is reduced, and the sawtooth cycle ‘aligns’ with the modulation until it is at rest at the same period as the ECCD modulation. The phase in locked situation is again such that the crash occurs shortly after the end of the pulse. The CRONOS simulation in figure 6.13 is thus in full agreement with the results presented in section 6.3.1.

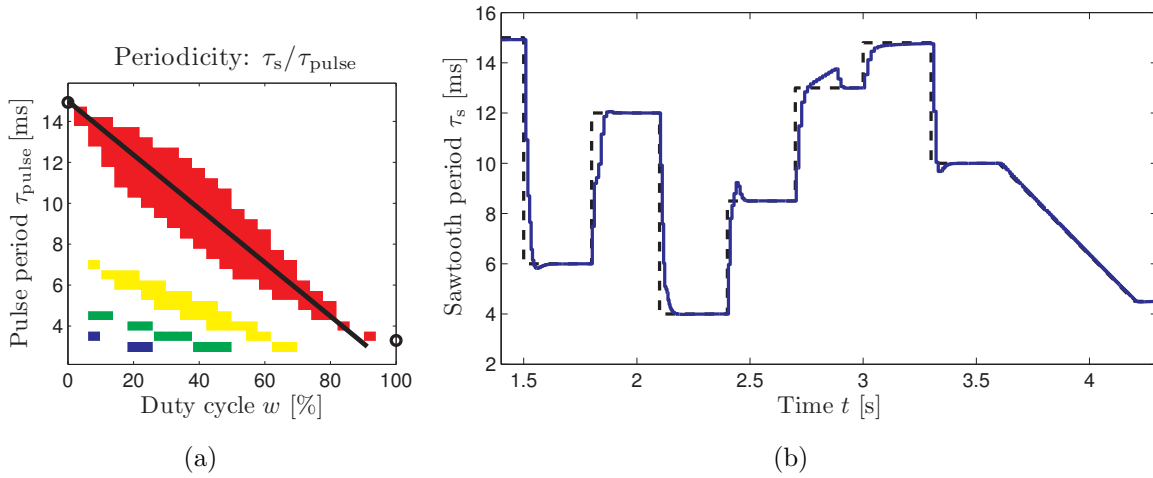


Figure 6.14: Open-loop locking control for $\vartheta = 6^\circ$ and 2 kA modulated current drive: (a) design of the modulation function given in (6.6), based on the first harmonic of the response; (b) simulation result using (6.6), where the desired period (dashed) changes to arbitrary values between 4 and 15 ms, which are tracked by the system perfectly (solid) within a only a small amount of crashes.

6.4 Open-loop locking controller design

The results in the previous section indicate under which conditions the sawtooth oscillation will lock to a constant *a priori* known period. Given certain fixed ϑ and I_{max} , this allows us to define combinations of τ_{pulse} and w such that the sawtooth settles at a certain desired period τ_s . Hence, we can define simple open-loop control routines in terms of τ_{pulse} and w as functions of a reference period $\tau_{s,\text{ref}}$.

As a proof of principle, this section will briefly discuss two specific locking controller designs and corresponding time-domain results: one for period shortening using a 2 kA current modulation, and one for period lengthening using a 4 kA current modulation.

6.4.1 Locking control to small periods

One of the main advantages of injection locking is its large robustness, which is closely related to the size of the locking range. Robustness is a very important issue for sawtooth period control, as sawteeth are often subject to uncertainties, parameter variations, and disturbances. Hence, locking controller design should focus on large locking ranges, which is why our design is based on the periodicity 1 region in figure 6.5(a). The design itself consists of finding a function for w which goes right through the locking range, preferably through the centre of the region to optimize robustness. A simple linear function which exactly satisfies this is depicted in figure 6.14(a). The controller thus consists of two functions, the periodicity and the modulation function, which relate a setpoint or desired sawtooth period $\tau_{s,\text{ref}}$ to τ_{pulse} and w :

$$\tau_{\text{pulse}} = \tau_{s,\text{ref}} \quad \text{and} \quad w = \frac{76}{10} (15 - \tau_{s,\text{ref}}), \quad (6.6)$$

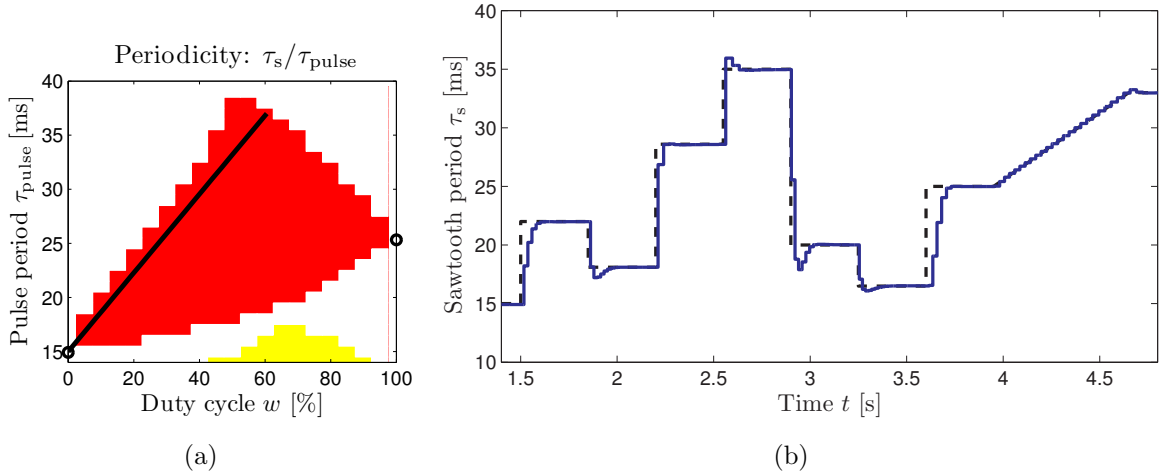


Figure 6.15: Open-loop locking control for $\vartheta = 8^\circ$ and 4 kA modulated current drive: (a) design of the modulation function given in (6.7), based on the fastest responses within the locking range; (b) simulation result using (6.7), again showing perfect and very fast tracking to arbitrary setpoints, needing less than 8 crashes to settle on each value.

where both τ_{pulse} and $\tau_{\text{s,ref}}$ are in ms, and w is a percentage of the pulse period τ_{pulse} . This open-loop controller has been combined with the original sawtooth model in a Simulink environment, in order to test its performance in time-domain. The obtained results are shown in figure 6.14(b). In this simulation the desired period $\tau_{\text{s,ref}}$ (dashed) is changed stepwise to different values between 4 and 15 ms. The sawtooth period locks perfectly at any of these values, in all cases within 30 crashes, corresponding to at most 0.2 seconds. For comparison, in [26] closed-loop settling times between 0.4 and 20 s were obtained. In some cases in figure 6.14(b) there is a little overshoot, which is only a few percent of the total step size. Even when the reference starts to decrease slowly at $t = 3.7$ s, the sawtooth period tracks $\tau_{\text{s,ref}}$ very accurately. Hence, a simple open-loop locking control algorithm as in (6.6) is indeed sufficient to achieve fast, accurate, and robust tracking of any desired small sawtooth period.

6.4.2 Locking control to large periods

The above locking controller design can be repeated for the case of sawtooth period lengthening. Here we use the case study of the 4 kA locking results as discussed in section 6.3.4. Again, we choose a large as possible locking range and therefore base the design on the periodicity 1 region. Instead of focusing on robustness as in the previous design, we now require the modulation function to satisfy two other objectives: the convergence speed should be maximized and a period of 35 ms or more should be realizable. Hence, the modulation function is tuned to stay at the left of the locking range, as depicted in figure 6.15(a), thereby going through the quickly converging part of figure 6.10(b) and nearly reaching the largest locked period. Again, the controller

consists of two simple linear functions, which are now defined as

$$\tau_{\text{pulse}} = \tau_{\text{s,ref}} \quad \text{and} \quad w = \frac{55}{20} (\tau_{\text{s,ref}} - 15). \quad (6.7)$$

The sawtooth model described in section 6.2.1 has been combined with this open-loop controller to test its time-domain performance in simulation. The results are shown in figure 6.15(b). The desired period $\tau_{\text{s,ref}}$ (dashed) is changed stepwise to different values between 15 and 35 ms; the sawtooth period (solid) locks perfectly to any of these values. Expressed in terms of number of crashes the convergence is indeed very fast, needing at most 8 crashes to lock, corresponding to at most 0.15 s. Moreover, the sawtooth remains locked, even if the setpoint slowly drifts to larger than CW periods.

6.4.3 Comments on control by sawtooth period locking

The results in figures 6.14(b) and 6.15(b) make a strong case for injection locking as a sawtooth period control strategy. For completeness, some additional remarks can be made though. Strictly speaking, for arbitrary time-varying setpoints we cannot provide *a priori* guarantees on injection locking convergence speed or overshoot merely based on the results in figure 6.5 or 6.10. Note that the convergence plots in figures 6.5(b) and 6.10(b) are only indicative for the case where the sawtooth system is initially in ohmic situation and the current drive modulation is then switched on. These results are not necessarily predictive for the case where the modulation changes over time, e.g. when its duty cycle changes either stepwise or gradually as in figures 6.14(b) and 6.15(b). In such situations the sawtooth period might somehow converge quite slow, or even oscillate with large overshoots like the green response in figure 6.3(a).

Although this behaviour cannot explicitly be ruled out beforehand, it is very likely that the speed of convergence for such time-varying setpoints is very similar to the results in figures 6.5(b) and 6.10(b). These plots show a very clear structure, strongly suggesting that the obtained values are not coincidental. Instead, they demonstrate a system property, which is expected to dominate in other situations also. This is underlined by the fact that the obtained convergence speeds in the controlled time-domain simulations in figures 6.14(b) and 6.15(b) are of the same magnitude as predicted by the convergence plots in figures 6.5(b) and 6.10(b). This justifies the control laws in (6.6) and (6.7), although their validity is, strictly speaking, not proven yet.

In any case, the demonstrated convergence speed by means of injection locking is quite impressive. Injection locking needs on average only 5 to 30 crashes to settle on a desired sawtooth period (with an error tolerance of just 0.1%). This clearly outperforms sawtooth control by means of a single linear controller for the EC mirror angle, as described in [26], where convergence speeds are typically between 9 and 950 crashes, or even slower when the dynamics of the mirror launcher is also taken into account. Another drawback of that method is the large spread in convergence speeds due to the gain variations of the system: large periods converge much slower than small ones. Control by injection locking does not have this problem, as all setpoints

are tracked with nearly the same speed. This performance improvement is partly due to the fact that injection locking utilizes a much faster actuator; the EC driven current I_{CD} can be altered much faster than the mirror angle ϑ .

It is important to note that open-loop locking control is very different from using a simple CW look-up table for ϑ or I_{CD} as a feedforward controller. Such an approach is not robust, as any disturbance or parameter variation will result in an error which will not be corrected. In contrast, due to the wide locking ranges shown in this paper, injection locking will remain locked at the required period, keeping the error small, even in the presence of disturbances or parameter variations, as has been illustrated in figures 6.8 and 6.9. In essence, on-off switching of the EC power enables us to utilize specific dynamic behaviour of the sawtooth, which would not be excited in CW operation.

One typical advantage of the method in [26] is that it limits the amount of overshoot in closed-loop responses *a priori* by means of defining a modulus margin; generally a smaller modulus margin allows less overshoot. Unfortunately, such explicit bounds are not available for injection locking. In fact, the amount of overshoot in figures 6.14(b) and 6.15(b) seems rather unpredictable, and even non-linear oscillatory responses as depicted in figure 6.3(a) can possibly occur. There is thus no *a priori* guarantee that, when the setpoint changes to a different value, the sawtooth period will not reach a very large value at some point and thereby accidentally triggers an NTM. Considering the previously shown tracking results, this is however not very likely to occur as long as the control law is properly tuned, i.e. with large robustness margins and utilizing the faster parts of the locking range.

6.5 Conclusions and discussion

In this paper we have presented injection locking as a new technique to control the sawtooth period using ECCD. A representative dynamic model of the sawtooth oscillation has been introduced, which has been used in an extensive analysis of the locking behaviour of the sawtooth. In this analysis the deposition location, determined by the EC mirror angle ϑ , is kept constant, while the EC power or current drive I_{CD} is modulated with a certain period τ_{pulse} and duty cycle w . For certain combinations of τ_{pulse} and w the sawtooth period will lock on the modulation period τ_{pulse} , or even on multiples of τ_{pulse} (subharmonics). Results show that injection locking can be used for both sawtooth period lengthening and shortening, dependent on the fixed deposition location. Any period between the ohmic and CW values can be achieved; for depositions close to $q = 1$ even larger than CW periods were obtained, while using effectively (time-averaged) less power. The locked period does appear to be upper bounded by the maximum CW period achievable with the selected I_{CD} , although this statement requires further research. The phase between pulse and sawtooth cycle in locked situation has been shown to be systematically dependent on the modulation parameters, while overall the convergence of the sawtooth period locking turns out to

be very quick. The recently reported case of sawtooth pacing [27] has been shown to be a special case of injection locking, where the phase is *a priori* fixed by a closed loop. Furthermore, a comprehensive CRONOS simulation indeed verifies the locking results.

The locking results have been used in a simple open-loop controller design to express the modulation parameters τ_{pulse} and w as functions of the desired sawtooth period $\tau_{\text{s,ref}}$. Simulations have shown that this control routine accurately tracks desired periods very quickly, much faster than with conventional sawtooth control methods based on deposition location variations [26]. Part of this performance improvement can be attributed to the fact that injection locking does not rely on the mechanics of the EC mirror launcher, but uses a much faster EC power modulation instead.

Another advantage of injection locking is its robustness, especially around $q = 1$. The large size of the locking ranges near this region implies that the method is rather insensitive to deviations in the duty cycle w , but it also indicates that the method is robust against uncertainties, disturbances and parameter variations. In particular, it has been shown that the sawtooth period will remain locked to the desired period even when the plasma current changes or the deposition location oscillates, either slowly or rapidly. As such, injection locking outperforms CW feedforward control in terms of robustness. Moreover, control of the sawtooth period using injection locking typically requires less time-averaged gyrotron power than CW operation, as mentioned above.

In this paper the feasibility and advantages of injection locking of the sawtooth period has been shown via extensive simulations. An early attempt to test sawtooth period locking experimentally, reported in [27], was unsuccessful, most likely because the chosen power modulation was outside the locking range. However, recent experiments on TCV [36] do demonstrate successful locking of the sawtooth, displaying large similarities with the simulation results in this paper. This shows that the presented analyses and controller designs can be applied to real tokamaks also.

Extrapolating to ITER, injection locking might have additional benefits. Since sawtooth period locking only needs the EC power during the duty cycle, the gyrotron is available for other purposes during the rest of the period. This is especially interesting on ITER, e.g. for the ELMy H-mode scenario 2, where the sawtooth period is foreseen to be in the order of 50 s or more; for a typical duty cycle of 50% this means that we have at least 25 s per cycle to use the same actuator for, e.g. NTM suppression, resistive wall mode (RWM) control or profile control. The power then needs to be deposited far away from the $q = 1$ surface, otherwise it interferes with the period locking. The necessary fast change in the deposition location of the gyrotron power could either require the EC mirror launcher installation [37] to be fast and accurate, or require the use of fast diplexers like the FADIS system [38] which can distribute the gyrotron power by switching between the equatorial and upper ports. This way we can possibly make optimal use of the available gyrotron power, which can perhaps contribute to the increase in the fusion energy gain factor Q . In any case, it is likely that on ITER both the EC mirror angle and the gyrotron power need to be feedback controlled to achieve this goal.

Finally, the principles of injection locking could possibly be applied more broadly. The various pacing techniques that have been suggested in the literature to influence repetitive plasma processes are possibly related to this approach. An example is ELM pacing, a method to control the frequency of an edge localized mode (ELM) by means of periodic pellet injection [39] or periodic magnetic perturbations [40]. It would be interesting to investigate similarities between sawtooth period locking and ELM pacing and their underlying mechanisms, which may shed new light on the ELM control problem using the analyses presented in this paper.

Acknowledgments

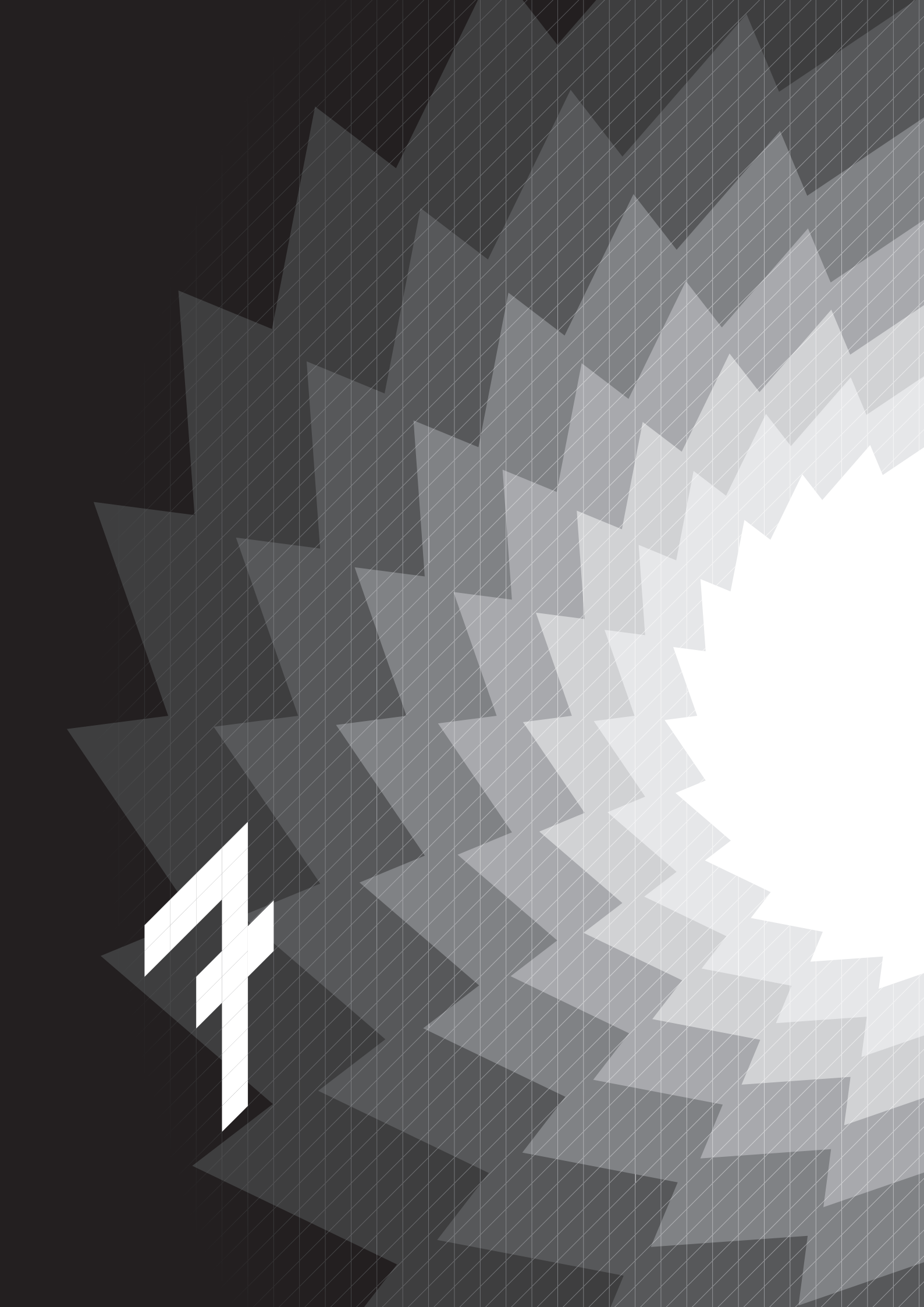
The authors would like to thank Gerd Vandersteen for his inspirational thoughts and suggestions regarding section 6.2.2, and Michael Ypma for carrying out the CRONOS simulation reported in section 6.3.5.

The work in this paper has been performed in the framework of the NWO-RFBR Centre of Excellence (grant 047.018.002) on Fusion Physics and Technology. This work, supported by NWO, ITER-NL and the European Communities under the contract of the Association EURATOM/FOM, was carried out within the framework of the European Fusion Programme. The views and opinions expressed herein do not necessarily reflect those of the European Commission.

References


- [1] von Goeler S. *et al.* 1974 *Phys. Rev. Lett.* **33**(20) 1201
- [2] Hastie R.J. 1997 *Astrophys. Space Sci.* **256**(1) 177
- [3] Wesson J.A. and Campbell D.J. 2004 *Tokamaks* 3rd edn. (Oxford: Oxford University Press)
- [4] Kadomtsev B.B. 1975 *Sov. J. Plasma Phys.* **1**(5) 389
- [5] Nave M.F.F. *et al.* 2003 *Nucl. Fusion* **43**(10) 1204
- [6] Gude A. *et al.* 1999 *Nucl. Fusion* **39**(1) 127
- [7] Chapman I.T. *et al.* 2010 *Nucl. Fusion* **50**(10) 102001
- [8] Sauter O. *et al.* 2002 *Phys. Rev. Lett.* **88**(10) 105001
- [9] Westerhof E. *et al.* 2002 *Nucl. Fusion* **42**(11) 1324
- [10] Chapman I.T. 2011 *Plasma Phys. Control. Fusion* **53**(1) 013001
- [11] Porcelli F. *et al.* 1996 *Plasma Phys. Control. Fusion* **38**(12) 2163
- [12] Campbell D.J. *et al.* 1988 *Phys. Rev. Lett.* **60**(21) 2148
- [13] Chapman I.T. *et al.* 2007 *Plasma Phys. Control. Fusion* **49**(12B) B385
- [14] Graves J.P. *et al.* 2009 *Phys. Rev. Lett.* **102**(6) 065005
- [15] Eriksson L.G. *et al.* 2006 *Nucl. Fusion* **46**(10) S951
- [16] Chapman I.T. *et al.* 2008 *Plasma Phys. Control. Fusion* **50**(4) 045006
- [17] Chapman I.T. *et al.* 2009 *Nucl. Fusion* **49**(3) 035006
- [18] Mück A. *et al.* 2005 *Plasma Phys. Control. Fusion* **47**(10) 1633
- [19] Merkulov A. *et al.* 2004 *Proc. of Joint Varenna-Lausanne Int. Workshop on Theory of Fusion Plasmas* (Varenna, Italy) 279

- [20] Angioni C. *et al.* 2003 *Nucl. Fusion* **43**(6) 455
- [21] Lennholm M. *et al.* 2009 *Fusion Sci. Technol.* **55**(1) 45
- [22] Lennholm M. *et al.* 2009 *Phys. Rev. Lett.* **102**(11) 115004
- [23] Paley J.I. *et al.* 2009 *Nucl. Fusion* **49**(8) 085017
- [24] Paley J.I. *et al.* 2009 *Plasma Phys. Control. Fusion* **51**(5) 055010
- [25] Paley J.I. *et al.* 2009 *Plasma Phys. Control. Fusion* **51**(12) 124041
- [26] Witvoet G. *et al.* 2011 *Nucl. Fusion* **51**(7) 073024
- [27] Goodman T.P. *et al.* 2011 *Phys. Rev. Lett.* **106**(24) 245002
- [28] van der Pol B. 1934 *Proc. IRE* **22**(9) 1051
- [29] Adler R. 1973 *Proc. IEEE* **61**(10) 1380
- [30] Kurokawa K. 1973 *Proc. IEEE* **61**(10) 1386
- [31] Strogatz S.H. 1994 *Nonlinear dynamics and chaos* (Boulder, CO: Westview Press)
- [32] van Berkel M. *et al.* 2011 *Fusion Eng. Des.* in press
- [33] Artaud J. *et al.* 2010 *Nucl. Fusion* **50**(4) 043001
- [34] The MathWorks, Inc. 2007 *Writing S-Functions* Version 6.6
- [35] Hennen B.A. *et al.* 2010 *Plasma Phys. Control. Fusion* **52**(10) 104006
- [36] Lauret M. *et al.* 2011 *Submitted to Phys. Rev. Lett.*
- [37] Henderson M.A. *et al.* 2008 *Nucl. Fusion* **48**(5) 054013
- [38] Kasperek W. *et al.* 2008 *Nucl. Fusion* **48**(5) 054010
- [39] Lang P.T. *et al.* 2003 *Nucl. Fusion* **43**(10) 1110
- [40] Lang P.T. *et al.* 2004 *Plasma Phys. Control. Fusion* **46**(11) L31



CHAPTER 7

Demonstration of sawtooth period locking in TCV plasmas



Abstract

The injection locking technique is applied experimentally on the TCV tokamak. Dedicated TCV-relevant locking simulations are carried out to predict the size and shape of the locking range, upon which initial actuator settings are based. Numerous experimental results are presented, which provide corroborating evidence that the sawtooth period can indeed lock to the modulation period of an externally applied electron cyclotron wave source. The identified locking range is used in the design of a simple open-loop locking controller, which achieves accurate, fast and robust tracking of a continuously changing reference period. Moreover, the experimental results show strong similarities with the predictive simulations.

Parts of this chapter are based on:

M. Lauret, F. Felici, G. Witvoet *et al.* 2011 *Submitted to Physical Review Letters*

7.1 Introduction

The numerical injection locking results [1], discussed in the previous chapter, indicate a novel open-loop method to control the sawtooth period. Where conventional continuous wave (CW) electron cyclotron current drive (ECCD) methods [2–6] use a constant amount of gyrotron power and alter the sawtooth period by a change in deposition location, sawtooth period locking involves a modulation of the gyrotron power and a fixed deposition location. The simulation results have shown that for certain combinations of modulation period and duty cycle, defined as the locking range, the sawtooth period will synchronize or ‘lock’ to the period of the power modulation, and remains in phase with the modulation (i.e. it remains locked) throughout the rest of the simulation run.

The application of this technique resembles the work on dynamic oscillators and injection locking in [7–9]. In essence, the sawtooth relaxation oscillation is a subclass of such dynamic systems. The simulation results displayed in chapter 6 show that the locking behaviour can be attributed to the dynamics of the underlying magnetic diffusion, which is reflected by the sensitivity of the shear at the $q = 1$ surface to the power modulation. This dynamics is expected to be dominant in actual sawtoothing plasmas as well. This hypothesis will be verified in this chapter, as experimental results from the application of the sawtooth period locking technique on a tokamak plasma will be presented [10].

An approach called sawtooth pacing [11], which in the previous chapter has been suggested to be a special case of injection locking, has recently been implemented on TCV. In pacing, sawtooth crashes are monitored in real-time, and a gyrotron pulse is started shortly after a crash has been detected. A sudden removal of this power after a pre-set time τ_{set} causes a next crash to occur shortly thereafter. The resulting power modulation (which is not completely constant as in locking) increases the sawtooth period to a value slightly larger than τ_{set} . The reported success of this approach seems to confirm the applicability of locking as well. However, in [11] it was stated that the sawtooth was not ‘simply locking’ when a constant modulation was applied. A probable explanation for this, based on the insights of [1], is that the applied power modulation was chosen outside the locking range. The gyrotron settings used in this chapter are therefore based on predictive simulations of the locking range, and will be verified afterwards.

This chapter addresses the experimental demonstration of sawtooth period lengthening by means of injection locking, and the subsequent open-loop controller design and implementation. First, the considered tokamak and operational conditions for the experiments is discussed in section 7.2. Section 7.3 presents a predictive locking simulation, which forms the starting point of the experiments. The experimental results are discussed in section 7.4, followed by the conclusions in section 7.5.

7.2 Experimental set-up

The experiments described in this chapter were performed on TCV (Tokamak à Configuration Variable), a relatively small tokamak (with major radius $R_0 = 0.88$ m and minor radius $a = 0.25$ m) which is capable of creating highly elongated plasmas in several shapes. However, in this research ordinary limiter L-mode plasmas are investigated (with elongation $\kappa = 1.48$ and triangularity $\delta = 0.33$), which are similar to the plasmas used in [11]. The main difference is an increase of $q_a = q(a)$, i.e. the value of q at the plasma edge. To avoid NTM triggering and disruptions seen in earlier experiments, $q_a = 3.2$ was used during the experiments.

TCV is equipped with a controllable ECCD system, involving multiple gyrotrons which can generate up to 500 kW of auxiliary power each. Since TCV is relatively small, its current diffusion time-scale is short, yielding relatively short ohmic sawtooth periods of around 2 ms in the above described plasmas. To increase the baseline period to about 10 ms, two gyrotrons (preprogrammed at 250 kW each) were employed during the experiments for a CW power deposition outside the $q = 1$ surface. A third gyrotron, depositing at the same location, was used for the power modulation. This gyrotron was preprogrammed at a 450 kW modulation, unless stated otherwise. The optimal deposition location for the experiments depends on the size and shape of the predicted locking range; figure 6.7 and 6.11 indicate that a deposition slightly outside $q = 1$ and inside the maximum of the steady-state input–output map is preferred in case of sawtooth period lengthening. On TCV this location was found by performing a scan of the toroidal field B_ϕ and plasma current I_p , given a constant $q_a = 3.2$. The obtained values, $B_\phi = 1.22$ T and $I_p = 0.284$ MA, were held constant for each reported experiment. The maximal period with these settings, when the third gyrotron generates 450 kW in CW, is in the order of 40 ms.

7.3 Predictive simulations

To determine suitable initial gyrotron settings, in terms of modulation period τ_{pulse} and duty cycle w , predictive simulations have been performed. To this end the Kadomtsev–Porcelli model discussed in section 2.2 was adjusted for TCV plasmas. The parameters R_0 , a and B_ϕ were changed to the above mentioned values. Furthermore, an electron temperature at the plasma centre $T_0 = 1.2$ keV, an ECCD deposition width $w_{\text{CD}} = 15$ mm and a critical shear $s_{\text{crit}} = 0.275$ were used. However, the plasma current I_p differs from the aforementioned value. The sawtooth model assumes a circular plasma shape, and can therefore contain less current than an elongated triangular TCV plasma. Hence, to obtain the same $q_a = 3.2$ the plasma current in the model was decreased to

$$I_p = \frac{2\pi a^2 B_\phi}{\mu_0 R_0 q_a} = 135.4 \text{ kA}. \quad (7.1)$$

The modified sawtooth model has a natural sawtooth period of 10.1 ms, which thus nearly matches the baseline period in the experiments.

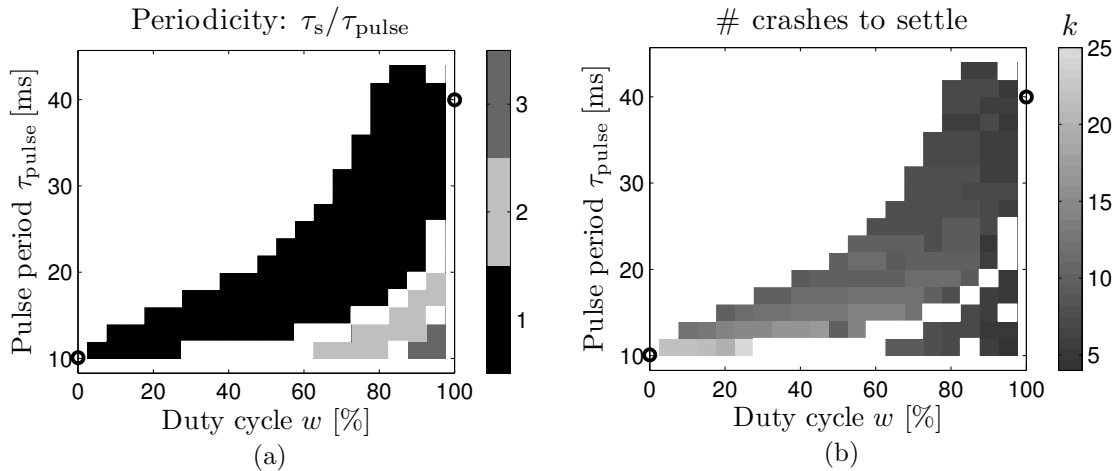


Figure 7.1: Sawtooth period locking range for a typical TCV simulation, with an ECCD deposition slightly outside $q = 1$. (a) Periodicity of the locked sawtooth, i.e., the ratio between locked period τ_s and pulse period τ_{pulse} . (b) Convergence speed, expressed as number of crashes k until the sawtooth period τ_s settles.

The 450 kW modulated gyrotron power is assumed to generate approximately $I_{CD} = 5$ kA of current drive. In agreement with the experimental set-up, in simulation this current drive is deposited slightly outside the $q = 1$ surface, inside the maximum of the input–output map. In CW this yields a sawtooth period of 40.0 ms, which again matches the experimental observation.

This TCV-relevant model has been used in a repeat of the locking simulations described in section 6.2.3. The results are shown in figure 7.1. The locking range is quite large; it covers all periods between the baseline and the CW value, and ‘leans’ towards higher duty cycles. Moreover, there are some small higher-periodicity regions. The locking convergence depicted in figure 7.1(b) is slightly faster than for the TEXTOR simulations in chapter 6. This is in accordance to the smaller dimensions of TCV, which leads to faster diffusion time-scales.

7.4 Experimental results

Under the operational conditions mentioned in section 7.2 the prediction of the locking range has been validated during multiple TCV discharges. This section presents and summarizes some of these discharges.

As mentioned before, there is a baseline CW power injection of 500 kW throughout the whole duration of each discharge. Only the additional power of the third gyrotron is varied. The beginning of each discharge is used to verify the operational conditions, so as to guarantee that the discharges are mutually comparable. This is done by assessing the extent to which the period can be lengthened (by an initial phase of 450 kW additional CW current drive), as well as the baseline sawtooth period (by a subsequent phase during which the additional power is removed). Next, the sawtooth locking

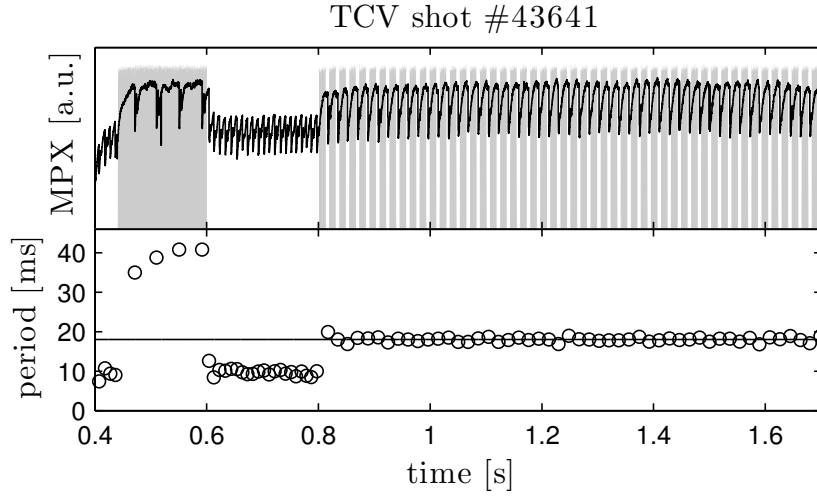


Figure 7.2: Locking experiment with $\tau_{\text{pulse}} = 18$ ms and $w = 70\%$. The top plot shows the central soft x-ray measurement of the sawtooth cycle (black line) and the additional ECCD power (grey). The bottom plot depicts the sawtooth period (circles) and power modulation period (solid line). Instantaneous locking is observed, and maintained throughout the discharge, as soon as the gyrotron modulation is enabled at $t = 0.8$ s.

experiment is commenced by injecting modulated power, with a certain prescribed power level, modulation period and duty cycle.

7.4.1 Individual discharges

Based on the prediction in figure 7.1, the initial modulation is chosen at $\tau_{\text{pulse}} = 18$ ms and $w = 70\%$. This modulation is commenced at 0.8 s and is held throughout the remainder of the discharge. The result is shown in figure 7.2. The top plot depicts the sawtoothed central soft x-ray measurement (black line) in comparison to the additional ECCD power (grey); the bottom plot depicts the derived sawtooth period in comparison to τ_{pulse} . It clearly demonstrates successful locking of the sawtooth, as the sawtooth period immediately synchronizes to the applied 18 ms pulse, and the sawtooth cycle is in phase with the modulation throughout the whole locking experiment. The crash always occurs when the power pulse is off, which is in agreement with the simulations in chapter 6. The sawtooth period from 0.8 s onwards has a mean of exactly 18.0 ms and a standard deviation of 0.53 ms. For comparison, the standard deviation for the baseline period (between 0.6 s and 0.8 s) is 0.67 ms.

In an attempt to map the experimental locking range, in the next discharge the modulation period is varied in three steps from 15 ms to 25 ms to 35 ms, for a fixed 80% duty cycle. Hence, the upper right part of figure 7.1(a) is explored. The result in figure 7.3 shows that the sawtooth period locks nearly instantaneous to 15 ms and 25 ms, whereas there is some transient behaviour before it locks at 35 ms. Similar transients have been observed in simulation, such as the green response in figure 6.3(a). A possible explanation of this rather slow response, is that the chosen power modulation

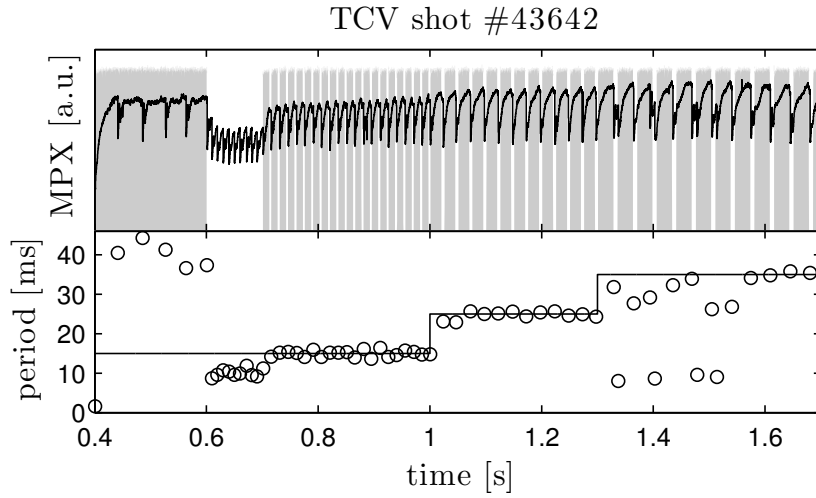


Figure 7.3: Locking experiment with steps in τ_{pulse} (from 15 ms to 25 ms to 35 ms) for a fixed $w = 80\%$, starting at $t = 0.7$ s. The sawtooth period successfully locks to each modulation, although the transients differ.

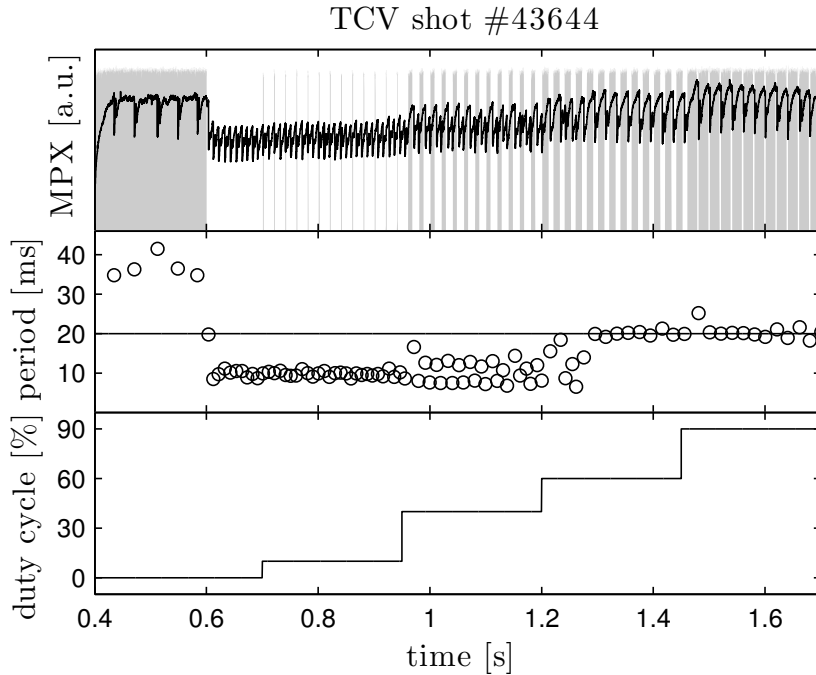


Figure 7.4: Experimental result showing the effect of the duty cycle (bottom plot) on the locking of the sawtooth. At $t = 0.7$ s the gyrotron modulation is enabled. Given a fixed $\tau_{\text{pulse}} = 20$ ms, no locking is observed for 10% and 40% duty cycles, whereas the period does lock for 60% and 90% duty cycles (middle plot).

is presumably on the edge of the locking range.

Similarly, the lower part of the locking range is explored during a discharge with a constant modulation period (20 ms) and stepwise variations of the duty cycle (from 10% to 40% to 60% to 90%). As can be seen in figure 7.4, the sawtooth is hardly

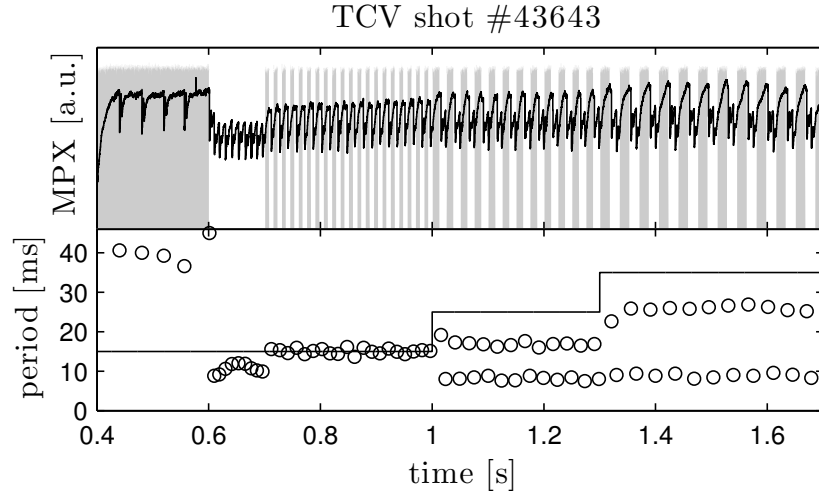


Figure 7.5: Experimental result with steps in the modulation period τ_{pulse} and a constant $w = 50\%$. During the modulation phase τ_{pulse} is stepped up from 15 ms (0.7 s – 1.0 s) to 25 ms (1.0 s – 1.3 s) to 35 ms (1.3 s – 1.7 s). Near instantaneous locking is observed for $\tau_{\text{pulse}} = 15$ ms. For 25 and 35 ms an alternating period is observed, of which the sum of the two successive period matches the modulation period.

affected by a 10% duty cycle, and the period does not lock to a 40% duty cycle either. However, locking does occur for the 60% and 90% duty cycle, the former after a short transient. Note that both figure 7.3 and 7.4 again confirm that in a locked situation the sawtooth crash always occurs when the power pulse is off.

It is interesting to note that the sawtooth period itself seems to behave in a periodic way for $\tau_{\text{pulse}} = 20$ ms and $w = 40\%$, i.e. from 0.95 s to 1.2 s in figure 7.4. The sawtooth period repeats itself every two crashes. This behaviour is more clearly observed in the discharge shown in figure 7.5, where modulation period is increased from 15 ms to 25 ms to 35 ms, given a fixed 50% duty cycle. The sawtooth locks on the 15 ms period, but for the other settings the sawtooth period alternates between two values. The sum of these values is equal to τ_{pulse} , and the smallest value is close to the 10 ms baseline period. This behaviour has also been observed in simulation [1]. A physical explanation of this phenomenon is that the off-time of the EC power pulse (which is, respectively, 12.5 ms and 17.5 ms in figure 7.5) is longer than the baseline period. As a consequence, two sawtooth crashes occur during this off-time, yielding an alternating sequence of long and short sawteeth.

The simulation results in chapter 6 have indicated that the peak power of the wave form generated by the gyrotron has a large effect on the size of the locking range. Experimentally this is verified by a simple test, of which the results are shown in figure 7.6. Given a fixed modulation period (23 ms) and duty cycle (70%) the preprogrammed gyrotron power is stepped down from 450 kW to 325 kW to 200 kW. In the 450 kW case the sawtooth period locks almost immediately to the 23 ms modulation period. When the power is lowered to 325 kW the sawtooth period temporarily unlocks,

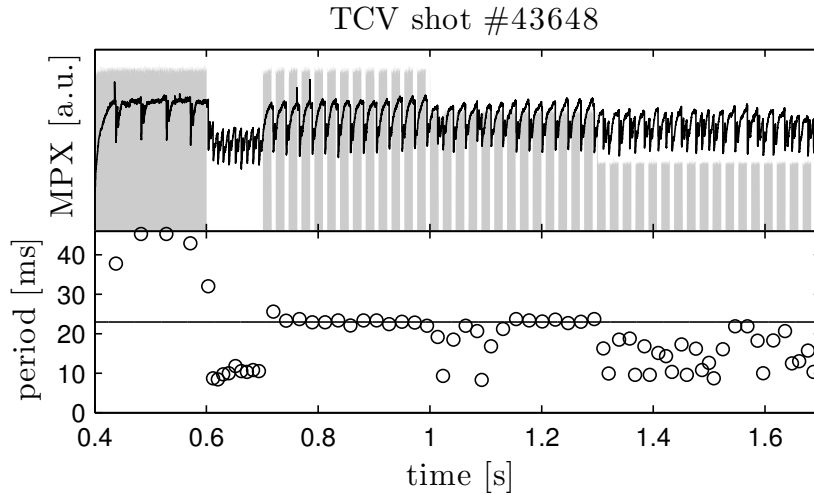


Figure 7.6: Locking experiment with downward steps in the gyrotron power, for fixed $\tau_{\text{pulse}} = 23$ ms and $w = 70\%$. The preprogrammed power is stepped down from 450 kW (0.7 s – 1.0 s) to 325 kW (1.0 s – 1.3 s) to 200 kW (1.3 s – 1.7 s) during the modulation phase. The sawtooth period locks for both 450 kW and 325 kW, but does not synchronize in the 200 kW case.

but locks again after a transient phase of about 0.15 s. This case is supposedly close to the edge of its locking range. For an even smaller power of 200 kW the locking is completely lost. This seems to confirm that the size of the locking range indeed depends on the gyrotron power level.

7.4.2 Experimental locking range

The above mentioned results, together with the results of numerous other experiments, are summarized in figure 7.7. In this diagram the squares indicate combinations of modulation period and duty cycle for which locking occurs, whereas the crosses indicate combinations for which locking does not occur. All squares lie in a sizeable, connected area in the bottom-right of the figure, indicated by the shaded area. This experimental locking range (which probably extends beyond the shaded area, but there are currently no data points available to verify this) shows a good resemblance with the simulation result in figure 7.1(a). There are basically two differences.

- The experiments do not show any higher periodicity behaviour, i.e. the sawtooth period does not lock at a constant value which is an integer times the modulation period τ_{pulse} .
- Instead, the (periodicity 1) locking range has a larger bulge towards combinations of small periods and large duty cycles, making the experimental locking range effectively somewhat wider.

The convergence speed predictions in figure 7.1(b) appear to be rather conservative compared to the experiments. In most situations locking occurred within one or two

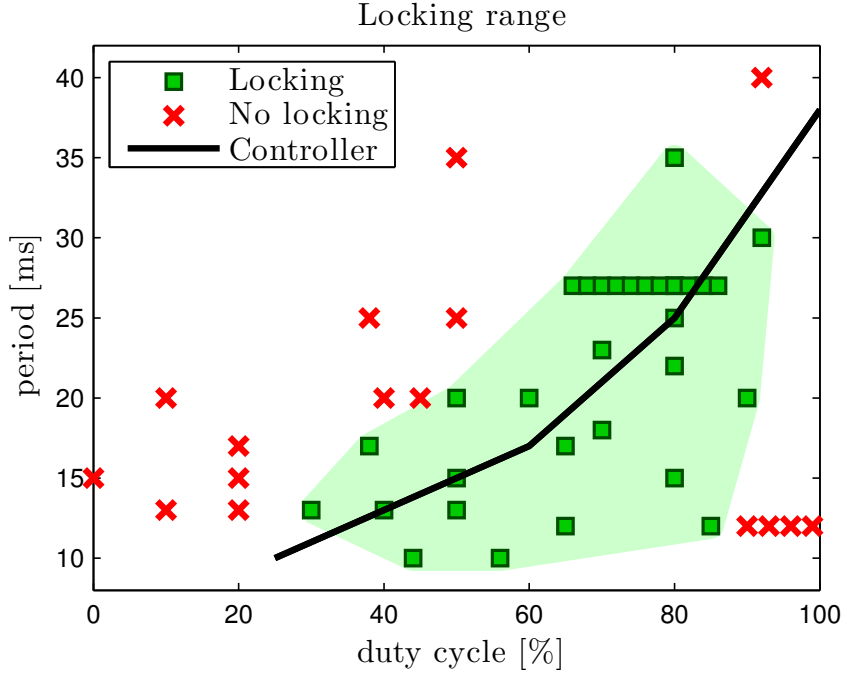


Figure 7.7: Experimentally determined sawtooth period locking range, as a function of the duty cycle and the power modulation period. Crosses indicate no locking, squares indicate successful locking. The open loop controller discussed in section 7.4.3 is based on the solid line.

crashes, in a worst case it took about 10 crashes. This fast convergence is in accordance to previous observations on TCV that a sawtooth cycle evolves effectively independent of its history [11]. Apparently, the sawtooth period dynamics in the considered TCV plasmas is faster than predicted by the sawtooth model.

7.4.3 Open-loop locking control

Analogous to the approach in section 6.4, the locking results summarized in figure 7.7 can be used in an open-loop sawtooth period controller. To this end a simple function is designed, i.e. the solid line in figure 7.7, which goes right through the locking range and covers a large spread of periods. To obtain a certain desired sawtooth period $\tau_{s,\text{ref}}$, the modulation period τ_{pulse} should be chosen identical to $\tau_{s,\text{ref}}$, while the controller function prescribes which accompanying duty cycle w should be used. Figure 7.8 shows a specific experimental result with this controller, where the desired period is preprogrammed to change linearly from 12 ms to 33 ms and back again, followed by a step to 25 ms. The sawtooth period locks within two crashes and then follows the changing modulation period very well, even for the step at 1.45 s. The top plot demonstrates that the sawtooth cycle remains in phase with the power modulation from 0.7 s onwards, and synchronizes in such a way that the crash always occurs when the pulse is off.

Note that in all presented results the locking phenomenon was insensitive to the jitter (or disturbance) on the sawtooth period. Hence, locking is robust against such

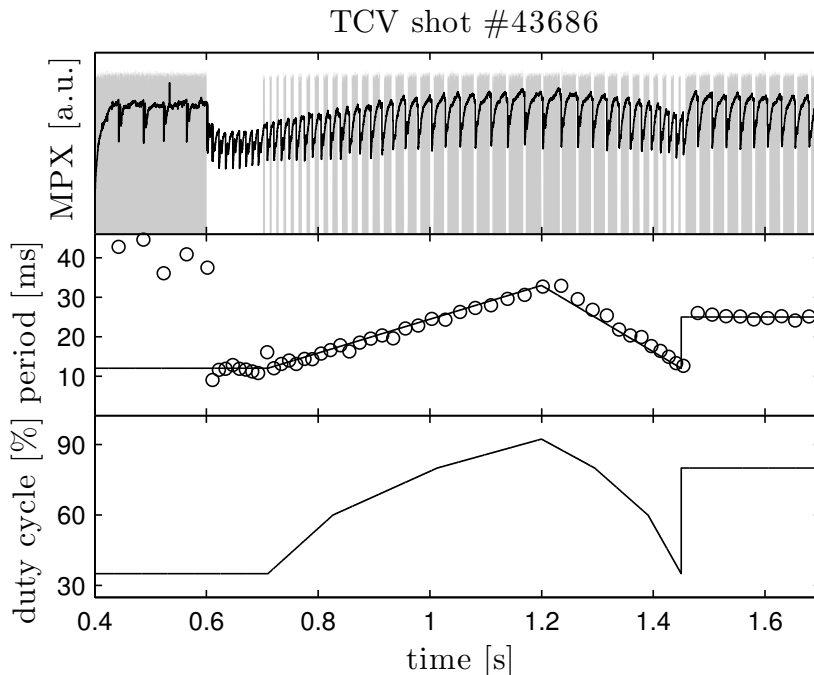


Figure 7.8: Open-loop locking control experiment, starting at 0.7 s. The requested period changes linearly and stepwise (middle plot), the corresponding duty cycle (bottom plot) is computed via the solid line in figure 7.7. The sawtooth cycle quickly locks and remains in phase with the modulation (top plot), resulting in consistent sawtooth period tracking.

disturbances, as has already been predicted in section 6.3.3. Moreover, convergence speed is generally very fast. This implies that the use of an open-loop locking controller is a fast and robust method to accurately control the sawtooth period, as demonstrated by figure 7.8. Additionally, this control method does not rely on any real-time sawtooth period detection algorithm, making it immune to missed or falsely detected crashes due to noisy diagnostics. This is clearly an advantage compared to sawtooth pacing [11] or control via the deposition location [4–6, 12, 13]. On the other hand, the locking range must first be identified in order to design and apply a successful locking controller.

7.5 Conclusions

Injection locking experiments have been carried out on TCV, demonstrating the success of sawtooth period locking, i.e. the sawtooth period indeed synchronizes with the modulation period of an externally applied EC wave source. The effects of the EC power, the modulation period and the duty cycle on the sawtooth period have been addressed, and the locking range for a specific power level has been identified. It has been shown that the experimental results are in good agreement with predictive simulations. More thorough comparisons, most notably on the phase during locking and the underlying evolution of the current density profile, remain to be carried out.

Since the experimentally obtained locking range, in terms of the modulation period and duty cycle, is a sizeable, well-defined region, it enables the derivation of a simple relation between duty cycle and period, which can be used as an open-loop sawtooth period controller. This relation has successfully been used in an experiment, achieving fast and accurate tracking of a continuously changing sawtooth period reference, which covers nearly the full range of achievable periods for the chosen operational conditions. The sawtooth cycle responds almost instantaneously to changes in the actuator settings, which suggests that the sawtooth period dynamics is very fast for the considered TCV plasmas. Furthermore, the locking controller is robust against disturbances, as the sawtooth remains locked despite the jitter on the sawtooth period. Moreover, locking does not require any diagnostic or model information. In conclusion, injection locking offers a novel open-loop approach to control the sawtooth period for physics studies or high-performance control schemes. Although the experiments have only demonstrated sawtooth period lengthening, the simulations in chapter 6 have shown that shortening is also possible.

On future fusion reactors, as well as on ITER, fusion-born helium ions will have a major effect on the sawtooth instability. These ions have been shown to considerably lengthen the sawtooth period [14, 15], which likely leads to NTM triggering [16]. The effectiveness of power modulation for sawtooth period control in such plasmas is an intriguing and important issue, which needs to be addressed in future research. To this end not only modulated ECCD should be employed, the effectiveness of power modulations of other actuators (like lower hybrid or ion cyclotron resonance heating) should also be investigated.

Finally, as already remarked in section 6.5, in literature various periodic actuation schemes have already been suggested to control Edge Localised Modes (ELMs), e.g. by means of modulated ECRH, vertical plasma kicks or periodic pellet injection [17–20]. The relation between these methods and injection locking is an interesting topic for future research, which may open new possibilities to control ELMs or other fusion-related problems.

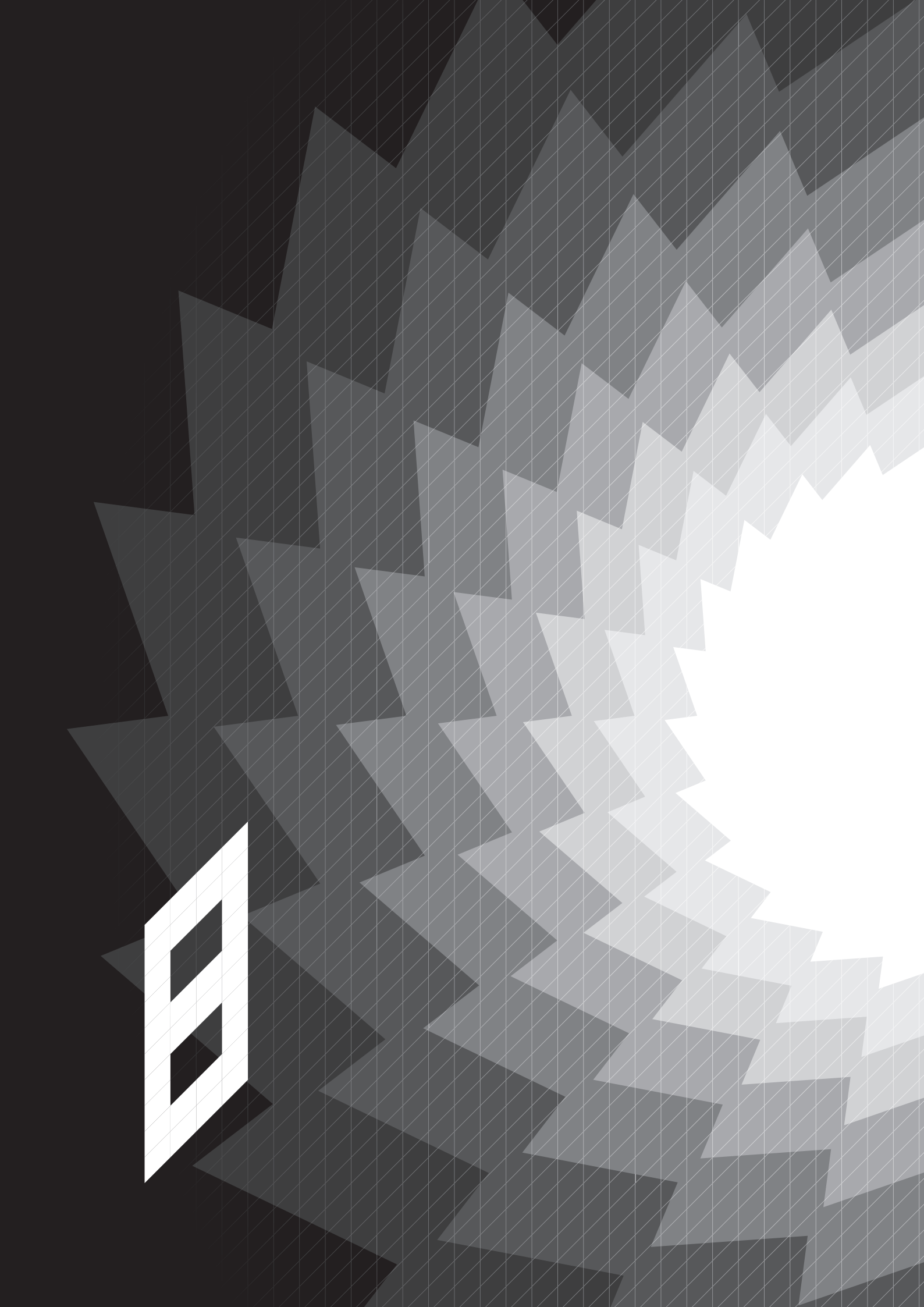
Acknowledgments

This work was supported in part by the Swiss National Science Foundation, in part by NWO, ITER-NL and the European Communities under the contract of the association Euratom/FOM and in part sponsored by the Vrije Universiteit Brussel, dept. ELEC, Fund for Scientific Research (FWO-Vlaanderen), the Flemish Government (Methusalem 1), and the Belgian Federal Government.

References

- [1] Witvoet G. *et al.* 2011 *Nucl. Fusion* **51**(10) 103043
- [2] Mück A. *et al.* 2005 *Plasma Phys. Control. Fusion* **47**(10) 1633

- [3] Angioni C. *et al.* 2003 *Nucl. Fusion* **43**(6) 455
- [4] Lennholm M. *et al.* 2009 *Phys. Rev. Lett.* **102**(11) 115004
- [5] Paley J.I. *et al.* 2009 *Plasma Phys. Control. Fusion* **51**(5) 055010
- [6] Witvoet G. *et al.* 2011 *Nucl. Fusion* **51**(7) 073024
- [7] van der Pol B. 1934 *Proc. IRE* **22**(9) 1051
- [8] Adler R. 1973 *Proc. IEEE* **61**(10) 1380
- [9] Kurokawa K. 1973 *Proc. IEEE* **61**(10) 1386
- [10] Lauret M. *et al.* 2011 *Submitted to Phys. Rev. Lett.*
- [11] Goodman T.P. *et al.* 2011 *Phys. Rev. Lett.* **106**(24) 245002
- [12] Witvoet G. *et al.* 2011 *Accepted for publication in Nucl. Fusion*
- [13] Bolder J.J. *et al.* 2011 *Submitted to Nucl. Fusion*
- [14] Graves J.P. *et al.* 2009 *Phys. Rev. Lett.* **102**(6) 065005
- [15] Nave M.F.F. *et al.* 2002 *Nucl. Fusion* **42**(3) 281
- [16] Sauter O. *et al.* 2002 *Phys. Rev. Lett.* **88**(10) 105001
- [17] Horton L.D. *et al.* 2004 *Plasma Phys. Control. Fusion* **46**(12B) B511
- [18] Degeling A.W. *et al.* 2003 *Plasma Phys. Control. Fusion* **45**(9) 1637
- [19] Lang P.T. *et al.* 2004 *Plasma Phys. Control. Fusion* **46**(11) L31
- [20] Lang P.T. *et al.* 2003 *Nucl. Fusion* **43**(10) 1110



Conclusions, discussion and outlook

This thesis addressed the modelling, detection and control of the sawtooth instability, which is a repetitive reorganization of the core of a tokamak plasma. Its periodicity affects various other plasma processes, such as the confinement of α particles (energetic helium) in the plasma core, the exhaust of thermal helium ash and the triggering of NTMs. As such, control of this sawtooth period is important for future fusion reactors.

8.1 Conclusions

A control-oriented model for the sawtooth period has been developed in chapter 2, based on the crash trigger condition of Porcelli *et al* [1] and the reconnection model of Kadomtsev [2]. This sawtooth model mimics the essential input–output behaviour of the sawtooth, while its complexity is relatively low. This model has been implemented in a real-time simulation environment, and is therefore suitable for control-oriented analysis of the underlying dynamics.

This sawtooth period dynamics has been described in the discrete-time framework, in which the sawtooth period is assumed to depend on inputs and outputs at previous crashes only. By means of linearizations around numerous operating points the frequency response functions in this crash-to-crash representation have been estimated, upon which different controller designs have been based.

First, the design of a linear controller, using the deposition location as control variable, has been discussed in chapter 2. Due to its low complexity this controller is easy to implement. Its parameters have been optimized with respect to stability, performance and robustness for each individual operating point. The designed controller is robust against small disturbances and uncertainties, but its performance is limited due to the large variations in the DC-gain of the sawtooth dynamics. This is especially true when the mirror launcher, i.e. the actuator for the deposition location, is slow compared to the sawtooth period, as is the case on most present-day tokamaks. For some operating points the settling time of the sawtooth period can then be in the order of 20 s or more.

Alternative control strategies to improve this performance have been suggested in chapter 3. Using gain-scheduling and feedforward techniques, with the deposition

location as control variable, zero steady-state errors have been achieved with settling times of around 0.35 s (given realistic TEXTOR settings) throughout the whole operating regime. Similar results have been obtained using the ECCD power level as control variable, in combination with a low-complexity linear controller. Moreover, the possibilities of high-performance multivariable control have been explored. These control strategies are particularly useful for future fusion reactors, where uncertainties are small and performance requirements are tight.

However, the above controllers are only applicable in a part of the total operating space, and can only handle a limited amount of disturbances and plasma variations. Experimental devices call for more robust approaches. Therefore, in chapter 4 a model-free adaptive optimization scheme based on online estimation of a cost function has been designed, which is known as extremum seeking control. Extensive simulation results have demonstrated its high robustness against disturbances and variations, which makes it readily applicable to present-day tokamaks. The expense of this robustness is a degraded closed-loop performance compared to the controllers in chapter 2 and 3.

All the above feedback controllers have been validated in real-time simulations, using the developed sawtooth model. Their future implementations on tokamak experiments require real-time sensing of the sawtooth period. To this end a sawtooth crash detection and period determination algorithm has been developed in chapter 5. Since this algorithm is based on multi-scale wavelet analysis, it can robustly detect various types of sawtooth crashes with a minimal amount of delay. Moreover, thanks to the additional maxima chain, the actual time instant of the crash can be determined with high accuracy. Offline application of the algorithm to TEXTOR ECE data has indeed demonstrated its success.

In addition to the feedback control techniques, this thesis has also introduced injection locking [3] as a novel open-loop control approach for the sawtooth period. In this approach the ECCD power is modulated with a certain period and duty cycle, given a fixed deposition location; under some conditions the sawtooth period locks (i.e. synchronizes) to the modulation period. Chapter 6 has presented extensive locking simulations with the Kadomtsev–Porcelli sawtooth model, revealing that the locking range is particularly large close to the $q = 1$ surface. The sawtooth period has been both lengthened and shortened, depending on the fixed deposition location. Similar periods as with continuous wave have been achieved, while requiring (time-averaged) less power. Moreover, the simulations have shown that this method yields fast convergence, and is quite robust against disturbances and variations.

Experimental proof of sawtooth period locking has been given in chapter 7, which has presented results from experiments on the TCV tokamak. These results are in good agreement with the simulations. Based on the identified locking range a simple open-loop locking controller has been derived, which has been shown to yield fast and accurate tracking of a constantly varying sawtooth period reference signal.

8.2 Discussion

A feedback controller design starts with the derivation of a model describing the input–output behaviour of the to-be-controlled system. Such a model does not necessarily have to be a comprehensive physics-based model; on the contrary, a simple model is often preferred, as long as its dynamics is representative of the actual behaviour of the system. The relatively simple Kadomtsev–Porcelli sawtooth model used in this thesis, which was based on the work presented in [4], is a good example of such a control-oriented model. It offers a valuable level of detail, as it mimics the essential input–output behaviour of the sawtooth. This has been confirmed by the comparison with the experimental locking results in chapter 7. As such, this model provides a good basis for controller design.

The controllers presented in this thesis cover a broad spectrum, varying from high-performance to high-robustness approaches. As mentioned before, the high-robustness controller is very suitable for present-day experimental tokamaks, where disturbances and uncertainties in plasma conditions are large and requirements are less stringent. In contrast, the high-performance approaches are foreseen to be useful for future fusion reactors, where plasmas are reproducible and predictable, and settling times and accuracy will be important. However, as mentioned in chapter 1, an accurate description of these requirements for any of these devices has not yet been formulated by the fusion community. Consequently, the presented controllers cannot be assessed objectively. At present, it is unknown under which circumstances a sawtooth period controller should work, and what to expect from it in terms of performance and robustness. Defining these requirements is a key element in future research on sawtooth control. This will involve, e.g. identification of disturbances, quantification of the plasma uncertainties, and defining bounds on accuracy and settling times.

In this thesis the feedback controllers are explicitly described in the discrete-time domain, i.e. they only intervene at a sawtooth crash measurement. Consequently, it always takes a number of sawtooth crashes before the period has converged to a desired value, even for the high-performance designs. Although this is acceptable in most situations, one should be aware that it takes just one long sawtooth to trigger an NTM. Strictly speaking, this can only be avoided when the closed loop converges *within* a sawtooth cycle. To this end the sampling rate of the controller has to be increased, i.e. there should be multiple period measurements *between* sawtooth crashes. This could be obtained by using real-time MSE (motional Stark effect) measurements, most likely in combination with an observer, such as RAPTOR [5]. By real-time reconstruction of current density profiles the next occurrence of a crash can be predicted, and the actuator setting (like deposition location or gyrotron power) can be adjusted in response to that. Derivation of such sawtooth period observers, and subsequent high-performance controller designs, requires further research.

In contrast to the feedback designs, the experimental results in chapter 7 have indicated that injection locking often converges within just one or two crashes. The power

modulation intervenes within a sawtooth cycle right from the start, and only appears to be restricted by the speed of the sawtooth period dynamics, which is generally very fast (especially for small tokamaks). Moreover, the locking simulations and experiments have indicated that the approach is robust against disturbances and plasma variations. Finally, injection locking does not require any sawtooth measurement, and is therefore insensitive to measurement noise. This is clearly a big advantage of this approach.

As such, sawtooth period locking is perhaps the most promising control approach in this thesis, but also the least understood. The feedback controller designs are based on well-defined concepts of stability, robustness and performance, which provide *a priori* guarantees on the closed-loop behaviour. For sawtooth period locking such a systematic approach does not exist yet; the open-loop controllers are merely based on intuition. Although there is a clear resemblance with dynamic oscillators in circuit theory [3], a full understanding of the underlying physics is lacking. Hence, further research on sawtooth period locking is needed, in which the Kadomtsev–Porcelli model can play an important role. Moreover, application of this method on other, preferably larger, tokamaks could provide more insight in its possibilities.

Apart from that, the injection locking technique can also be extended in various directions. The ECCD modulation can be combined with a frequency locked loop (FLL), in which the duty cycle (or gyrotron power level) is adjusted by a feedback loop until the sawtooth cycle matches a desired frequency, i.e. until it is locked. Such an injection locked FLL (ILFLL) automatically searches for the locking range and thereby effectively increases the robustness. Moreover, injection locking can also be combined with a feedback loop on the EC mirror angle. Changes in the current density profile affects the deposition location, and thereby alters the locking range. By monitoring the inversion radius, such deposition variations can be estimated and the mirror angle can be adjusted accordingly. As such, the locking of the sawtooth period can be optimized, maintaining the deposition location close to $q = 1$ and thus keeping the locking range as large as possible. This again increases the robustness. Finally, the effect of modulated power sources on the sawtooth period should be explored for other actuators as well, such as ICRH and lower hybrid heating.

Another possible research direction is an extension or combination of the presented feedback controllers. In particular, the embedding of extremum seeking control in a multivariable control framework could be of interest. As mentioned in chapter 3, such a controller can combine a high performance control loop for the sawtooth period with a slow optimization loop for the requested power. This way the power consumption of the gyrotron can be minimized, yielding a more efficient tokamak. Hence, such an approach can be useful for future fusion reactors to increase the energy gain factor Q .

8.3 Outlook

The research in this thesis has focused on ordinary non-burning plasmas where the magnetic shear at $q = 1$ is the main trigger for the sawtooth crash. The presented

feedback control strategies have been tested and verified in simulation on a representative sawtooth model. In a next step of this research, these control strategies should be applied to a tokamak experiment, similarly as injection locking has been validated on TCV. Successful implementation of any of the presented control approaches on a tokamak creates a controlled environment in which new physics experiments can be conducted. Since we can force specific sawtooth periods (either constant or time-varying) onto the plasma, the influence of the period on other plasma processes can be investigated. This could lead to an increased insight in, e.g. NTM triggering, impurity accumulation and heat transport.

It should be noted that projected operation scenarios for future fusion reactors, such as DEMO, feature plasmas with $q > 1.5$ at their centre. Such reversed shear plasmas can exhibit an internal transport barrier, which improves the energy confinement. One of the claimed advantages of these advanced scenarios is that no sawteeth occur, due to the absence of the $q = 1$ surface, so that NTM triggering is avoided. This would allow for high pressures and high fusion yield. Note, however, that such scenarios also lack the advantages of the sawtooth, e.g. in terms of exhaust of helium ash and refuelling, which are important issues in a fusion reactor. Moreover, we point out that in some reversed shear discharges off-axis sawtooth-like MHD modes have been observed at $q = \frac{3}{2}$, $q = 2$ and $q = 3$ [6–8]. These high order modes could in principle also trigger NTMs. The control strategies in this thesis can be adapted to these off-axis annular sawteeth, and are therefore relevant for DEMO scenarios as well.

In any case, one of the major challenges in nuclear fusion for the coming years is the control of burning plasmas. A burning plasma has never been achieved on earth, but ITER is meant to change this. Sawteeth will appear in both the L-mode and H-mode ITER scenarios, and the corresponding sawtooth periods will be very long. The physics of the sawtooth oscillation in these burning plasmas will be different [9], due to the presence of fast particles [10], i.e. energetic α particles created by the fusion reaction. This raises the question how well the controllers derived in this thesis will perform in reactor-relevant plasmas. In future research, the effect of fast particles on the sawtooth dynamics should therefore be identified, a new sawtooth model should be derived and the implications for the feedback control approaches should be assessed. Similarly, the sensitivity of plasmas dominated by fast particles to injection locking should again be investigated. Moreover, the advancing insights in burning plasmas that ITER will return, will most likely lead to new requirements on sawtooth period controllers. These will have to be taken into account in future controller designs.

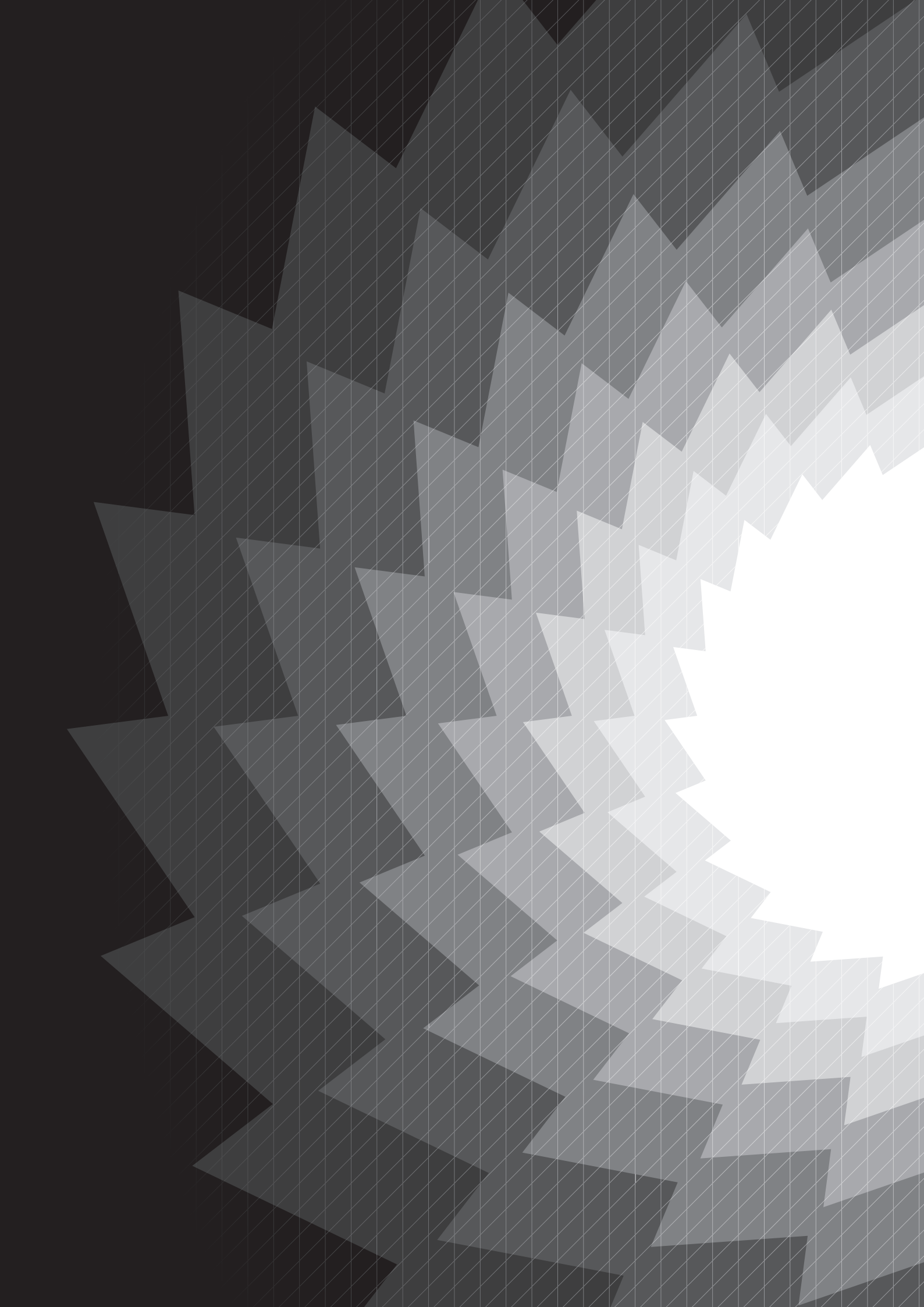
Such controller requirements also have repercussions on the actuator requirements. An example has been addressed in chapter 2, where it has been shown that a slow actuator can severely limit the achievable performance. Hence, fast and accurate EC mirror launchers (and gyrotrons) are essential; ideally, the launcher should respond faster than the smallest possible sawtooth period. Expected sawtooth periods on ITER vary from 10 s to several minutes (in the presence of fast particles) [1], which in itself is not likely to pose any tight requirements on the ITER launchers [11, 12]. However, the

ITER ECCD installation is not exclusively designed for sawtooth control, but will also be used for, e.g. NTM suppression and ELM control. Hence, given the limited amount of ECCD launchers on ITER, it is imaginable that an individual launcher should be able to quickly switch its deposition location from one resonant surface (e.g. $q = 1$) to another (e.g. $q = 3/2$ or $q = 2$), or even to the plasma edge (where ELMs occur). As such, it is desirable to have fast (i.e. high bandwidth) feedback controlled mirror launchers. These demands will have to be quantified in the near future, with which the current ITER launcher designs should be assessed. Moreover, high-level supervisory control loops have to be developed to decide upon the availability of the launchers for ELM, NTM or sawtooth control.

In any case, the performance of a sawtooth period controller, whether it is a feedback or locking controller, is always bounded by the capacities of the actuators. Note that none of the controllers presented here has been able to decrease the period more than with CW open-loop power injection; controllers only affect convergence speed, accuracy and robustness for operating points within the range of the actuator. Some experts believe that the amount of auxiliary power on ITER is not sufficient to keep the sawtooth period small enough, i.e. the range of the actuator will be insufficient. A controller will not be able to change this. If these speculations are really true, and ITER sawteeth indeed turn out to be too long, there is a clear need for new or more powerful actuators. Hence, development of such actuators is of uttermost importance, since the success of ITER might depend on it.

References

- [1] Porcelli F. *et al.* 1996 *Plasma Phys. Control. Fusion* **38**(12) 2163
- [2] Kadomtsev B.B. 1975 *Sov. J. Plasma Phys.* **1**(5) 389
- [3] Adler R. 1973 *Proc. IEEE* **61**(10) 1380
- [4] Merkulov O. 2006 *Control of plasma profiles and stability through localised electron cyclotron current drive* Ph.D. thesis Utrecht University
- [5] Felici F. *et al.* 2011 *Nucl. Fusion* **51**(8) 083052
- [6] de Baar M.R. *et al.* 1997 *Phys. Rev. Lett.* **78**(24) 4573
- [7] Meulenbroeks R.F.G. *et al.* 1999 *Phys. Plasmas* **6**(10) 3898
- [8] Günter S. *et al.* 2001 *Nucl. Fusion* **41**(9) 1283
- [9] Hender T.C. *et al.* 2007 *Nucl. Fusion* **47**(6) S128
- [10] Lennholm M. *et al.* 2009 *Phys. Rev. Lett.* **102**(11) 115004
- [11] Henderson M.A. *et al.* 2005 *J. Phys.: Conf. Ser.* **25**(1) 143
- [12] Henderson M.A. *et al.* 2008 *Nucl. Fusion* **48**(5) 054013



Bibliography

- P.S. Addison (2002). *The illustrated wavelet transform handbook: introductory theory and applications in science, engineering, medicine and finance* (Bristol: Institute of Physics).
- R. Adler (1973). ‘A study of locking phenomena in oscillators’. *Proceedings of the IEEE* **61**(10), 1380.
- C. Angioni, T.P. Goodman, M.A. Henderson and O. Sauter (2003). ‘Effects of localized electron heating and current drive on the sawtooth period’. *Nuclear Fusion* **43**(6), 455.
- K.B. Ariyur and M. Krstić (2003). *Real-time optimization by extremum-seeking control* (Hoboken, NJ: Wiley-Interscience).
- J. Artaud, V. Basiuk, F. Imbeaux, M. Schneider, J. Garcia, G. Giruzzi *et al.* (2010). ‘The CRONOS suite of codes for integrated tokamak modelling’. *Nuclear Fusion* **50**(4), 043001.
- K.J. Åström and L. Rundqwist (1989). ‘Integrator windup and how to avoid it’. In ‘*Proc. 1989 American Control Conference*’, (Pittsburgh, PA, USA), 1693–1698.
- K.J. Åström and B. Wittenmark (1997). *Computer-Controlled Systems: Theory and Design*. 3rd edn. (Englewood Cliffs, NJ: Prentice Hall).
- M.R. de Baar, G.M.D. Hogeweyj, N.J. Lopes Cardozo, A.A.M. Oomens and F.C. Schüller (1997). ‘Electron thermal transport barrier and magnetohydrodynamic activity observed in tokamak plasmas with negative central shear’. *Physical Review Letters* **78**(24), 4573.
- M. van Berkel, G. Witvoet, M.R. de Baar, P.W.J.M. Nuij, H.G. ter Morsche and M. Steinbuch (2011). ‘Real-time wavelet detection of crashes in limit cycles of non-stationary fusion plasmas’. *Fusion Engineering and Design*, in press.
- J.P.S. Bizarro and A.C.A. Figueiredo (1999). ‘The Wigner distribution as a tool for time–frequency analysis of fusion plasma signals: application to broadband reflectometry data’. *Nuclear Fusion* **39**(1), 61.

- J.P.S. Bizarro and A.C.A. Figueiredo (2008). ‘Time–frequency analysis of fusion plasma signals beyond the short-time Fourier transform paradigm: an overview’. *Fusion Engineering and Design* **83**(2-3), 350.
- J.J. Bolder, G. Witvoet, M.R. de Baar, N. van de Wouw, M.A.M. Haring, E. Westerhof, N.J. Doelman and M. Steinbuch (2011). ‘Robust sawtooth period control based on adaptive online optimization’. *Submitted to Nuclear Fusion* .
- C.S. Burrus, R.A. Gopinath and H. Guo (1998). *Introduction to wavelets and wavelet transforms: a primer* (Upper Saddle River, NJ: Prentice Hall).
- R. Buttery, T. Hender, D. Howell, R.L. Haye, S. Parris, O. Sauter, C. Windsor and JET-EFDA Contributors (2004). ‘On the form of NTM onset scalings’. *Nuclear Fusion* **44**(5), 678.
- A.P. Calderon (1964). ‘Intermediate spaces and interpolation, the complex method’. *Studia Math* **24**(2), 113.
- D.J. Campbell, D.F.H. Start, J.A. Wesson, D.V. Bartlett, V.P. Bhatnagar, M. Bures *et al.* (1988). ‘Stabilization of sawteeth with additional heating in the JET tokamak’. *Physical Review Letters* **60**(21), 2148.
- J. Canny (1986). ‘A computational approach to edge detection’. *IEEE Transactions on Pattern Analysis and Machine Intelligence* **PAMI-8**(6), 679.
- I.T. Chapman (2011). ‘Controlling sawtooth oscillations in tokamak plasmas’. *Plasma Physics and Controlled Fusion* **53**(1), 013001.
- I.T. Chapman, M.F. de Bock, S.D. Pinches, M.R. Turnyanskiy, MAST Team, V.G. Igochine *et al.* (2009a). ‘The effect of off-axis neutral beam injection on sawtooth stability in ASDEX Upgrade and Mega-Ampere Spherical Tokamak’. *Physics of Plasmas* **16**(7), 072506.
- I.T. Chapman, R.J. Buttery, S. Coda, S. Gerhardt, J.P. Graves, D.F. Howell *et al.* (2010). ‘Empirical scaling of sawtooth period for onset of neoclassical tearing modes’. *Nuclear Fusion* **50**(10), 102001.
- I.T. Chapman, V.G. Igochine, J.P. Graves, S.D. Pinches, A. Gude, I. Jenkins *et al.* (2009b). ‘Sawtooth control and the interaction of energetic particles’. *Nuclear Fusion* **49**(3), 035006.
- I.T. Chapman, I. Jenkins, R.V. Budny, J.P. Graves, S.D. Pinches, S. Saarelma and JET EFDA Contributors (2008a). ‘Sawtooth control using off-axis NBI’. *Plasma Physics and Controlled Fusion* **50**(4), 045006.
- I.T. Chapman, S.D. Pinches, J.P. Graves, R.J. Akers, L.C. Appel, R.V. Budny *et al.* (2007). ‘The physics of sawtooth stabilization’. *Plasma Physics and Controlled Fusion* **49**(12B), B385.
- I.T. Chapman, S.D. Pinches, H.R. Koslowski, Y. Liang, A. Krämer-Flecken, the TEXTOR Team and M. de Bock (2008b). ‘Sawtooth stability in neutral beam heated plasmas in TEXTOR’. *Nuclear Fusion* **48**(3), 035004.

- J.Y. Choi, M. Krstić, K.B. Ariyur and J.S. Lee (2002). ‘Extremum seeking for discrete-time systems’. *IEEE Transactions on Automatic Control* **47**(2), 318.
- C.K. Chui (1992). *An introduction to wavelets* (San Diego, CA: Academic press).
- G. Cima, R.V. Bravenec, A.J. Wootton, T.D. Rempel, R.F. Gandy, C. Watts and M. Kwon (1995). ‘Core temperature fluctuations and related heat transport in the Texas Experimental Tokamak-Upgrade’. *Physics of Plasmas* **2**(3), 720.
- I. Daubechies (1992). *Ten Lectures on Wavelets*, vol. 61 of *CMBMS-NSF Series in Applied Mathematics* (Philadelphia, PA: Siam publications).
- B. de Schutter (2000). ‘Minimal state-space realization in linear system theory: an overview’. *Journal of Computational and Applied Mathematics* **121**(1-2), 331.
- A.W. Degeling, Y.R. Martin, J.B. Lister, L. Villard, V.N. Dokouka, V.E. Lukash and R.R. Khayrutdinov (2003). ‘Magnetic triggering of ELMs in TCV’. *Plasma Physics and Controlled Fusion* **45**(9), 1637.
- D.L. Donoho and J.M. Johnstone (1994). ‘Ideal spatial adaptation by wavelet shrinkage’. *Biometrika* **81**(3), 425.
- E. Elong, M. Krstić and K.B. Ariyur (2000). ‘A case study of performance improvement in extremum seeking control’. In *Proc. 2000 American Control Conference*, (Chicago, IL, USA), 428–432.
- L.G. Eriksson, T. Johnson, M.L. Mayoral, S. Coda, O. Sauter, R.J. Buttery *et al.* (2006). ‘On ion cyclotron current drive for sawtooth control’. *Nuclear Fusion* **46**(10), S951.
- F. Felici, O. Sauter, S. Coda, B.P. Duval, T.P. Goodman, J.M. Moret, J.I. Paley and the TCV Team (2011). ‘Real-time physics-model-based simulation of the current density profile in tokamak plasmas’. *Nuclear Fusion* **51**(8), 083052.
- A.C.A. Figueiredo, M.F.F. Nave and EFDA-JET Contributors (2004). ‘Time–frequency analysis of nonstationary fusion plasma signals: a comparison between the Choi–Williams distribution and wavelets’. *Review of Scientific Instruments* **75**(10), 4268.
- G.F. Franklin, J.D. Powell and M.L. Workman (1998). *Digital control of dynamic systems*. 3rd edn. (Menlo Park, CA: Addison-Wesley).
- C.G. Gimblett and R.J. Hastie (1994). ‘Calculation of the post-crash state and $1\frac{1}{2}$ D simulation of sawtooth cycles’. *Plasma Physics and Controlled Fusion* **36**(9), 1439.
- S. von Goeler, W. Stodiek and N. Sauthoff (1974). ‘Studies of internal disruptions and $m = 1$ oscillations in tokamak discharges with soft-X-ray techniques’. *Physical Review Letters* **33**(20), 1201.
- T.P. Goodman, F. Felici, O. Sauter, J.P. Graves and the TCV Team (2011). ‘Sawtooth pacing by real-time auxiliary power control in a tokamak plasma’. *Physical Review Letters* **106**(24), 245002.

- J.P. Graves, C. Angioni, R.V. Budny, R.J. Buttery, S. Coda, L.G. Eriksson *et al.* (2005). ‘Sawtooth control in fusion plasmas’. *Plasma Physics and Controlled Fusion* **47**(12B), B121.
- J.P. Graves, I. Chapman, S. Coda, L.G. Eriksson and T. Johnson (2009). ‘Sawtooth-control mechanism using toroidally propagating ion-cyclotron-resonance waves in tokamaks’. *Physical Review Letters* **102**(6), 065005.
- A. Gude, S. Günter, M. Maraschek, H. Zohm and the ASDEX Upgrade Team (2002). ‘Temporal evolution of neoclassical tearing modes and its effect on confinement reduction in asdex upgrade’. *Nuclear Fusion* **42**(7), 833.
- A. Gude, S. Günter, S. Sesnic and ASDEX Upgrade Team (1999). ‘Seed island of neoclassical tearing modes at ASDEX Upgrade’. *Nuclear Fusion* **39**(1), 127.
- S. Günter, A. Gude, J. Hobirk, M. Maraschek, S. Saarelma, S. Schade, R.C. Wolf and ASDEX Upgrade Team (2001). ‘MHD phenomena in advanced scenarios on ASDEX Upgrade and the influence of localized electron heating and current drive’. *Nuclear Fusion* **41**(9), 1283.
- W.M. Haddad, V. Chellaboina and S.G. Nersesov (2006). *Impulsive and hybrid dynamical systems* (Princeton, NJ: Princeton University Press).
- K. Hallatschek and M. Zilker (1998). ‘Real time data acquisition with transputers and PowerPCs using the wavelet transform for event detection’. *IEEE Transactions on Nuclear Science* **45**(4 Part 1), 1872.
- H.J. Hartfuss, T. Geist and M. Hirsch (1997). ‘Heterodyne methods in millimetre wave plasma diagnostics with applications to ECE, interferometry and reflectometry’. *Plasma Physics and Controlled Fusion* **39**(11), 1693.
- R.J. Hastie (1997). ‘Sawtooth instability in tokamak plasmas’. *Astrophysics and Space Science* **256**(1), 177.
- T.C. Hender, J.C. Wesley, J. Bialek, A. Bondeson, A.H. Boozer, R.J. Buttery *et al.* (2007). ‘Chapter 3: MHD stability, operational limits and disruptions’. *Nuclear Fusion* **47**(6), S128.
- M.A. Henderson, R. Chavan, R. Heidinger, P. Nikkola, G. Ramponi, G. Saibene *et al.* (2005). ‘The front steering launcher design for the ITER ECRH upper port’. *Journal of Physics: Conference Series* **25**(1), 143.
- M.A. Henderson, R. Heidinger, D. Strauss, R. Bertizzolo, A. Bruschi, R. Chavan *et al.* (2008). ‘Overview of the ITER EC upper launcher’. *Nuclear Fusion* **48**(5), 054013.
- B.A. Hennen, E. Westerhof, P.W.J.M. Nuij, J.W. Oosterbeek, M.R. de Baar, W.A. Bongers *et al.* (2010). ‘Real-time control of tearing modes using a line-of-sight electron cyclotron emission diagnostic’. *Plasma Physics and Controlled Fusion* **52**(10), 104006.

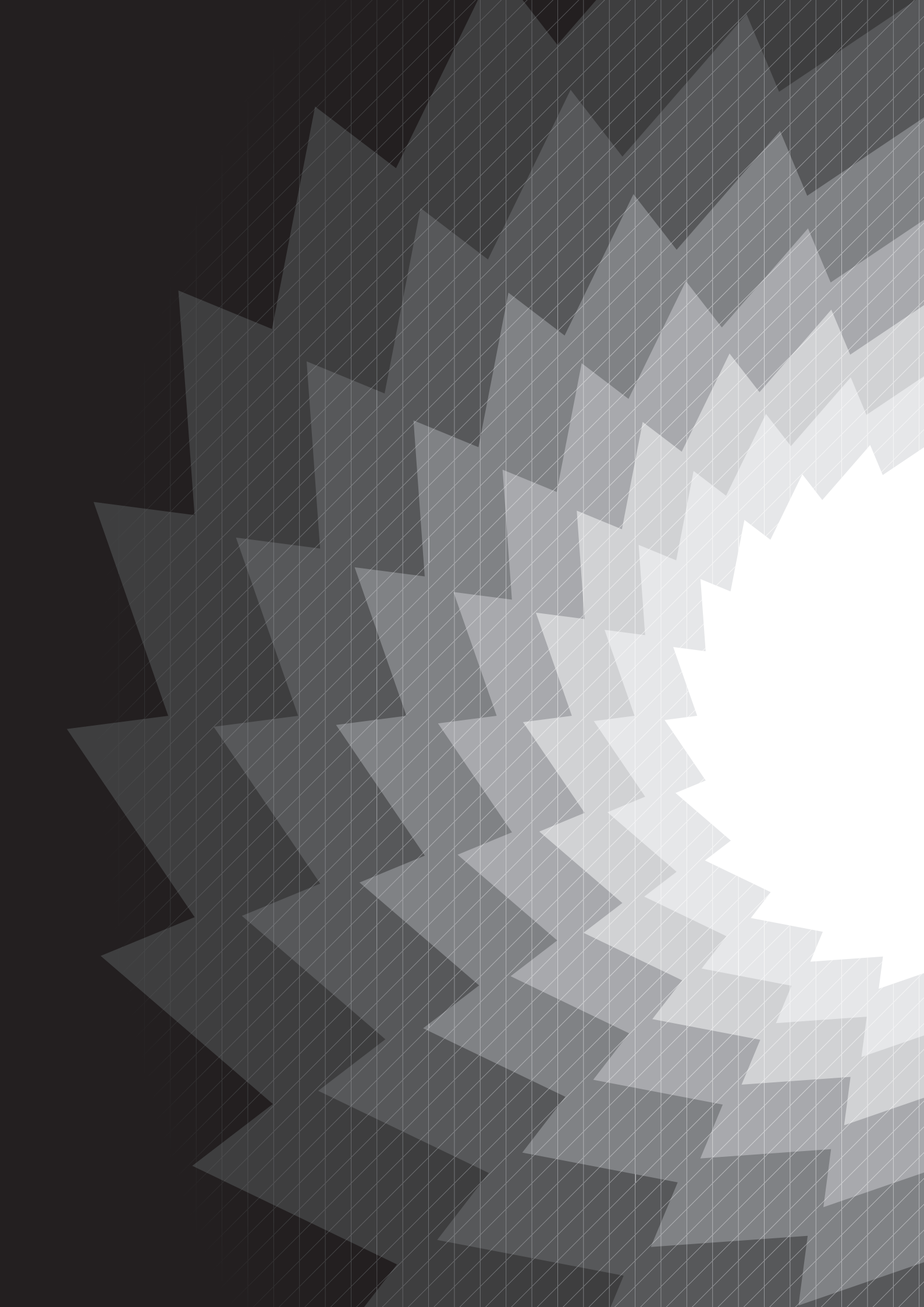
- B.A. Hennen, E. Westerhof, J.W. Oosterbeek, P. Nuij, D.D. Lazzari, G.W. Spakman *et al.* (2009). ‘A closed-loop control system for stabilization of MHD events on TEXTOR’. *Fusion Engineering and Design* **84**(2-6), 928.
- R.A. Horn and C.R. Johnson (1985). *Matrix Analysis* (Cambridge University Press).
- L.D. Horton, G.D. Conway, A.W. Degeling, T. Eich, A. Kallenbach, P.T. Lang *et al.* (2004). ‘ITER-relevant H-mode physics at ASDEX Upgrade’. *Plasma Physics and Controlled Fusion* **46**(12B), B511.
- M. Hovd and S. Skogestad (1994). ‘Sequential design of decentralized controllers’. *Automatica* **30**(10), 1601.
- Y. Ikeda, S. Ide, T. Suzuki, A. Kasugai, K. Takahashi, K. Kajiwara *et al.* (2002). ‘ECRF experiments for local heating and current drive by fundamental O-mode launch from the low-field side on JT-60U’. *Nuclear Fusion* **42**(4), 375.
- B.B. Kadomtsev (1975). ‘Disruptive instability in tokamaks’. *Soviet Journal of Plasma Physics* **1**(5), 389.
- W. Kasperek, M. Petelin, D. Shchegolkov, V. Erckmann, B. Plaum, A. Bruschi and ECRH Groups at IPP Greifswald and FZK Karlsruhe and IPF Stuttgart (2008). ‘A fast switch, combiner and narrow-band filter for high-power millimetre wave beams’. *Nuclear Fusion* **48**(5), 054010.
- T. Kass, S. Günter, M. Maraschek, W. Suttrop, H. Zohm and ASDEX-Upgrade Team (1998). ‘Characteristics of type I and type III ELM precursors in ASDEX upgrade’. *Nuclear Fusion* **38**(1), 111.
- H.K. Khalil (2002). *Nonlinear Systems*. 3rd edn. (Upper Saddle River, NJ: Prentice Hall).
- M. Krstić (2000). ‘Performance improvement and limitations in extremum seeking control’. *Systems & Control Letters* **39**(5), 313.
- M. Krstić and H.H. Wang (2000). ‘Stability of extremum seeking feedback for general nonlinear dynamic systems’. *Automatica* **36**(4), 595.
- K. Kurokawa (1973). ‘Injection locking of microwave solid-state oscillators’. *Proceedings of the IEEE* **61**(10), 1386.
- P.T. Lang, A.W. Degeling, J.B. Lister, Y.R. Martin, P.J.M. Carthy, A.C.C. Sips *et al.* (2004). ‘Frequency control of type-I ELMs by magnetic triggering in ASDEX Upgrade’. *Plasma Physics and Controlled Fusion* **46**(11), L31.
- P.T. Lang, J. Neuhauser, L.D. Horton, T. Eich, L. Fattorini, J.C. Fuchs *et al.* (2003). ‘ELM frequency control by continuous small pellet injection in ASDEX Upgrade’. *Nuclear Fusion* **43**(10), 1110.
- M. Lauret, F. Felici, G. Witvoet, T. Goodman, G. Vandersteen, O. Sauter, M. de Baar and the TCV team (2011). ‘Demonstration of sawtooth period locking in TCV plasmas’. *Submitted to Physical Review Letters* .

- J.D. Lawson (1957). ‘Some criteria for a power producing thermonuclear reactor’. *Proceedings of the Physical Society. Section B* **70**(1), 6.
- M. Lennholm, T. Blackman, I.T. Chapman, L.G. Eriksson, J.P. Graves, D.F. Howell *et al.* (2011). ‘Feedback control of the sawtooth period through real time control of the ion cyclotron resonance frequency’. *Nuclear Fusion* **51**(7), 073032.
- M. Lennholm, L.G. Eriksson, F. Turco, F. Bouquey, C. Darbos, R. Dumont *et al.* (2009a). ‘Closed loop sawtooth period control using variable ECCD injection angles on Tore Supra’. *Fusion Science and Technology* **55**(1), 45.
- M. Lennholm, L.G. Eriksson, F. Turco, F. Bouquey, C. Darbos, R. Dumont *et al.* (2009b). ‘Demonstration of effective control of fast-ion-stabilized sawteeth by electron-cyclotron current drive’. *Physical Review Letters* **102**(11), 115004.
- S. Mallat (2009). *A wavelet tour of signal processing: the Sparse way*. 3rd edn. (London: Academic Press).
- S. Mallat and S. Zhong (1992). ‘Characterization of signals from multiscale edges’. *IEEE Transactions on Pattern Analysis and Machine Intelligence* **14**(7), 710.
- The MathWorks, Inc. (2007). *Writing S-Functions*. Version 6.6.
- D.Q. Mayne (1973). ‘The design of linear multivariable systems’. *Automatica* **9**(2), 201.
- A. Merkulov, F.C. Schüller, E. Westerhof, M.R. de Baar, A. Krämer-Flecken, Y. Liang and TEXTOR Team (2004). ‘Sawtooth period control by localized non-inductive current drive’. In ‘*Proc. of Joint Varenna-Lausanne Int. Workshop on Theory of Fusion Plasmas*’, (Varenna, Italy), 279.
- O. Merkulov (2006). *Control of plasma profiles and stability through localised electron cyclotron current drive*. Ph.D. thesis, Utrecht University.
- R.F.G. Meulenbroeks, M.R. de Baar, M.N.A. Beurskens, H.J. de Blank, B.H. Deng, A.J.H. Donné *et al.* (1999). ‘Steady state off-axis sawtoothing in the Rijnhuizen Tokamak project’. *Physics of Plasmas* **6**(10), 3898.
- M. Misiti, Y. Misiti, G. Oppenheim and J. Poggi (2009). *Matlab Wavelet Toolbox™ User’s Guide*.
- A. Mück, T.P. Goodman, M. Maraschek, G. Pereverzev, F. Ryter, H. Zohm and ASDEX Upgrade team (2005). ‘Sawtooth control experiments on ASDEX Upgrade’. *Plasma Physics and Controlled Fusion* **47**(10), 1633.
- M.F.F. Nave, S. Ali-Arshad, B. Alper, B. Balet, H.J. de Blank, D. Borba *et al.* (1995). ‘MHD activity in JET hot ion H mode discharges’. *Nuclear Fusion* **35**(4), 409.
- M.F.F. Nave, N.N. Gorelenkov, K.G. McClements, S.J. Allfrey, B. Balet, D.N. Borba *et al.* (2002). ‘Fast particle effects on the sawtooth stability of JET DT discharges*’. *Nuclear Fusion* **42**(3), 281.

- M.F.F. Nave, H.R. Koslowski, S. Coda, J.P. Graves, M. Brix, R. Buttery *et al.* (2006). ‘Exploring a small sawtooth regime in Joint European Torus plasmas with counterinjected neutral beams’. *Physics of Plasmas* **13**(1), 014503.
- M.F.F. Nave, E. Lazzaro, R. Coelho, P. Belo, D. Borba, R.J. Buttery *et al.* (2003a). ‘Triggering of neo-classical tearing modes by mode coupling’. *Nuclear Fusion* **43**(3), 179.
- M.F.F. Nave, J. Rapp, T. Bolzonella, R. Dux, M.J. Mantsinen, R. Budny *et al.* (2003b). ‘Role of sawtooth in avoiding impurity accumulation and maintaining good confinement in JET radiative mantle discharges’. *Nuclear Fusion* **43**(10), 1204.
- O. Neubauer, G. Czymek, B. Giesen, P.W. Hüttemann, M. Sauer, W. Schalt and J. Schruoff (2005). ‘Design features of the tokamak TEXTOR’. *Fusion Science and Technology* **47**(2), 76.
- D. Nešić (2009). ‘Extremum seeking control: convergence analysis’. *European Journal of Control* **15**(3-4), 331.
- D. Nešić, Y. Tan, H. Moase and C. Manzie (2010). ‘A unifying approach to extremum seeking: adaptive schemes based on estimation of derivatives’. In ‘*Proc. 49th IEEE Conference on Decision and Control*’, (Atlanta, GA, USA), 4625–4630.
- Y. Nishimura, J.D. Callen and C.C. Hegna (1999). ‘Onset of high- n ballooning modes during tokamak sawtooth crashes’. *Physics of Plasmas* **6**(12), 4685.
- J.W. Oosterbeek, A. Bürger, E. Westerhof, M.R. de Baar, M.A. van den Berg, W.A. Bongers *et al.* (2008). ‘A line-of-sight electron cyclotron emission receiver for electron cyclotron resonance heating feedback control of tearing modes’. *Review of Scientific Instruments* **79**(9), 093503.
- J.I. Paley, J. Berrino, S. Coda, N. Cruz, B.P. Duval, F. Felici *et al.* (2009a). ‘Real time control of plasmas and ECRH systems on TCV’. *Nuclear Fusion* **49**(8), 085017.
- J.I. Paley, F. Felici, S. Coda, T.P. Goodman, F. Piras and the TCV Team (2009b). ‘Real time control of the sawtooth period using EC launchers’. *Plasma Physics and Controlled Fusion* **51**(5), 055010.
- J.I. Paley, F. Felici, S. Coda, T.P. Goodman and the TCV Team (2009c). ‘From profile to sawtooth control: developing feedback control using ECRH/ECCD systems on the TCV tokamak’. *Plasma Physics and Controlled Fusion* **51**(12), 124041.
- Y. Pan, U. Özgüner and T. Acarman (2003). ‘Stability and performance improvement of extremum seeking control with sliding mode’. *International Journal of Control* **76**(9-10), 968.
- W. Park, D.A. Monticello, E. Fredrickson and K. McGuire (1991). ‘Finite pressure effects on sawtooth oscillations’. *Physics of Fluids B* **3**(3), 507.
- A. Pironti and M.L. Walker (2005). ‘Control of tokamak plasmas: introduction to a special section’. *IEEE Control Systems Magazine* **25**(5), 24.

- B. van der Pol (1934). ‘The nonlinear theory of electric oscillations’. *Proceedings of the IRE* **22**(9), 1051.
- F.M. Poli, S.E. Sharapov, S.C. Chapman and JET-EFDA contributors (2008). ‘Study of the spectral properties of ELM precursors by means of wavelets’. *Plasma Physics and Controlled Fusion* **50**(9), 095009.
- F. Porcelli, D. Boucher and M.N. Rosenbluth (1996). ‘Model for the sawtooth period and amplitude’. *Plasma Physics and Controlled Fusion* **38**(12), 2163.
- W.J. Rugh and J.S. Shamma (2000). ‘Research on gain scheduling’. *Automatica* **36**(10), 1401.
- S. Santoso, E.J. Powers, R.D. Bengtson and A. Ouroua (1997). ‘Time-series analysis of nonstationary plasma fluctuations using wavelet transforms’. *Review of Scientific Instruments* **68**(1), 898.
- O. Sauter, E. Westerhof, M.L. Mayoral, B. Alper, P.A. Belo, R.J. Buttery *et al.* (2002). ‘Control of neoclassical tearing modes by sawtooth control’. *Physical Review Letters* **88**(10), 105001.
- K.R. Schultz (2006). ‘Why fusion? A discussion of energy alternatives’. *IEEE Control Systems Magazine* **26**(2), 32.
- S. Skogestad and I. Postlethwaite (2005). *Multivariable Feedback Control: analysis and design* (Chichester, UK: John Wiley).
- J.J.E. Slotine and W. Li (1991). *Applied nonlinear control* (Englewood Cliffs, NJ: Prentice Hall).
- J. Stober, M. Maraschek, G.D. Conway, O. Gruber, A. Herrmann, A.C.C. Sips *et al.* (2001). ‘Type II ELMy H modes on ASDEX Upgrade with good confinement at high density’. *Nuclear Fusion* **41**(9), 1123.
- G. Strang and T. Nguyen (1996). *Wavelets and filter banks* (Wellesley, MA: Wellesley-Cambridge Press).
- S.H. Strogatz (1994). *Nonlinear dynamics and chaos* (Boulder, CO: Westview Press).
- A. Sykes and J.A. Wesson (1976). ‘Relaxation instability in tokamaks’. *Physical Review Letters* **37**(3), 140.
- Y. Tan, W.H. Moase, C. Manzie, D. Nešić and I.M.Y. Mareels (2010). ‘Extremum seeking from 1922 to 2010’. In ‘*Proc. 29th Chinese Control Conference*’, (Beijing, China), 14–26.
- Y. Tan, D. Nešić and I. Mareels (2006). ‘On non-local stability properties of extremum seeking control’. *Automatica* **42**(6), 889.
- Y. Tan, D. Nešić and I. Mareels (2008). ‘On the choice of dither in extremum seeking systems: a case study’. *Automatica* **44**(5), 1446.
- M. Unser (1997). ‘Ten good reasons for using spline wavelets’. In ‘*Proc. SPIE*’, vol. 3169 (San Diego, CA, USA), 422–431.

- M. Unser (1999). ‘Splines: a perfect fit for signal and image processing’. *IEEE Signal Processing Magazine* **16**(6), 22.
- V.A. Vershkov and S.V. Mirnov (1974). ‘Role of impurities in current tokamak experiments’. *Nuclear Fusion* **14**(3), 383.
- M.L. Walker, D.A. Humphreys, D. Mazon, D. Moreau, M. Okabayashi, T.H. Osborne and E. Schuster (2006). ‘Emerging applications in tokamak plasma control’. *IEEE Control Systems Magazine* **26**(2), 35.
- J.A. Wesson and D.J. Campbell (2004). *Tokamaks*. 3rd edn. (Oxford: Oxford University Press).
- E. Westerhof, J.A. Hoekzema, G. Hogeweij, R. Jaspers, F. Schüller, C. Barth *et al.* (2003). ‘Electron cyclotron resonance heating on TEXTOR’. *Nuclear Fusion* **43**(11), 1371.
- E. Westerhof, O. Sauter, M.L. Mayoral, D.F. Howell, M.J. Mantsinen, M.F.F. Nave *et al.* (2002). ‘Control of sawteeth and triggering of NTMs with ion cyclotron resonance frequency waves in JET’. *Nuclear Fusion* **42**(11), 1324.
- G. Witvoet, M.R. de Baar, E. Westerhof, M. Steinbuch and N.J. Doelman (2011a). ‘Systematic design of a sawtooth period feedback controller using a Kadomtsev–Porcelli sawtooth model’. *Nuclear Fusion* **51**(7), 073024.
- G. Witvoet, M. Lauret, M.R. de Baar, E. Westerhof and M. Steinbuch (2011b). ‘Numerical demonstration of injection locking of the sawtooth period by means of modulated EC current drive’. *Nuclear Fusion* **51**(10), 103043.
- G. Witvoet, M. Steinbuch, M.R. de Baar, N.J. Doelman and E. Westerhof (2011c). ‘Sawtooth period control strategies and designs for improved performance’. *Accepted for publication in Nuclear Fusion* .
- G. Witvoet, M. Steinbuch, E. Westerhof, N.J. Doelman, M.R. de Baar and the TEXTOR team (2010a). ‘Closed loop control of the sawtooth instability in nuclear fusion’. In ‘*Proc. 2010 American Control Conference*’, (Baltimore, MD, USA), 1979–1984.
- G. Witvoet, E. Westerhof, M. Steinbuch, M.R. de Baar and N.J. Doelman (2010b). ‘Control oriented analysis and feedback control of a sawtooth instability model’. In ‘*Proc 16th Joint Workshop on Electron Cyclotron Emission and Electron Cyclotron Resonance Heating*’, (Sanya, China), 390–395.
- G. Witvoet, E. Westerhof, M. Steinbuch, N.J. Doelman and M.R. de Baar (2009). ‘Control oriented modeling and simulation of the sawtooth instability in nuclear fusion tokamak plasmas’. In ‘*Proc. 48th IEEE Conference on Decision and Control*’, (Shanghai, China), 1360–1366.



Summary

Feedback control and injection locking of the sawtooth oscillation in fusion plasmas

In this thesis various control strategies have been developed to control the period of the sawtooth oscillation in tokamak plasmas. This sawtooth instability is located in the core of nuclear fusion plasmas and manifests itself as a repetitive slow rise and sudden crash of the plasma core quantities, such as temperature and pressure. The sawtooth crash affects the exhaust of helium ash from and the fuelling of deuterium and tritium into the plasma core. Moreover, the crash can trigger secondary undesired instabilities, such as neoclassical tearing modes. These processes depend on the periodicity of the sawtooth oscillation, hence, control over the sawtooth period is essential to enable optimization of the plasma performance.

A control-relevant sawtooth model, which captures the dominant dynamics of the sawtooth cycle, has been developed and numerically implemented. This model is actuated via an electron cyclotron current drive (ECCD) term, characterized by two inputs: the amount of driven current and its deposition location. The output of the model is the sawtooth period. This sawtooth model mimics the static input–output behaviour observed on tokamaks, and has therefore been used as a case-study for the controller designs. Two different control strategies have been investigated: feedback control (closed loop) and injection locking (open loop).

Feedback control

In the closed loop approach, first the sawtooth period dynamics has been determined. Via dedicated step response simulations and the application of approximate realization techniques, the dynamic behaviour around various operating points has been identified and represented in the frequency domain. Next, three different feedback control approaches have been derived, based upon these identified systems:

Low complexity - First, a standard linear controller has been designed, considering only the deposition location as a control variable. The parameters of the chosen controller structure (PII) have been optimized based on frequency domain

specifications. The resulting closed loop is relatively robust, but its performance can sometimes be unsatisfactory whenever the ECCD mirror launcher, i.e. the actuator for the deposition location, is slow compared to the sawtooth period.

High performance - In a second approach the closed-loop performance has been improved by the employment of gain-scheduling, feedforward and anti-windup techniques. Alternatively, the amount of driven current has been used as a control variable, which yields a closed-loop performance improvement as well. Moreover, a multivariable controller design has been proposed to combine fast settling times of the sawtooth period with power efficiency. These high-performance control designs are particularly interesting for future fusion reactors.

High robustness - On experimental devices plasma uncertainties and disturbances are relatively large. For such applications a very robust feedback controller has been designed, based on extremum seeking. This adaptive controller makes online estimations of the sawtooth input–output behaviour via an external perturbation, based upon which the deposition location is adjusted to steer towards a desired sawtooth period. Various simulations have demonstrated the high robustness of the approach.

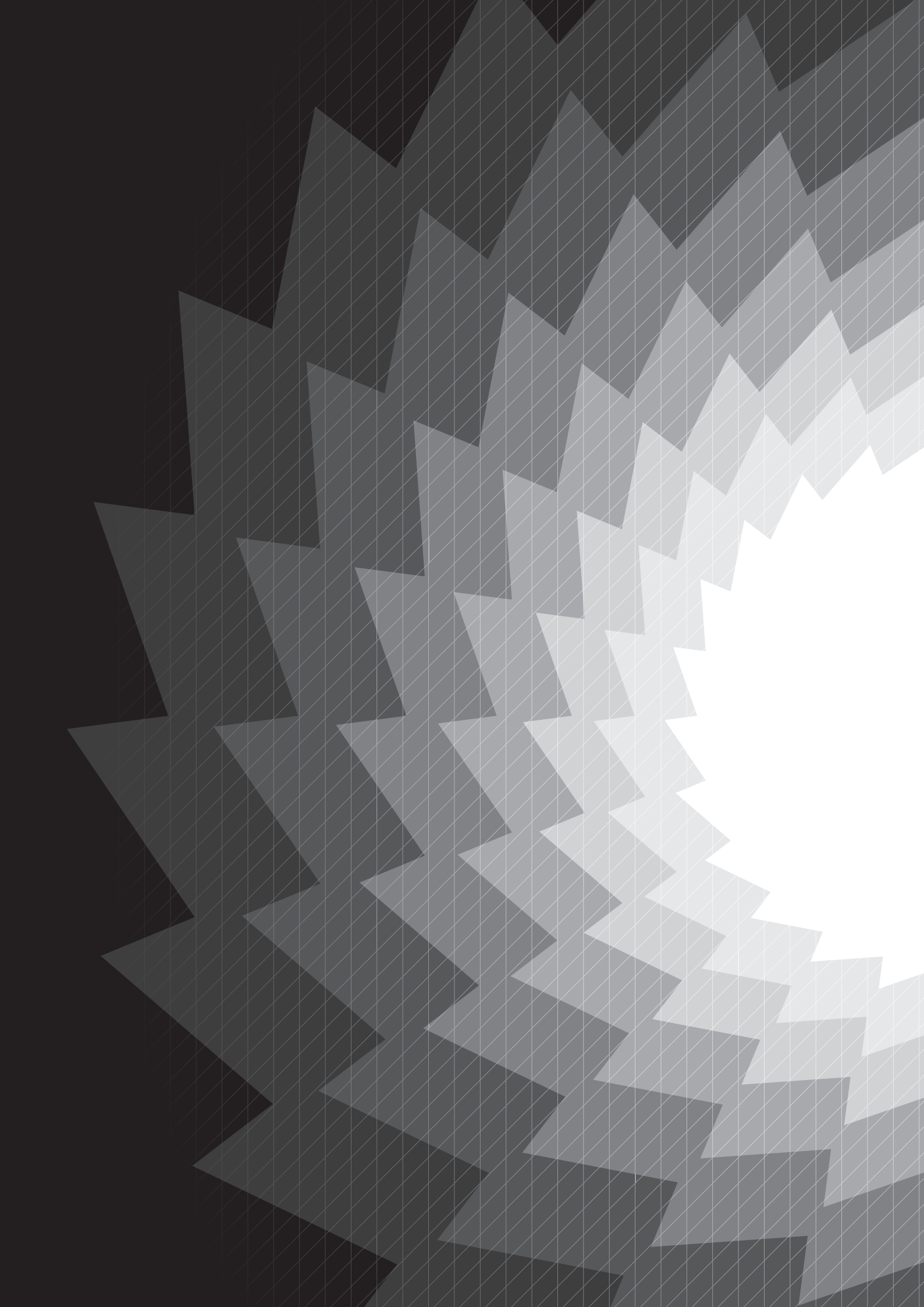
Injection locking

In addition, open-loop injection locking has been presented as an alternative sawtooth period control strategy. In this strategy, the deposition location is kept constant while the driven current (or gyrotron power) is modulated with a certain period and duty cycle. Extensive simulations have revealed that the sawtooth period can lock to the modulation period. All combinations of modulation period and duty cycle for which locking occurs define the locking range; its size typically depends on the deposition location. Similar sawtooth periods as with continuous wave ECCD can be achieved, while consuming time-averaged less power.

Sawtooth period locking can be both fast and robust; simulations have demonstrated convergence speeds within only a handful of crashes, while locking is maintained even in the presence of plasma variations or disturbances. These predictions have been validated by experimental results; injection locking of the sawtooth period has been demonstrated on TCV plasmas. The experimentally obtained time responses and locking range show strong resemblances with the predictive simulations.

Based on the identified locking range, an open-loop controller has been designed and implemented. Successful application to a TCV discharge has demonstrated that this controller can force a desired sawtooth period unto the plasma, even if this setpoint is slowly changing over time.

The results in this thesis form a basis for further research on sawtooth control. Future work includes the application of the feedback control strategies in tokamak experiments, and further investigation of the locking phenomenon.



Dankwoord

“Knowledge is in the end based on acknowledgement.”

Ludwig Wittgenstein

Zo, na jaren hard ploeteren zet ik dan bijna een punt achter een belangrijk hoofdstuk van mijn leven. Na 1785 uur in de trein zitten, waarvan 107 uren zinloos vertraagd waren, 8169 km op de vouwfiets resulterend in 3 lekke banden, 693.023 bytes aan m-files en 14.422.362.228 bytes aan overige data, 260 liter thee en 743 koppen soep ligt hier dan eindelijk mijn eigen boekje. Dit boekje is het resultaat van een mooi en bijzonder promotietraject dat ik alles behalve alleen heb afgelegd. De mensen die ik in die tijd heb mogen ontmoeten, en al dan niet mee heb mogen samenwerken, hebben mij gevormd als wetenschapper en als mens, en hebben daarmee direct of indirect meegewerkt aan de totstandkoming van de voorgaande 200 pagina’s. Tegen iedereen die zich hierdoor aangesproken voelt, wil ik zeggen: bedankt! Daarmee zou mijn dankwoord in principe al af kunnen zijn, maar desondanks wil ik aan een aantal mensen in het bijzonder nog even een pluim uitdelen.

Allereerst aan mijn promotoren, Maarten Steinbuch en Marco de Baar. Maarten, jouw vertrouwen en geloof in mijn capaciteiten zijn doorslaggevend geweest om aan deze promotie te beginnen. Ik wil je bedanken voor de moeite die je gedaan hebt om mij in Delft te kunnen stationeren, voor je enthousiasme en voor je interesse in mijn eigen ontwikkeling. Je bent een inspirator die mij zowel inhoudelijk als persoonlijk op de rails hebt gehouden. Marco, ik ben heel blij dat jij er als promotor bij bent gekomen en mede richting hebt gegeven aan mijn onderzoek. Bedankt voor je aanstekelijke passie voor fusie, je doelgerichtheid en je grote betrokkenheid. Zonder jou had ik het laatste jaar nooit zoveel papers uit kunnen poepen.

Mijn copromotor, Egbert Westerhof, ben ik ook veel dank verschuldigd. Egbert, jouw input in de afleiding en uitwerking van het model was onmisbaar. Je bent zagezegd het ‘fysisch geweten’ geweest in mijn onderzoek, en ik ben je dankbaar dat je altijd met een kritische blik naar de resultaten hebt gekeken. Bedankt voor je scherpe inzichten en je vertrouwen in die fanatieke regeltechnici uit Eindhoven.

Het grootste gedeelte van mijn promotietijd heb ik doorgebracht bij TNO in Delft, waar Niek Doelman een soort ‘tweede copromotor’ voor mij is geweest. Niek, bedankt

dat je mijn inhoudelijke sparring partner wilde zijn; bedankt voor de regelmatige overlegmomenten, je regeltechnische input en je heldere visie als ik even in de stress zat. Ook Ed Doppenberg en Remco den Breeje verdienen een pluim voor hun hulp bij het implementeren van het model in bruikbare C-code. Ik wil ook Machteld de Kroon en Jan Hoegge noemen voor het faciliteren van een werkplek in Delft. Bedankt dat ik deel mocht zijn van jullie afdelingen, en zo een uitgebreid kijkje in de boeiende TNO-keuken mocht nemen.

Ik heb tijdens mijn promotie met meerdere wijze mensen van gedachten mogen wisselen over mijn onderzoek. Okko Bosgra, Maurice Heemels en Nathan van de Wouw, bedankt voor jullie regeltechnische input en inzichten. Tony Donné, Niek Lopes Cardozo, Dick Hogewij en Hugo de Blank, bedankt dat jullie mij op fysisch gebied verder hebben willen en kunnen helpen. Gerd Vandersteen, bedankt voor je humor, je wilde locking-ideeën en de spannende experimenten op Tore Supra en TCV. I would also like to thank Gabriele d'Antona for being part of my promotion committee and giving feedback on the draft version of my thesis.

During my Ph.D. project I had the opportunity to visit many different tokamaks, and was even lucky to do experiments on some of them. This would not have been possible without the help of many people. I would like to thank Eugenio Schuster and Mike Walker for the chance to visit DIII-D and the contact we've had afterwards. My first attempts to play with plasmas at TEXTOR were only possible thanks to the commitment and skills of Hans Oosterbeek, Bart Hennen, Andreas Bürger and Pieter Nuij, and dozens of other people I'm probably forgetting now. Morten Lennholm and Gerardo Giruzzi, thank you for the valuable discussions and the chance to do experiments on Tore Supra. Finally, many thanks go to the TCV team, in particular Federico Felici, Tim Goodman, Olivier Sauter and Jon Graves, for a very fruitful collaboration, resulting in some thrilling experimental locking results.

Dit proefschrift had nooit zo dik kunnen worden zonder de hulp van een aantal studenten. Mijn dank gaat uit naar Imke, Michaël en Niek voor hun bijdragen aan dit proefschrift en de onderliggende kennisontwikkeling. Maar vooral ook naar Joost en Matthijs: jullie werk heeft uiteindelijk twee papers en daarmee twee hoofdstukken opgeleverd. Bedankt voor jullie geweldige inzet! Daarnaast wil ik ook mijn overige collega-fusie-fanatici binnen DCT bedanken, en dan met name Menno en Bart. Menno, bedankt voor de samenwerking, jouw ideeën over de zaagtand en de experimenten die we samen hebben gedaan. Bart, je bent een grote hulp geweest aan het begin van mijn promotie. Bedankt dat ik af en toe de oren van je kop mocht vragen en dat ik mocht meeliften op jouw succesvolle werk op TEXTOR.

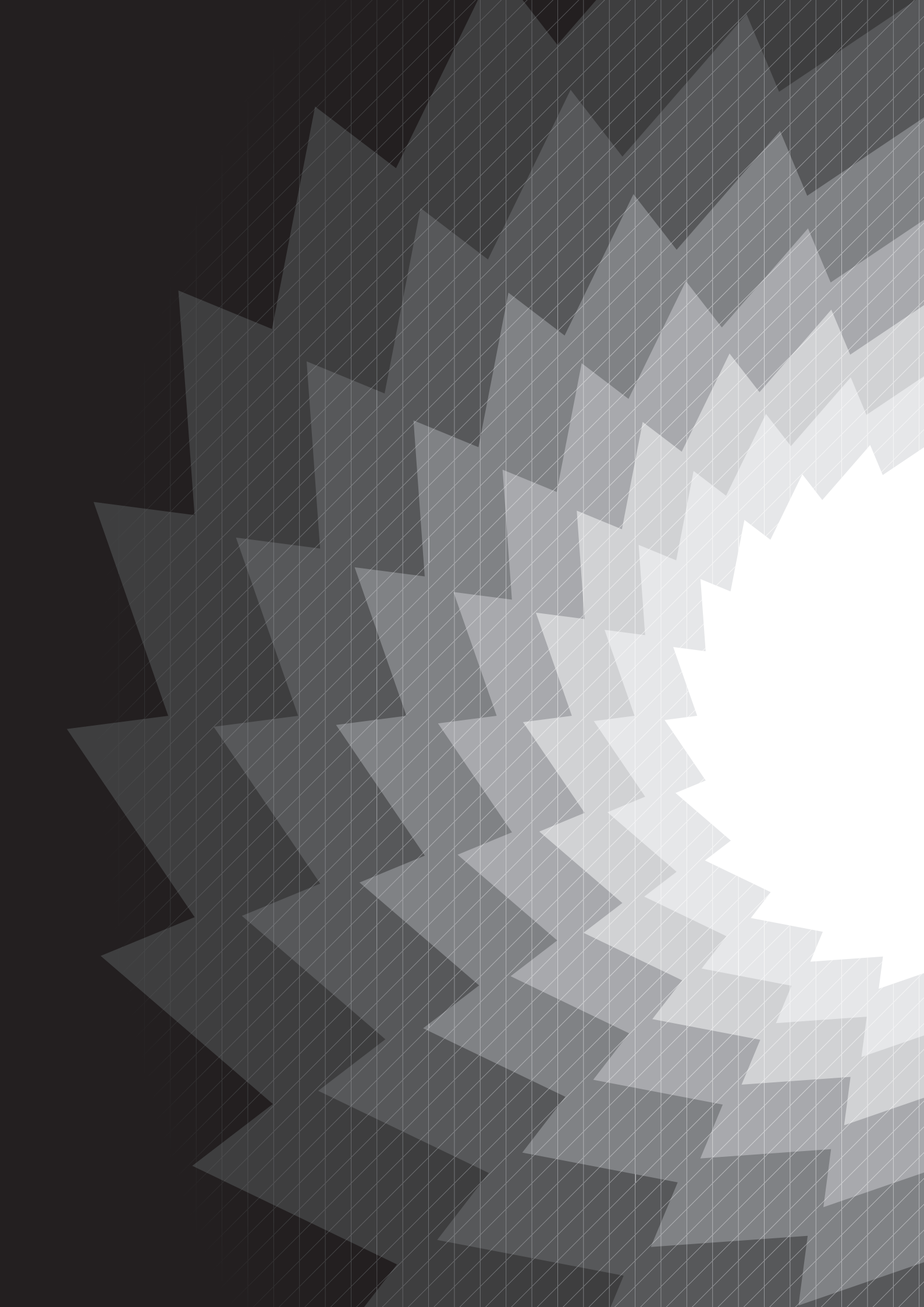
Door de mensen die ik dagelijks om mij heen had, ben ik elke werkdag met een glimlach op mijn gezicht de overvolle trein ingestapt. De gezellige lunches, de boeiende koffiepraatjes, de Seinfeld-sessies, de uitstapjes, ik heb er enorm van genoten. Ik wil de collega's van DCT en TNO daar hartelijk voor bedanken. In het bijzonder de kamergenoten die ik versleten heb. Bij TNO: Doctor Fringe en Master Rhinefield, en later Niek, Björn, Roger en Martijn. Bij DCT: Roel, Jeroen, Bram, Marcel en Zhenyu.

Allen bedankt voor de mooie herinneringen.

De laatste dankwoorden zijn voor de mensen die het verst van mijn onderzoek, maar het dichtst bij mij persoonlijk staan. Voor mijn vrienden, mijn broer, mijn zus, en alle aanhang die daar inmiddels bij hoort. En voor mijn ouders. Jullie hebben mij gevoed en gevormd, naar school gestuurd en in liefde en veiligheid laten opgroeien en ontwikkelen. Jullie hebben mij onvoorwaardelijk gesteund, mij op eigen benen leren staan, mij losgelaten toen ik naar het verre Eindhoven ging en achter mij blijven staan toen ik van studie switchte. Zie dit proefschrift maar als eerbetoon aan jullie steun. Pa en ma, bedankt!

En tot slot, mijn eigen kleine gezinnetje. Sietske, je bent al jaren mijn rots in de branding. In alle hoogte- en dieptepunten was jij erbij. Je motiveerde me, hield me scherp als ik dat nodig had, en twijfelde nooit aan mijn kunnen. Je spoorde me aan en remde me af, en hield mij zo gefocust op de dingen die belangrijk zijn. Zonder jouw onvoorwaardelijke liefde en steun had ik het nooit zo ver geschopt. En natuurlijk Rutger, mijn kleine boef. Je krijgt er allemaal maar weinig van mee, behalve dat je mij de laatste maanden een aantal papa-dagen hebt moeten missen. Sorry kerel. Maar stiekem was jij een grote stimulans om dit onderzoek netjes op tijd af te ronden. Ik hoop dat je later net zo trots zal zijn op jouw papa als papa is op jou.

Gert Witvoet
Oktober 2011



Curriculum Vitae

Gert Witvoet was born on March 27, 1981 in Leiden, the Netherlands. He completed his pre-university education in 1999 at Andreas College in Katwijk. After finishing the first two years of the study Industrial Engineering and Management Science, he started studying Mechanical Engineering at the Eindhoven University of Technology (TU/e) in 2001. In 2007 he received his Master's degree (*Cum Laude*) within the Control Systems Technology group. His Master's thesis was entitled "LMI-approaches to the performance analysis of reset control systems". This work has been awarded the Unilever Research Prize 2007, and was also nominated for the 2008 TU/e Final Project Award.

In April 2007, Gert Witvoet started his Ph.D. research within the Control Systems Technology Group at the department of Mechanical Engineering at the Eindhoven University of Technology. This research was performed in collaboration with the FOM-Institute for plasma physics Rijnhuizen and TNO Technical Sciences. The results are presented in this dissertation. In March 2008 he was awarded the Best Junior Presentation Award at the 27th Benelux Meeting on Systems and Control, for which he was again nominated the next two years. During his Ph.D. project he completed the educational program of the DISC graduate school. Moreover, he provided Motion Control lectures to Master students, and has been involved in various other teaching activities as well.

